

**Novel and Inexpensive Three-dimensional Velocimetry Techniques for  
Flows Visualization and Measurements**

Dissertation by

Andrés Alejandro Aguirre Pablo

In Partial Fulfillment of the Requirements

For the Degree of

Doctor of Philosophy

King Abdullah University of Science and Technology

Thuwal, Kingdom of Saudi Arabia

© October, 2018

Andrés A. Aguirre Pablo

All Rights Reserved

## **EXAMINATION COMMITTEE PAGE**

The dissertation of Andrés Alejandro Aguirre Pablo is approved by the examination committee.

Committee Chairperson: Professor Aamir Farooq

Committee Member: Professor Sigurdur Thoroddsen, Professor Wolfgang Heidrich,  
Professor Alfonso Castrejón-Pita



## **ABSTRACT**

Over the last 30 years, Particle Image Velocimetry (PIV) has become the most powerful tool to study velocity fields in fluid mechanics. This technique is non-intrusive requiring seeding the flow with small tracer particles. The hardware required for these sophisticated PIV methods is very expensive (CCD or CMOS high-speed cameras and lasers), and the present dissertation aims to develop novel and inexpensive alternatives.

The first part of this work investigates the use of multiple smartphones as a lower-cost Tomographic-PIV system for reconstructing 3D-3C velocity fields. We use colored shadows to imprint two or three different time-steps on the same image in a RGB-backlit configuration. We use commercially available Tomo-PIV software for the calibration, 3-D particle reconstruction, and particle-field correlations, to obtain three velocity components in a volume. The proposed system is tested with a vortex ring and the results are compared to stereoscopic-PIV for error estimations.

We expand this work to a high-speed time-resolved setup to obtain 3D-3C velocity fields in time. This improvement is possible using newer smartphones capable of recording high-speed video at HD resolution. The challenges of using such cameras are presented and tackled. The illumination system, testing flow and image processing is similar to the one presented in the first section. A benchmark of the smartphone system is carried out comparing it to a Tomo-PIV system capable of recording 4K video resolution.

A different approach is proposed to reconstruct a 3D-3C velocity field using a single color video camera. This technique uses chromatic structured light with color-gradients

projected perpendicularly with respect to the color camera. Thus, we encode the depth position of the particles with a different wavelength of light. Different light sources are used to produce such color gradients.

Finally, a variation of the previous technique is tested using a single monochromatic camera and structured volumetric illumination with spatially varying intensity profiles. This technique enables us to encode the depth position of every particle in their intrinsic brightness. The proposed system can achieve a depth resolution of 200 levels, i.e., an order of magnitude higher than previously proposed systems.

## **ACKNOWLEDGMENTS**

I would like to thank KAUST, as an institution, for supporting and believing in me since my undergraduate studies and giving me the chance to participate in this exciting and great vision for the Kingdom of Saudi Arabia. I want to acknowledge KAUST faculty and lecturers that helped me to grow as a person and a professional.

Especially, I would like to express my gratitude to Professor Sigg Thoroddsen for accepting me as part of his team in the High-Speed Fluids Imaging Laboratory, a place where I was able to expand my creativity and skills in the Lab. Thank you for your guidance, support and fruitful discussions along the way. Also thanks to my lab-mates and colleagues that were always there for a casual or work related discussion.

My appreciation goes to my friends at KAUST, they have become my family far from home, thanks for being there in the highs and lows.

Ultimately I want to thank my parents Hortensia and Carlos, my sister Karla, and my brother César. Without you, I wouldn't be where I am right now. Thanks for supporting and encouraging me to continue in this adventure. This work is for you.

## TABLE OF CONTENTS

<b>EXAMINATION COMMITTEE PAGE .....</b>	<b>2</b>
<b>ABSTRACT .....</b>	<b>3</b>
<b>ACKNOWLEDGMENTS.....</b>	<b>5</b>
<b>LIST OF ABBREVIATIONS .....</b>	<b>10</b>
<b>LIST OF ILLUSTRATIONS .....</b>	<b>11</b>
<b>LIST OF TABLES .....</b>	<b>22</b>
<b>Chapter 1 : Introduction.....</b>	<b>23</b>
1.1 Particle Image Velocimetry (PIV) for 2D and 3D measurements .....	23
1.2 Shake the box (4D Particle Tracking Velocimetry) .....	27
1.3 Single camera, three-dimensional particle tracking efforts.....	28
1.3.1 Three pin-hole aperture Defocused Particle Tracking.....	29
1.3.2 Image splitters .....	30
1.3.3 Depth estimation by optical aberrations.....	32
1.3.4 Plenoptic (light-field) cameras.....	33
1.3.5 Color coded-illumination .....	36
1.4 Motivation, dissertation structure and list of publications.....	40
<b>Chapter 2 : Tomographic PIV using Colored Shadows and Smartphones .....</b>	<b>43</b>
2.1 Experimental setup.....	44
2.1.1 Cameras and imaging systems.....	46
2.1.2 Vortex ring generator .....	48
2.1.3 Flow tracers.....	50
2.1.4 Illumination.....	51
2.1.5 Tomographic PIV calibration.....	53
2.1.6 Two and Three-Colored Shadows.....	54
2.1.7 Color crosstalk and Chromatic aberrations .....	58
2.2 Results .....	62
2.2.1 Pre-processing of images.....	62
2.2.2 Tomographic PIV reconstruction and correlation procedures.....	66
2.2.3 Estimating the acceleration field .....	73

2.2.4 Circulation and continuity verification. ....	74
2.2.5 Comparison with concurrent Stereoscopic PIV measurements.....	76
2.3 Conclusions .....	81
<b>Chapter 3 : High-Speed Time-resolved smartphone based Tomographic PSV system.</b> .....	<b>83</b>
3.1 Experimental Setup .....	84
3.1.1 Overall Tomographic setup.....	84
3.1.2 Cameras and imaging system synchronization.....	84
3.1.3 Challenges .....	85
3.1.4 Vortex Ring generator and flow tracers .....	89
3.1.5 Illumination and synchronization .....	90
3.1.6 Tomographic PIV calibration.....	90
3.2 Results .....	92
3.2.1 Pre-processing of the images.....	92
3.2.2 Tomographic PIV reconstruction and correlation procedures.....	94
3.2.3 Circulation, Continuity verification and Comparison with High-resolution Tomographic-PIV measurements .....	97
3.3 Conclusions .....	106
<b>Chapter 4 : 3D PIV/PTV using single color cameras .....</b>	<b>108</b>
4.1 Rainbow PIV/PTV using a linear chromatic filter and a single camera (first iteration). ....	109
4.1.1 Experimental setup.....	110
4.1.2 Reconstruction procedure. ....	112
4.1.3 Results .....	113
4.1.4 Areas of opportunity.....	114
4.2 Single camera: Rainbow 3D PIV/PTV using LCD projectors.....	114
4.2.1 3LCD technology .....	115
4.2.2 Projector specifications .....	115
4.2.3 Experimental setup.....	116
4.2.4 Particle Tracking and depth ( $z'$ ) estimation. ....	129
4.3 Conclusions .....	134
<b>Chapter 5 : Single-Camera 3-D PTV using particle intensities and monochromatic structured light (3D-IPTV) .....</b>	<b>137</b>
5.1 Experimental setup.....	138

5.2	Illumination sequence .....	139
5.3	Calibration.....	141
5.3.1	Light Intensity calibration with a 3-D calibration glass cube and particles ...	141
5.3.2	Intensity of Isolated Particles.....	142
5.3.3	3-D spatial Calibration cube.....	145
5.4	Computational algorithm .....	148
5.4.1	Obtaining the depth position $z'$ .....	148
5.4.2	Mapping functions: from digital $(x', y', z')$ to real world coordinates $(x, y, z)$ ... .....	153
5.5	Tracking results.....	155
5.5.1	Experiments in a rotational flow .....	155
5.6	Conclusions.....	158
	<b>Summary and overall conclusions.....</b>	<b>160</b>
	Future work .....	163
	<b>References .....</b>	<b>165</b>
<b>A</b>	<b>APPENDIX .....</b>	<b>171</b>
<b>A 1</b>	<b>: Matlab code “<i>Gausswiegthfunction_colorsquares.m</i>” for determining the characteristic color in RGB and HUE.....</b>	<b>177</b>
<b>A 2</b>	<b>: Matlab code “<i>savebins_trackmate_fillmiss.m</i>” for determining the digital depth of the particle based on the characteristic color detected in the previous algorithm. ....</b>	<b>179</b>
<b>A 3</b>	<b>: Matlab code “<i>Trackmate_read_finna_movingparticles_v4.m</i>” used in Chapter 5 to determine the digital depth (<math>z'</math>) of each particle based on its intrinsic brightness. ....</b>	<b>184</b>
<b>A 4</b>	<b>: Matlab function “<i>gauss_fit.m</i>” used as a reference to calculate <math>I_0</math>. ....</b>	<b>192</b>
<b>A 5</b>	<b>: Matlab function “<i>finnacentroid.m</i>” used to obtain the centroid of the particle and ventral intensities.....</b>	<b>192</b>
<b>A 6</b>	<b>: Matlab function “<i>ggfit.m</i>” that calculates a Gaussian on a matrix <math>x, y</math> locations around the center of the particle .....</b>	<b>193</b>
<b>A 7</b>	<b>: Matlab function “<i>ff_diff.m</i>” that finds RMS difference between data and fit... .....</b>	<b>193</b>

**A 8 : Matlab function ("*volume\_calibration.m*") to obtain mapping functions mdlX, mdlY and f1 using the cube and real particles ..... 195**

## LIST OF ABBREVIATIONS

2D-2C:	Two-Dimensional, Two Components
3D-3C:	Three-Dimensional, Three Components
CCD:	Charge-Coupled Device
CMOS:	Complementary Metal Oxide Semiconductor
DOE:	Diffractive Optic Element
HTML:	Hypertext Markup language
LCD:	Liquid Crystal Display
LED:	Light-Emitting Diode
LIF:	Laser Induced Fluorescence
MAD:	Mean Absolute Deviation
MART:	Multiplicative Algebraic Reconstruction Technique
MLOS:	Multiplied Line of Sight
PIV:	Particle Image Velocimetry
PSV:	Particle Shadow Velocimetry
PTV:	Particle Tracking Velocimetry
RMS:	Root Mean Square
ROI:	Region of Interest
s-CMOS:	Scientific Complementary Metal-Oxide Semiconductor



## LIST OF ILLUSTRATIONS

Figure 1.1. Experimental setup used by Willert and Gharib [3]. For the 2D Digital PIV system. (Image reproduced from Willert and Gharib [3]).....	24
Figure 1.2. Schematic representation of the tomographic PIV system proposed by Elsinga, et al. in 2006 for full 3D-3C flow visualization. (Image reproduced from Elsinga , et al.[6]) .....	26
Figure 1.3. Images of a water-jet flow by Estevadeordal and Goss captured using LED and colored shadows to encode time information and some of the 2D PIV results. (Image reproduced from Estevadeordal and Goss[17]) .....	27
Figure 1.4. STB results for water jet experiments after interpolating to an Eulerian grid ("Flowfit"). (a) Isosurfaces of vorticity $175 \text{ s}^{-1}$ and particle tracks extending five steps back in time. (b) Single time step tracks with a tail of ten time-steps colored by vertical acceleration. (c) Isosurfaces of vertical acceleration at a single time step. (Image reproduced from Schanz, et al.[21]) .....	28
Figure 1.5. Summary of some of the techniques using defocusing and pin-hole imaging for 3-D reconstruction. (a) Experimental setup used by Willert and Gharib [22] with a single camera. (b) Typical image produced by this system. (c) Visualization of some resulting pathlines. (a-c are reproduced from Willert, C. E., and Gharib, M. [22]). (d) Typical image captured by the defocusing technique proposed by Wu, M., et al [25]. (e) Some of the pathlines reconstructed for bacteria. (d,e are reproduced from Wu, M, et al.[25]). (f) Experimental setup used by Toprak, E., et al. [26]. (g) Typical image captured by bifocal imaging. (h) 3-D pathline of a single melanosome. (f-h images are extracted from Toprak, E., et al. [26]).....	30
Figure 1.6. (a) Image splitting system proposed by Kreizer and Liberzon [27]. Depicting a (1) tank and (2) driving belt system, (3) four view image splitter, (4) back-side mirrors, (5) a camera. (b) Results reported using the system in a. (Figures a and b are reproduced from Kreizer, M. and Liberzon, A.[27]). (c) Experimental setup proposed by Gao, Q., et al. [28]. (d) Typical multiple view image produced by the system in c. (d) Results presented by Gao, Q. et al. (c-e figures are reproduced from Gao, Q., et al. [28]).....	31
Figure 1.7. (a) Experimental setup proposed by Peterson, K., et al. [29] (b) Typical result from the system proposed in a. (Figures a and b are reproduced from Peterson, K., et al. [29]). (c) Experimental setup proposed by Maekawa, A. and Sakakibara, J. [31] (d) Typical image produced by the setup in c. (c) a typical result from the system proposed in c. (Figures c-e are reproduced from Maekawa, A. and Sakakibara, J. [31]).....	32
Figure 1.8. Schematic concept of a light-field camera (Image reproduced from Ng, R., et al. [35]) .....	33

Figure 1.9. (a) Experimental setup proposed by Skupsch, C. and Brücker, C. [37]. (b) Typical image produced by their plenoptic camera system. (c) 2D velocity field at multiple planes. (Figures a-c are reproduced from Skupsch, C. and Brücker, C. [37]). (d) Experimental setup proposed by Rice, B., et al. [38] (e) Results of Tomographic PIV system vs (f) results produced by the plenoptic camera. (Figures d-e are reproduced from Rice, B., et al. [38]). (g) Experimental setup of a low-speed jet flow proposed by Shi, S., et al. [39] (h) Results of the Light-field camera vs (i) tomographic PIV system. (Figures g-i are reproduced from Shi, S., et al. [39]). ..... 35

Figure 1.10. (a) Experimental setup proposed by Ido, T., et al. [40] (b) illumination profile used in a. (c) Experimental results obtained by Ido, T., et al. [40] (Figures a-c are reproduced from Ido, T., et al. [40]) (d) Proposed experimental setup to produce a continuous chromatic spectrum (RVV lighting device)[41, 42]. (e) Typical image obtained by the RVV system proposed by Malfara, R., et al. [42] (f) Vector field obtained with RVV. (Figure d-f are reproduced from Malfara, R., et al. [42]). (g) Experimental setup proposed by McGregor, T. J., et al. [43] (h) Image produced by the system in Figure g, where chalk dust particles are placed in a tilted plane. (i) Results from the reconstruction of the chalk particles in a single plane. (Figures g-i are reproduced from McGregor, T. J., et al. [43]). (j) Color-coded tomography experimental setup proposed by Ruck, B. [44] (k) Typical streak of a vortex structure using the system proposed in j. (Figures j, k are reproduced from Ruck, B. [44]). ..... 37

Figure 1.11. (a) Experimental setup proposed by Watamura, T., et al. [45] (b) Result of 3D-3C velocity field produced by the setup in Figure a. (Figures a, b are reproduced from Watamura, T., et al. [45]). (c) Six-layer color PIV experimental setup proposed by Murai, Y., et al. [46]. (d) 3D-2C velocity field reconstructed in six layers from the setup in Figure c. (Figures c, d are reproduced from Murai, Y., et al. [46]) (e) Experimental setup for a three-color grid proposed by Dennis, K. and Siddiqui, K. [47] (f) Typical image of a particle streak produced by the system in Figure e. (g) Single reconstructed particle pathline based on the streak color. (Figures e-g are reproduced from Dennis, K. and Siddiqui, K. [47]). 39

Figure 1.12. Ph.D Dissertation structure..... 42

Figure 2.1. Schematic experimental setup of the smartphones, vortex ring generator, LEDs and the components required to trigger and synchronize the system, while capturing three different time steps shown as yellow, cyan and magenta colors. The angles between the cameras are  $\alpha=45^\circ$  and  $\beta=10^\circ$ . [48]..... 45

Figure 2.2. 3D model for smartphone holder ..... 47

Figure 2.3. (a) Top view of the setup. (b) Actual photography of the setup, showing the mounting structure for precise and fine adjustment of the smartphones. (c) Detail of the support structure and 3d printed holder. [48] ..... 48

Figure 2.4. Schematic drawing of the vortex ring generator. Pulsed air is introduced into the enclosed bottom chamber, pushing a latex membrane to force out a fraction of the fluid in the chamber through a circular orifice, thus creating a vortex ring. The liquid inside the chamber has been pre-seeded with black micro-spheres. [48] ..... 49

Figure 2.5. (a) Photo of a set of RGB PT-120 LED's. (b) Spectrum of light emitted by each of these LED's by color.[50] ..... 53

Figure 2.6. Image of the calibration target (type 22 from LaVision) viewed from two angles. (a) From central bottom camera 3 and (b) from the off-axis camera 4. The image shows the optical distortions produced by the lens and by the angled view through the Plexiglas walls. [48] ..... 54

Figure 2.7. (a) Original image using only Red and Blue flashes (obtained with a Nikon sensor). The captured image is separated in its RGB channels red (b), green (c), and blue (d). (e) The color intensities cut through the blue and red dots.[48]..... 55

Figure 2.8. . The RGB color space represented in Cartesian coordinates. The white dashed arrows link the corresponding negative colors that are captured in the images.[48]..... 56

Figure 2.9. Schematic representation of the color time-coding approach used for the CMOS sensors. As the particle travels, the colored lights are flashed at different times, leaving their corresponding shadowed pixels recorded in the camera sensor. The final result is an image of the negative colors for each time step, i.e., green flash marks the particle location by magenta pixels, red by cyan and blue by yellow.[48]..... 56

Figure 2.10. (a) Typical JPEG image obtained from the smartphones. (b) Magnified image of a small region, it is noticeable that yellow particles fade away due to the interpolation algorithms. .... 57

Figure 2.11. Representation of the Color Filter Array (Bayer filter) configuration found in the Nokia Lumia 1020 camera sensor. It presents a GR/BG structure..... 58

Figure 2.12. (a) Captured image from the bottom central camera (phone 3) in DNG format . In this image, we clearly observe the three different colored shadows and the vortex ring structure in a “mushroom” shape. (b) 9x magnification of a sampled area, inside the white square.[48] ..... 58

Figure 2.13. Images of the dotted calibration glass slide inside the water-tank, back-illuminated by red (a), green (b) or blue (c) LED flashes. The middle column images are magnified sections of the dots corresponding to the white square in panel (a). On the right column, we show the corresponding RGB intensity histograms. [48] ..... 60

Figure 2.14. (a) Particle images with the three color LED's flashed simultaneously, i.e., with zero time-delay. (b) Close-up of two particles, which shows clearly the effects of the chromatic aberrations in one of the most affected areas, near the edge of the image. (c)

The color profiles of a single particle, taken along the dashed line in (b). One can clearly see the vertical shifting of the colored shadows, due to the chromatic aberrations. [48] ..... 62

Figure 2.15. Steps for preprocessing of the raw image file, showing the same region as in Figure 2.12(b). (a) The raw image from the Bayer filter array in gray-scale intensity. (b-d) Separation of the color channels based on pixel location in the array, with other pixels filled by zeros. (e-f) Resulting images after demosaic interpolation (Malvar, et al.[54]). (h-j) Final images for each color after background subtraction and filtering by local standard deviation levels.[48]..... 64

Figure 2.16. (a) Cropped portion of two particles from the raw captured image with the default color interpolation by the smartphone, (b) the interpolated raw image after separation of each channel array and combining them for clarity. (c) Inverted image after background subtraction and filtering by local standard deviation in each subregion, combining the color channels for clarity. For comparison, the color intensities are plotted on the right side, along with cuts through the image, marked by the dashed line.[48].. 66

Figure 2.17. (a) Standard deviation of the original calibration fit (OC, cyan color), and corrected calibration (CC, red color) after three iterations of the self-calibration algorithm as a function of depth position  $z$ . (b) Detailed plot of the corrected calibration.[48] ..... 67

Figure 2.18. Instantaneous velocity field vectors obtained after direct cross-correlation at the plane  $z = 0$  mm captured with  $\Delta t = 1000 \mu s$ , comparison between 96 (a), 128 (b), and 208 (c) voxel3 interrogation volumes. [48] ..... 69

Figure 2.19. Side by side comparison of the original velocity field (a,c) vs the chromatic aberration corrected velocity field (b,d). Top figures (a,b) correspond to the  $t_1 - t_2$  correlation, bottom figures (c,d) correspond to the successive  $t_2 - t_3$  correlation. All figures belong to the  $Re=24,000$  case. [48] ..... 70

Figure 2.20. Instantaneous velocity fields for the density-matched case with  $Re=24,000$  for consecutive time steps in the plane  $z=0$  mm for (a)  $t_1-t_2$  correlation (G-R) and (b)  $t_2-t_3$  correlation (R-B), both with  $\Delta t=1300 \mu s$ . The corresponding isocontours of vorticity magnitude ranging from  $70$  to  $230 s^{-1}$  for (c) G-R correlation and (d) R-B correlation. The corresponding vortex ring visualized in 3D by the isosurface of vorticity magnitude  $110 s^{-1}$  as well as every fifth vector of the instantaneous velocity field (e) G-R correlation (f) R-B correlation.[48] ..... 72

Figure 2.21. Contour plots for (a,b) local acceleration ( $\partial u / \partial t$ ) and (c,d) advected acceleration ( $u \cdot \nabla u$ ). Top figures (a,c) correspond to the X component, bottom figures (b,d) correspond to the Y component. The velocity vectors are included for position reference. The maximum local accelerations are about 4 times larger than the advected accelerations. [48]..... 74

Figure 2.22. Circulation  $\Gamma$  as a function of radius from vortex core, in four different planes, for  $t_1$ - $t_2$  correlation (red) and for  $t_2$ - $t_3$  correlation (cyan), with  $Re=24,000$ . [48] ..... 75

Figure 2.23. Contours of normalized residuals from the continuity equation,  $\nabla \cdot u$ , for (a) first time-step (G-R) and (b) second time-step (R-B), taken at the plane  $Z = 0$  mm. [48] 76

Figure 2.24. Scheimpflug configuration of the angular displacement method proposed by Prasad, A. K and Jensen, K. (figure reproduced from Prasad, A. K and Jensen, K. [59]) .. 77

Figure 2.25. (a) Original image captured by one of the CCD cameras of the stereo PIV system, notice the significant background noise due to out of focus particles. (b) Particle field after image processing and filtering of the out-of-focus particle images. .... 78

Figure 2.26. Side by side comparison of an instantaneous velocity field ( $\Delta t=1300 \mu s$ ) between (a) stereo PIV system vs (b) smartphone Tomo PIV system, colored by the velocity magnitude. Comparison of contour plots of vorticity in  $Z$  between (c) stereo PIV system vs (d) smartphone Tomo PIV system (velocity vectors are included for further orientation reference). All images are presented in the plane  $Z=0$  mm. [48] ..... 80

Figure 2.27. (a) Comparison of the velocity magnitude along a cut through the vortex cores in the plane  $Z=0$  mm for our Tomo-PIV system (cyan) vs 2-camera stereoscopic PIV system (red). (b) Comparison of the circulation  $\Gamma$  as a function of the radial distance from the center of the vortex cores. [48] ..... 81

Figure 3.1. Schematic representation of the synchronization system, proposed for simultaneous capturing high-speed video at 960 fps by multiple smartphone cameras. The TTL signal is generated by a digital delay generator. This signal is sent in parallel to multiple optocouplers that trigger the Xperia™ XZ cameras through the headphone Jack. .... 87

Figure 3.2. Signal characterization of the optocouplers (cyan) vs the trigger signal from the digital delay generator (yellow). The typical response time of the optocoupler is approximately 500 ns. The horizontal axis smallest divisions are 100 ns, while the vertical axis smallest marks are 1 V and 4 mV for the digital delay generator and the optocouplers respectively). .... 87

Figure 3.3. (a) Left, (b) right, (c) top and (d) bottom camera images of a vortex ring captured close to the same time. One can note that the scanning of the sensor produces overlapped flashes in (a) and (d). Whereas for (b) and (c) the flash is in phase with the recorded frame. .... 88

Figure 3.4. Images captured in the manual mode for the calibration plate at  $Z=0$  mm by (a) left camera and (b) central bottom camera. .... 91

Figure 3.5. Top central camera view of a dotted calibration target located at the central plane of the vortex ring. (a) Captured with manual settings at 19Mpx resolution. (b) Image

of 2x2 binned image from 19 Mpx resolution and centered cropped to 1280x 720 pixels (see the red region from a). (c) Image captured at the same location with the High-Speed video mode (1280 x 720 resolution)..... 91

Figure 3.6. Region of Interest (ROI) zoom (253 x 247 pixels) from the dotted calibration target. (a) High-speed video recording mode, (b) centered binning of 2x2 with top left corner located at  $x=624$  and  $y=588$  px (centered downsampled image) (c) Binning of  $1.9267 \times 1.9267$  with top left corner located in  $x=648$  and  $y=590$  px of the binned image. A rectangular grid is shown for comparison..... 92

Figure 3.7. (a) Single frame of a Vortex ring from a High-speed video. (b) Post-processed image. (c) Magnification of a sampled area inside the yellow region in (b). ..... 94

Figure 3.8. (a) Initial standard deviation of the calibration fit. (b) Final calibration standard deviation after three iterations of the self-calibration algorithm..... 94

Figure 3.9. (a-c) Two dimensional XY cuts through the center of the vortex ring, showing the instantaneous velocity field. (d-f) Two dimensional vertical cut of the instantaneous velocity field in a 45-degree XZ plane. (g-i) Two-dimensional YZ cut of the instantaneous velocity field at the center of the vortex ring (note that this plane is not directly visible and is perpendicular to the central camera sensors). Different times are plotted from left to right (0, 22.92 and 45.84 ms respectively, showing the upward translation of the vortex ring). Vectors are colored by their velocity magnitude..... 96

Figure 3.10. Time evolution of the Isovorticity magnitude surfaces of  $|\omega| = 220 \text{ s}^{-1}$ . The color of the surface is given by the magnitude of the velocity where we can see that the inner surface near the axis of symmetry of the vortex ring, has a larger magnitude. .... 97

Figure 3.11 Circulation  $\Gamma$  vs radius from vortex core; data is presented for 2D cuts of planes XY and YZ (later one not visible to the central cameras) colored by the three different instants  $t=0$  (red), 22.92 (black) and 45.84 (blue) ms. The Reynolds number for this vortex ring is  $Re \approx 16,500$ ..... 98

Figure 3.12. Contour plot of the normalized residual  $\delta_{cont}$  obtained from continuity equation  $\nabla \cdot \mathbf{u} = 0$ . This plot is obtained at the XY central plane of the vortex ring at  $t=43.75$  ms. .... 99

Figure 3.13 (a) Tomographic PIV experimental setup for simultaneous recording of the vortex ring using Red Cinema cameras (marked by red circles) and Xperia smartphone cameras (marked with green circles). The illumination is provided by three sets of three LED's each (R, G, B) in a backlit configuration (marked with yellow circles). (b) Image of a single set of LED's, one of each color (R,G,B). .... 100

Figure 3.14. Vortex ring captured simultaneously with (a) Red camera and (c) Xperia™ smartphones in the central face of the tank. Figures b and d show the magnified region marked in the respective squares. One can note the difference in the resolution of the two systems. The viewing angle for Figures a and c is slightly different. Therefore images are not fully comparable..... 101

Figure 3.15. (a) Red Cinema Camera system results showing isosurfaces of vorticity magnitude  $|\omega| = 210 \text{ s}^{-1}$  and the velocity field around that volume. Only every 6<sup>th</sup> vector is presented for visualization purposes. (b) Smartphone system results showing isosurfaces of vorticity magnitude  $\omega = 210 \text{ s}^{-1}$  and the velocity field around that volume. Only every 3<sup>rd</sup> vector is presented for visualization purposes. (c) Overlay of the results from both systems, the smartphone system result is presented as a blue surface and cyan velocity vectors while the Red camera system results are presented as a red surface and orange velocity vectors. One can visually notice both results overlap and are very similar qualitatively..... 103

Figure 3.16. (a) Mean relative error of velocity magnitude on isosurfaces of vorticity magnitude. The error bars represent the standard deviation of the relative error. (b) The contours of the relative error shown on the Isovorticity surface of magnitude  $\omega = 210 \text{ s}^{-1}$ . These regions represent an upper bound of the error due to the large velocity gradients present in this region of the flow. .... 104

Figure 3.17. Side by side comparison between velocity magnitude on the center plane XY for (a) High-resolution Red camera system and (b) High-speed Smartphone camera system. Contour plots of Vorticity magnitude are presented for (c) High-resolution camera system and (b) high-speed Smartphone camera system. Visually one can notice the difference in spatial resolution of the two systems. .... 105

Figure 3.18. Comparison of the results along  $y = 44 \text{ mm}$  for (a) Velocity magnitude and (b) Vorticity magnitude. The red lines represent the results obtained from the Red Cinema camera system. Cyan curves represent the results by the “slow-mo” smartphone system proposed in this chapter..... 106

Figure 4.1. (a) Schematic representation of Rainbow PIV system by Xiong, J., et al.[62]. (b) Actual photograph of the experimental setup. (Figure reproduced from Xiong, J. et al. [62]. )..... 110

Figure 4.2. Comparison of images captured using (a) DOE + regular lens and (b, c, d) using a regular lens for different focal planes corresponding approximately to the blue green and red levels. It is important to notice the narrow focal depth due to the large aperture used.[62] (Figure is reproduced from Xiong, et al. [62]). .... 111

Figure 4.3. (Left) The Diffractive Optical Element (DOE) mounted on a support. (Right) Magnification of the central region of the DOE.[62]..... 112

- Figure 4.4. Resulting velocity fields after translation in the (a) X axis, (b) Z axis and (c) Rotation around Y axis. [62]..... 113
- Figure 4.5. Schematic representation of a 3-LCD projection system. Red, Green and blue light is separated with dichroic mirrors, in order to pass through a single LCD for each of this colors to form the desired color channel. The 3 colored images are combined within a prism and then projected onto the screen forming a full color image.(Figure is reproduced from Epson [65]) ..... 115
- Figure 4.6. Projector Epson EX-9200 Pro proposed to be used due to the high resolution and relatively low cost. (Figure is reproduced from Epson, official website [66]) ..... 116
- Figure 4.7 Red 6K Epic Dragon™ camera. (Figure is reproduced from Red[67]) ..... 117
- Figure 4.8. Schematic of the rainbow PIV system using the 3LCD projector. .... 117
- Figure 4.9. (a) Cartesian Coordinates of RGB color space and (b) HSV color space cylindrical coordinates. (Images by Michael Horvath, available under Creative Commons Attribution-Share Alike 3.0 Unported license)..... 119
- Figure 4.10. (a) Gradient for every 16 pixels group. (b,c,d) Represent the intensity levels for the red, green and blue channels respectively. .... 120
- Figure 4.11. Red Cinema camera response and an intensity plot along the yellow dashed line for grouping pixels in (a) 4 px, (b) 8 px, and (c) 16 px in width. Each dot is separated by 1 mm on the calibration plate. The plate is placed at 45° with respect to the camera. .... 121
- Figure 4.12. Camera response images from projected checkered patterns of 10 px for (a) purely red, (b) purely green, (c) purely blue projected images..... 121
- Figure 4.13 (a) Projected color image, (b) the respective RGB linear profile and the (c) camera mean response curve with error bars representing the standard deviation  $\pm\sigma$ ..... 123
- Figure 4.14. Typical color camera response used for projector-camera system characterization with real particles, a single Hue (R,G,B) value is projected in each case: Hue of (a)  $H=-60^\circ$  (255, 0, 255); (b)  $H=0^\circ$  (255, 0, 0); (c)  $H=120^\circ$  (0, 255, 0); (d)  $H=240^\circ$  (0, 0, 255); (e)  $H=180^\circ$  (0, 255, 255)..... 123
- Figure 4.15. Typical atanh piecewise function used for creating color profiles..... 124
- Figure 4.16 Projected RGB profile (Red, Green and Blue channels) for (a)  $a=1.9$ , (c)  $a=1.95$  and (e)  $a=2.0$ . With the respective Hue color space camera-projector mean response curve (b, d, f). Error bars represent  $\pm$  the standard deviation ( $\sigma$ ). Note that the horizontal responses as the projected hue changes are reduced as the coefficient  $a$  increases. .. 125



Figure 4.17. Twenty selected Hue projected values represented as red vertical lines. The plot of the camera response (blue line) is presented for reference. .... 127

Figure 4.18. Projected images with their corresponding Hue values plot. (a)  $L_{10}$  Hue levels (from left to right  $H = -60^\circ, -19.3^\circ, 21.9^\circ, 40.7^\circ, 53.2^\circ, 75.5^\circ, 120^\circ, 151.1^\circ, 186.1^\circ, 215.3^\circ$ ). (b)  $L_{20}$  Hue levels (from left to right  $H = -60^\circ, -36.7^\circ, -19.3^\circ, 15.5^\circ, 21.9^\circ, 31.1^\circ, 40.7^\circ, 46.4^\circ, 53.2^\circ, 60^\circ, 75.5^\circ, 91.1^\circ, 120^\circ, 135.5^\circ, 151.1^\circ, 180^\circ, 186^\circ, 197.4^\circ, 215.3^\circ, 240^\circ$ .) ..... 128

Figure 4.19. 3D model of the vortex ring generator components. (a) top chamber and (b) bottom chamber. Both parts are assembled having a flexible membrane between them. .... 129

Figure 4.20. 2-D projection of the vortex ring particle field showing the pathlines during 20 time frames. .... 130

Figure 4.21. Typical weight function ( $w$ ) for a particle that is 23 pixels in diameter. .... 131

Figure 4.22. (a) Red camera image region of 700 x 700 pixels showing the multiple colors sensed. (b) Same region after obtaining the Gaussian weighted average Hue ( $wavg, H$ ) of each particle. This process aids assigning a single Hue value for every (x, y) coordinate of each particle. .... 132

Figure 4.23. Pathlines views of every other 3 particles in the 3D result. (a)  $x' y'$  plane. (b)  $y' z'$  plane. (c)  $x' z'$  plane and (d) 3D view of the reconstructed volume. It is clear from (b) and (c) that many of the depth estimations ( $z'$ ) are biased towards certain planes. .... 134

Figure 5.1. PCO edge 5.5 camera used for this iteration. The camera has a high quantum efficiency which translates to high sensitivity. This camera produces 16-bit images.... 138

Figure 5.2. Experimental setup of the monochromatic camera and the illuminating projector. The multiple intensity gradients are produced in the depth direction with respect to the camera planes. .... 139

Figure 5.3. Projected images with their corresponding intensity profile. (a) Constant intensity. (b) 10 sectors of different intensities ( $L_{10}$ ). (c) 10 sectors mirrored. (d) 10 subgradients with 20 intensity levels each ( $L_{20}$ ). .... 140

Figure 5.4. Typical projector-camera system response obtained from a real particle field. Error bars represent  $\pm\sigma$  (std. deviation). The solid lines represent a typical master curve used for light intensity calibration. .... 142

Figure 5.5. Typical Intensity signature of a random particle, this particle is shown over 9 consecutive video frames with a uniform projected illumination. The radial width ( $R$ ) of the particle is approximately  $R \approx 2$ . .... 143

- Figure 5.6. The best fit values of  $C$ ,  $R$  and  $C R^{3/2}$  for the particle in Figure 5.5 over 9 consecutive frames with uniform illumination. The values are normalized by their corresponding averages..... 144
- Figure 5.7. Design of a 3D calibration dotted pattern in (a) 3D view and (b) top view. Auxiliary lines are visible..... 146
- Figure 5.8. (a) 3D pattern in PMMA, illuminated by a white light, notice the air bubbles trapped during the bonding process. (b) Color gradient test with the projector, notice the planes clearly delimited by different colors or RGB values..... 146
- Figure 5.9. (a) Real cube illuminated by the projector. (b) Top view of the cube showing the multiple planes present in the cube..... 147
- Figure 5.10. (a) Typical frame from the PCO camera of the calibration cube illuminated by a uniform intensity frame. Note the different intensity levels for each particle. (b) XY view of the cube reconstruction. (c) XZ (top view) of the cube reconstruction. Note the volume distortion due to the projection divergence. (d) 3D view of the reconstructed cube, particles are colored by their depth position ( $z'$ ). ..... 148
- Figure 5.11. Comparison of the mean camera response with three different parameters  $I_w$ ,  $I_{max}$  and  $I_o$ . The total length of the error bars represents two times the Mean Absolute Deviation (MAD) around the mean response value..... 150
- Figure 5.12. Estimated depth ( $z'$ ) vs Frames in time for different particle trajectories. The solid line of each trajectory represents the polynomial fit of the depth while the markers show the initially estimated depth. Note that erroneous depth detection is corrected during this process..... 152
- Figure 5.13. Top view ( $x, z$ ) of the corrected reconstruction (red) of the calibration cube after applying the mapping functions. Real coordinates of the reconstructed cube (cyan). ..... 154
- Figure 5.14. Schematic drawing of a von Karman pump. The studied region of the flow is enclosed in the magenta dashed box. .... 156
- Figure 5.15. 2-D projection of the 3-D particle pathline obtained with Trackmate. The rotating plate is 15 mm above the top of the image. The colors are fixed for each particle. The width of the image spans  $\approx 60$  mm inside the tank..... 157
- Figure 5.16. Reconstructed rotating flow pathlines of 960 unique particles. (a) xy view. (b) yz view. (c) xz view (top) view. (d) 3D view of the pathlines. Note that (b) and (c) views are not visible by the camera. .... 157
- Figure 5.17. Velocity bias errors due to chromatic aberration. They are obtained from the Zero-time-delay images (all colors flashed at the same time) for (a)  $t_1 - t_2$  correlation

(Green-red) and (b)  $t_2 - t_3$  correlation (Red-Blue). The arrows in both cases are colored by their vector magnitudes. Both results are presented in plane  $z=0$  mm. Note that most of the fields have aberration magnitudes less than 0.1 m/s. [48] ..... 171

Figure 5.18. Instantaneous velocity fields for a single time step in the plane  $z=0$  mm for (a)  $Re=44,000$ ,  $\Delta t=1000 \mu s$  and (b)  $Re=56,000$ ,  $\Delta t=500 \mu s$ . (c,d) The corresponding iso-contours of vorticity magnitude ranging from 30 to  $120 s^{-1}$  in (c) for the  $Re=44,000$  and (d) from 40 to  $220 s^{-1}$  for  $Re=56,000$ . (e,f) The vortex ring visualized in 3D by the iso-surface of vorticity magnitude  $90 s^{-1}$  as well as every fifth vector of the instantaneous velocity field for  $Re=44,000$  (e) and  $Re=56,000$  (f). [48]..... 172

Figure 5.19. Circulation  $\Gamma$  as a function of the radial distance from the vortex core, in four different vertical planes, for  $Re=44,000$ ,  $\Delta t=1000 \mu s$  (red) and  $Re=56,000$ ,  $\Delta t=500 \mu s$  (cyan). This shows that the circulation is approximately constant around every cross-section through the vortex core.[48]..... 173

Figure 5.20. Plot representing the cumulative area vs the relative error magnitude ( $|erel|$ ) in percentage. The dashed lines clearly show that 84% of the vectors have an error of 20% or less. Keep in mind that “error” means here the difference between the simultaneous measurements of the stereo-PIV and tomo-PIV systems. [48] ..... 173

Figure 5.21. Side view (YZ) of the reconstructed particle field based on their RGB values. Note that the reconstruction is biased towards certain planes. .... 174

Figure 5.22. Flowchart summarizing the algorithm used to reconstruct the 3D position of multiple particles based on monochromatic structured light and a single camera..... 175

Figure 5.23 Schematic representation of the experimental setup proposed using single camera systems to reconstruct in 3D particle trajectories. This system in principle will reduce the complexity and heat load into the test cell at a temperature of 1.3 K..... 176

## LIST OF TABLES

Table 1. Summary of parameters used for capturing tomographic PIV images of a vortex ring. ....	45
Table 2. Summary of relevant specifications of the Sony Xperia™ XZ premium smartphone[60]. ....	85
Table 3. Mapping functions polynomial coefficients and goodness of fit data. ....	155

## **Chapter 1 : Introduction**

In conjunction with numerical simulations and theory, experimental fluid mechanics has expanded and developed our understanding of a whole variety of flows nowadays. These techniques are used to understand qualitatively and quantitatively the flow in pipes, around objects or free moving flows, bacteria behavior, among others. They help in the design and improvement of aerodynamic components such as airfoils, turbine blades, among other applications in transportation, energy, and other engineering and scientific fields. Moreover, they are used to experimentally validate numerical models from Computational Fluid Dynamics (CFD) simulations.

Some of the most used visualization techniques, at present, include Laser Induced Fluorescence (LIF), Schlieren Shadowgraphy, Hot-wire anemometry and Particle image velocimetry (PIV), among others. However, the cost and complexity of this kind of systems restrict the mainstream use of these techniques.

### **1.1 Particle Image Velocimetry (PIV) for 2D and 3D measurements**

Particle Image Velocimetry (PIV) is arguably the most powerful and widely spread technique for flows visualization and quantification studies [1-3]. This technique consists of seeding a flow with small tracer particles that are illuminated by a laser sheet. This type of illumination allows us to record in time the scattered light or fluorescence from the particles. Using CMOS or CCD cameras one can pin down the location of the particles in

2D (see Figure 1.1). The velocity field is subsequently extracted through image correlations with specialized software. The development of state of the art cameras, such as high-speed cameras, have allowed obtaining time-resolved measurements of high Reynolds number flows. Additionally, the three-dimensional nature of fluid flows and the need for more accurate and higher resolution measurements has led to the development of Stereoscopic PIV[4], Scanning PIV with a laser plane [5], and Tomographic PIV[6]. Stereoscopic PIV consists of a laser illuminated thin volume instead of a 2D sheet and uses two cameras observing the flow from different angles. This technique allows obtaining a three-component velocity field in a single plane (2D-3C)[4]. On the other hand, the Scanning PIV technique can obtain a 3D velocity field in a volume (3D-3C) but only for slow motion flows, where the flow does not change appreciably during the scanning period[5].

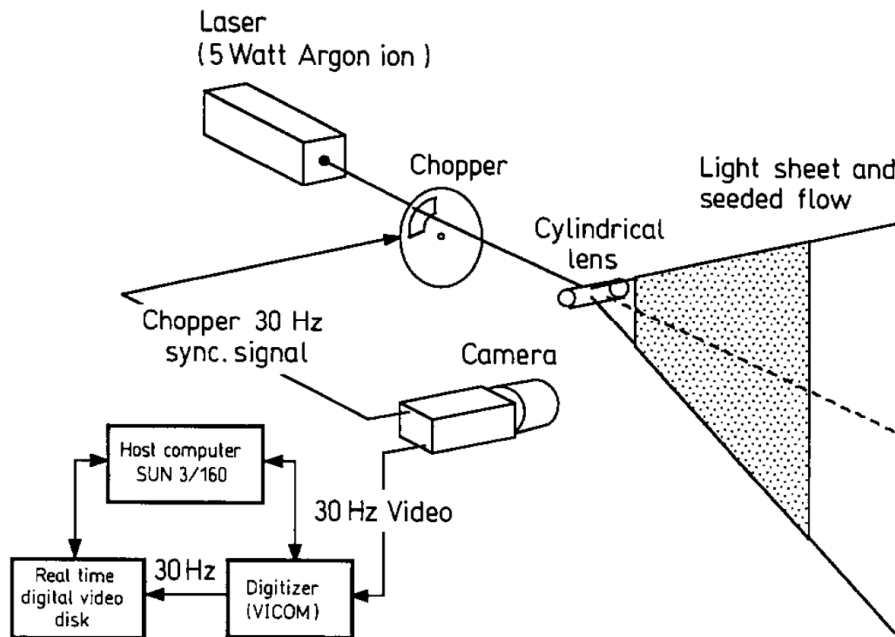


Figure 1.1. Experimental setup used by Willert and Gharib [3]. For the 2D Digital PIV system. (Image reproduced from Willert and Gharib [3]).

Tomographic PIV is one of the latest evolutions on PIV techniques, and it has been adopted as the standard technique for 3D-3C measurements in many fields. Here, three or more synchronized cameras view the flow from different directions and record simultaneously the particles illuminated with a laser volume-slice[6] (see Figure 1.2). After doing a spatial calibration, the 3D particle location is obtained by using the images from all cameras in a Multiplicative Algebraic Reconstruction Technique (MART) based on a Multiple Line of Sight (MLOS) initialization[7]. Once the 3D particle location of the particles is obtained, we can obtain the 3D-3C velocity field by carrying out volume correlations.

Despite the fast development and high accuracy of all the previously mentioned techniques, they involve using very complicated setups, multiple research-level cameras, and high power lasers, posing safety hazards and representing an expensive proposition for most labs and educational institutions.

Noteworthy efforts to overcome the complexity, increase resolution and reduce the cost of Tomographic PIV systems have been made. Discetti, et al. [8], have used multiple single shutter commercial cameras. Dangerous and expensive laser systems have been replaced with high power LED's as an illumination source[9-13]. Buchmann, et al.[14] used multiple high-sensitivity CCD cameras with LED's to illuminate the volume and study the 3D features of grid turbulence. Casey, et al.[15] scanned rapidly with laser volumes rather than sheets in a Tomographic camera setup, to significantly increase the size of the measured volume. A combination of monochromatic LED's, shadows and multiple

cameras has been reported by Klinner and Willert[16], to reconstruct the 3D spatial distribution of a cone spray.

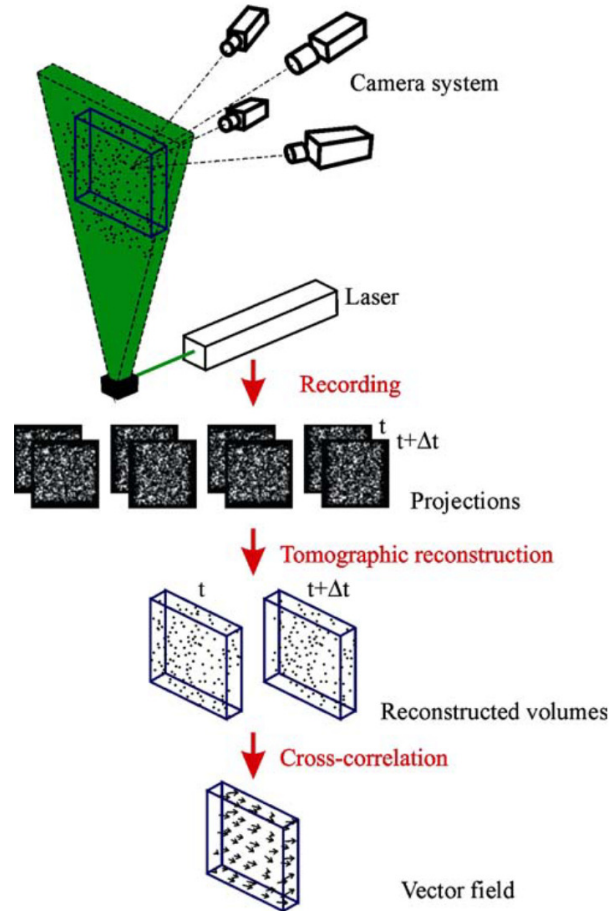


Figure 1.2. Schematic representation of the tomographic PIV system proposed by Elsinga, et al. in 2006 for full 3D-3C flow visualization. (Image reproduced from Elsinga , et al.[6])

Particle Shadow Velocimetry (PSV) has proven to be an effective alternative to PIV systems. In principle, it is very similar to PIV, with the main difference being the illumination system configuration. In PSV, rather than recording scattered light or fluorescence from the particles, shadows of tracer particles produced by backlight are captured. This configuration reduces the sensitivity required by the camera sensor. Estevadeordal and Goss[17] have reported the use of color-coded LED flashes for



computing 2D velocity fields (see Figure 1.3). McPhail, et al.[18] have carried out in-depth studies on the effect of chromatic aberrations and how to correct them in color PSV. Some other alternatives to Tomo-PIV are based on 3D particle tracking[19, 20].

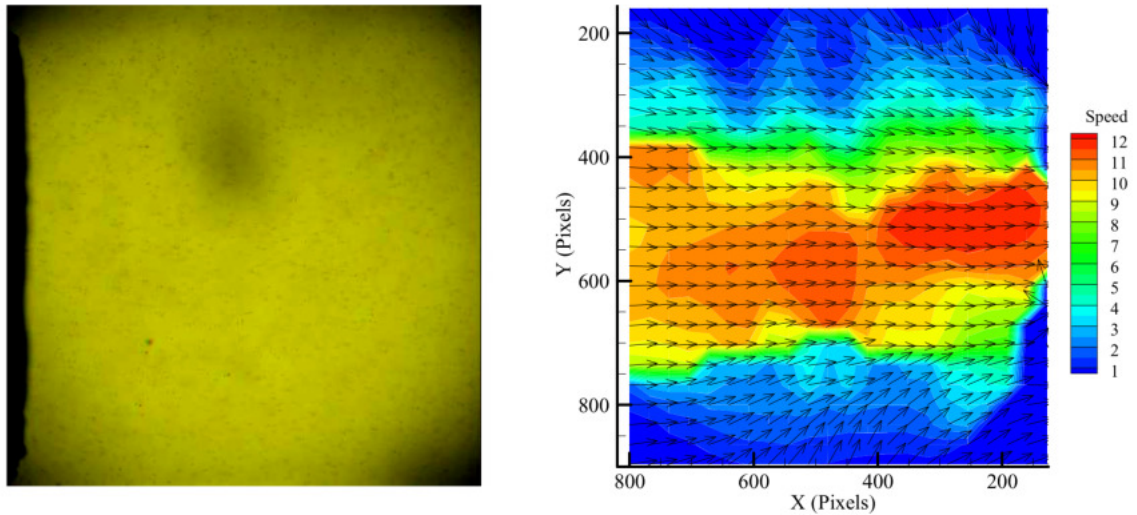


Figure 1.3. Images of a water-jet flow by Estevadeordal and Goss captured using LED and colored shadows to encode time information and some of the 2D PIV results. (Image reproduced from Estevadeordal and Goss[17])

## 1.2 Shake the box (4D Particle Tracking Velocimetry)

Recently the “Shake-the-Box” (STB) algorithm has been introduced by Schanz, D., et al. [21], where the main difference with the relatively mainstream Tomo-PIV is the Lagrangian approach (single particle tracking) used by STB. The hardware setup and calibration process are the same as for Tomo-PIV. However, the seeding density of particle tracers in the flow can be greatly increased. This method combines developments of 3D PTV and Tomographic-PIV, complementing them with temporal information of individual particles, i.e., “shaking” them to predict and match their next three-dimensional position. This process bounds the estimated particle positions to previously computed coordinates, giving the particles “temporal memory”. This technique produces

high temporal and spatial resolution of the reconstructed flow. Additionally, calculations are notoriously speed-up arising from the absence of tomographic volume reconstructions at every time-step (contrary to Tomographic PIV). Some of the results achieved by Schanz, et al. are presented in Figure 1.4.

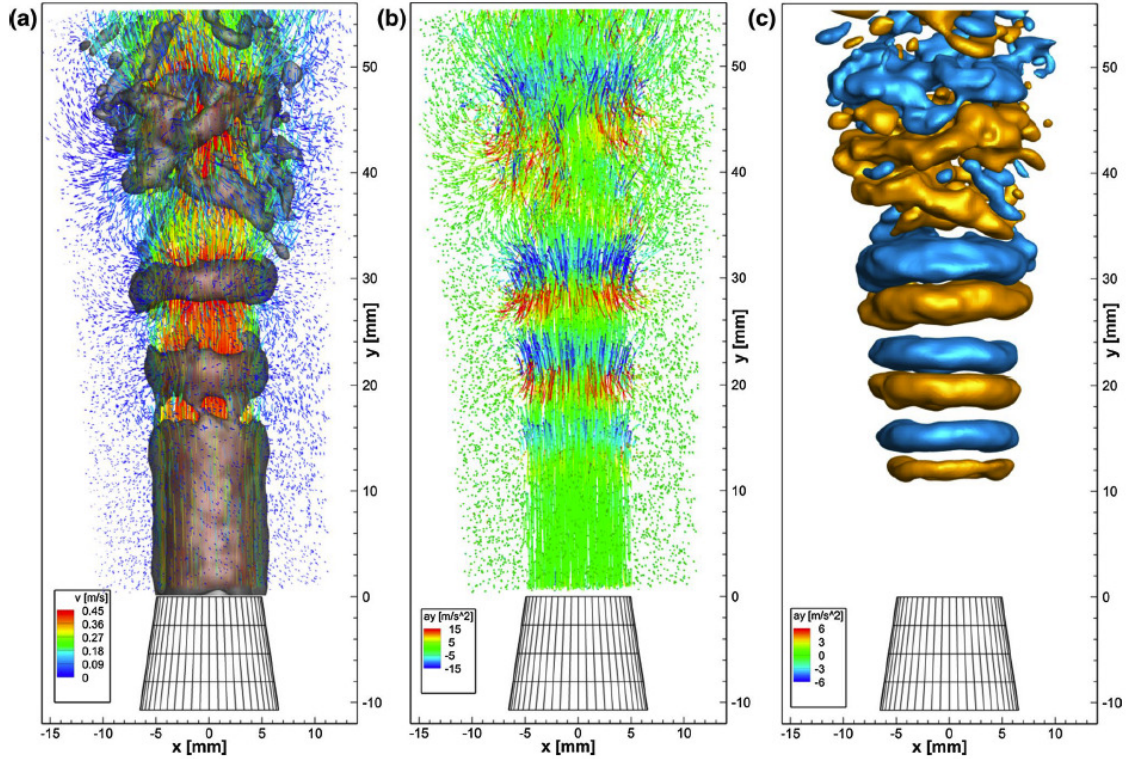


Figure 1.4. STB results for water jet experiments after interpolating to an Eulerian grid ("Flowfit"). (a) Isosurfaces of vorticity  $175 \text{ s}^{-1}$  and particle tracks extending five steps back in time. (b) Single time step tracks with a tail of ten time-steps colored by vertical acceleration. (c) Isosurfaces of vertical acceleration at a single time step. (Image reproduced from Schanz, et al.[21])

### 1.3 Single camera, three-dimensional particle tracking efforts

Additionally, efforts to use a single camera for 3D reconstruction have been carried out by numerous authors. These efforts have the main goal of reducing the complexity and costs of this kind of setups. These efforts can be divided into the following main categories:

- Three pin-hole aperture Defocused Particle Tracking
- Image splitters to produce multiple views
- Depth estimation by optical aberrations
- Plenoptic (light field) cameras
- Color-coded illumination

### 1.3.1 Three pin-hole aperture Defocused Particle Tracking

Willert, C.E. and Gharib, M.[22], use defocusing combined with a 3-pin hole aperture mask embedded in a single camera lens to encode the 3D location of particles in a single image, they tested this technique in a vortex ring (Figure 1.5 (a-c) ). Pereira, F., et al.[23] patented an “Aperture coded camera for three-dimensional imaging” system. Rohlay, J. and Hart, D.[24] patented a “Monocular three-dimensional imaging” system, similar to the previously mentioned system, where the multiple pin-hole configurations allow to encode the three dimensions of a particle. Furthermore, Wu, M., et al.[25] estimated the depth of a fluorescent particle (*E. Coli* bacteria in this case) by correlating the size of the defocused image with their depth. They were able to reconstruct a volume of  $418 \times 335 \times 75 \mu\text{m}^3$  capturing images every 0.752 seconds (Figure 1.5 (d,e)). Toprak, E., et al.[26] used a bifocal imaging method to track in three dimensions fluorescent and non-fluorescent particles. They simultaneously record the  $(x,y)$  position of a focused image, and estimate the depth  $(z)$  with a defocused image captured with a CCD camera (see Figure 1.5 (f-h)). Experiments recording the trajectory of only 28 melanosomes in a volume of  $500 \times 2000 \times 1600 \text{ nm}^3$  are presented in this work.

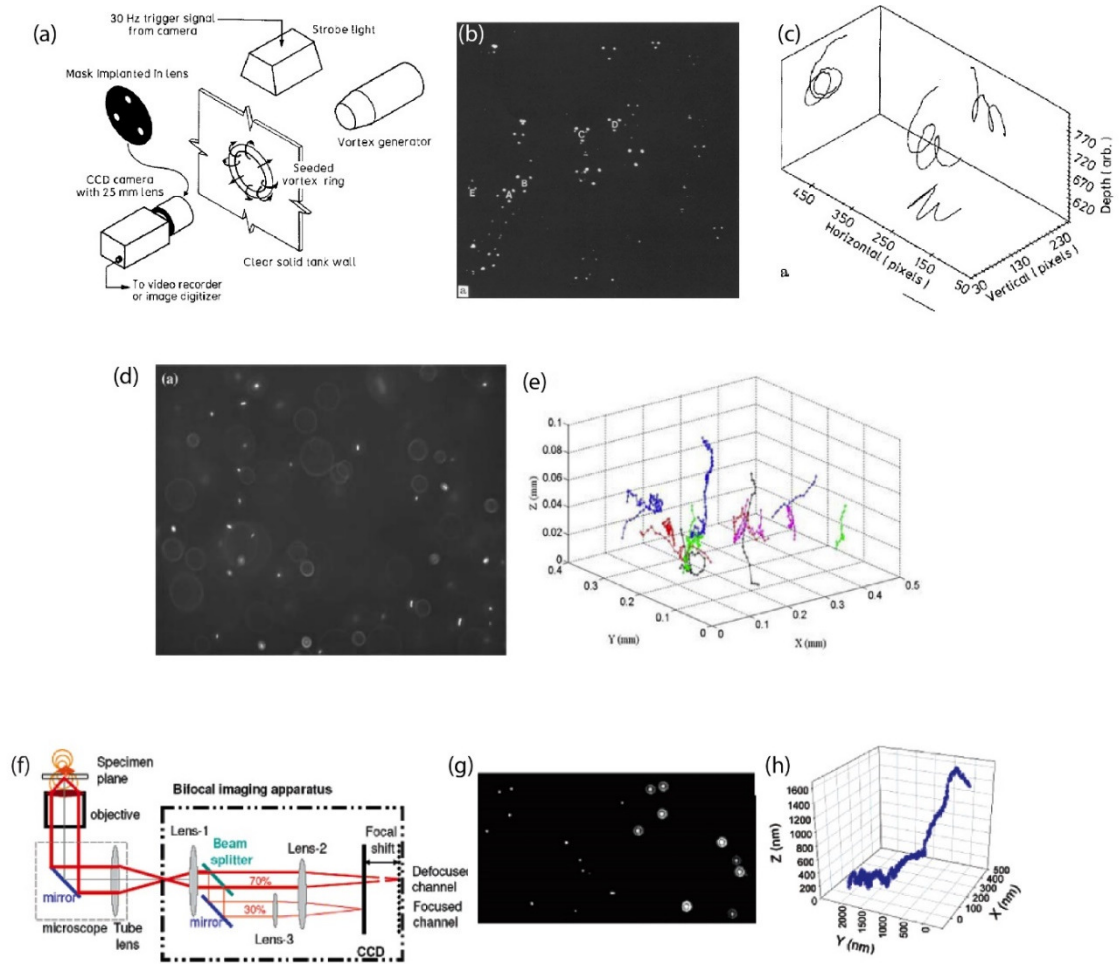


Figure 1.5. Summary of some of the techniques using defocusing and pin-hole imaging for 3-D reconstruction. (a) Experimental setup used by Willert and Gharib [22] with a single camera. (b) Typical image produced by this system. (c) Visualization of some resulting pathlines. (a-c are reproduced from Willert, C. E., and Gharib, M. [22]). (d) Typical image captured by the defocusing technique proposed by Wu, M., et al [25]. (e) Some of the pathlines reconstructed for bacteria. (d,e are reproduced from Wu, M, et al.[25]). (f) Experimental setup used by Toprak, E., et al. [26]. (g) Typical image captured by bifocal imaging. (h) 3-D pathline of a single melanosome. (f-h images are extracted from Toprak, E., et al. [26]).

### 1.3.2 Image splitters

In this category, efforts have been made by splitting the resolution of a full image captured by a single camera to record multiple viewing angles of the same region of interest. Kreizer, M. and Liberzon, A. [27] have used an arrange of mirrors as a four-view split-screen device. With this information, they are capable of processing the camera data for real-time particle tracking. This experiment is focused on large-scale flows, and they

reconstruct a volume of  $60 \times 80 \times 80 \text{ mm}^3$  (see Figure 1.6 (a,b) ). Furthermore, Gao, Q., et al.[28] use a “three-vision prism” placed between the measured volume and the camera allowing to record particles from three different viewing angles of a jet flow. (see Figure 1.6 (c-e)).

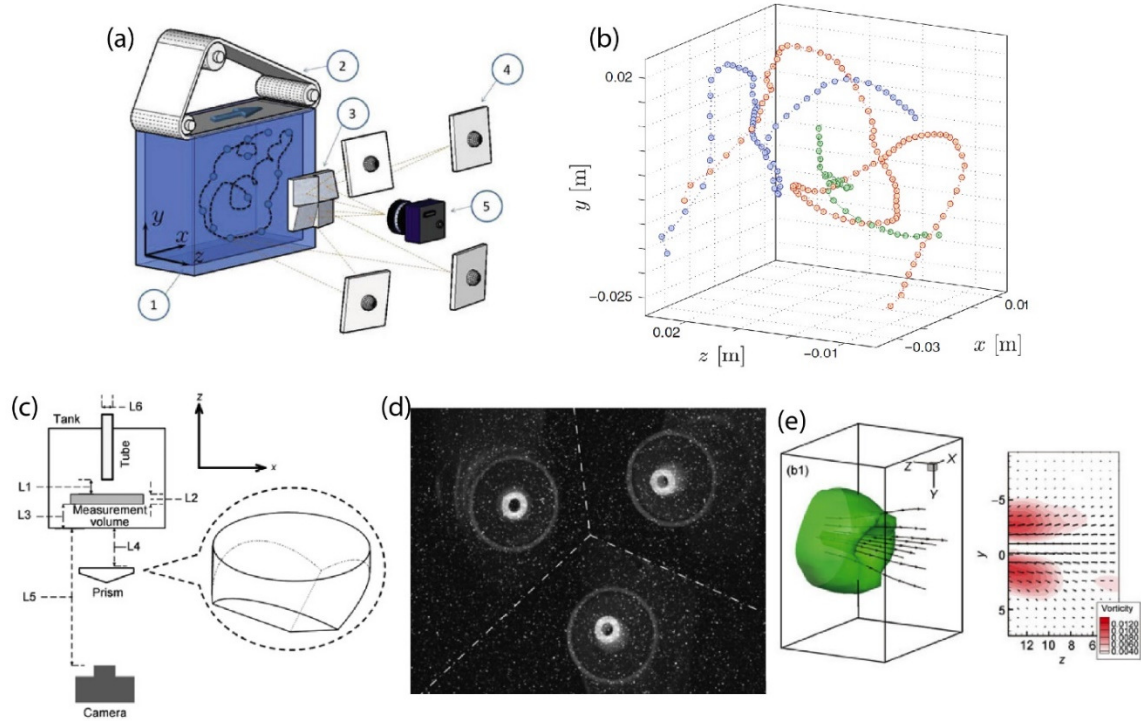


Figure 1.6. (a) Image splitting system proposed by Kreizer and Liberzon [27]. Depicting a (1) tank and (2) driving belt system, (3) four view image splitter, (4) back-side mirrors, (5) a camera. (b) Results reported using the system in a. (Figures a and b are reproduced from Kreizer, M. and Liberzon, A.[27]). (c) Experimental setup proposed by Gao, Q., et al. [28]. (d) Typical multiple view image produced by the system in c. (d) Results presented by Gao, Q. et al. (c-e figures are reproduced from Gao, Q., et al. [28]).

Peterson, K., et al. [29] used two off-center optical paths (similar to stereoscopic- $\mu$ PIV[30]) to create two imaging subsystems that view the measured volume from different angles. The volume measured is  $6 \times 6 \times 2 \text{ mm}^3$ , and it was tested with an air jet seeded with silicone oil mist (Figure 1.7 (a,b) ). Maekawa, A. and Sakakibara, J. [31] use an “ellipsoidal polyhedral mirror” to capture the region of interest with up to 80 different viewing angles. The measurements in this work include a volume of  $5 \times 10 \times 2 \text{ mm}^3$ . This



technique increases the accuracy of the 3D components of the velocity dramatically, however, the trade-off is the reduced reconstructed volume (see Figure 1.7 (c-e) ). Hoyer, K., et al. [32] propose a scanning system to track particles in time using a single camera and a high frequency scanning laser sheet, combining it with a four-way image splitter. They proceed to do ray tracing to estimate each particle 3D position and generate pathlines. This technique increases the image density of seeding particles.

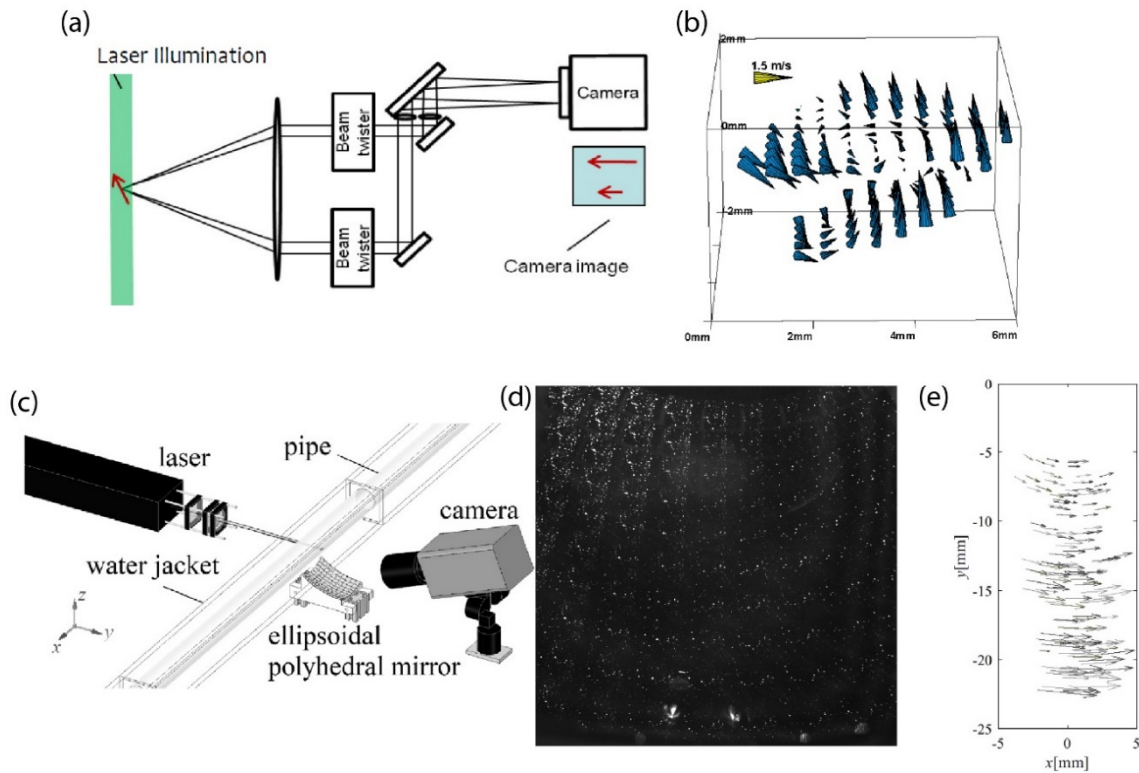


Figure 1.7. (a) Experimental setup proposed by Peterson, K., et al. [29] (b) Typical result from the system proposed in a. (Figures a and b are reproduced from Peterson, K., et al. [29]). (c) Experimental setup proposed by Maekawa, A. and Sakakibara, J. [31] (d) Typical image produced by the setup in c. (e) a typical result from the system proposed in c. (Figures c-e are reproduced from Maekawa, A. and Sakakibara, J. [31]).

### 1.3.3 Depth estimation by optical aberrations

Cierpka, C., et al. [33] proposed a system that is based on tracking individual particles in a microscale setup ( $500 \times 500 \times 90 \mu\text{m}^3$ ). They encode the depth position of

the particles in optical distortions produced by a cylindrical lens. Additionally, Hain, R. and Khäler, C. [34] propose a similar system using optical aberrations to encode the depth of the particle position, more specifically, astigmatism. This type of distortion produces an elliptical shape in the recorded particles. They link the length of the semi-axes of the ellipse to its depth.

#### 1.3.4 Plenoptic (light-field) cameras

Light field cameras use an array of micro-lenses placed in front of the image sensor. This type of camera allows tracing each ray on every micro-lens. Therefore, one can produce “refocused” images after capturing[35], as seen in Figure 1.8. This imaging system opens up the possibilities to estimate 3D locations from a single image.

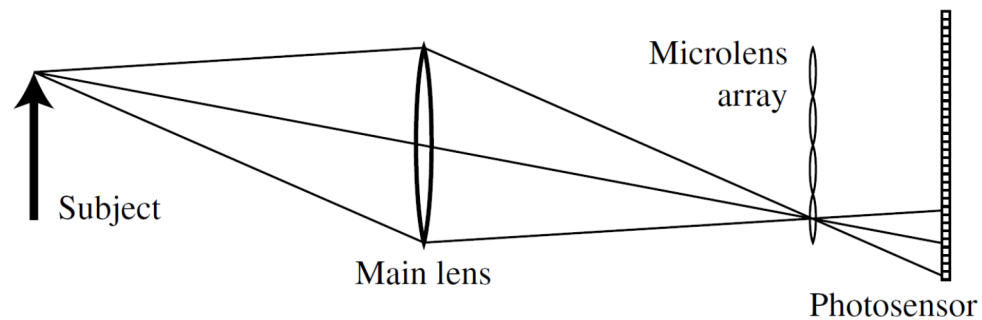


Figure 1.8. Schematic concept of a light-field camera (Image reproduced from Ng, R., et al. [35])

Cenedese, A., et al. [36] discuss the possibility to use a light-field camera to track particles in 3D space and time. However, they mention that the spatial and temporal resolution is reduced when using a light field camera at the time. Skupsch, C. and Brücker, C. [37] determine planar velocity fields on simultaneous parallel measurement planes using a light-field camera. They illuminate the studied volume of  $30 \times 30 \times 50 \text{ mm}^3$  with

multiple laser light sheets with constant spacing. They produce a 3D-2C velocity field (two components of velocity in each plane), see Figure 1.9 (a-c).

Furthermore, Rice, B., et al. [38] compare the results of a four-camera Tomographic-PIV system with the ones of a single plenoptic camera (see Figure 1.9 (d-f) ). They highlight that the precision in depth estimation in plenoptic cameras is reduced due to the microlens array.

Shi, S., et al. [39] also produced a detailed comparison of the PIV results with a light-field camera and Tomographic PIV setup. They produce synthetic data for both systems and finally do experimental studies measuring a low-speed jet flow simultaneously using a four camera Tomographic PIV and a 29 Mpx light-field camera. They conclude that a very high-resolution light-field camera can produce comparable results to those of a four camera system with 0.15 Mpx resolution in each camera (see Figure 1.9 (g,h) ). However, such high resolution restricts this kind of system to low frame rates.



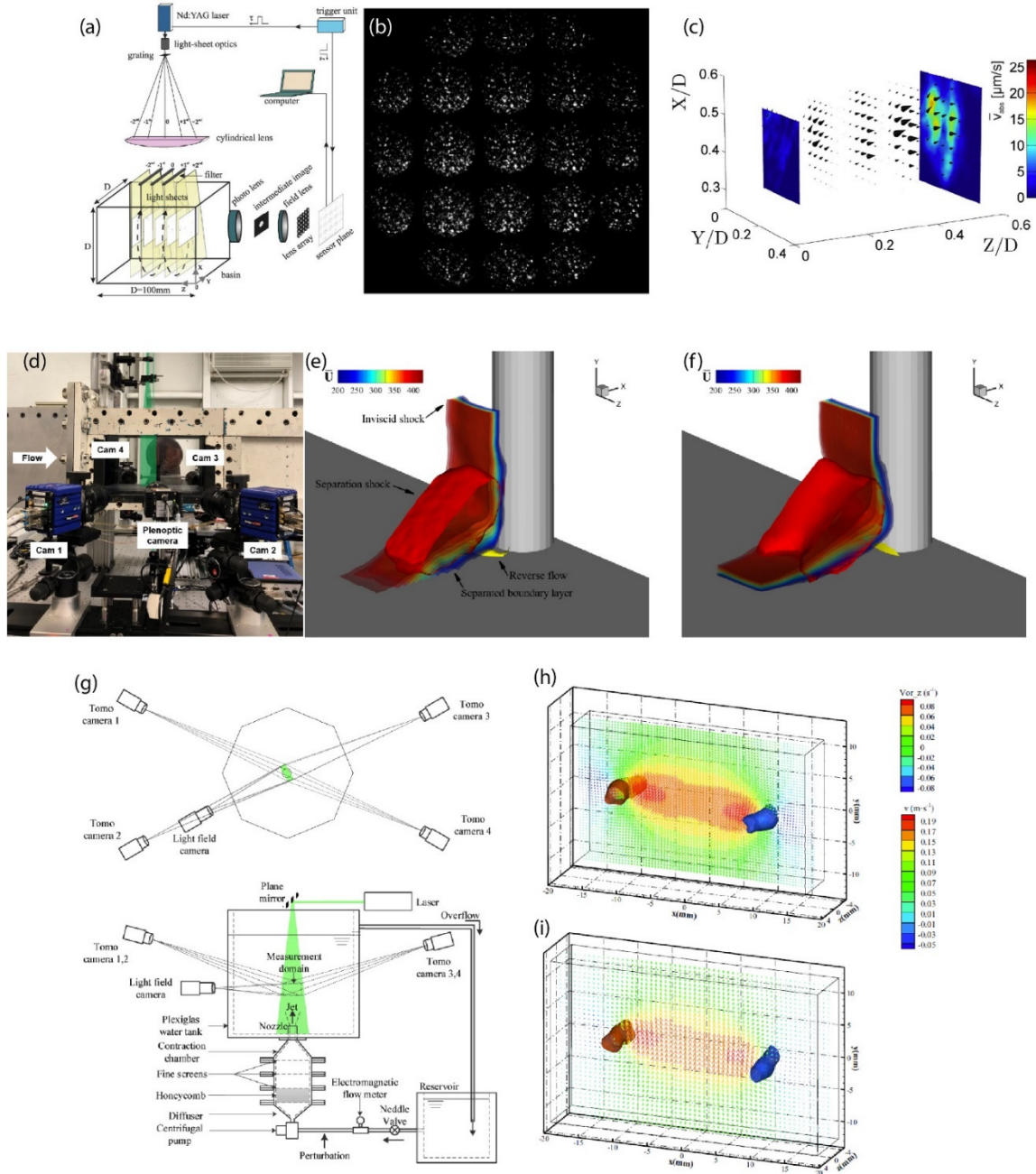


Figure 1.9. (a) Experimental setup proposed by Skupsch, C. and Brücker, C. [37]. (b) Typical image produced by their plenoptic camera system. (c) 2D velocity field at multiple planes. (Figures a-c are reproduced from Skupsch, C. and Brücker, C. [37]). (d) Experimental setup proposed by Rice, B., et al. [38] (e) Results of Tomographic PIV system vs (f) results produced by the plenoptic camera. (Figures d-e are reproduced from Rice, B., et al. [38]). (g) Experimental setup of a low-speed jet flow proposed by Shi, S., et al. [39] (h) Results of the Light-field camera vs (i) tomographic PIV system. (Figures g-i are reproduced from Shi, S., et al. [39]).

### 1.3.5 Color coded-illumination

The main characteristic of this category is the use of a colored light source to encode the depth of the particles. Ido, T., et al. [40] use a liquid crystal display (LCD) projector to illuminate the studied volume, where they project a sine function of each RGB channel to produce color gradients, encoding the depth of each particle in its hue value or color and recording the particles with a 3-CCD color camera (one sensor for each color channel, see Figure 1.10 (a-c) )

Zibret, D., et al. [41] and Malfara, R., et al. [42] developed Rainbow Volumic Velocimetry (RVV) where they carry out 2D Particle Tracking Velocimetry encoding the depth position of each particle in the color or wavelength scattered by it. The light source used is a white discharge lamp and dispersed with a blazed reflecting grating, this produces a continuous chromatic spectrum. This technique is tested with synthetic images as well as experiments in a jet (see Figure 1.10 (d-f) ).

Similarly, McGregor, T. J., et al. [43] propose a proof of principle 3D imaging system by encoding the depth of each particle with color. To generate depth color levels a copper vapor laser is pumped through multiple order Stimulated Raman Scattering (SRS), producing 11 discrete depth levels. They test this technique in a static chalk dust 3D field along a plane (See Figure 1.10 (g-i) ). Ruck, B. [44], proposes encoding color depth using a white laser (which combines a Red, green and blue laser) as the light source, he is able to produce 30 depth levels where he captures multiple time steps in a single image presented as streaks(see Figure 1.10 j,k).

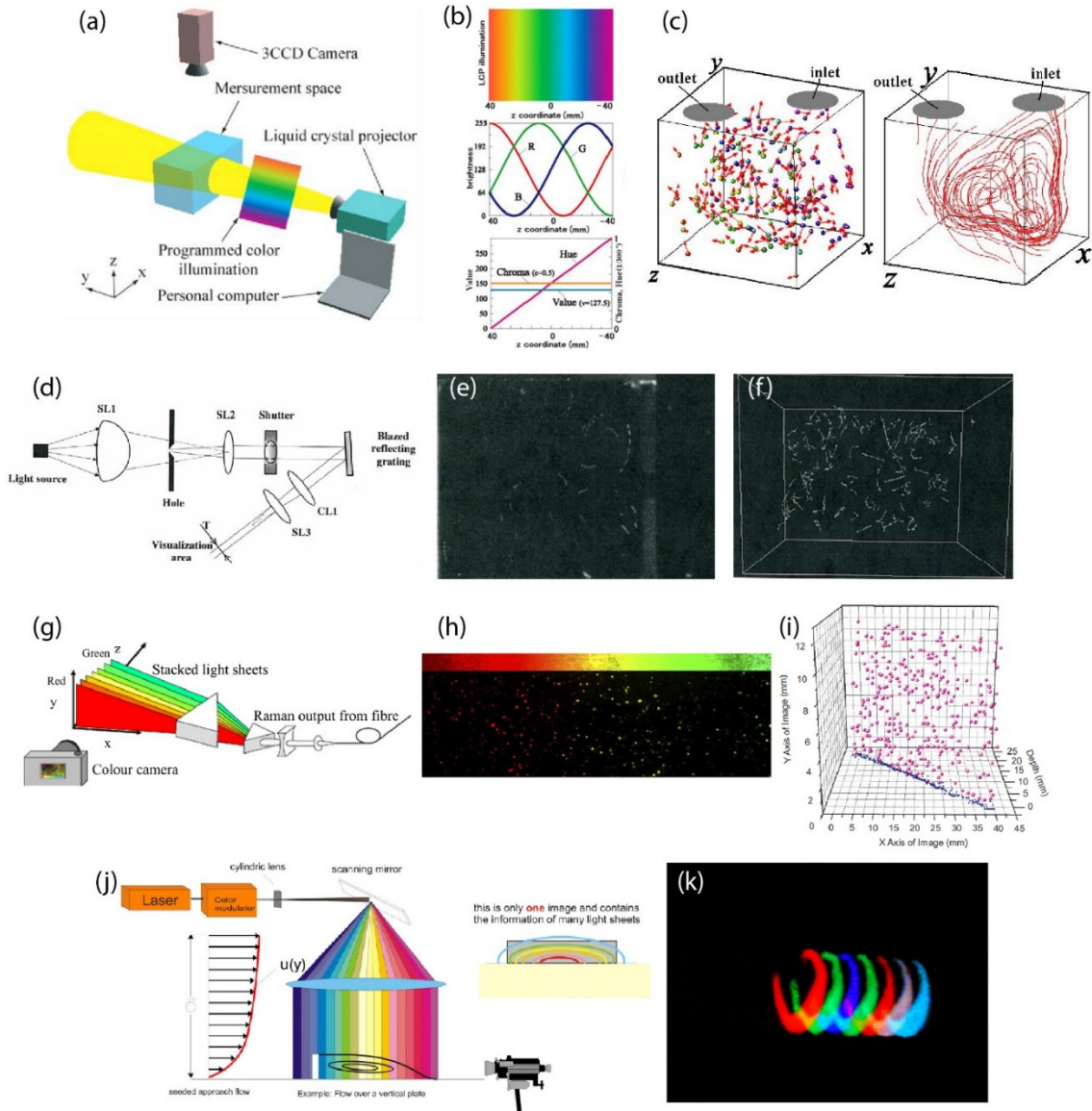


Figure 1.10. (a) Experimental setup proposed by Ido, T., et al. [40] (b) illumination profile used in a. (c) Experimental results obtained by Ido, T., et al. [40] (Figures a-c are reproduced from Ido, T., et al. [40]) (d) Proposed experimental setup to produce a continuous chromatic spectrum (RVV lighting device)[41, 42]. (e) Typical image obtained by the RVV system proposed by Malfara, R., et al. [42] (f) Vector field obtained with RVV. (Figure d-f are reproduced from Malfara, R., et al. [42]). (g) Experimental setup proposed by McGregor, T. J., et al. [43] (h) Image produced by the system in Figure g, where chalk dust particles are placed in a tilted plane. (i) Results from the reconstruction of the chalk particles in a single plane. (Figures g-i are reproduced from McGregor, T. J., et al. [43]). (j) Color-coded tomography experimental setup proposed by Ruck, B. [44] (k) Typical streak of a vortex structure using the system proposed in j. (Figures j, k are reproduced from Ruck, B. [44]).

Watamura, T., et al. [45] uses an LCD color projector to obtain 3D-3C PTV. To minimize errors in the depth estimation, they propose to study the images captured in

the Hue color, averaging the color of each particle in polar coordinates space rather than linear coordinates or RGB color space. Moreover, they use multiple color-cycle gradients in time, in order to improve the accuracy of the results. They tested this technique reconstructing the flow produced by a rotating impeller (see Figure 1.11 a,b). Similarly, Murai, Y., et al. [46] propose a single camera system where they study in detail the color contamination arising from using a color LCD projector in air seeded with smoke. They study this for three and six thick discrete layers, where the final results are 3D-2C simultaneous velocity fields (see Figure 1.11 c,d). Dennis, K. and Siddiqui, K. [47] use an LCD projector to produce a color grid of 3x3 or 6 x 6 colors and record particle streaks (see Figure 1.11 e-g). However, this technique has a very low resolution in the depth direction with respect to the camera.

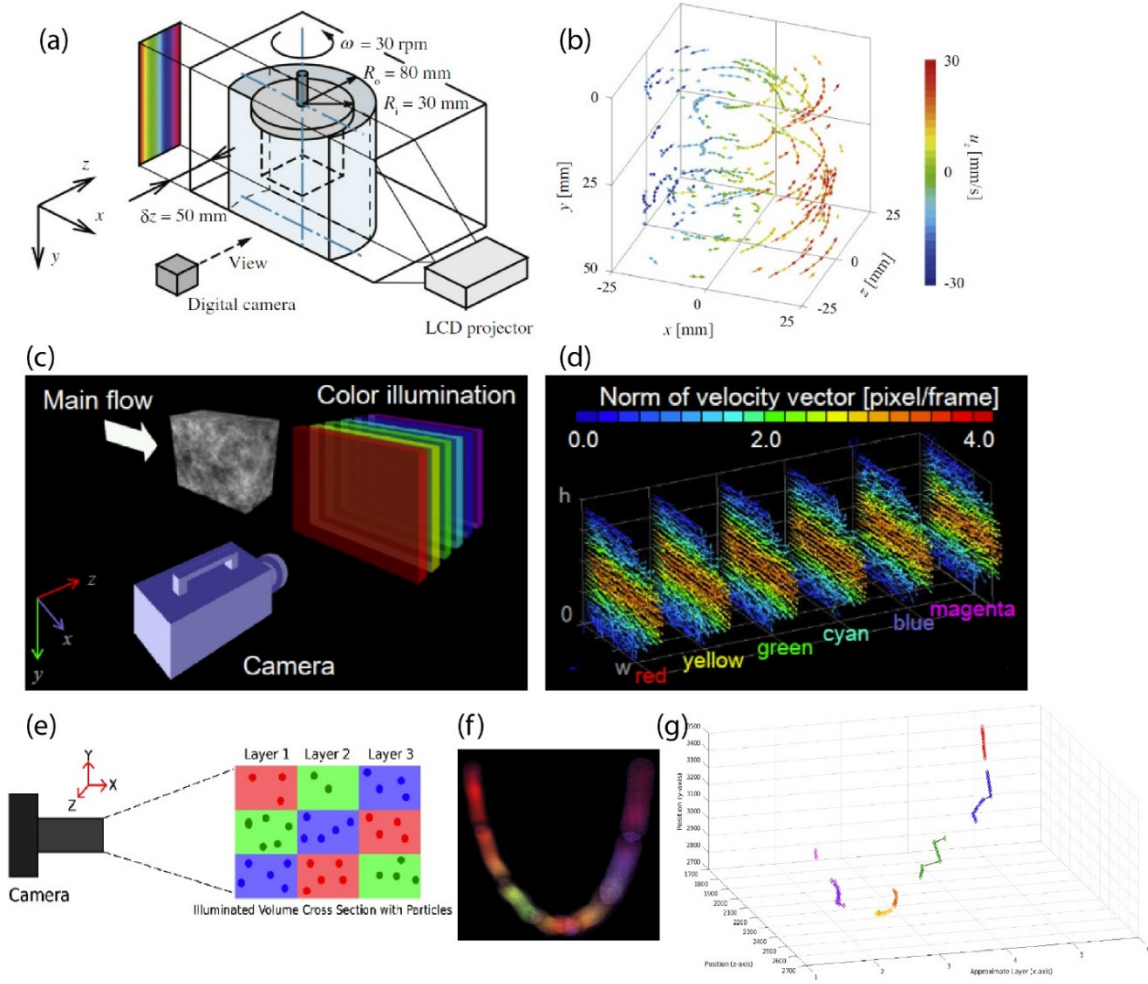


Figure 1.11. (a) Experimental setup proposed by Watamura, T., et al. [45] (b) Result of 3D-3C velocity field produced by the setup in Figure a. (Figures a, b are reproduced from Watamura, T., et al. [45]). (c) Six-layer color PIV experimental setup proposed by Murai, Y., et al. [46]. (d) 3D-2C velocity field reconstructed in six layers from the setup in Figure c. (Figures c, d are reproduced from Murai, Y., et al. [46]) (e) Experimental setup for a three-color grid proposed by Dennis, K. and Siddiqui, K. [47] (f) Typical image of a particle streak produced by the system in Figure e. (g) Single reconstructed particle pathline based on the streak color. (Figures e-g are reproduced from Dennis, K. and Siddiqui, K. [47])

The previously mentioned systems, provide 3-D particle tracking. However, they have many limitations such as very low spatial and temporal resolution. Some of the previously mentioned systems add cost and complexity by using specialized equipment such as the Stimulated Raman Scattering (SRS). Some of them only produce 3D- 2C fields at different planes simultaneously. In addition, the reconstructed volume is usually limited to 10mm or less in depth.

## 1.4 Motivation, dissertation structure and list of publications

In this chapter, we have described different systems used to produce three dimensional measurements in fluid flows. However, in the actual techniques there is always a trade-off between simplicity, cost and accuracy.

The proposed work herein, uses multiple smartphone cameras and single camera systems. These techniques simplify the experimental arrangement allowing to reduce the setup time and hardware costs by using consumer electronics, while preserving high accuracy and resolution. Additionally, the use of LED's and consumer projectors for the light engines, reduce the safety hazards related to high power lasers and give flexibility in the illumination volume size.

The proposed methods in this work will increase adoption of experimental techniques for three dimensional flow studies in Science and Engineering, lowering the entry bar to research institutions and companies that previously considered these methods prohibitively expensive and complex. The general structure of this dissertation is presented in Figure 1.12.

A list of publications resulting from my Ph. D. work is summarized in the following list:

1. Zhang, J. M., Li, E. Q., Aguirre-Pablo, A. A., & Thoroddsen, S. T. (2016). A simple and low-cost fully 3D-printed non-planar emulsion generator. RSC Advances, 6(4), 2793-2799.

2. Zhang, J. M., Aguirre-Pablo, A. A., Li, E. Q., Buttner, U., & Thoroddsen, S. T. (2016). Droplet generation in cross-flow for cost-effective 3D-printed “plug-and-play” microfluidic devices. *RSC Advances*, 6(84), 81120-81129.
3. Aguirre-Pablo, A. A., Alarfaj, M. K., Li, E. Q., Hernández-Sánchez, J. F., & Thoroddsen, S. T. (2017). Tomographic Particle Image Velocimetry using Smartphones and Colored Shadows. *Scientific Reports*, 7(1), 3714.
4. Nassar, J. M., Mishra, K., Lau, K., Aguirre-Pablo, A. A., & Hussain, M. M. (2017). Recyclable Nonfunctionalized Paper-Based Ultralow-Cost Wearable Health Monitoring System. *Advanced Materials Technologies*, 2(4).
5. Vakarelski, I. U., Klaseboer, E., Jetly, A., Mansoor, M. M., Aguirre-Pablo, A. A., Chan, D. Y., & Thoroddsen, S. T. (2017). Self-determined shapes and velocities of giant near-zero drag gas cavities. *Science advances*, 3(9), e1701558.
6. Xiong, J., Idoughi, R., Aguirre-Pablo, A. A., Aljedaani, A. B., Dun, X., Fu, Q., . . . Heidrich, W. (2017). Rainbow particle imaging velocimetry for dense 3D fluid velocity imaging. *ACM Transactions on Graphics (TOG)*, 36(4), 36.
7. Aguirre-Pablo, A. A., Aljedaani, A. B., Xiong, J., Idoughi, R., Heidrich, W., Thoroddsen, S. T. (2018). Single-camera 3-D PTV using particle intensities and structured light . *Experiments in Fluids*. (Under review)



Provisional and Published Patent applications:

1. Heidrich, W., Xiong, J., Dun, X., Idoughi, R., Thoroddsen, S.T., Aguirre-Pablo, A.A., Aljedaani, A.B. and Li, E., King Abdullah University of Science and Technology (KAUST), 2018. Rainbow Particle Imaging Velocimetry for Dense 3D Fluid Velocity Imaging. U.S. Patent Application 15/498,317.
2. Aguirre-Pablo, A. A., Thoroddsen, S.T., Heidrich, W., Aljedaani, A.B, Xiong, J., Idoughi, R., King Abdullah University of Science and Technology (KAUST), 2018. Single-camera 3-D Particle Tracking System and Method using particle intensities and structured light. U.S. Provisional Patent Application 62/683,879

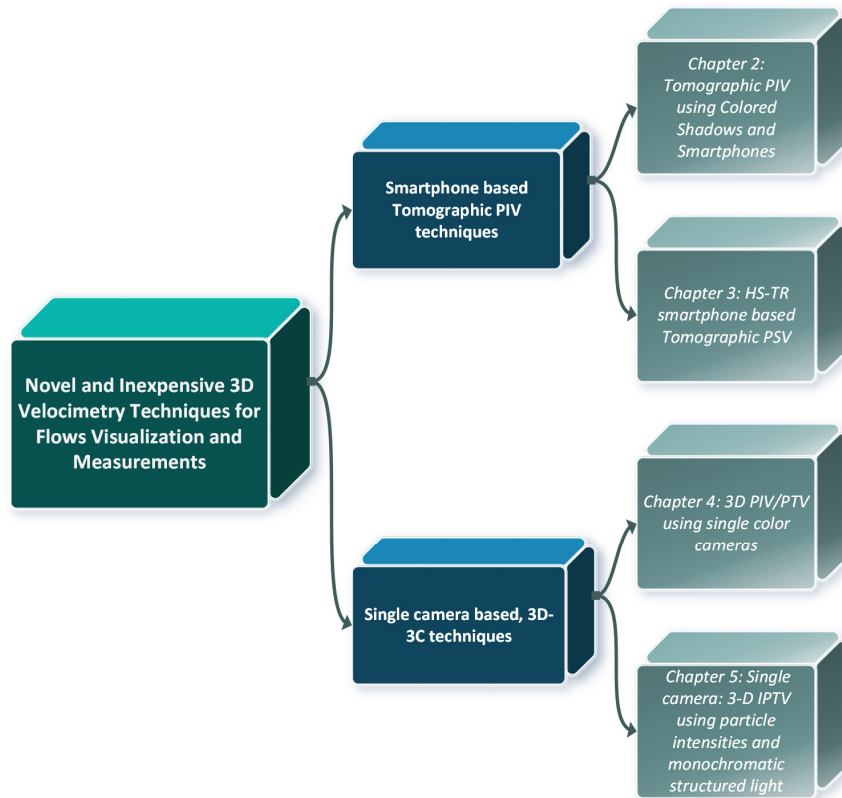


Figure 1.12. Ph.D Dissertation structure



## **Chapter 2 : Tomographic PIV using Colored Shadows and Smartphones**

In this chapter, we demonstrate the feasibility to use four low-cost smartphone cameras to perform Tomographic PIV. We encode two and three different instants in a single image using colored shadows. The light source in pulsed backlight configuration consists of three sets of Red, Green and Blue Light Emitting Diodes (LED's). To create a uniform background, each set of Red, Green and Blue LEDs is flashed on a diffuser screen facing each of the cameras. Therefore, instead of recording the conventionally scattered light from the particles we record the RGB-colored shadows of opaque suspended particles. In order to represent the separate times, we process the captured images to separate the RGB color channels and minimize noise. We use commercially available Tomo-PIV software for the calibration, 3-D particle reconstruction, and particle-field correlations, to obtain all three velocity components in a volume (3D-3C velocity field). Acceleration can be estimated thanks to the triple pulse illumination. To test the proposed technique, we carry out measurements of a vortex ring. The ring is produced by forcing pulsed flow through a circular orifice, using a flexible membrane, which is driven by a pressurized air pulse. We then compare the proposed system to a commercial stereoscopic PIV system for error estimations. We believe this proof of concept will make this technique available for education, industry, and scientists for a fraction of the hardware cost needed for traditional Tomo-PIV.

## 2.1 Experimental setup

As mentioned in previous sections, the motivation for designing new alternatives to the traditional tomographic PIV systems is to reduce their cost and minimize the health hazards that the laser systems represent. In this section, the proposed system consists of four smartphone cameras that observe the trajectories of the particles in an octagonal tank of water from different angles for the first iteration. On a second iteration, the water was replaced by an aqueous solution of sodium chloride, with a density ( $\rho$ ) of 1.18 g/cm<sup>3</sup>. This aqueous solution is used instead of pure water due to the limited availability of tracer particles. In this way, the difference in density does not affect as much the quantitative results, as discussed further in a later section.

The studied flow is a vortex ring seeded with opaque black particles since it has a clear 3D structure and will demonstrate the system capabilities. Long exposure in the captured images allows observing the flow, flashing the three sets of three color LED's in a synchronized mode. Therefore, recording shadows of particles in a single image at exactly the same instant in all the cameras. Due to the prolonged exposure, the room has to be isolated as much as possible from exterior light to avoid any external light contamination. A summary of this system components and specifications are presented in Table 1.

Flow	Vortex ring pulse width air pressure	Generated by pulsed membrane 150 ms 2.3, 3.2 bar
LED lighting	Model Pulse width $\Delta t$ Current Voltage	RGB PT-120 Luminus 80 $\mu s$ 1300, 1000, 500 $\mu s$ 15 A 12 V
Camera properties	4x Nokia Lumia 1020 Type Lens Aperture Sensor size Resolution Pixel pitch in sensor Color Depth	Back camera CMOS 26 mm F# 2.2 2/3" 38 Mpx 1.12 $\mu m$ 8 bit
Seeding properties	Manufacturer Type Density Size	Cospheric Black polyethylene 1.28 g/cm <sup>3</sup> 212-250 $\mu m$
Image properties	Viewing angles Total PIV system angle Particle diameter Pixel size in focal plane Particle density N Source Density (Ns)	$\pm 45^\circ, \pm 10^\circ$ 90° 6 px 38 $\mu m/px$ 0.005 ppp 0.3

Table 1. Summary of parameters used for capturing tomographic PIV images of a vortex ring.

A detailed description of the previous process and components is presented later in this chapter. A schematic representation of the experimental setup is presented in Figure 2.1. This work has been published in the Nature Journal: Scientific Reports[48].

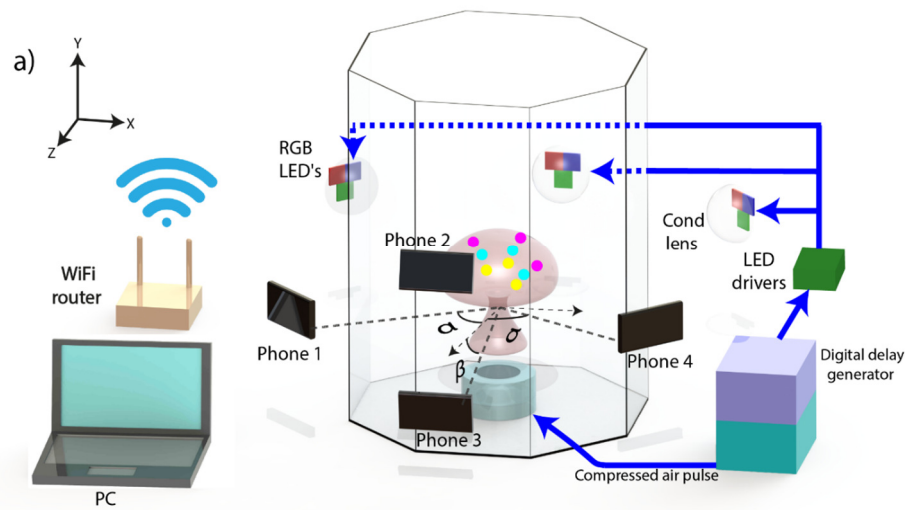


Figure 2.1. Schematic experimental setup of the smartphones, vortex ring generator, LEDs and the components required to trigger and synchronize the system, while capturing three different time steps shown as yellow, cyan and magenta colors. The angles between the cameras are  $\alpha=45^\circ$  and  $\beta=10^\circ$ . [48]

### 2.1.1 Cameras and imaging systems

The smartphones selected for this experiments were four Nokia Lumia 1020, this is due to their large pixel count and relatively large pixel size compared to other smartphones. The back camera sensor consist of an active area of 38 Mpx with a sensor size of 2/3 inch, having a pixel size in the sensor of  $1.12\text{ }\mu\text{m}$  with a Bayer filter, providing 8-bit color depth per channel, i.e., 256 intensity levels for each color. Unfortunately, the optics and lenses utilized in smartphones are always fixed having a large aperture and wide angle, this will restrict the control over the magnification and depth of focus. These cameras are equipped with a fixed aperture of F# 2.2 and a fixed focal length of 26mm[49]. These optical characteristics will allow us to have a depth of field of approximately 100 mm. The small pixel size in the sensor compromises the sensitivity to illumination. However, this is overcome by using high-power LEDs as a light source and registering shadows rather than the scattered light or fluorescence from particles, typically employed in PIV. This decreases the illumination intensity requirements significantly.

One of the advantages of actual smartphone cameras is the capability of saving the captured images in RAW format, DNG for this case. This will allow processing the images without losing information due to the default color-interpolation when taking pictures in JPG format.

All cameras settings such as exposure time, white balance, gain, ISO and triggering can be controlled wirelessly through a WiFi network from a PC. The PC sends

simultaneous HTML commands over the network to the smartphones to trigger them all within 2 ms, which is the typical delay of the wireless network equipment used. The ISO is set to 200 minimizing noise in the sensor. The exposure time of all the smartphones is set to 1 second, such that all the cameras can sense the light coming from the LEDs at the same time, overcoming any delay in the trigger of each camera due to the network ping times.

The smartphones are mounted on a tripod geared head, using a stiff 3D printed casing made of Polylactic Acid polymer (PLA) fabricated in-house (see Figure 2.2). This configuration will allow to align and finely adjust the position and angles of the smartphones. In Figure 2.3 (a,b) the position of the cameras can be observed. The smartphones observe the flow through three adjacent windows. The two central cameras have a Field of view through the central window, at an angle of  $\beta=\pm 10^\circ$ , while the side cameras have an angle  $\alpha=\pm 45^\circ$  with respect to the center.

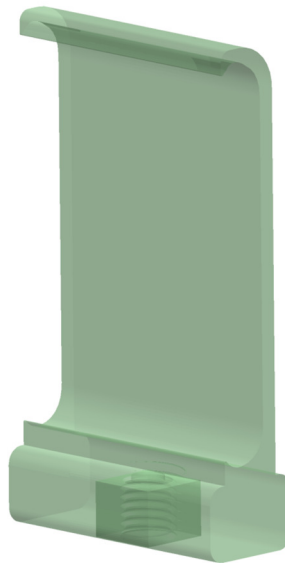


Figure 2.2. 3D model for smartphone holder

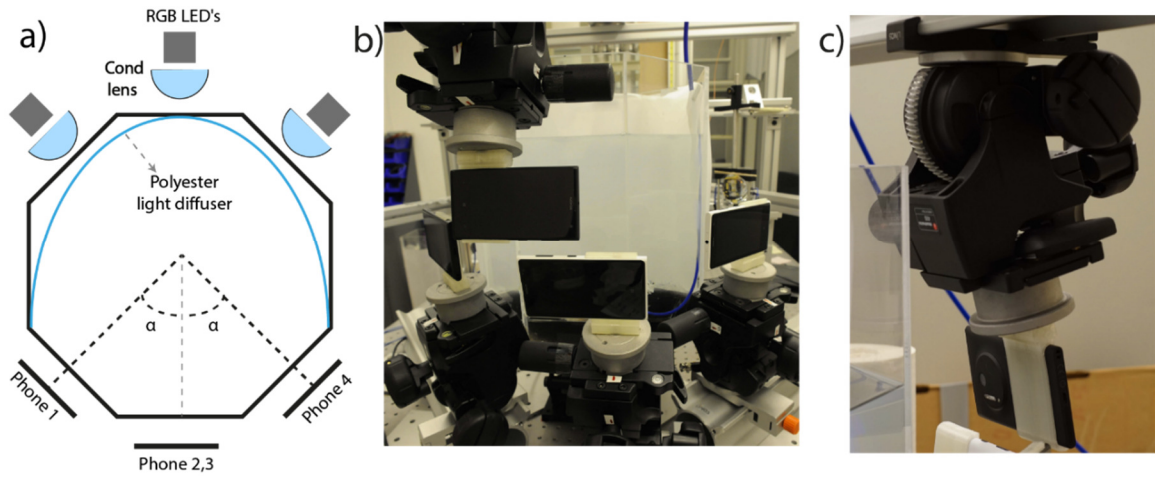


Figure 2.3. (a) Top view of the setup. (b) Actual photography of the setup, showing the mounting structure for precise and fine adjustment of the smartphones. (c) Detail of the support structure and 3d printed holder.[48]

### 2.1.2 Vortex ring generator

In order to test this technique, a vortex ring is produced and observed as it travels up inside an octagonal water tank, through the field of view of the four cameras. Figure 2.4 shows the device used to generate this vortex ring. This device for generating the vortex ring is placed at the bottom of the 390 mm deep plexiglass tank with a horizontal width of 340 mm. Each of the flat octagonal segments is 145 mm wide. Figure 2.1(a) shows the orientation of the coordinate system we use. This device consists of a circular chamber of 100 mm in diameter, which is covered with an impermeable, elastic latex membrane that isolates both sides of a cylindrical container. The bottom side of this container is sealed from the water, and it is connected by a hose to an air flow controller that is operated in pulsed mode. The flexible membrane is enclosed at the top by a 3D printed cap with a smaller circular central hole of 60 mm in diameter. The duration and pressure level of the air pulse, delivered into the chamber, can be regulated and is

synchronized with the LEDs via a digital delay generator (DG645 from Stanford Research). The air pulse drives the membrane upwards pressurizing the chamber and forcing the water to pass through the reduced cross-section in the cap, accelerating the flow and finally separating the boundary layer to generate the vortex ring, as explained in Figure 2.4. As expected, increasing the pressure of the air pulse gives more impulse to the membrane and produces a faster translation and rotation of the vortex ring. We selected two pressure levels, of 2.3 and 3.2 bar, to drive vortices at different translational velocities of 0.15 to 0.25 m/s, which required time steps between flashes of  $\Delta t = 1000$  and  $500 \mu\text{s}$ , for the case of pure water, and  $\Delta t = 1300 \mu\text{s}$  when using the sodium chloride solution.

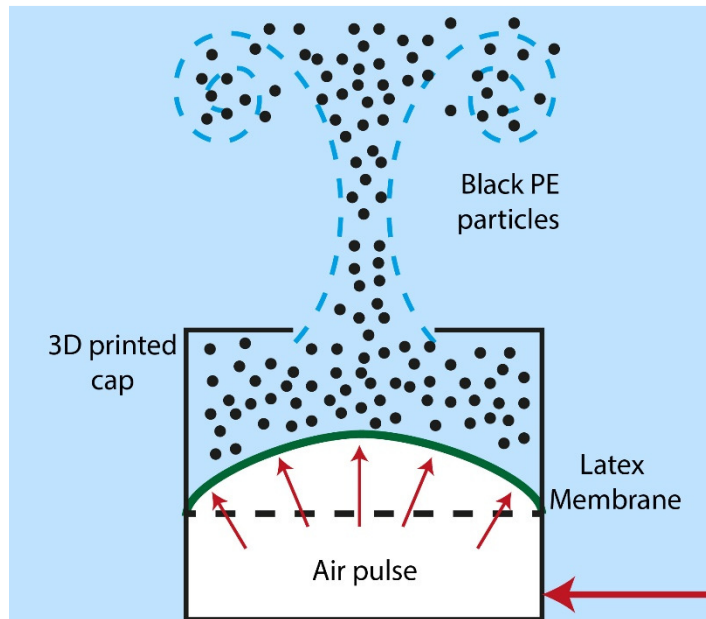


Figure 2.4. Schematic drawing of the vortex ring generator. Pulsed air is introduced into the enclosed bottom chamber, pushing a latex membrane to force out a fraction of the fluid in the chamber through a circular orifice, thus creating a vortex ring. The liquid inside the chamber has been pre-seeded with black micro-spheres. [48]

### 2.1.3 Flow tracers

As mentioned in section 1.1, the material density of the tracer particles should be nearly neutrally buoyant to follow the fluid motion. However, in contrast to the silver coated or fluorescent particles used in traditional PIV systems, our proposed technique requires opaque particles to block the light into the camera sensors, obtaining sharper shadows. Due to the color nature of the illumination technique, the Bayer Filter pattern (that uses an array of 2x2 GR/BG pixels) present in most color sensors and the fixed non-interchangeable optics of the smartphone cameras, present a challenge to locate the tracer particles accurately. Therefore a particle size of at least 4 to 5 pixels ( $>200\text{ }\mu\text{m}$  in the actual configuration) is necessary to minimize location bias and diffractive effects. This limited our options in selecting commercially available opaque microparticles  $\sim 250\text{ }\mu\text{m}$  in diameter to seed the flow. Thus, we were forced to use black polyethylene microspheres (Cospheric) with a size range of 212-250  $\mu\text{m}$  and density  $1.28\text{ g/cm}^3$ , as they are opaque and are approximately 6 pixels in the captured images. To reduce the density differences between the particles and the fluid, we use a sodium chloride aqueous solution as the working fluid, to make the particles follow better the fluid motions. For practical reasons, the density of this solution is set to  $\rho=1.18\text{ g/cm}^3$ , which is marginally lower than the density of the particles. This allows slow particle sedimentation between experiments without significantly affecting their flow-tracing properties. This reduces the number of defocused particles that add noise in the captured images. The Stokes number is the ratio between the characteristic time of the particles and the characteristic time scale of the fluid. We estimate the Stokes number ( $St$ ) for the actual particles to be  $St \leq$



0.05, this value represents an upper bound where the time scale of our fluid is the lowest. Such a value indicates that our particles will follow the flow closely.

The particles are seeded and stirred inside the chamber within the cylinder on top of the membrane, allowing them to be dragged by the vortex ring and tracing the trajectory of the vortex ring. Denser particles will settle, minimizing the effect of out-of-focus particles which add noise to the captured images. In Figure 2.4, a schematic representation of the device and procedure is presented.

For a first iteration, experiments in pure water were carried on. Nevertheless, as expected, it was observed that the tracing properties of the particles were affected by gravity due to the density difference between the tracers and the pure water. The core of the vortex ring has a lower particle concentration due to the centrifugal force in that region. In order to circumvent these adverse effects, a sodium chloride aqueous solution is used with a density of  $1.18 \text{ g/cm}^3$ , minimizing the effects of gravity on the tracer particles.

#### **2.1.4 Illumination**

Each camera views a set of multiple colored LED's, red, green and blue as shown in Figure 2.1. The High power LED's used for this experiments are Luminus PT-120 (Figure 2.5a), the typical emitted spectrum for each color is presented in Figure 2.5(b). The response time for this kind of LED's was studied previously by Buchmann, N., et al.[14], having a response time of less than 200 ns to full brightness making them a suitable choice for this technique. They are driven with Phlatlight DKM-136 development kit drivers.

These drivers can be operated in pulsed or continuous wave modes. They are energized by a power supply of 12V and up to 15A each, providing enough power to operate the LEDs at high brightness while protecting them from being overloaded. Each set of RGB LED's is placed behind an aspheric condenser lens ( $\varnothing = 75$  mm and  $F=60$  mm,  $NA=0.61$ ), in order to concentrate the light in the region of interest. The light is projected through a curved sheet of matte white polyester sheet that acts as a diffuser, distributing the light intensity more evenly, as seen in Figure 2.3(a).

The duration of the illumination faces the typical trade-off between sufficient intensity and the need to freeze the instantaneous location of the particles. In this setup, it was found via trial and error that for the actual setup and velocity of the flow, the optimal exposure time is 80  $\mu s$  to avoid smearing of fast-moving particles. The light flashes are synchronized and triggered by the digital delay generator. Different time delays between colors were used to test the capabilities of our system depending on the strength of the vortex rings. Therefore, 1300, 1000 and 500  $\mu s$  were selected as our  $\Delta t$ , capturing the three color time steps in a single frame. Much smaller time steps can be achieved by the camera and illumination systems, being only constrained by the velocity of the flow and vortex generation system.

Using multi-color illumination can cause systematic bias in the position of the particles recorded in the different colors, due to differences in the diffraction through the transparent walls of the tank. The amount of this diffraction varies slightly with the

wavelength of the light. Detailed study of this effect has been carried out by McPhail *et al.*[18]. Further discussion about this bias error will be addressed in a later section.

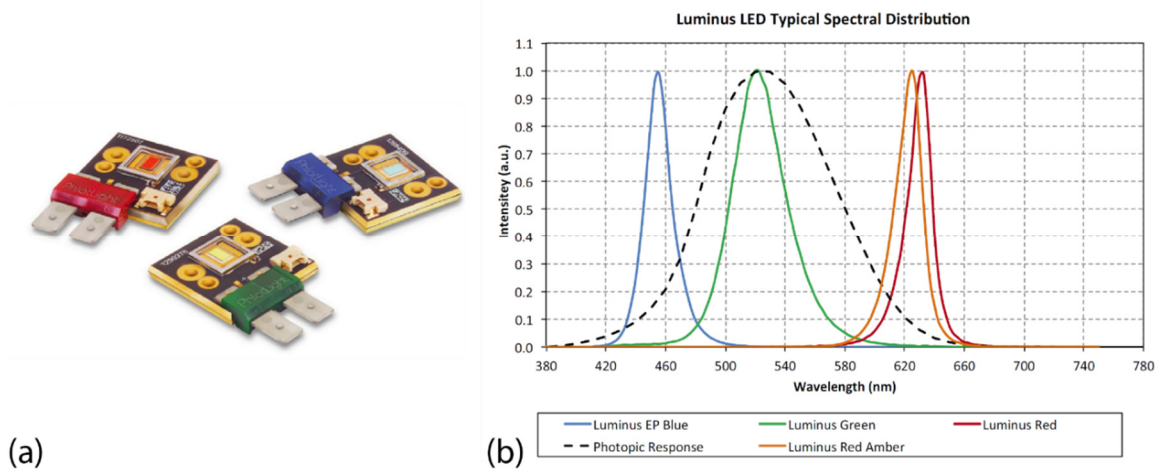


Figure 2.5. (a) Photo of a set of RGB PT-120 LED's. (b) Spectrum of light emitted by each of these LED's by color.[50]

### 2.1.5 Tomographic PIV calibration

In order to reconstruct the 3D position of the multitude of tracer particles, it is crucial to obtain a high-quality calibration from in-situ images from all four cameras. We used a dotted bi-planar calibration target type 22 from LaVision for calibration purposes. The calibration target is a 30 cm wide which covers a more significant area than the vortex ring, (see Figure 2.6). The target is translated precisely with a stepper motor and translation stage (VT-80 from miCos) along the volume of interest in the Z direction from -40 to +40 mm, with steps of 5 mm.

The primary goal of the calibration is to obtain a 3D space mapping function where the particles will be moving. At the same time, it corrects for distortions arising from the

imperfect lenses and diffraction due to non-perpendicular viewing angles through the tank walls. This original calibration will be subsequently improved with the self-calibration algorithm described in a later section[51].

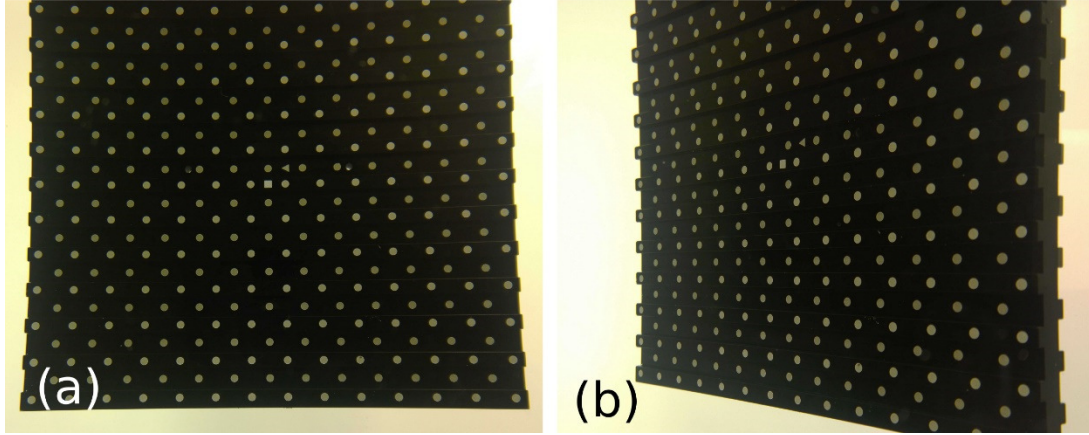


Figure 2.6. Image of the calibration target (type 22 from LaVision) viewed from two angles. (a) From central bottom camera 3 and (b) from the off-axis camera 4. The image shows the optical distortions produced by the lens and by the angled view through the Plexiglas walls. [48]

### 2.1.6 Two and Three-Colored Shadows

Once the cameras are triggered, and the vortex ring is generated, the two or three color-coded lights are flashed in a sequence to produce shadows of the particles at different times,  $t_1$  and  $t_2$  as well as  $t_3$ . We obtained a pair or triplet of images of each particle in a single frame, as shown in Figure 2.7 (a). Note that the order of the colors of the dots is reversed from that of the illumination, i.e., if the first flash at  $t_1$  is red and second flash at  $t_2$  is blue, then the particle color at the location corresponding to  $t_1$  will be blue and vice versa for the two-color case. This is because the particle at  $t_1$  blocks the red light and moves before the blue light fills in the shadow. The power of shadow PIV imaging (PSV) was demonstrated by Estevadeordal and Goss in previous research [17]. For two-color cases, we use the blue and red flashes to minimize cross-talk between

them, as these wavelengths are the most separated of the three colors in the light spectrum (see Figure 2.5 b). However, getting sufficient energy in the blue LED can be a challenge [52]. Cross-contamination will, of course, depend both on the spectral content of the illuminating light and the shape of the band-pass filter in the Bayer matrix on the sensor. This greatly facilitated the separation of color channels without any pre-processing of the images, as is clearly shown in Figure 2.7 (b-d). Very early experiments were carried out with 4 Nikon 3Dx cameras in the same configuration. However, these cameras could be complicated to operate, and the cost of such a system can be dramatically reduced with the use of smartphone cameras.

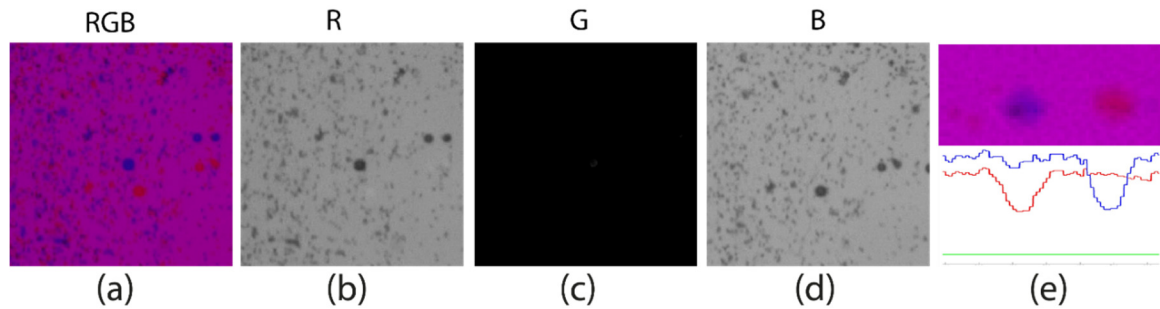


Figure 2.7. (a) Original image using only Red and Blue flashes (obtained with a Nikon sensor). The captured image is separated in its RGB channels red (b), green (c), and blue (d). (e) The color intensities cut through the blue and red dots.[48]

For a second implementation of the technique, of primary focus herein, we exploited all three color-channels on the sensors of the cameras, by using a three-color LED illumination. Each color of the LED light was pulsed separately, e.g., in a green-red-blue sequence, thereby encoding three different time-instants,  $t_1$ ,  $t_2$  and  $t_3$  on the same image. All three flashes occur within the same exposure time of the cameras, capturing three different spatial positions of each particle. The particle-color denoting each time step on the sensor is detected as the corresponding negative color in the RGB color space,

as depicted in Figure 2.8. From this diagram, we observe the yellow pixels in Figure 2.9 correspond to the blue flash. Similarly, the cyan and magenta pixels in Figure 2.9 correspond to the red and green flashes, respectively. In both implementations (two and three colors), the experiments were performed by varying the intervals between the color flashes ( $\Delta t$ ) from 1300  $\mu\text{s}$  for the slowest vortex ring to 500  $\mu\text{s}$  for the fastest one.

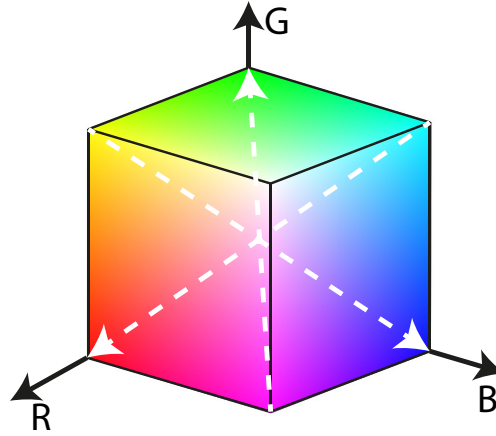


Figure 2.8. . The RGB color space represented in Cartesian coordinates. The white dashed arrows link the corresponding negative colors that are captured in the images.[48]

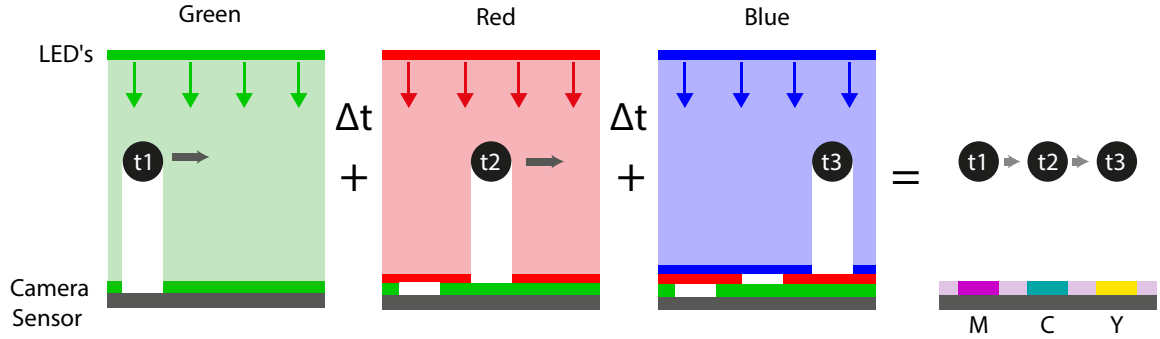


Figure 2.9. Schematic representation of the color time-coding approach used for the CMOS sensors. As the particle travels, the colored lights are flashed at different times, leaving their corresponding shadowed pixels recorded in the camera sensor. The final result is an image of the negative colors for each time step, i.e., green flash marks the particle location by magenta pixels, red by cyan and blue by yellow.[48]

This implementation, at the same time, had two sub-iterations where the recorded images are captured in JPEG and DNG format. The first one is the result of interpolations of the intensity for each color captured in the Bayer Filter Array. The result is a

compressed image, where the color had been adjusted according to proprietary algorithms by Nokia, as shown in Figure 2.10(a, b). It is noticed that the blue color is overcompensated due to the lower sensitivity of this kind of sensors. Thus, the separation of the color shadows, especially the yellow color (corresponding to the blue flash), becomes very difficult and almost impossible due to data loss in the interpolation process.

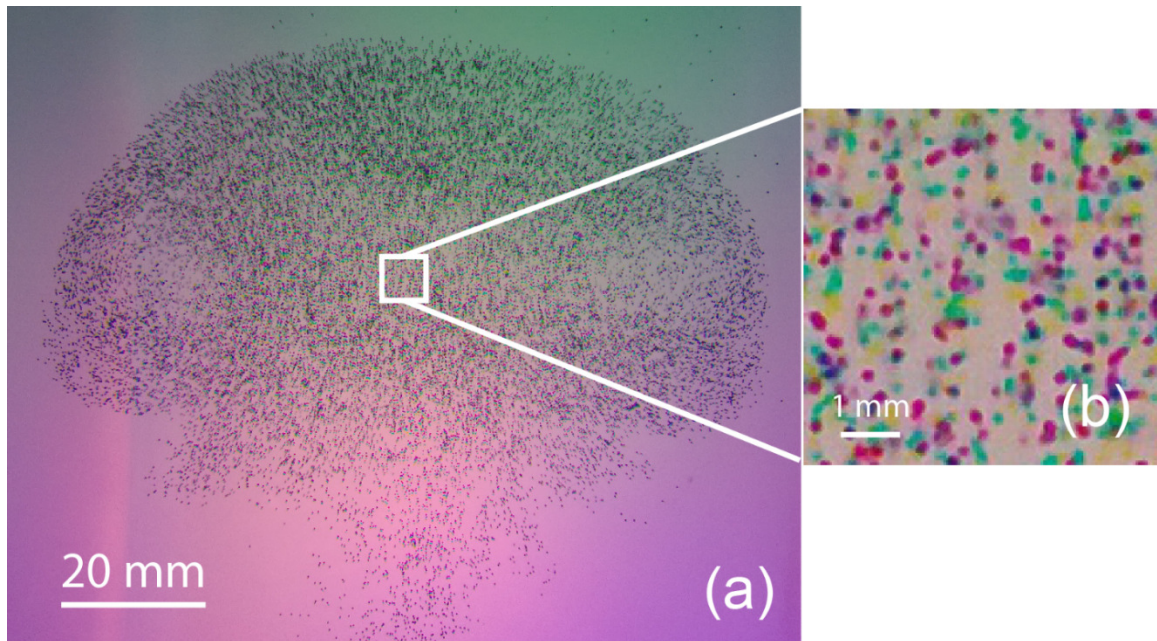


Figure 2.10. (a) Typical JPEG image obtained from the smartphones. (b) Magnified image of a small region, it is noticeable that yellow particles fade away due to the interpolation algorithms.

As a result of the previously mentioned problems, it is necessary to record images in RAW format. Latest smartphones are able to record in Digital Negative (DNG) format created by Adobe®. This format keeps the RAW information captured by the sensor, i.e., we have access to the intensity values for each pixel, regardless of the color of the filter. As this technique uses purely red, green and blue illumination, we can separate the color channels by the location of the color filter array. For this cameras, the filter array has a GR/BG configuration as depicted in Figure 2.11. Due to the higher quality of the DNG files,



we continued working with DNG files only. In Figure 2.12 (a, b), one can see the result obtained by using DNG format and the improvement in the color captured.

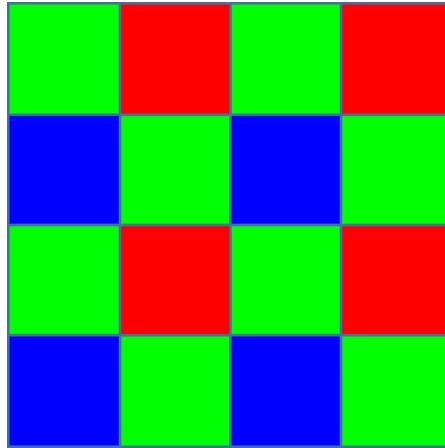


Figure 2.11. Representation of the Color Filter Array (Bayer filter) configuration found in the Nokia Lumia 1020 camera sensor. It presents a GR/BG structure.

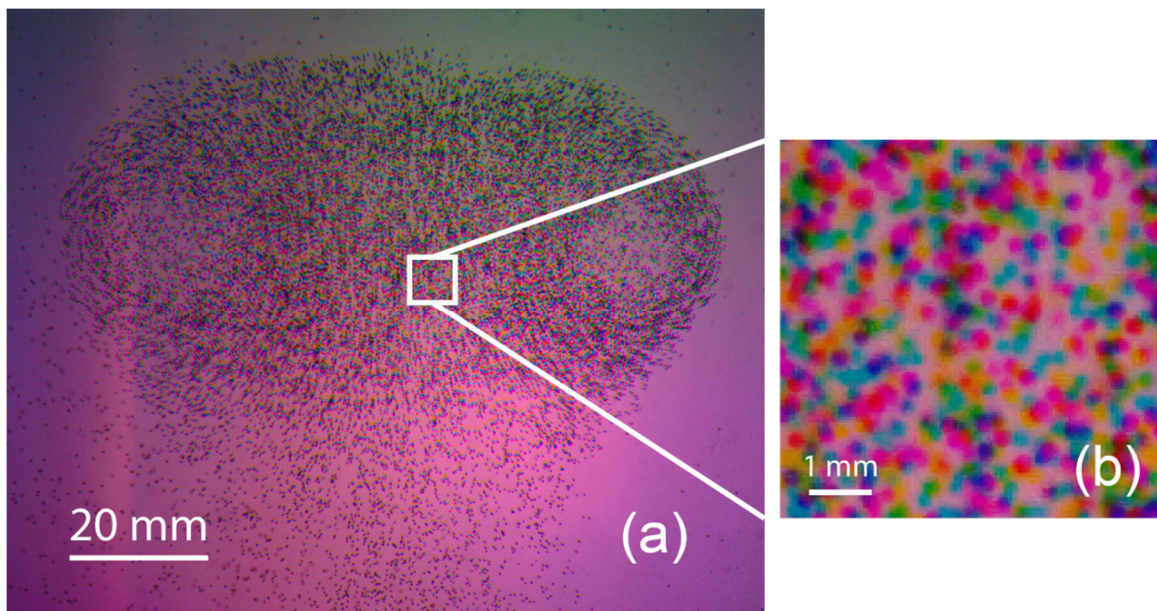


Figure 2.12. (a) Captured image from the bottom central camera (phone 3) in DNG format . In this image, we clearly observe the three different colored shadows and the vortex ring structure in a “mushroom” shape. (b) 9x magnification of a sampled area, inside the white square.[48]

### 2.1.7 Color crosstalk and Chromatic aberrations

One of the problems encountered by using multi-chromatic illumination is the introduction of bias errors of the particles locations. This arises due to the differences in



refraction of the three different wavelengths of the light used as the light passes through the tank walls. Additionally, color crosstalk between the RGB channels due to mismatch of the emission bandwidth of the LED lights and the transmission spectra of the Bayer filter array used in the camera sensor, can negatively affect the results. These effects were studied in great detail by McPhail et al.[18] for 2D PSV, where they propose some chromatic corrections to minimize bias errors in the system.

To quantify color cross-talk, we use a glass calibration plate which contains a dotted pattern of different sizes. This target is placed inside the water-tank at the location of the vortex ring. Separate images are then captured by flashing the background diffusers with a single color at a time, allowing us to quantify the shift in the position of the dots due to chromatic aberration and to quantify the crosstalk between the color channels, as is depicted in Figure 2.13.

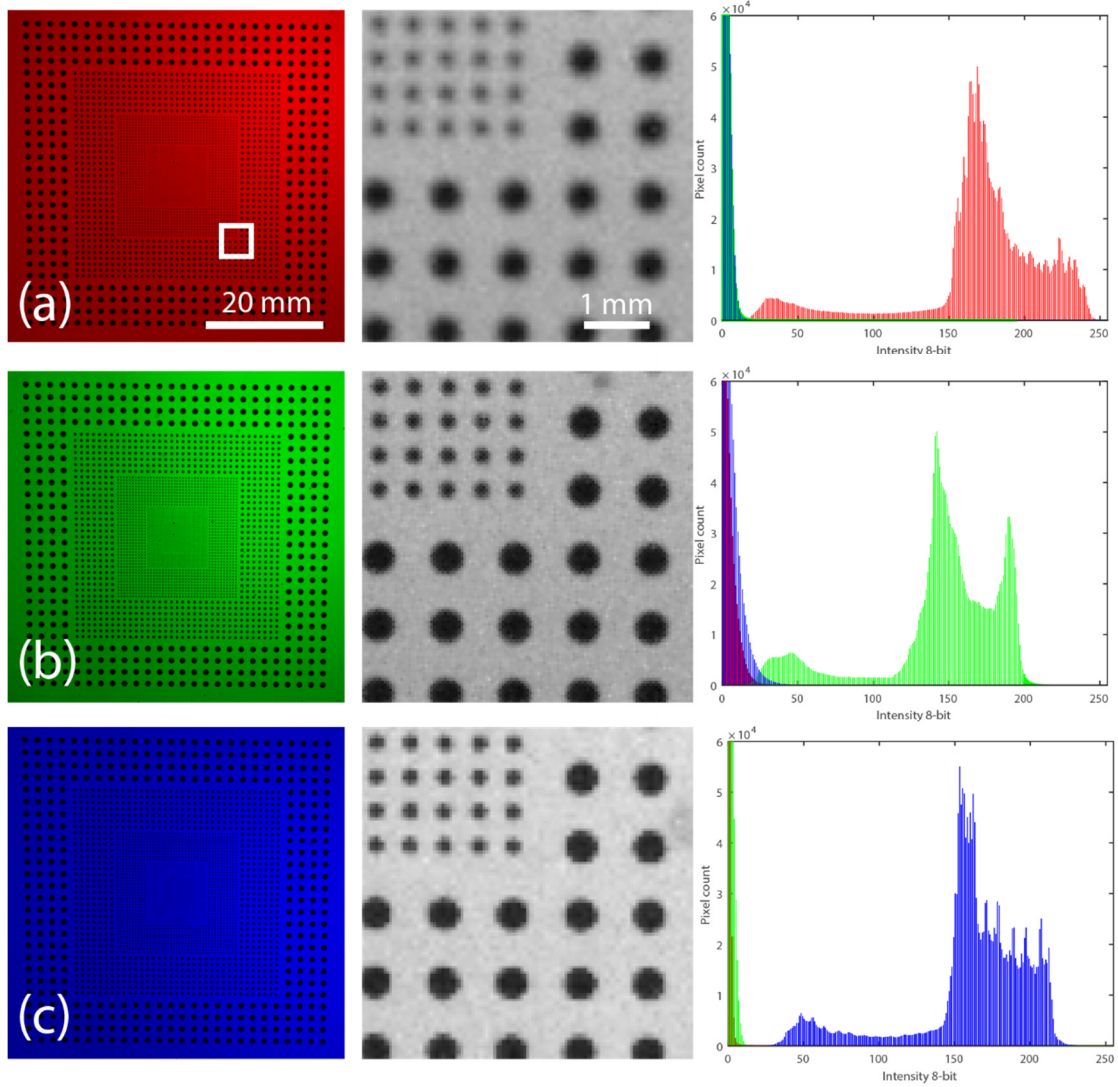


Figure 2.13. Images of the dotted calibration glass slide inside the water-tank, back-illuminated by red (a), green (b) or blue (c) LED flashes. The middle column images are magnified sections of the dots corresponding to the white square in panel (a). On the right column, we show the corresponding RGB intensity histograms. [48]

From the histograms in Figure 1.7 we observe that color crosstalk is quite limited in our setup, which allows us to remove any crosstalk by thresholding at a low-intensity level, without losing any details of the particles.

McPhail *et al.*[18] report adjusting for the chromatic aberrations of the colors by a “Zero-time-delay” correction, which consists of triggering all of the color flashes simultaneously. We expand their method to our 3D technique, capturing the “Zero-time-delay images” of a typical particle field, for all the cameras at the same time, so the particles do not move between the different colored flashes. This allows us to reconstruct the three particle fields and calculate the two 3D displacement-vector fields, between the green and red flash, as well as between the red and blue. Without chromatic aberrations, no displacement of particles should be observed. However, it is clear from the images in Figure 2.14, that some areas of the images are highly affected by the chromatic aberrations and the particle locations shift between the flashes. At the edge of the image, we have a displacement of 2 to 3 pixels between the colors, which corresponds to around 80 to 120  $\mu\text{m}$ . The images are then loaded and processed by the tomographic PIV algorithm with the same parameters as for the moving particles. This chromatic-aberration shift is primarily related to the angle of viewing through the wall and is, therefore, a slowly varying function over the image area and should remain fixed throughout the experiments if the cameras are not moved. An example of these displacement fields is shown in Figure 5.17. The magnitude of this effect is also different between green-red vs red-blue particle fields. The final velocity fields are corrected by subtracting these error velocity fields from their corresponding final velocity fields.

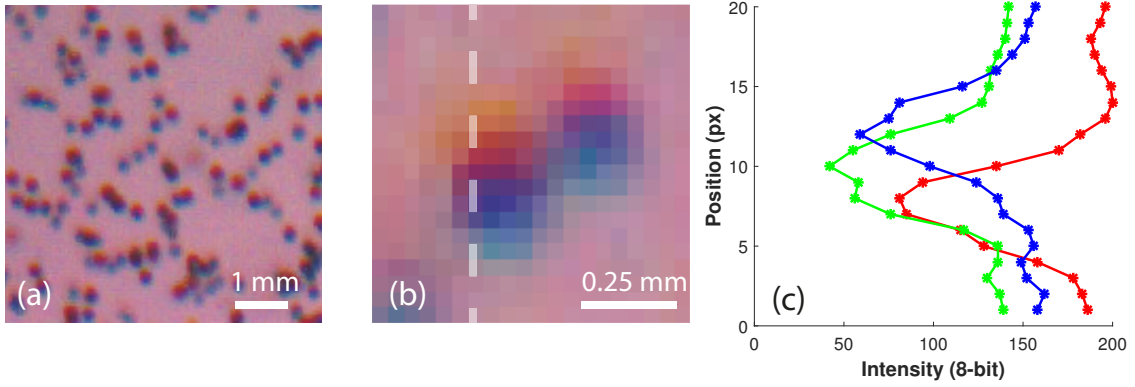


Figure 2.14. (a) Particle images with the three color LED's flashed simultaneously, i.e., with zero time-delay. (b) Close-up of two particles, which shows clearly the effects of the chromatic aberrations in one of the most affected areas, near the edge of the image. (c) The color profiles of a single particle, taken along the dashed line in (b). One can clearly see the vertical shifting of the colored shadows, due to the chromatic aberrations. [48]

## 2.2 Results

### 2.2.1 Pre-processing of images

Figure 2.12 shows a typical smartphone image captured by our method, revealing the vortex ring structure demarcated by the seeding particles in a “mushroom” shape. The tracer particles average image density within the vortex is  $N=0.015$  ppp (particles per pixel) considering the three RGB color channels; this translates into  $N=0.005$  ppp for each time step. When estimating the particles per pixel density, it is important to keep in mind the relatively large size of the particles used in our setup. Using a color sensor, one needs more pixels than is required for regular monochrome PIV sensor setup, to pin down the particle center effectively. Additionally one can obtain the source density ( $N_s$ ), i.e., the fraction of the image occupied by particles [53], this translates to  $N_s=0.3$ . Reducing the particle size makes it possible to increase the particle per pixel density ( $N$ ) while keeping the source density ( $N_s$ ) constant. For this technique, we estimate that the lower limit of each particle size is 4 pixels to avoid false color due to pixel binning, which can arise from

the interpolation of the Bayer filter array, as previously mentioned. The single color channel concentration in ppp is relatively low compared to traditional tomographic PIV, but is necessary to separate the particles for each color channel without devising too much overlap that may affect the color separation and low-quality reconstruction.

The maximum particle displacement between the flash instants was approximately 15 pixels, as measured in the fastest regions around the vortex core. As observed in Figure 2.12(a, b), the background exhibits significant large-scale spatial gradients in the color intensities. This inhomogeneous background in the picture occurs due to the different locations of each of the LEDs behind the projection lens and a slight unbalance in the intensity of each colored light. Owing to the fixed camera lenses, with constant focal length and aperture, the depth of focus is also fixed. These inflexible optics in addition to the size of our tank, limit the accessible region of interest (ROI). Thus, the 38 Mpx image area has to be cropped to an ROI of 2500 x 2000, i.e., an active area of approximately 5 Mpx. Considering that most of the commercial cameras used for PIV have a typical resolution of 4 Mpx or less, for configurations where the full image resolution of the smartphones can be used, the 40 Mpx would be almost ten times larger than the specialized equipment.

We use the DNG image files of the particles, which are acquired using the GRBG Bayer filter array present on the smartphone sensor, see Figure 2.15(a), before the interpolation is performed to generate the three color channels. We first show, in Figure 2.15(b-d), the three separate images for each color array, assigning a 0 level of intensity

for the other color pixels. Each of these images is then interpolated using the demosaic method proposed by Malvar *et al.*[54], which consists of gradient-corrected bilinear interpolation, creating sharper edges than simple bilinear interpolation, see Figure 2.15(e-g).

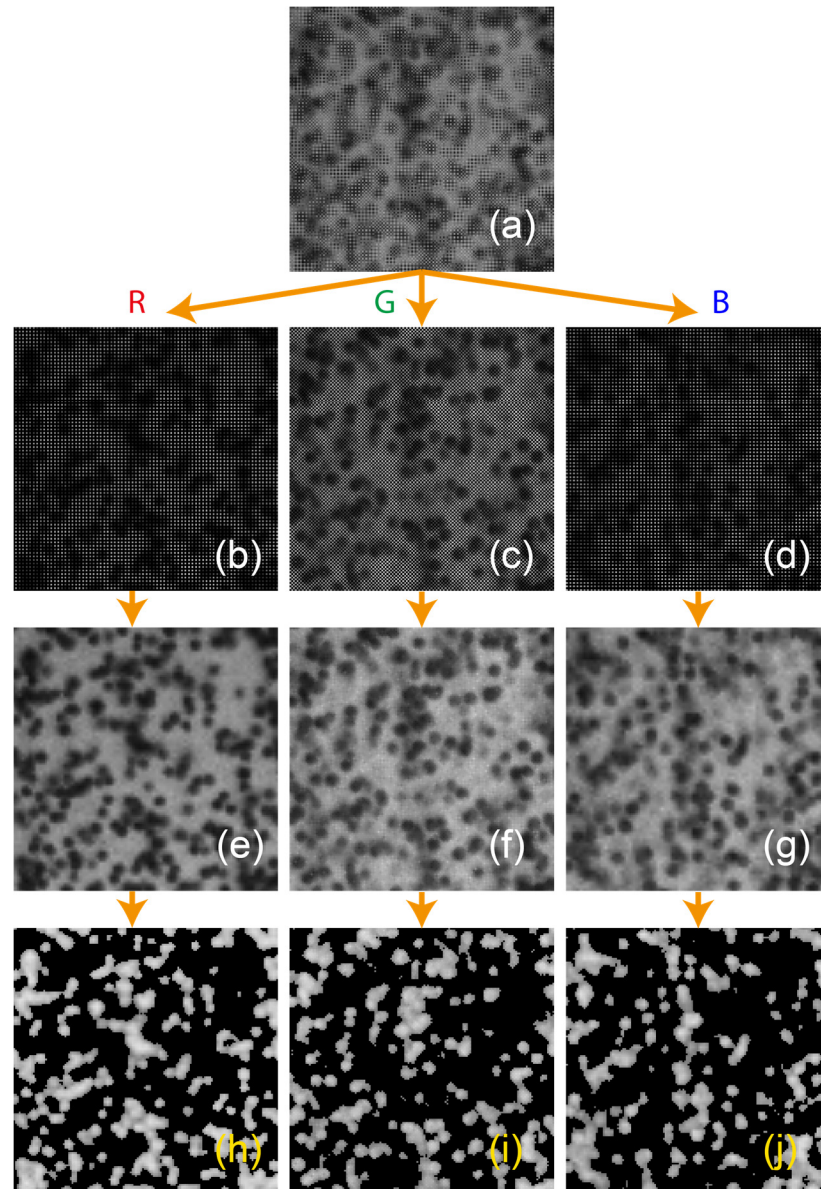


Figure 2.15. Steps for preprocessing of the raw image file, showing the same region as in Figure 2.12(b). (a) The raw image from the Bayer filter array in gray-scale intensity. (b-d) Separation of the color channels based on pixel location in the array, with other pixels filled by zeros. (e-f) Resulting images after demosaic interpolation (Malvar, et al.[54]). (h-j) Final images for each color after background subtraction and filtering by local standard deviation levels.[48]

The effects of the inhomogeneous background-color intensities can be minimized with additional image pre-processing steps in the following manner. First, we record several images of the same 3-color pulse-lighted background without any particles in the field of view. We use these images to normalize the background and intensities of the particle shadows subsequently. We do this by treating the background RAW image-files in the same way of separation and demosaic interpolation as the particle images, thus, obtaining the background reference frames for each color. Taking the local average background for each color and inverting the color intensities of both, the averaged background and particle images, allow us to subtract their intensities, resulting in a more uniform background and enhancing the particle signals. To further reduce background noise and any far-out-of-focus particles, the image is divided into subregions of 100 x 100 px to obtain their mean intensity ( $\bar{I}$ ) and standard deviation ( $\sigma$ ) locally. Pixels with intensity levels lower than  $\bar{I} + 3\sigma$  are filtered out inside each region, the threshold is strict, but real particles have a much higher intensity than the background at this point, Figure 2.15(h-j). An animation of the final split of the three frames played in sequence can be found in the Supplementary Video S1. The pixel intensity curves for the processing steps of the images are explained in Figure 2.16.

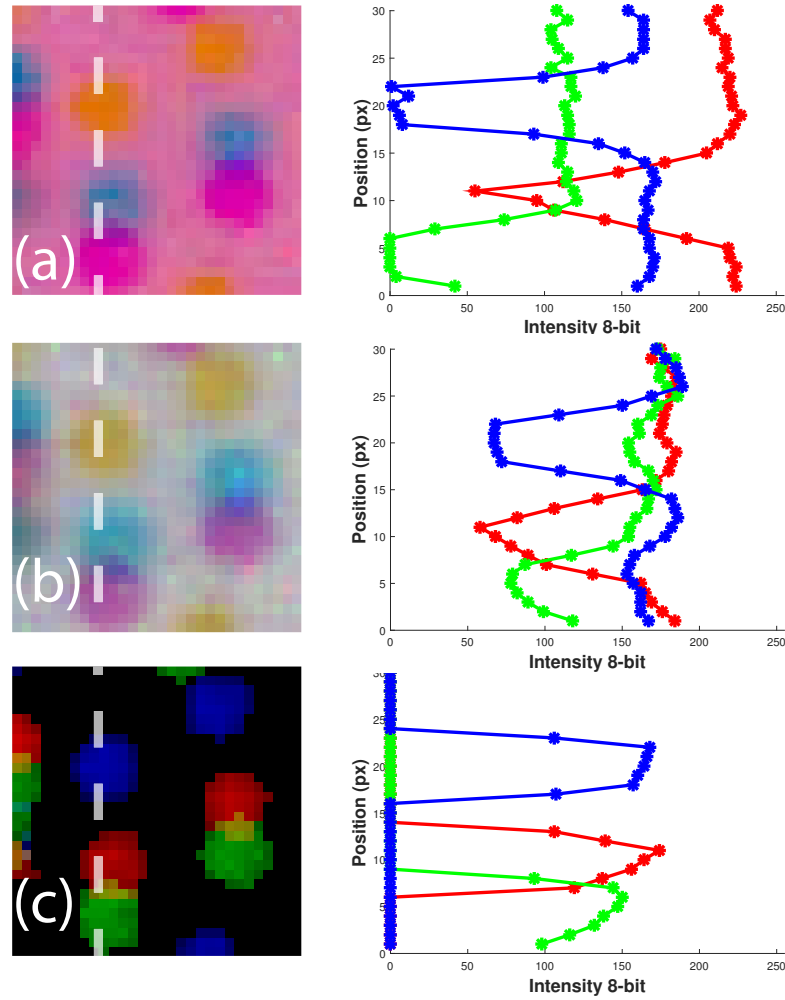


Figure 2.16. (a) Cropped portion of two particles from the raw captured image with the default color interpolation by the smartphone, (b) the interpolated raw image after separation of each channel array and combining them for clarity. (c) Inverted image after background subtraction and filtering by local standard deviation in each subregion, combining the color channels for clarity. For comparison, the color intensities are plotted on the right side, along with cuts through the image, marked by the dashed line.[48]

### 2.2.2 Tomographic PIV reconstruction and correlation procedures

After processing of the images and splitting the color channels (time steps). All the cameras images are imported into DaVis Software 8.2.2. To the best of our knowledge, there is currently no open-source alternative for a tomographic PIV software, since DaVis software is already heavily optimized and is in a mature state, offering sophisticated reconstruction algorithms utilizing GPU's parallel computing. Other algorithms for 3D



reconstructions and cross-correlations have been published, but adapting them for efficient computing is a challenge in its own right. Any current Tomo-PIV system will, therefore, bear the cost of this software, irrespective of the hardware.

An initial calibration is then carried out with all 17 images of the calibration plate for each camera. The fit model used is a third order polynomial. The raw calibration results in a significant error for the two off-axis cameras (1 & 4 in Figure 2.1b) with a standard deviation of the order of 3.5 pixels, while the two center cameras have subpixel deviations see Figure 2.17 (a). It is important to mention that cameras 1 and 4 view the calibration target from a much larger angle than the cameras at the center. However, this is greatly improved by subsequently performing self-calibration, where the reconstructed particles are triangulated and used directly to correct the calibrations via disparity maps[51]. This reduces the calibration error for all cameras bellow 0.05 pixels after three iterations, as shown in Figure 2.17(b).

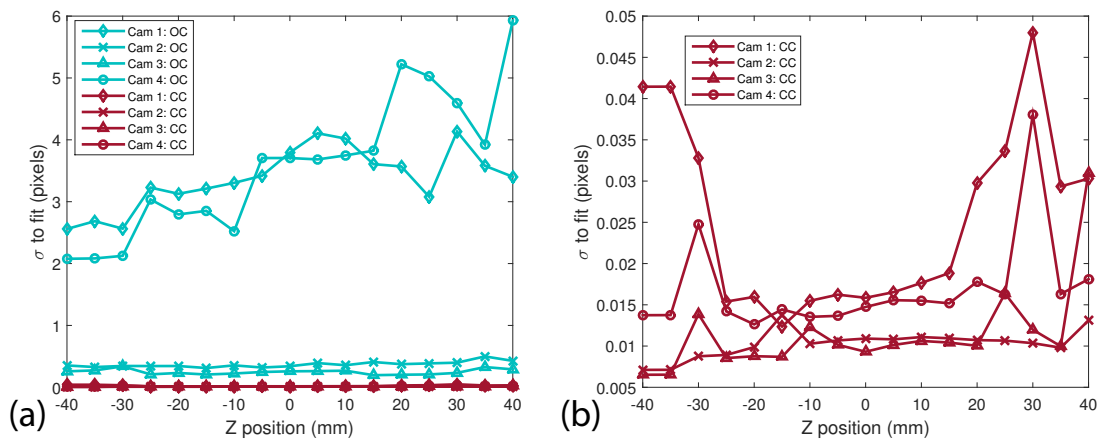


Figure 2.17. (a) Standard deviation of the original calibration fit (OC, cyan color), and corrected calibration (CC, red color) after three iterations of the self-calibration algorithm as a function of depth position  $z$ . (b) Detailed plot of the corrected calibration.[48]

After obtaining the calibration, the particle images are assigned for each camera and time step. The particle locations are reconstructed in the 3D volume, plane by plane, with the Fast MART algorithm, which comprehends an MLOS initialization and 10 iterations of CSMART[7]. As a result, the volume of  $200 \times 160 \times 120 \text{ mm}^3$  is discretized with  $3044 \times 2436 \times 1822$  voxels, resulting in approximately  $3500 \text{ voxels/mm}^3$ .

After the 3D reconstruction, we proceed to do Direct Cross-Correlation between the different time steps ( $t_1-t_2$  and  $t_2-t_3$ ). Figure 2.18 compares the velocity results of the three different sequences, i.e.,  $512 \rightarrow 320 \rightarrow 208 \text{ voxel}^3$ ,  $512 \rightarrow 256 \rightarrow 128 \text{ voxel}^3$  and  $352 \rightarrow 128 \rightarrow 96 \text{ voxel}^3$ . Each size reduction step in the correlation is performed with a 75% interrogation volume overlap and iterated with 8 passes at the final resolution. Gaussian smoothing is also used between iterations to improve the quality of the vector field. The purpose of initializing the process with bigger interrogation volumes is to obtain a rough initial estimation of the velocity field, while refining it using the general direction of the flow when the interrogation volume is reduced. This will allow us to obtain a more detailed and accurate velocity field resulting on a 3D grid of 3.3, 2.1 and 1.55 mm vector pitch respectively.

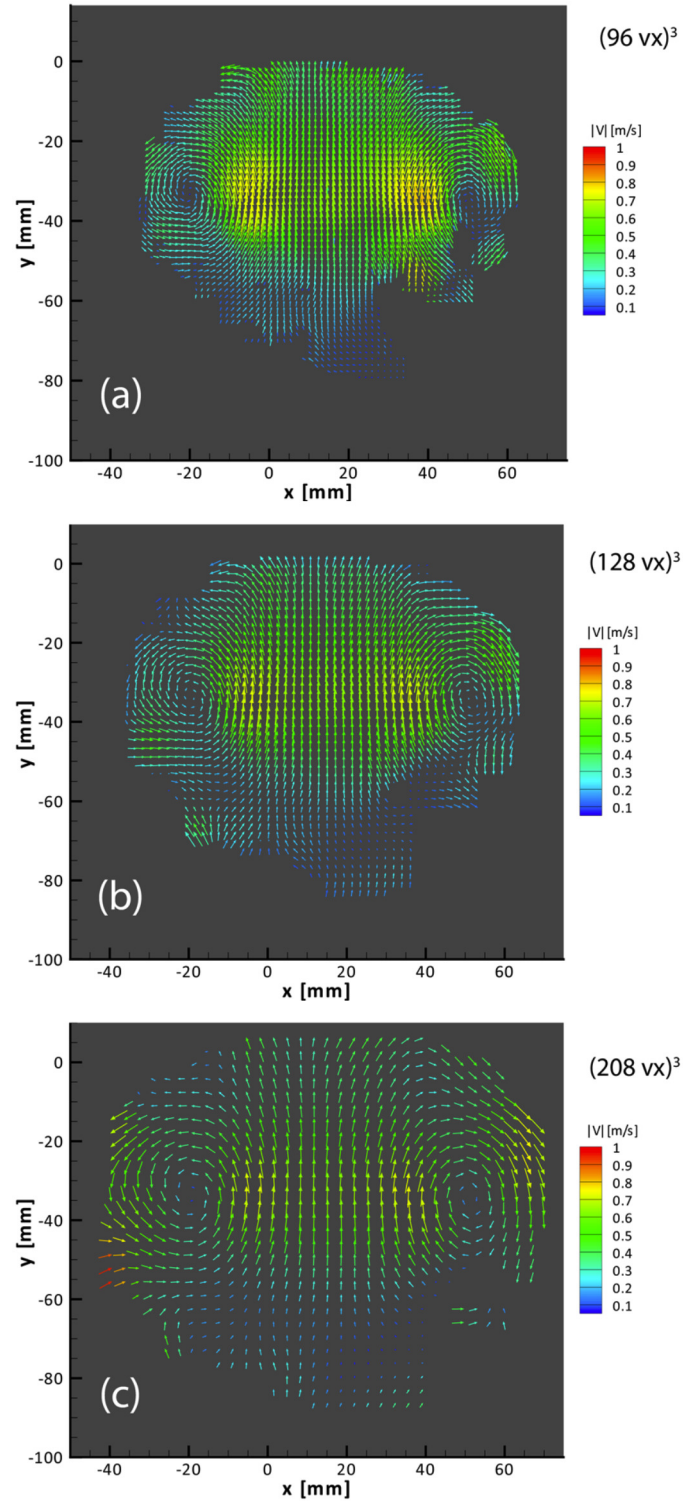


Figure 2.18. Instantaneous velocity field vectors obtained after direct cross-correlation at the plane  $z = 0$  mm captured with  $\Delta t = 1000 \mu s$ , comparison between 96 (a), 128 (b), and 208 (c) voxel3 interrogation volumes. [48]

At this point, the 3D Zero-time-delay correction for chromatic aberration is subtracted from the resulting velocity field. It is obtained using the same parameters for reconstruction and direct cross-correlation used for the moving particles, as explained in an earlier section. The Zero-time-delay velocity field is presented in Figure 5.17. A comparison of the results before and after the color aberration correction is available in Figure 2.19.

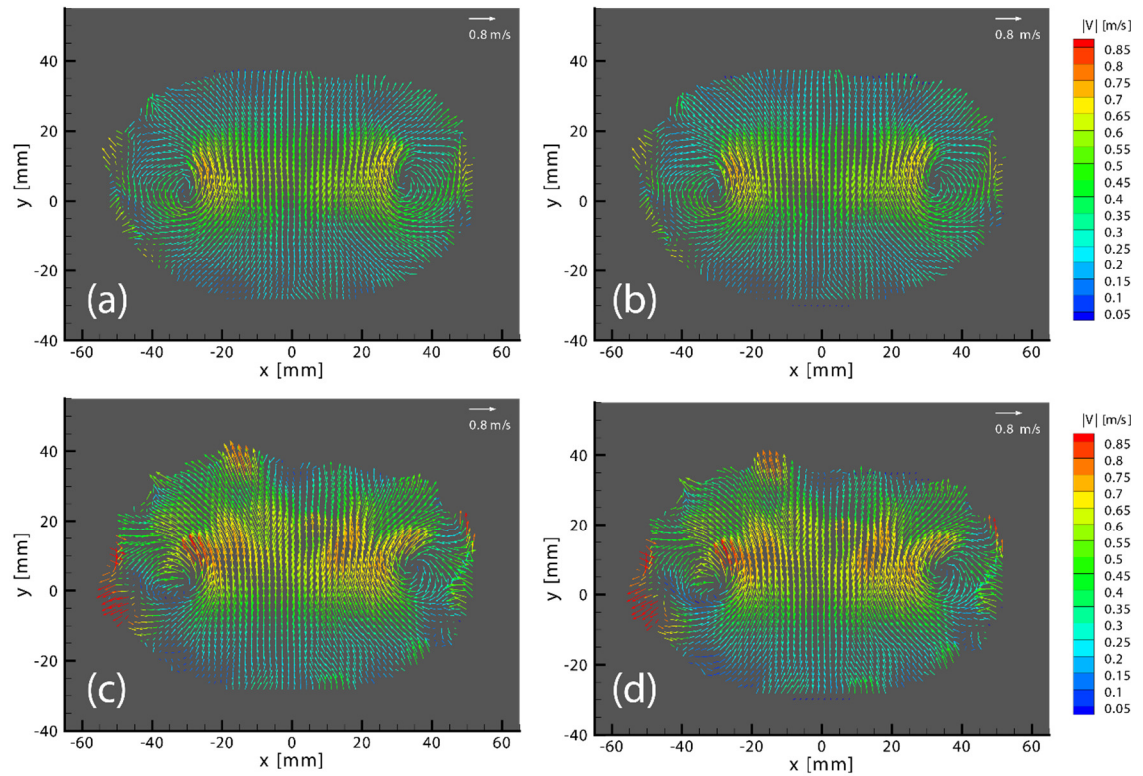


Figure 2.19. Side by side comparison of the original velocity field (a,c) vs the chromatic aberration corrected velocity field (b,d). Top figures (a,b) correspond to the  $t_1 - t_2$  correlation, bottom figures (c,d) correspond to the successive  $t_2 - t_3$  correlation. All figures belong to the  $Re=24,000$  case. [48]

It is observed that the case of  $128 \text{ voxel}^3$  is most suitable for this study, as it shows the detailed velocity field without the loss in accuracy observed for the smallest

interrogation volume of 96 voxel<sup>3</sup>, nor losing some details at the bigger volume of 206 voxel<sup>3</sup>. Bad vectors outside the well-seeded region have been removed by masking.

Additionally, we compare the instantaneous velocity fields for different air-impulse pressures, i.e., different circulation strength and translational velocities of the vortex rings. This required reducing  $\Delta t$  from 1000 to 500  $\mu\text{s}$  for the faster ring in the case of pure water, and using  $\Delta t=1300 \mu\text{s}$  for the aqueous sodium chloride solution. In all cases, the method reproduces accurate velocity fields. Results for  $\Delta t=1000$  and 500  $\mu\text{s}$  are presented in Figure 5.18. For the case of  $\Delta t= 1300 \mu\text{s}$ , an increase in velocity magnitudes in Figure 2.20 (a) vs (b) can be observed for the successive velocity fields due to the accelerating motion.

The core structure can be extracted from the vorticity field, such as the isocontours of vorticity magnitude, ranging from 70 to 230  $\text{s}^{-1}$  plotted in Figure 2.20(c, d), which allows us to locate the core of the vortex. Furthermore, Figure 2.20 (e, f), shows 3-D perspective plots of the isosurfaces of the 110  $\text{s}^{-1}$  vorticity magnitude and the surrounding 3D-3C velocity vectors, in order to highlight the ring structure in 3D. Results for the  $\Delta t = 1000$ , and 500  $\mu\text{s}$  in water cases are presented in the Appendix in Figure 5.18.

The Reynolds number of the flow can be approximated as  $Re = \Gamma/\nu$  (see Gharib *et al.*[55]) where the maximum circulation ( $\Gamma$ ) value for the pure water cases results in  $Re = 44,000$  and 56,000 for  $\Delta t = 1000$  and 500  $\mu\text{s}$ , respectively. The aqueous sodium chloride solution results in a  $Re = 24,000$  using  $\Delta t = 1300 \mu\text{s}$  shown herein, since the

salt increases the kinematic viscosity. Our results show a similar vortex ring structure as reported in previous experimental studies [3, 55, 56].

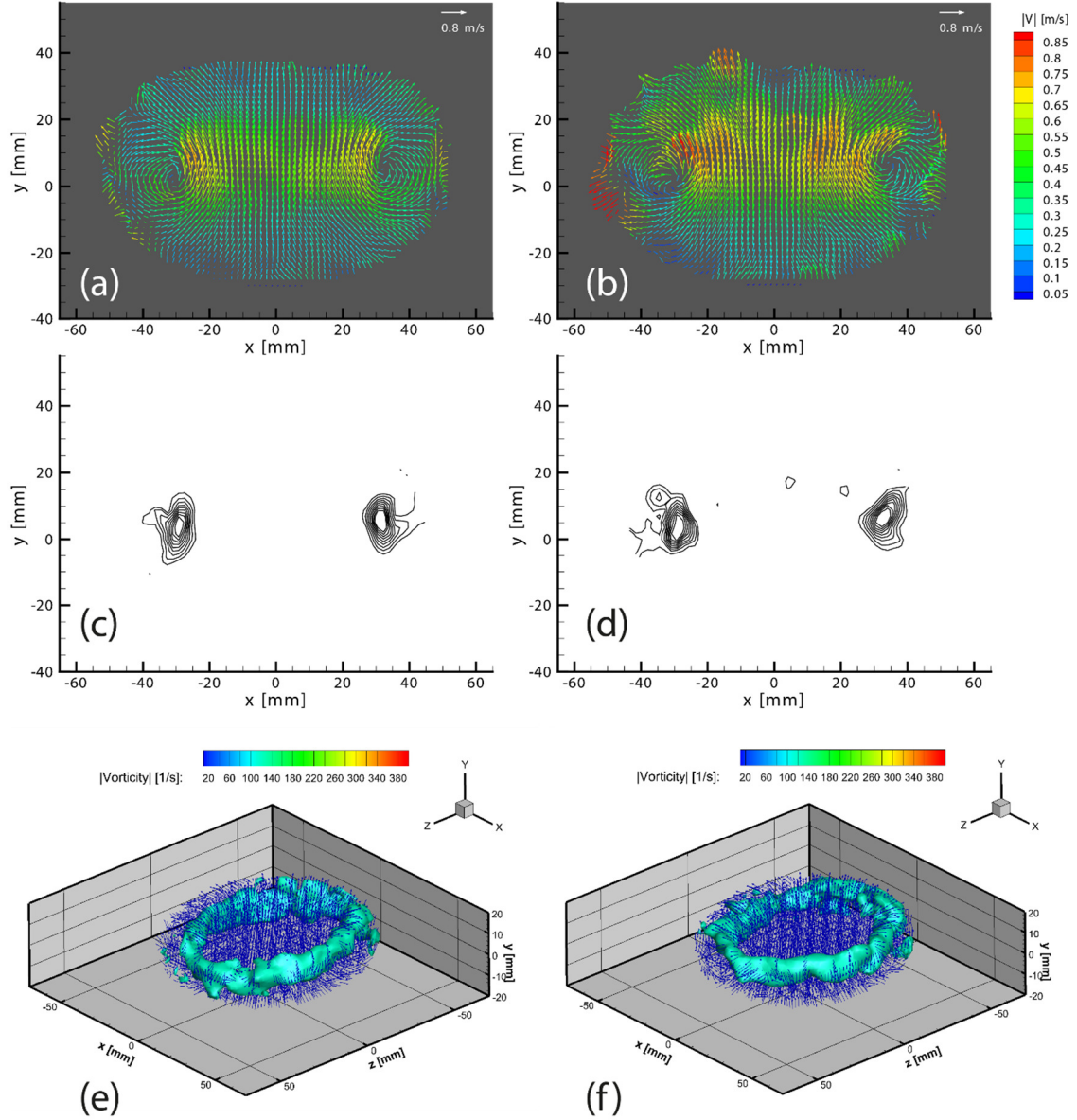


Figure 2.20. Instantaneous velocity fields for the density-matched case with  $Re=24,000$  for consecutive time steps in the plane  $z=0$  mm for (a)  $t_1$ - $t_2$  correlation (G-R) and (b)  $t_2$ - $t_3$  correlation (R-B), both with  $\Delta t=1300 \mu s$ . The corresponding isocontours of vorticity magnitude ranging from 70 to  $230 s^{-1}$  for (c) G-R correlation and (d) R-B correlation. The corresponding vortex ring visualized in 3D by the isosurface of vorticity magnitude  $110 s^{-1}$  as well as every fifth vector of the instantaneous velocity field (e) G-R correlation (f) R-B correlation.[48]

### 2.2.3 Estimating the acceleration field

The three color measurements allowed us to obtain two consecutive instantaneous velocity fields, and it opens the possibility of calculating the acceleration of the fluid elements. An estimation of the instantaneous local acceleration field  $\partial u / \partial t$  can be approximated with the first order finite difference of the two instantaneous velocity fields. This has been demonstrated by McPhail, et al.[57] for their planar PSV experiments. However, having the full 3-D velocity field, we can also obtain the advected acceleration term  $u \cdot \nabla u$ . Figure 2.21 shows the resulting local and advected acceleration fields in a cut through the vortex ring. However, we have to keep in mind that obtaining derivatives of the velocity field will propagate the errors inherently. Thus, for a detailed study of the accelerations, one should optimize the velocity measurements and increase the spatial and temporal resolutions, beyond the scope of this work.

We also note that having three subsequent images of the particles opens up new possibilities for the correlation method, where third-order correlations can be used to refine the velocity estimate [58]. This has been highlighted as a promising avenue for improvements, in the recent review of Westerweel, *et al.* [2]



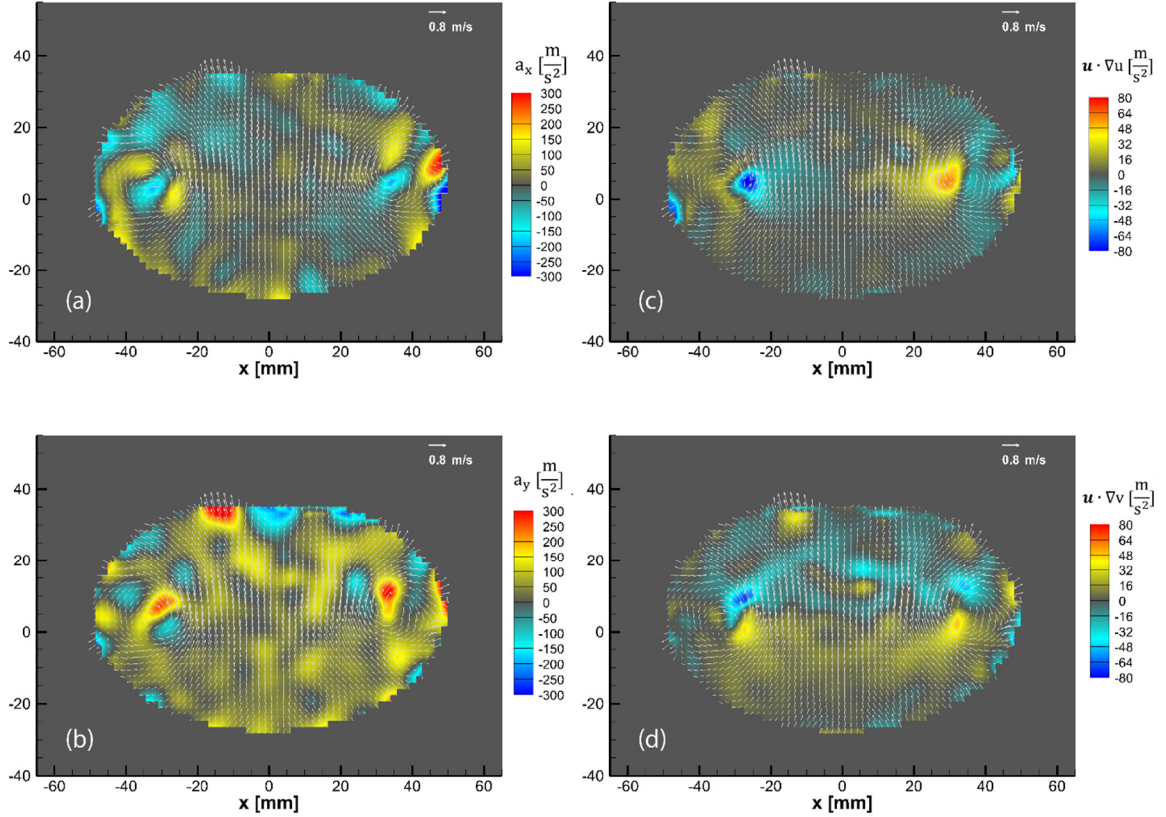


Figure 2.21. Contour plots for (a,b) local acceleration ( $\partial u / \partial t$ ) and (c,d) advected acceleration ( $u \cdot \nabla u$ ). Top figures (a,c) correspond to the X component, bottom figures (b,d) correspond to the Y component. The velocity vectors are included for position reference. The maximum local accelerations are about 4 times larger than the advected accelerations. [48]

### 2.2.4 Circulation and continuity verification.

In order to test the consistency of the obtained results, we can calculate the circulation  $\Gamma$  at different radii from the core of the vortex ring, i.e., from 2 to 22 mm. This is done at different planes by performing the line integral of the velocity vector  $\bar{u}$  along closed circles around the center of the vortex core with differential length  $dl$ . This approach integrates the tangential velocity vectors to the contour  $C$ .

$$\Gamma = \oint_C \bar{u} \cdot dl$$



We compare the circulation at planar cuts through the vortex ring in the planes perpendicular to the x and z axes, as well as the planes at  $\pm 45^\circ$  between them, all of them cutting the vortex ring through the axis of symmetry. From Figure 2.22, we observe that the circulation for the case  $Re=24,000$  has the same structure for all the cuts taken at the different azimuthal angles for both successive velocity fields. Circulation is close to constant between the two fields. This is particularly true for radii under 12 mm, which is close to the size of the vortex ring. For larger radii, limitations from the masking on the outer edge make the data less accurate in some of the planes. Keep in mind that the y-z plane is only viewed edge-on by the front cameras (2 & 3 in Figure 2.1) while viewed from a  $45^\circ$  angle in the other two cameras (1 & 4). This conservation of the circulation supports the consistency of the results. The corresponding results for the  $Re=44,000$  and  $56,000$  are presented in Figure 5.19.

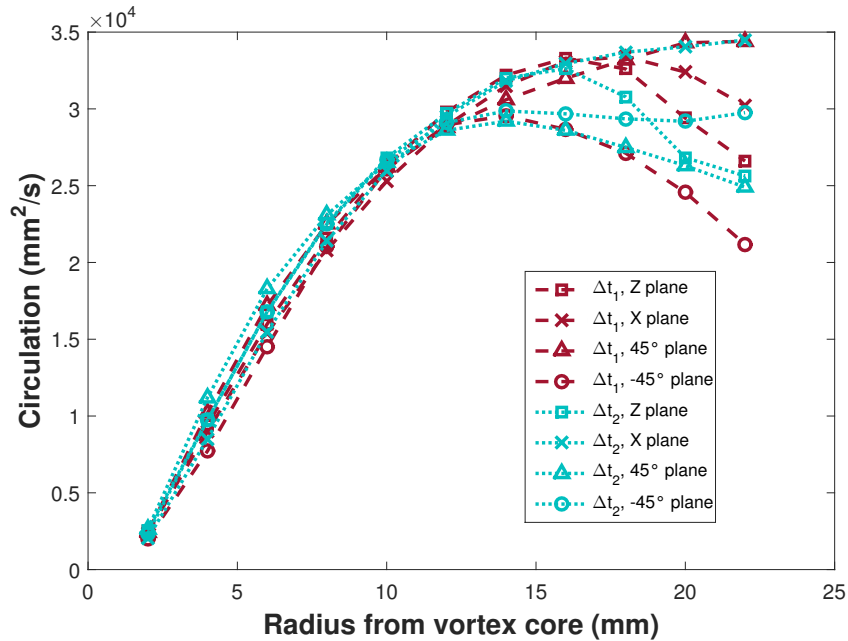


Figure 2.22. Circulation  $\Gamma$  as a function of radius from vortex core, in four different planes, for  $t_1$ - $t_2$  correlation (red) and for  $t_2$ - $t_3$  correlation (cyan), with  $Re=24,000$ . [48]

Another approach taken to check the consistency of the results obtained is by verifying conservation of mass. The closure of the continuity equation for incompressible flows ( $\nabla \cdot \mathbf{u} = 0$ ) should yield a residual near to 0. The residual of continuity  $\delta_{cont}$ , is normalized by the inverse of a characteristic time scale ( $\tau = 0.081$  s) defined as the ratio of the vortex ring diameter ( $D = 0.065$  m in this case) divided by vortex ring maximum magnitude of velocity  $|V| \sim 0.8$  m/s. Figure 2.23 shows the resulting normalized residual in a single plane for the two consecutive velocity fields. The mean normalized residual of the whole volume considering only their absolute values is  $\overline{\delta_{cont}} = 1.43 \times 10^{-3}$  with a standard deviation  $\sigma = 2.20 \times 10^{-3}$ .

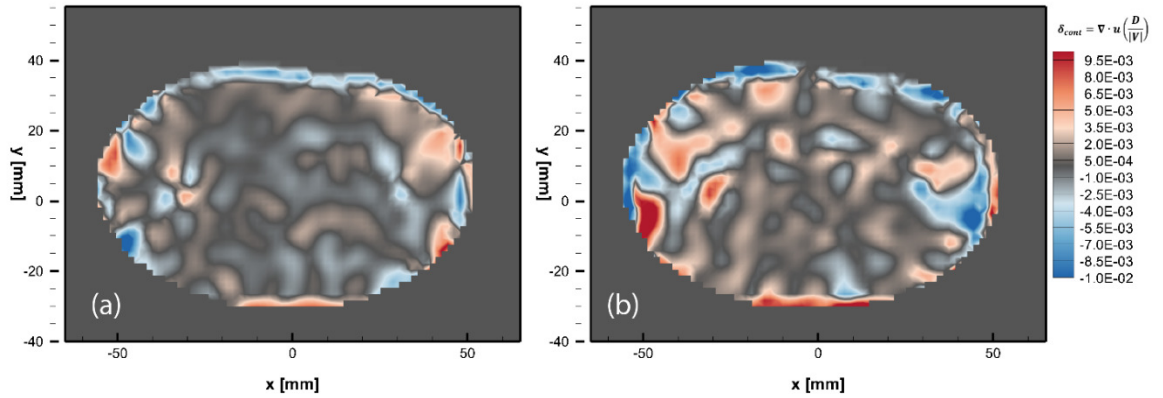


Figure 2.23. Contours of normalized residuals from the continuity equation,  $\nabla \cdot \mathbf{u}$ , for (a) first time-step (G-R) and (b) second time-step (R-B), taken at the plane  $Z = 0$  mm. [48]

### 2.2.5 Comparison with concurrent Stereoscopic PIV measurements

In order to benchmark our proposed system with commercially available specialized systems, we have carried out simultaneous measurements using the proposed system and a Stereoscopic PIV system. The later one is comprised of two 4 Mpx Imager Pro X dual frame CCD cameras supplied by LaVision.

These cameras are placed just above cameras 1 and 4, (see sketch in Figure 2.1) looking at the same ROI of plane  $Z=0$  mm with 50 mm Nikkor lenses in a Scheimpflug configuration (see Figure 2.24) to focus both cameras on the same plane [59]. We use the largest possible aperture to reduce the depth-of-focus. The same LED illumination system must be used to acquire the tomo and stereo PIV data concurrently. The backlit volumetric illumination will add defocused particles to the images captured in the stereo PIV system. For this reason, it is necessary to preprocess the stereo images by inverting their intensities and dividing the 4 Mpx region into subregions of  $100 \times 100$  px to obtain their mean intensity ( $\bar{I}$ ) and standard deviation ( $\sigma$ ). Pixels with intensity levels lower than  $\bar{I} - \sigma$  are filtered out minimizing defocused particles and creating a uniform background. The particle density in the stereo-PIV images is therefore much lower than for ideal conditions, as is shown in Figure 2.25.

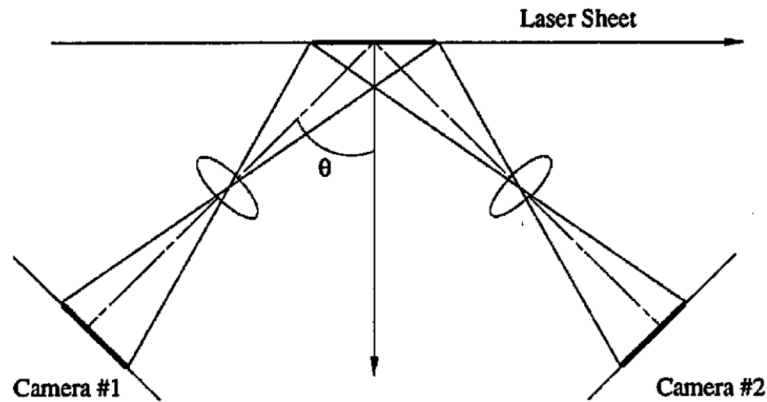


Figure 2.24. Scheimpflug configuration of the angular displacement method proposed by Prasad, A. K and Jensen, K. (figure reproduced from Prasad, A. K and Jensen, K. [59])

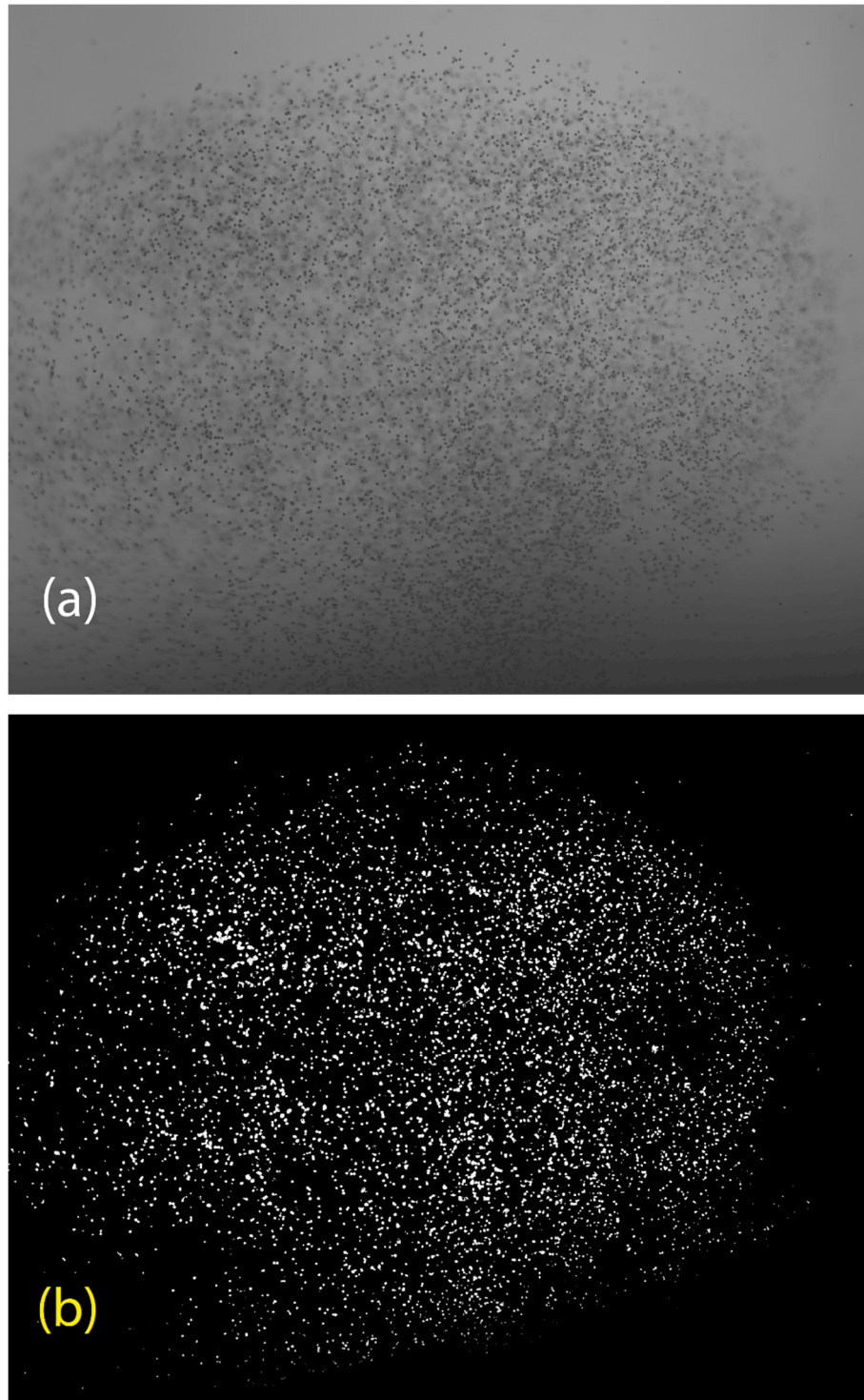


Figure 2.25. (a) Original image captured by one of the CCD cameras of the stereo PIV system, notice the significant background noise due to out of focus particles. (b) Particle field after image processing and filtering of the out-of-focus particle images.

The stereo PIV system is synchronized with the illumination and vortex generation ring with the digital delay generator. Therefore we are able to capture the same two time steps for the smartphone Tomo and stereo systems. The results obtained from the stereo PIV system provides a benchmark of the three velocity components in a single plane ( $Z=0$  mm).

A side by side comparison for the velocity fields and vorticity in the  $Z=0$  plane is presented in Figure 2.26. We can clearly observe that the main features of the vortex ring, such as the structure and magnitude of the velocity field and vorticity, are reproduced with a good degree of accuracy in our proposed system. Keep in mind that for this setup one can expect the Tomo system to give more accurate results, as the seeding density is lower than it is used for conventional stereo PIV, where a thick laser-sheet illuminates the plane of interest.

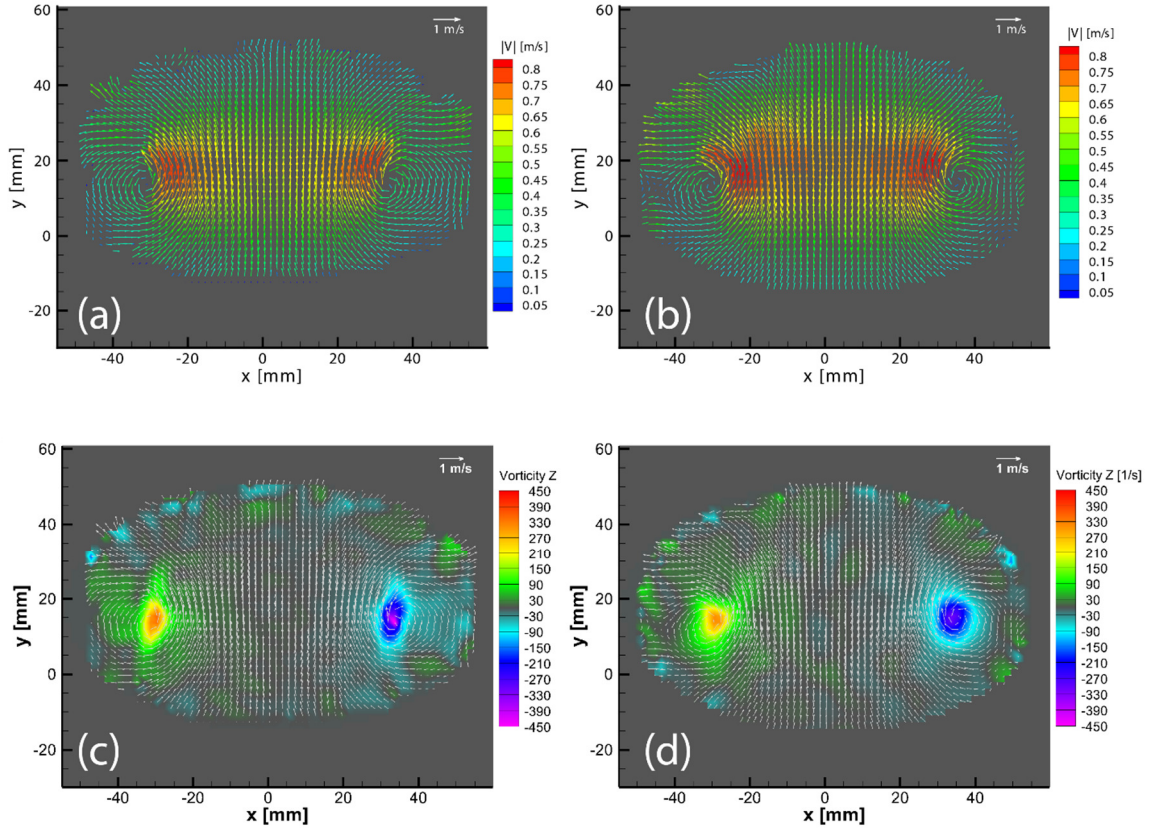


Figure 2.26. Side by side comparison of an instantaneous velocity field ( $\Delta t=1300 \mu s$ ) between (a) stereo PIV system vs (b) smartphone Tomo PIV system, colored by the velocity magnitude. Comparison of contour plots of vorticity in Z between (c) stereo PIV system vs (d) smartphone Tomo PIV system (velocity vectors are included for further orientation reference). All images are presented in the plane  $Z=0$  mm.[48]

Furthermore, a detailed comparison is presented in Figure 2.27 (a) where we plot the 3D velocity magnitude along a horizontal cut through the center of the vortex cores. The figure shows close similarity of the velocity profiles between the two independent measurements. The largest difference in velocity magnitudes is on the edges, primarily due to slight shifting in the location of the vortex cores, where the velocity gradients are largest. By normalizing these differences with respect to the maximum magnitude of  $\sim 0.8$  m/s, this yields a relative error of less than 15%. Figure 5.20 compares these deviations over the entire overlapping area of the plane at  $Z=0$  mm. It shows that 84% of the total area has an error of 20% or less. We emphasize that the largest errors are due to the

slight offset in the location of the centers of the vortices. Similarly, we assess the consistency of the results, by calculating the circulation obtained from both experimental techniques showing very similar results in Figure 2.27 (b) , with deviations of less than 8%.

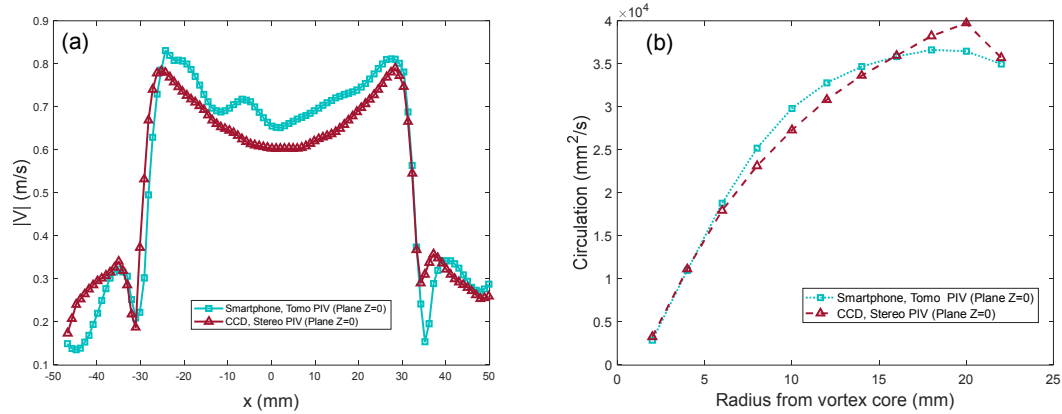


Figure 2.27. (a) Comparison of the velocity magnitude along a cut through the vortex cores in the plane  $Z=0$  mm for our Tomo-PIV system (cyan) vs 2-camera stereoscopic PIV system (red). (b) Comparison of the circulation  $\Gamma$  as a function of the radial distance from the center of the vortex cores.[48]

## 2.3 Conclusions

In the current chapter, we have demonstrated the feasibility of using low-cost smartphone cameras and high-power LEDs to replace the currently used specialized high-cost Tomo-PIV hardware. The synchronization of the cameras is accomplished with a Wi-Fi router, which has shown to introduce random delays that may interfere with the precise timing of lights and camera exposures. This we have overcome by opening the shutters for 1 second and using synchronized flashes. We successfully reconstructed the flow field of a vortex ring of 70 mm approximately in diameter at the core. Measurements at  $Re \sim 24,000$ ,  $44,000$  and  $56,000$  are carried out. In the highest Reynolds number case, the maximum velocity magnitude is approximately 1.2 m/s. We overcome the slow frame-rate of the smartphone-cameras by encoding two or three time-steps on the same frame,

by forming colored shadows of the particles, using red, green and blue LED light pulses. This system can capture fast-moving flows, as the time-step between pulses only needs to be 5-10 times the pulse duration. In our setup, this pulse duration is 80  $\mu\text{s}$  and could be reduced by adding more LEDs for each color. The full capturing speed potential of this system can be tested in higher Reynolds number systems.

Additionally to the 3D-3C velocity fields, we can estimate the acceleration fields in three dimensions. The instantaneous local acceleration field ( $\partial \mathbf{u} / \partial t$ ) is estimated with the first order finite difference of the two instantaneous velocity fields. Furthermore, due to the Eulerian nature of Tomographic PIV we, can estimate the advected acceleration term ( $\mathbf{u} \cdot \nabla \mathbf{u}$ ). However spatial differentiation of the instantaneous velocity field will propagate inherently the errors.

Validation of the results is carried out by verification of continuity, circulation along different planes of the vortex ring and concurrent experiments. The latter one consists on capturing the same time instants simultaneously with the proposed Smartphone Tomo-PIV system and a Stereoscopic-PIV setup. As presented in this chapter, the proposed system has similar circulation profiles along different planes and times. Continuity verification yields a mean normalized residual of  $\overline{\delta_{cont}} = 1.43 \times 10^{-3}$  in the whole volume. Finally, the benchmark with stereoscopic PIV system yields a relative error of 15% in the regions where the velocity gradients are the greatest, i.e., close to the vortex core).



### **Chapter 3 : High-Speed Time-resolved smartphone based Tomographic PSV system.**

As an expansion of the previous chapter, we increase the capabilities demonstrated before by using newer smartphones that integrate performance and hardware improvements to the camera. As an example, one of the latest trends in smartphones cameras is the use of an infrared low power laser for instantaneous autofocus. This kind of system uses the laser in a “Time of Flight” camera fashion to calculate the depth where the laser is pointed. Another trend implemented by large smartphone manufacturers is the deployment of dual back cameras, improving the performance of one of the sensors in low light environments and expanding their potential to use them as stereoscopic imaging systems. Additionally, nowadays it is not uncommon to find smartphones on the market capable of recording video with a High-Definition (HD) resolution (1280X 720 px) and high frame rates (in this case 960 fps) which we can be used to our advantage. We can therefore, obtain experimental measurements of a fast-moving transient flow. Moreover, the use of an open source operating system, such as Android OS, opens up vast new possibilities for the control and simultaneous use of all the sensors equipped in actual smartphones.

### **3.1 Experimental Setup**

#### **3.1.1 Overall Tomographic setup**

The experimental setup is very similar to the one from the previous chapter (see Figure 2.1 and Figure 2.3), where we seed a vortex ring with black opaque polyethylene particles. The system is backlit through diffusers to obtain a uniform background color. We again use particle shadows to capture particle motions. The main difference from the previous chapter is the smartphone model and the system intended to synchronize the cameras and trigger them simultaneously. In the previous iteration, only 3 instants are captured with 3 different colors, using a very long exposure (approximately 1 second) in all the cameras, therefore obtaining three time steps in a single image. In this section we use high-speed video. Therefore we can use monochromatic illumination for time-resolved experiments. However, color illumination is required later on in the study for comparison with a high spatial resolution tomographic PIV system.

#### **3.1.2 Cameras and imaging system synchronization**

One of the most innovative approaches in the smartphone industry is the one taken by Sony, with their smartphone Xperia™ XZ Premium which includes a new sensor of 19 Mpx and the capability of recording “slow-mo” video at nearly 1000 fps at a lower pixel resolution of approximately 1 Mpx.

In order to expand our earlier work, we use the capabilities of this smartphone that was released in June 2017. Some of the most relevant specifications are summarized in

Table 2. The use of a new sensor technology named “ Exmor RS™”, which has a memory stacked to the camera sensor, allows faster image capturing and scanning space[60].

PLATFORM	OS	Android 7.1 (Nougat)
	Chipset	Qualcomm MSM8998 Snapdragon 835
	CPU	Octa-core (4x2.45 GHz Kryo & 4x1.9 GHz Kryo)
	GPU	Adreno 540
MEMORY	Card Slot	microSD, up to 256 GB
	Internal	64 GB, 4 GB RAM
CAMERAS	Primary	19 MP, f/2.0, 25mm, EIS (gyro), predictive phase detection and laser autofocus, LED flash
	Features	1/2.3" sensor size, 1.22 $\mu$ m pixel size, geo-tagging, touch focus, face detection, HDR, panorama
	Video	2160p@30fps, 720p@960fps, HDR
	Secondary	13 MP, f/2.0, 22mm, 1/3" sensor size, 1.12 $\mu$ m pixel size, 1080p

Table 2. Summary of relevant specifications of the Sony Xperia™ XZ premium smartphone[60].

One of the main features that we exploit, is the capability to record high-speed video at 960 fps with a resolution of 1280 x 720 px. One of the drawbacks when recording high-speed video, is that the phone is capable of recording only 180 successive frames. Frame straddling and color combinations could allow us to increase our effective frame rate. However, this comes at the cost of sacrificing the particle concentration for every time step, thus, reducing the spatial resolution of the reconstructed volume.

We propose to overcome the limitations of the previous technique in Chapter 2, being able to obtain time-resolved evolution of the flow. However, synchronization of the recorded video in all the smartphones turns out to be a challenge.

### 3.1.3 Challenges

In the previous chapter, we used a WiFi router to synchronize and trigger all of the smartphones within a ms of each other followed by a long exposure time. Thus, the color

flashes were able to “freeze” the same instant for all of the cameras. In contrast, recording at 960 fps translates onto a captured frame every 1.04 ms, which is faster than the typical response time achieved by the WiFi router used in the earlier study. To circumvent this difficulty, we use high-performance optocouplers in parallel. Optocouplers or optoisolators typically consist of an LED and a phototransistor that is packed in an Integrated circuit. These components allow two separate electronic circuits to interact, therefore preventing voltage fluctuations bleeding into the received signal.

In our experiments, optocouplers act as an electrical switch between a TTL signal from a digital delay generator and an electrical input to the smartphones. We use the phone capability of triggering the camera with the pins present on the 3.5 mm audio jack. To trigger the camera with the audio jack on the Xperia XZ premium smartphones, the GND and MIC pins are shorted, creating a trigger command for the camera. See Figure 3.1.

High-performance optocouplers model 6N136-1443B from Fisher are used for our triggering device. The time response characteristics are essential for our high-speed application. Therefore, a test using the digital delay generator to check the response time of the optocoupler is carried out using a digital oscilloscope (see Figure 3.2).

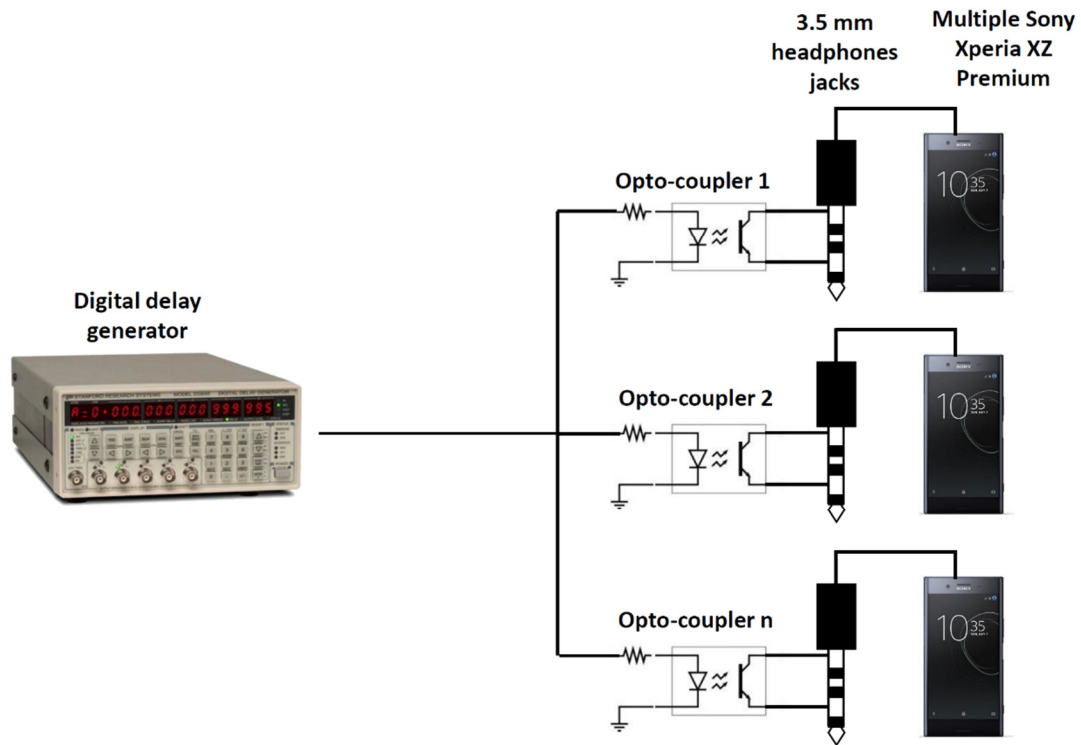


Figure 3.1. Schematic representation of the synchronization system, proposed for simultaneous capturing high-speed video at 960 fps by multiple smartphone cameras. The TTL signal is generated by a digital delay generator. This signal is sent in parallel to multiple optocouplers that trigger the Xperia™ XZ cameras through the headphone Jack.

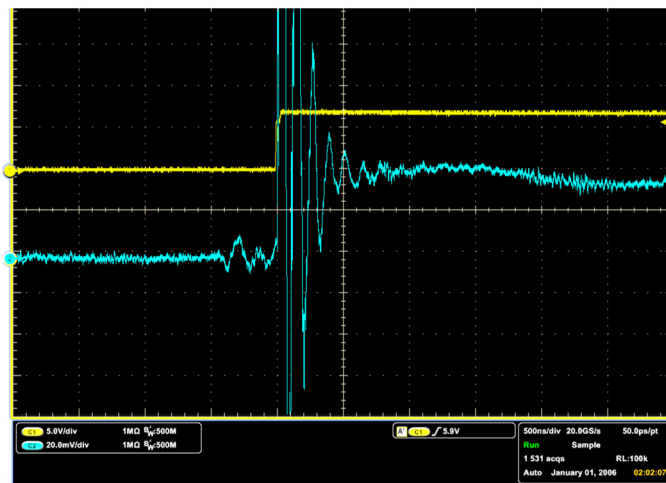


Figure 3.2. Signal characterization of the optocouplers (cyan) vs the trigger signal from the digital delay generator (yellow). The typical response time of the optocoupler is approximately 500 ns. The horizontal axis smallest divisions are 100 ns, while the vertical axis smallest marks are 1 V and 4 mV for the digital delay generator and the optocouplers respectively).

From Figure 3.2, one can see that the response time of the optocouplers is approximately 500 ns. This response is perfectly adequate for our relatively much lower frequency when recording video at 960 fps (exposure time of 1.04 ms). The fast response time will, therefore, allow us in principle to synchronize the LED illumination and trigger the cameras simultaneously.

However, when connecting the optocouplers to the smartphones and testing them with the LED system, we found that there is a random delay between the trigger and the start of the frame captured by the smartphone cameras. This problem limits the length of the video clip that can be reconstructed. Thus, we are only able to reconstruct the frames that overlap in time for all the cameras. An additional problem we found while testing is that the camera sensor scanning occasionally is out of phase with the illumination in certain phones. This produces dark stripes in the sensor or overlapped adjacent flashes in a single frame. To test this problem the green LED is flashed for a frame followed by blue and green LED's simultaneously, finalizing only with green flashes. Some of the captured images of the vortex ring show overlapped instants in a single frame (see Figure 3.3).

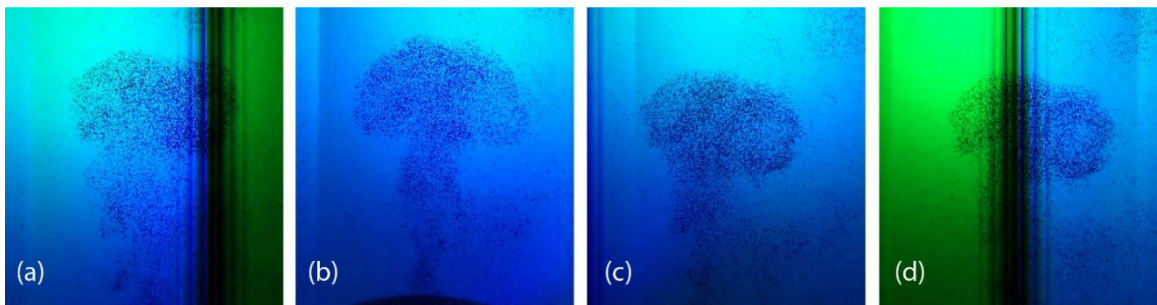


Figure 3.3. (a) Left, (b) right, (c) top and (d) bottom camera images of a vortex ring captured close to the same time. One can note that the scanning of the sensor produces overlapped flashes in (a) and (d). Whereas for (b) and (c) the flash is in phase with the recorded frame.

The previously mentioned problems may be caused by the out-of-sync internal clock in the different smartphones or the processing of background services typical for the Android OS. Tweaking the internal clock to synchronize all the phones should solve these problems. However, this is beyond the scope of this work and requires deep knowledge on modifying smartphones hardware and operating systems. For the current proof-of-concept study, we overcome this problem by trial and error until capturing in-phase images in all of the camera sensors.

On the other hand, the lack of control of the camera settings when using the high-speed video mode increases the difficulty of our experiment. Due to the commercial nature of these devices and the low exposure, of each frame, as the consequence of the high framerate, the camera application used by Sony gives very limited control to the end user. Parameters such as ISO, exposure time, manual focus, RAW capture, etc. are not manually controlled and are set automatically to obtain optimum illumination of the “slow-mo” video. These features, in our case, produce out of focus images with a very high ISO (grainy images) or overexposed images. To overcome this problem, empirically we found that just before starting the recording we need to flash the LED’s for a few seconds in order to let the camera sensor adjust the parameters for the current lighting conditions.

### **3.1.4 Vortex Ring generator and flow tracers**

The vortex ring generator used is the same as presented in section 2.1.2 and is placed at the bottom of a tank (see Figure 3.4). The tank is filled with a mix of 60% -40%

by volume of water-glycerol to better match the density of the particles available for us. Such a mixture has a density  $\rho = 1.12 \text{ g/cm}^3$  and kinematic viscosity  $\nu = 4.03 \text{ cSt}$ .

The air impulse driving the vortex ring is therefore synchronized with the smartphones through the digital delay generator. The vortex ring is seeded beforehand with dark particles of size 212-250  $\mu\text{m}$  (described in section 2.1.3) and density  $\rho = 1.28 \text{ g/cm}^3$  and stirred, allowing them to be dragged by the vortex ring. (See Figure 3.3)

### **3.1.5 Illumination and synchronization**

In contrast to the three-colored shadows case (Chapter 2), for the present setup we use monochromatic green LED flashes to capture a single shadow of each particle per recorded frame. Therefore, we avoid the typical chromatic aberrations described in 2.1.7. However, due to the synchronization problems mentioned in 3.1.3, the recording of 180 frames-long clips in each phone, are out of phase, i.e., not all the phones start recording at the same instant. In order to identify an exact instant in all the videoclips, once the recording starts with the green LED flashes, a single blue frame is flashed simultaneously for all sensors, the exposure time is 80  $\mu\text{s}$ . This information will allow us to pair together and synchronize the recordings during post-processing. However, we must limit the total number of frames used for the 3D measurements. For the experiment presented in a later section, 58 synchronized frames overlap and are used in all the cameras.

### **3.1.6 Tomographic PIV calibration**

Similarly to the previous section 2.1.5. A calibration plate Type 22 from LaVision, is translated along the volume to be reconstructed, from  $z = -35 \text{ mm}$  to  $+35 \text{ mm}$  in 5 mm



steps (see Figure 3.4). However, since in high-speed mode the camera's focal plane is automatically adjusted, we are forced to capture full frame calibration images of 19 Mpx in Manual mode. We fix the focal plane of each camera at the center of the vortex ring generator and carry out the calibration procedure. Nevertheless, the high-speed video mode of 1280 x 720 px carries out around 2 x 2 pixel binning from the actual 19 Mpx image sensor see Figure 3.5.

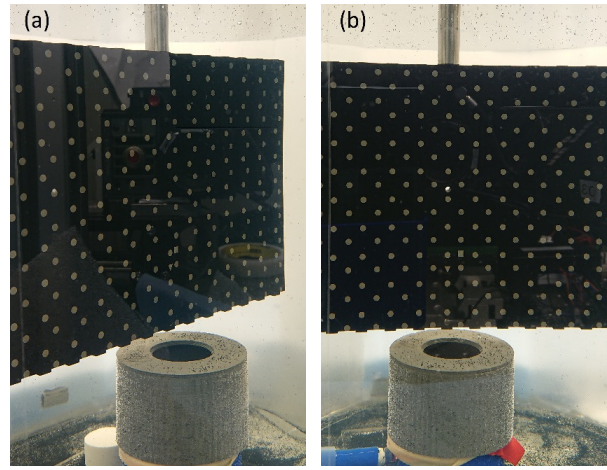


Figure 3.4. Images captured in the manual mode for the calibration plate at  $Z=0$  mm by (a) left camera and (b) central bottom camera.

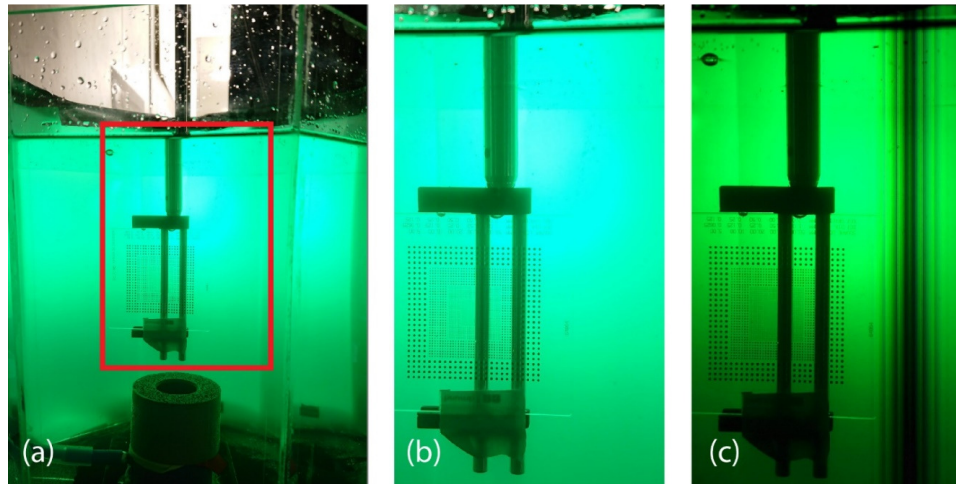


Figure 3.5. Top central camera view of a dotted calibration target located at the central plane of the vortex ring. (a) Captured with manual settings at 19Mpx resolution. (b) Image of 2x2 binned image from 19 Mpx resolution and centered cropped to 1280x 720 pixels (see the red region from a). (c) Image captured at the same location with the High-Speed video mode (1280 x 720 resolution).

Originally it is assumed that a centered binning of 2x2 in the central portion of the full frame image is used in high-speed video mode (see Figure 3.5b). However, by testing the captured images with a dotted calibration target we found empirically that this is slightly off the center and the scaling of the image is not exactly 2, but 1.9267. (see Figure 3.6)

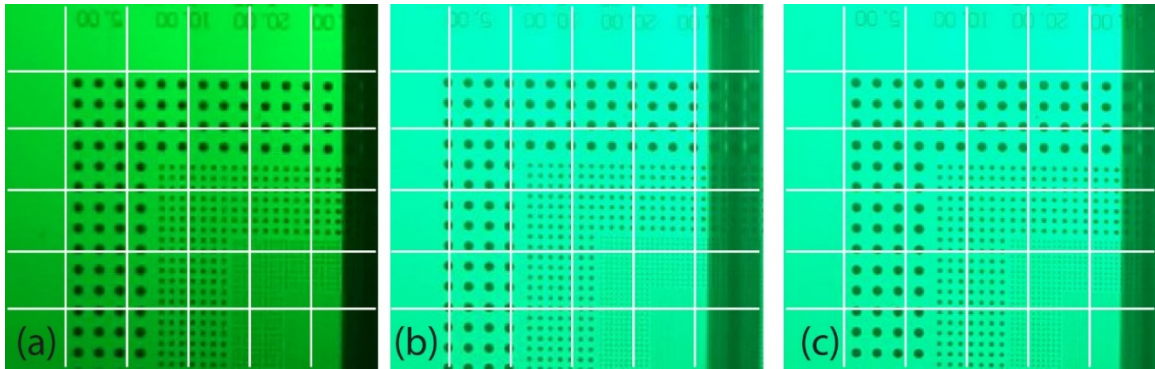


Figure 3.6. Region of Interest (ROI) zoom (253 x 247 pixels) from the dotted calibration target. (a) High-speed video recording mode, (b) centered binning of 2x2 with top left corner located at  $x=624$  and  $y=588$  px (centered downsampled image) (c) Binning of  $1.9267 \times 1.9267$  with top left corner located in  $x=648$  and  $y=590$  px of the binned image. A rectangular grid is shown for comparison.

It is clearly observed from Figure 3.6 (b) that binning of 2x2 produces an out of scale image compared to the High-speed video capture mode (Figure 3.6a). Therefore all the calibration images recorded at 19 Mpx resolution have to be adjusted and Binned with a factor of  $1.9267 \times 1.9267$  (Figure 3.6c) in order to reproduce the same field of view when recording in High-speed video mode.

## 3.2 Results

### 3.2.1 Pre-processing of the images

Figure 3.7 shows the typical image captured in the High-speed video mode, here we can clearly see the vortex ring structure seeded with the black particles forming a

“mushroom” shape. The particles average density inside the seeded region is  $N \sim 0.08 \text{ ppp}$ . The source density described in section 2.2.1 is  $N_s \sim 0.5$  for these experiments. Each particle is approximately 2 pixels in diameter.

The maximum particle displacement between frames in the fastest regions is approximately 5 pixels near the vortex core. However, a non-uniform background (see Figure 3.7a) requires some image pre-processing to feed cleaner images to the DaVis software. We split the channels of the captured images, and only the green channel is processed. The open-source package, “Fiji”, is used to process the images and the “subtract background” command is used for this purpose. This command employs the “rolling ball” algorithm proposed by Sternberg [61]. A Rolling ball radius of 20 pixels is used and smoothing is disabled to avoid blurring out individual particles. After removing the background, the images are inverted and enhanced by normalizing each frame by its maximum pixel value. Final images exhibit bright particles in a dark background as is required for the DaVis software (see Figure 3.7 b, c ). The captured images have a large pixel size of approximately  $150 \text{ } \mu\text{m}/\text{px}$  while our particles are approximately  $200 \text{ } \mu\text{m}$  in diameter. The high particle density results in many particles that overlap. However, due to the robust nature of the Tomographic-PIV algorithm, this does not represent a major problem during the correlation process.

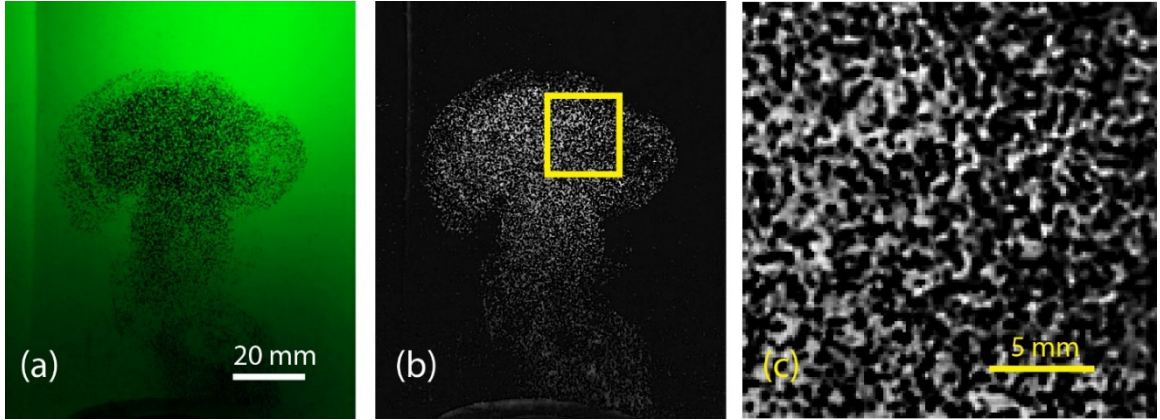


Figure 3.7. (a) Single frame of a Vortex ring from a High-speed video. (b) Post-processed image. (c) Magnification of a sampled area inside the yellow region in (b).

### 3.2.2 Tomographic PIV reconstruction and correlation procedures

All the video frames are loaded into the DaVis Tomographic PIV Software, together with the calibration images. The initial calibration is carried out on all images of the calibration plate, and the initial calibration error estimation is obtained (see Figure 3.8a). Similarly to the Nokia smartphone case, a third order polynomial is used for the fit model. The largest deviation for the calibration fit has an RMS of 1.65 pixels for Camera 2. After three iterations of the self-calibration algorithm, the maximum standard deviation of the fit falls below 0.025 pixels as shown in Figure 3.8(b).

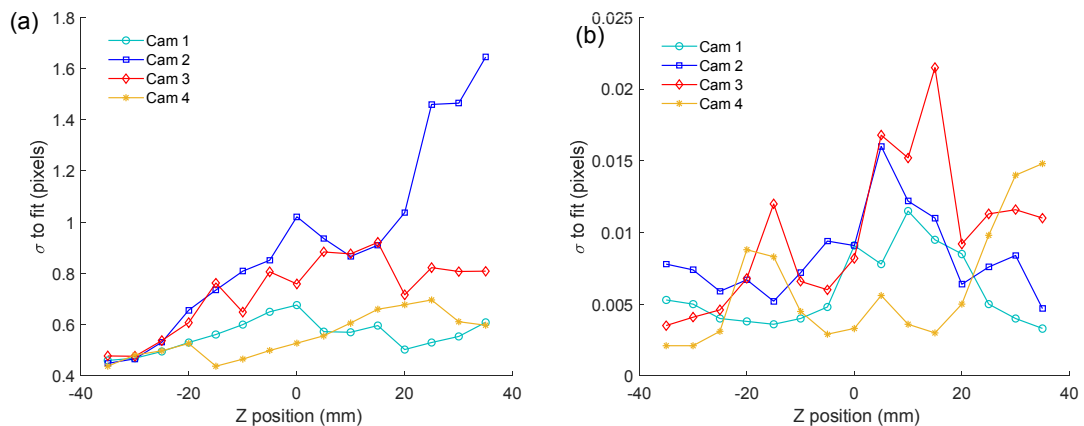


Figure 3.8. (a) Initial standard deviation of the calibration fit. (b) Final calibration standard deviation after three iterations of the self-calibration algorithm.

Particle locations are then reconstructed in a 3D volume using the Fast MART algorithm (including MLOS initial estimation and 10 iterations of CSMART [7]). Therefore the volume of approximately  $80 \times 100 \times 90 \text{ mm}^3$  is discretized in the process to  $500 \times 625 \times 593$  voxels, having approximately  $257 \text{ voxels/mm}^3$ . This is carried out for every single time step (in total 58 frames) recorded at 960 fps, i.e.,  $\Delta t = 1.041 \text{ ms}$ .

Direct cross-correlation is carried out between subsequent reconstructions in order to estimate 57 instantaneous velocity fields. This is done in four steps with an initial interrogation volume size of  $128^3$  voxels with  $8 \times 8 \times 8$  volume binning. In order to refine the velocity fields, we reduce the interrogation volume size to  $96^3$  voxels and binning of  $4 \times 4 \times 4$ ,  $64^3$  voxels and  $2 \times 2 \times 2$  binning with a final interrogation volume size of  $48^3$  voxels with no binning. All steps are repeated with two passes to reduce the number of outlier vectors with a 75% interrogation volume overlap. With the final step having 3 passes. Gaussian smoothing of the velocity field is used between iterations to improve the quality of the vector field. As a result, we obtain a velocity field with approximately 1.6 mm vector pitch and approximately 91,500 vectors (in the seeded region), i.e., a total of 5.2 million vectors considering the 57 instantaneous velocity fields. Figure 3.9 shows 2D cuts of the 3D velocity field at  $t = 0, 22.92, 45.84 \text{ ms}$  in different vertical planes. The core structure of the vortex ring is extracted from the vorticity field. Figure 3.10 shows surfaces of isovorticity magnitude  $|\omega| = 220 \text{ s}^{-1}$  at different times, where the translation of the vortex ring structure is highlighted over time, an animation of this process is also presented in Supplementary video S2.



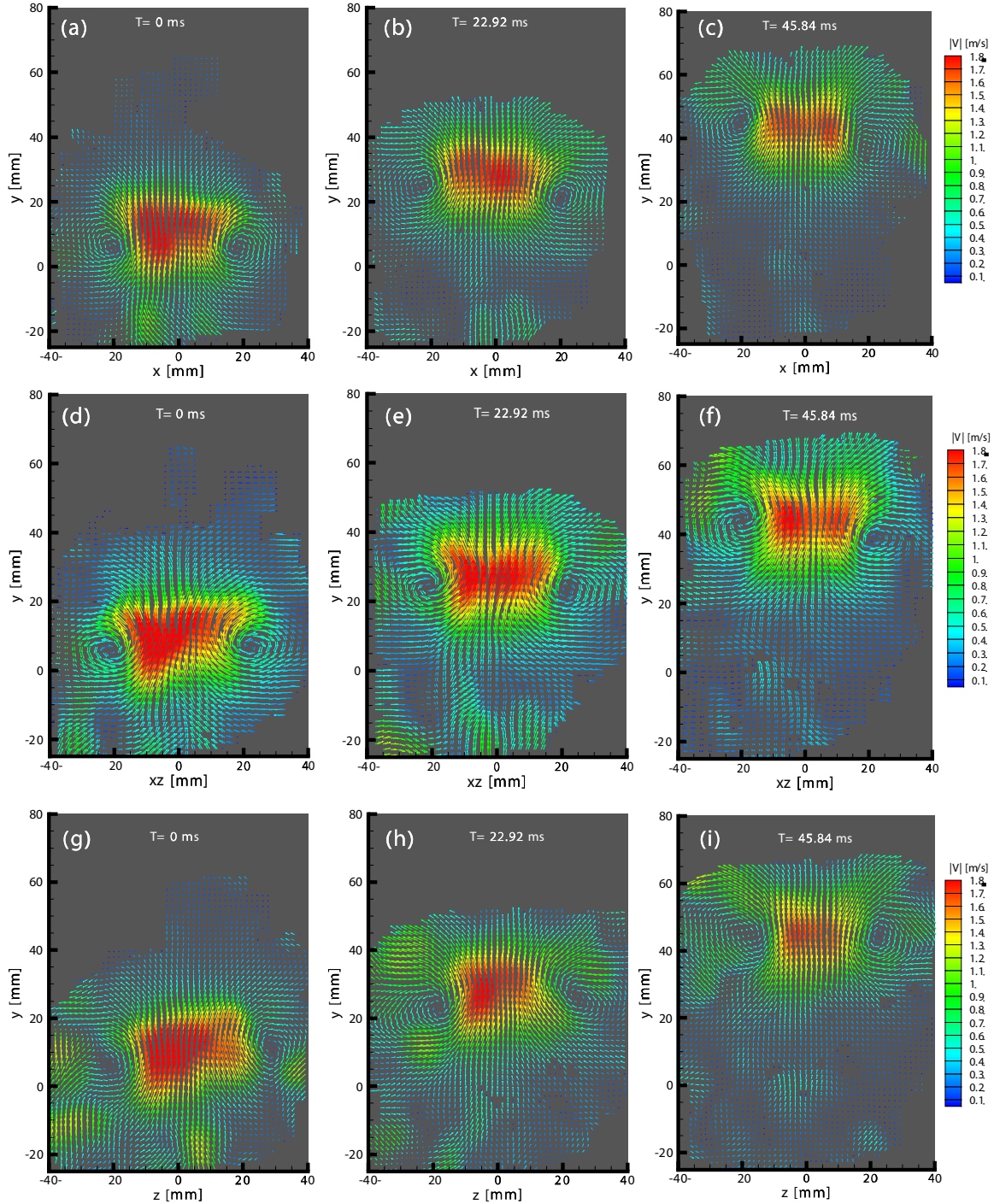


Figure 3.9. (a-c) Two dimensional XY cuts through the center of the vortex ring, showing the instantaneous velocity field. (d-f) Two dimensional vertical cut of the instantaneous velocity field in a 45-degree XZ plane. (g-i) Two-dimensional YZ cut of the instantaneous velocity field at the center of the vortex ring (note that this plane is not directly visible and is perpendicular to the central camera sensors). Different times are plotted from left to right (0, 22.92 and 45.84 ms respectively, showing the upward translation of the vortex ring). Vectors are colored by their velocity magnitude.

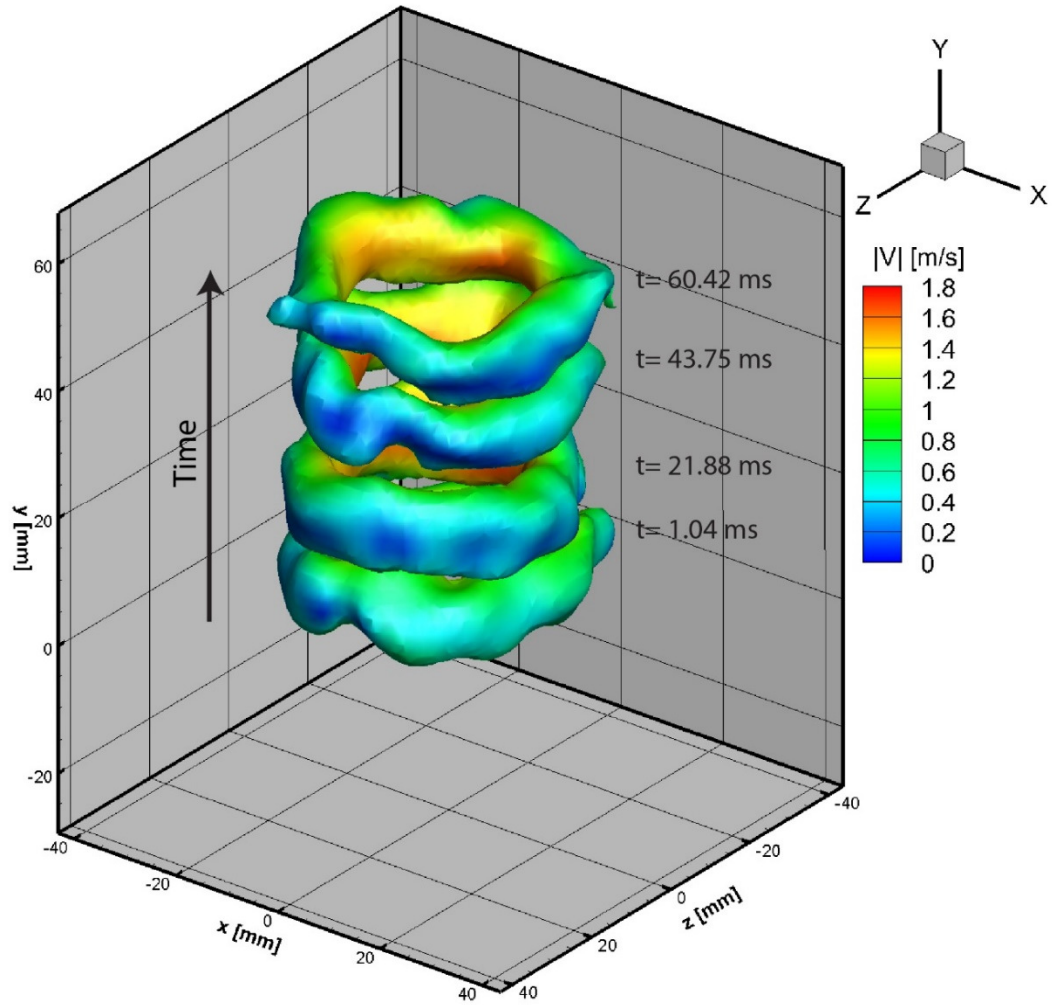


Figure 3.10. Time evolution of the Isovorticity magnitude surfaces of  $|\omega| = 220 \text{ s}^{-1}$ . The color of the surface is given by the magnitude of the velocity where we can see that the inner surface near the axis of symmetry of the vortex ring, has a larger magnitude.

### 3.2.3 Circulation, Continuity verification and Comparison with High-resolution Tomographic-PIV measurements

The circulation of the vortex ring should be constant around the periphery. This can be estimated the same way as in section 2.2.4. Here we indeed measure a constant maximum circulation of  $\Gamma = 6.6 \times 10^4 \text{ mm}^2/\text{s}$  irrespective of the plane. This is plotted for three different times in Figure 3.11. One can see how circulation is close to constant

in space and time, especially in radius below 16 mm. The conservation of the circulation supports the consistency of the results. The Reynolds number of the vortex ring is estimated the same way as in section 2.2.2, i.e.,  $Re = \Gamma/\nu$ . Using the maximum circulation around the vortex core results in a Reynolds number of  $Re = 16,500$ . This  $Re$  is lower than that presented in section 2.2.2 despite of having higher velocity magnitude. However, one has to keep in mind that the mix of water-glycerol increases dramatically the kinematic viscosity of the liquid.

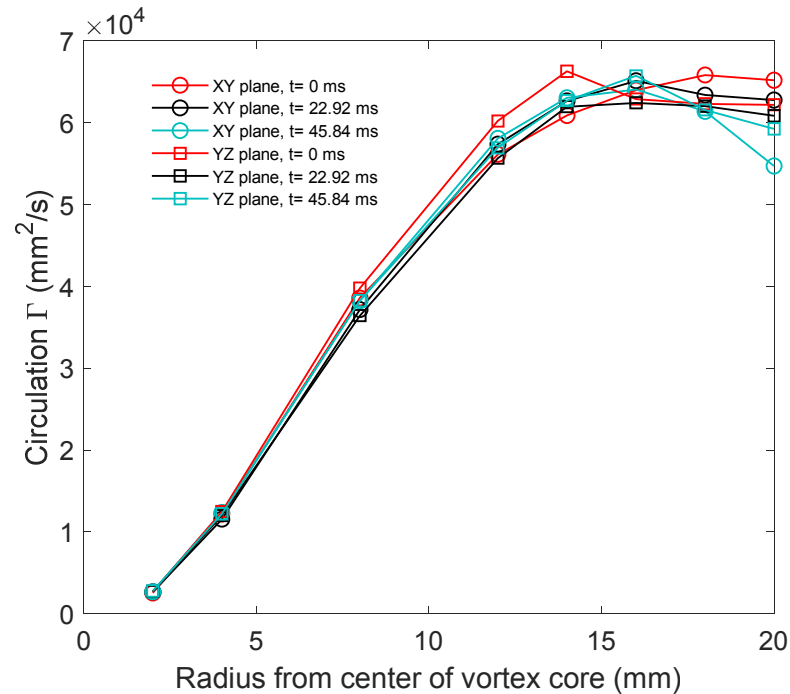


Figure 3.11 Circulation  $\Gamma$  vs radius from vortex core; data is presented for 2D cuts of planes XY and YZ (later one not visible to the central cameras) colored by the three different instants  $t=0$  (red), 22.92 (black) and 45.84 (blue) ms. The Reynolds number for this vortex ring is  $Re \approx 16,500$ .

Furthermore, the consistency of the velocity field results is tested by verifying with conservation of mass for an incompressible fluid. The residual ( $\delta_{cont}$ ) of the Continuity equation ( $\nabla \cdot \mathbf{u} = 0$ ) should be near zero and is normalized by the inversed characteristic time scale of ( $\tau = 0.022$  s) which is the ratio of the vortex ring diameter ( $D = 0.04m$ )



divided by the maximum velocity magnitude ( $|V| = 1.8 \text{ m/s}$ ). (See Figure 3.12). This mean normalized residual in absolute value considering all velocity fields in time is  $\delta_{cont} = 6.27 \times 10^{-4}$  with a standard deviation  $\sigma = 1.186 \times 10^{-3}$ .

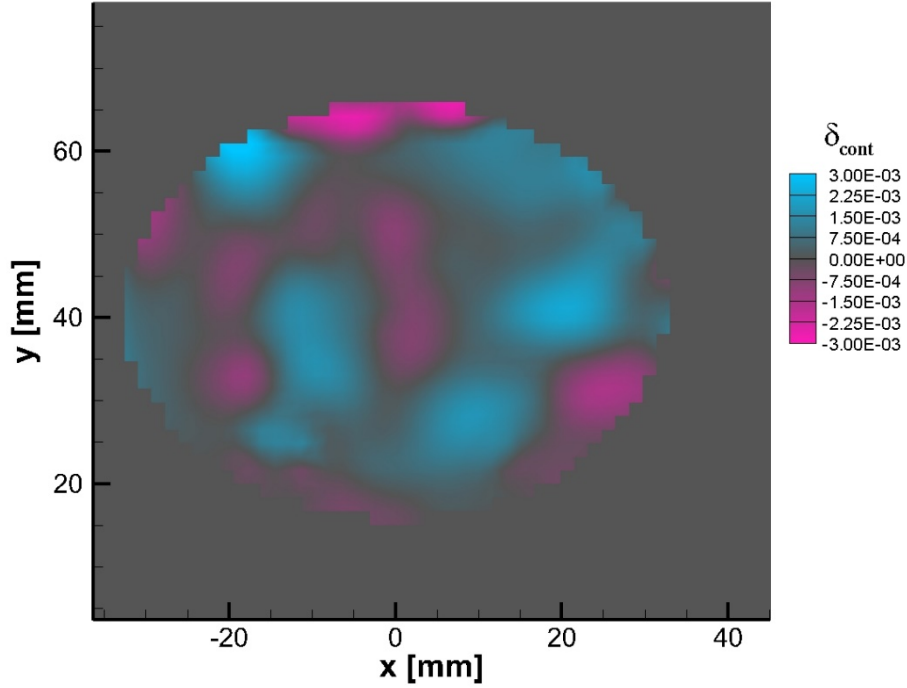


Figure 3.12. Contour plot of the normalized residual  $\delta_{cont}$  obtained from continuity equation  $\nabla \cdot \mathbf{u} = 0$ . This plot is obtained at the XY central plane of the vortex ring at  $t=43.75 \text{ ms}$ .

To further ascertain the accuracy of these measurements, we make a benchmark comparison between our High-speed smartphone system and simultaneous Ultra-High resolution camera system measurements. The cameras used for this benchmark are 4 Red Scarlet-X cameras. These cameras are capable of recording 4K resolution ( $3840 \times 2160$ ) at 30 fps. The disadvantage of using these high-resolution devices is the relatively low framerate. However, we use the strategy of section 2.1.6, where we encode the time in the color of three LED flashes; this will allow us to record the position of all the particles at the same instant in both systems (smartphones and Red Cameras) concurrently. The

Red cinema cameras are placed close to the location of each of the smartphones (Figure 3.13). The same calibration plate, type 22, is used to obtain images in the smartphones and Red Cinema cameras. Therefore the calibration will yield the same coordinate system. The results of this concurrent experiment will be a single image containing the three time steps for each Red Cinema camera (3840 x 2160 pixels), while the smartphone system will produce three frames in time (1280 x 720 pixels) for each camera. This is approximately nine times difference in total image resolution or number of pixels, allowing us to reconstruct a very detailed velocity field as a reference using the Red Cinema cameras.

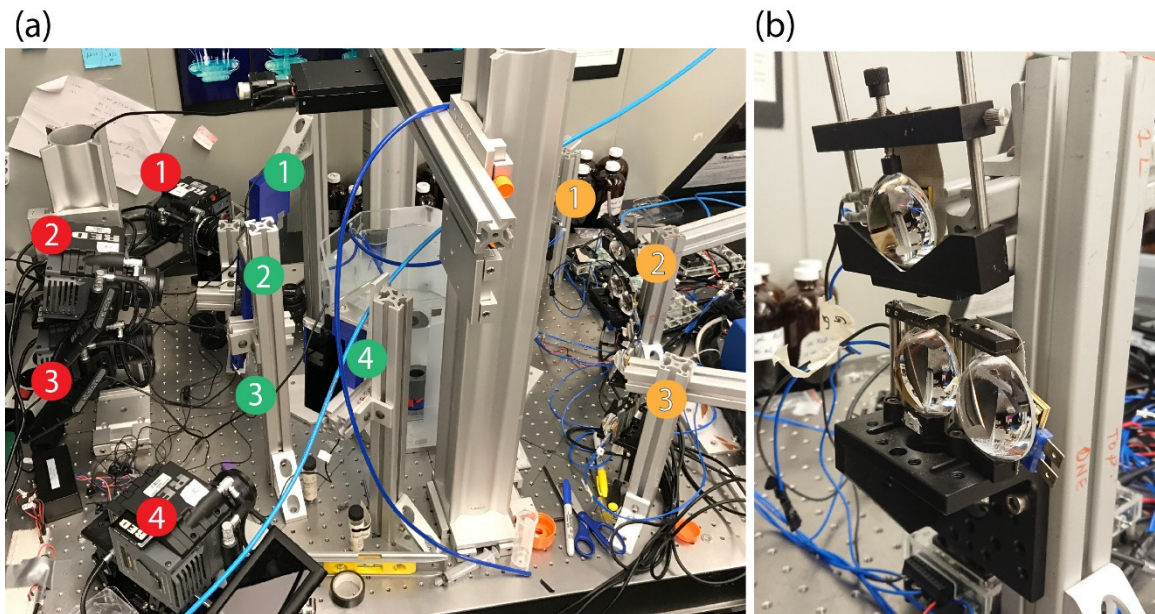


Figure 3.13 (a) Tomographic PIV experimental setup for simultaneous recording of the vortex ring using Red Cinema cameras (marked by red circles) and Xperia smartphone cameras (marked with green circles). The illumination is provided by three sets of three LED's each (R, G, B) in a backlit configuration (marked with yellow circles). (b) Image of a single set of LED's, one of each color (R,G,B).

We flash green, blue and red LED's subsequently with a  $\Delta t = 1/960 \text{ s}$  and  $80 \mu\text{s}$  exposure time. This allows us to compare two different velocity fields produced by each system independently. A vortex ring captured by the central High-resolution Red camera

is presented in Figure 3.14 a. For the Red cameras, the captured raw images have to be processed to separate the color channels, i.e., the different time steps, the same way as it is described in detail in section 2.2.1. Additionally, a “Zero-time delay” correction (section 2.1.7) is applied to reduce the systematic errors that arise from chromatic aberrations[18, 48]. On the other hand, the images captured by the smartphones follow the same post-processing flow as specified in section 3.2.1.

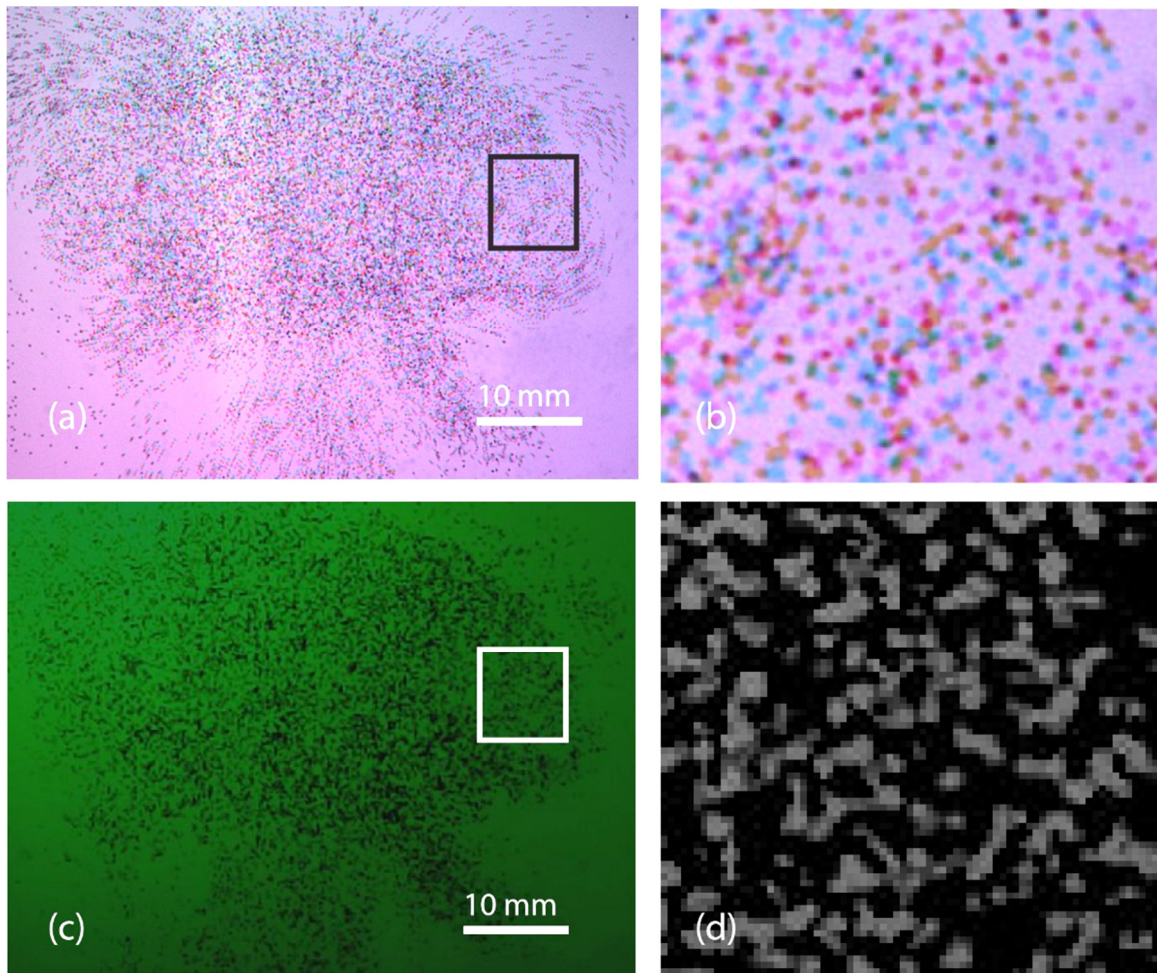


Figure 3.14. Vortex ring captured simultaneously with (a) Red camera and (c) Xperia™ smartphones in the central face of the tank. Figures b and d show the magnified region marked in the respective squares. One can note the difference in the resolution of the two systems. The viewing angle for Figures a and c is slightly different. Therefore images are not fully comparable.

For the Red Cinema camera system, the 3D reconstruction procedure yields  $2025 \times 2025 \times 1922$  voxels for each time step. The same process for the smartphone camera system yields  $586 \times 586 \times 557$  voxels. The volume reconstructed in both cases is approximately  $80 \times 80 \times 76 \text{ mm}^3$ . The direct correlation procedure for both systems is the same as described in the previous section 2.2.2. However, the interrogation volume size differs between the Red Cinema cameras and the smartphones systems. For the Red Cinema cameras, the final correlation volume size is  $104^3$  voxels with 75% overlap, whereas for the Xperia™ system the final interrogation volume size is  $48^3$  voxels with 75% overlap. This produces approximately 4 times more 3D vectors for the Red camera system.

In Figure 3.15 (c), we present an overlay of the results obtained with both systems at the same instant. Visually, the isovorticity surfaces and velocity vectors are comparable and describe the same qualitative features of the vortex ring. Nevertheless, one has to keep in mind that the spatial resolution of the velocity field produced by the smartphones is approximately  $1/4$  of the spatial resolution of the Red cameras.



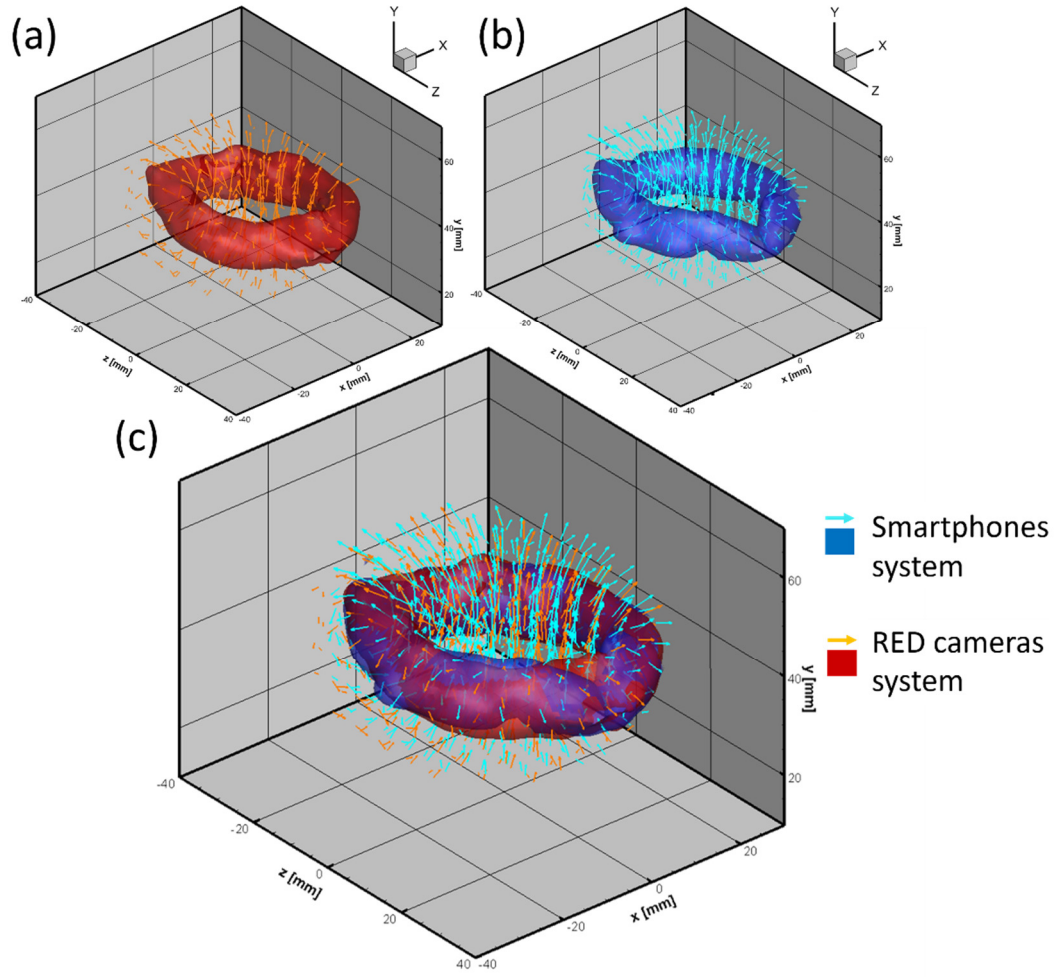


Figure 3.15. (a) Red Cinema Camera system results showing isosurfaces of vorticity magnitude  $|\omega| = 210 \text{ s}^{-1}$  and the velocity field around that volume. Only every 6<sup>th</sup> vector is presented for visualization purposes. (b) Smartphone system results showing isosurfaces of vorticity magnitude  $|\omega| = 210 \text{ s}^{-1}$  and the velocity field around that volume. Only every 3<sup>rd</sup> vector is presented for visualization purposes. (c) Overlay of the results from both systems, the smartphone system result is presented as a blue surface and cyan velocity vectors while the Red camera system results are presented as a red surface and orange velocity vectors. One can visually notice both results overlap and are very similar qualitatively.

Furthermore, one can perform a node-by-node comparison and obtain an error estimation of the velocity components. Since the resolution of the two systems is different, the Red camera results are downsampled by linear interpolation to match the same grid size as the Smartphone system case (i.e., from the original  $1.03 \times 1.03 \times 1.03 \text{ mm}^3$  mesh to a  $1.64 \times 1.64 \times 1.64 \text{ mm}^3$  per node). This interpolation allows us to obtain

the relative error vector of the velocity at every node is obtained and normalized by the maximum magnitude of velocity (herein, 1.8 m/s). Therefore, we compare the mean relative error magnitude present in isosurfaces of different vorticity magnitude ranging from 150 to  $310 \text{ s}^{-1}$  in Figure 3.16(a). One has to keep in mind that regions close to the vortex core have the greatest velocity gradient. Therefore, the values presented in the plot represent an upper bound of our error. Figure 3.16(b) present an isovorticity surface of  $210 \text{ s}^{-1}$  colored by the relative error, this way we can detect the regions where the error is higher.

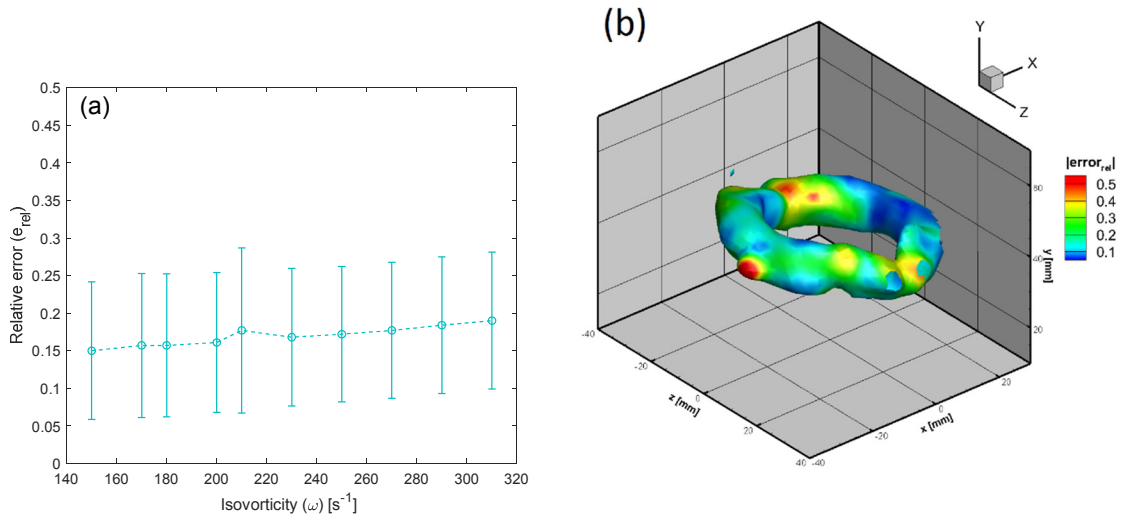


Figure 3.16. (a) Mean relative error of velocity magnitude on isosurfaces of vorticity magnitude. The error bars represent the standard deviation of the relative error. (b) The contours of the relative error shown on the Isovorticity surface of magnitude  $|\omega| = 210 \text{ s}^{-1}$ . These regions represent an upper bound of the error due to the large velocity gradients present in this region of the flow.

We also compare qualitatively the planar velocity fields and the out of plane azimuthal vorticity. The central XY plane is presented in Figure 3.17 and shows that the main qualitative features such as the location of the vortex core, velocity, and vorticity magnitude are comparable for both systems. However, the relatively lower resolution in the case of the smartphones is evident from this figure. Further comparison is carried out

at a horizontal line (at  $y = 44$  mm) that cuts one side of the vortex core (since the vortex core is not completely horizontal). Despite the high-velocity gradients in the area, Figure 3.18(a) shows close similarity between the velocity profiles reconstructed by the two independent systems. Figure 3.18(b) shows similar results for the isovorticity magnitude values along the same line. We highlight that the largest errors are due to slight offsets in the vortex core location combined with the strong velocity gradients close to the outer edge of the cores.

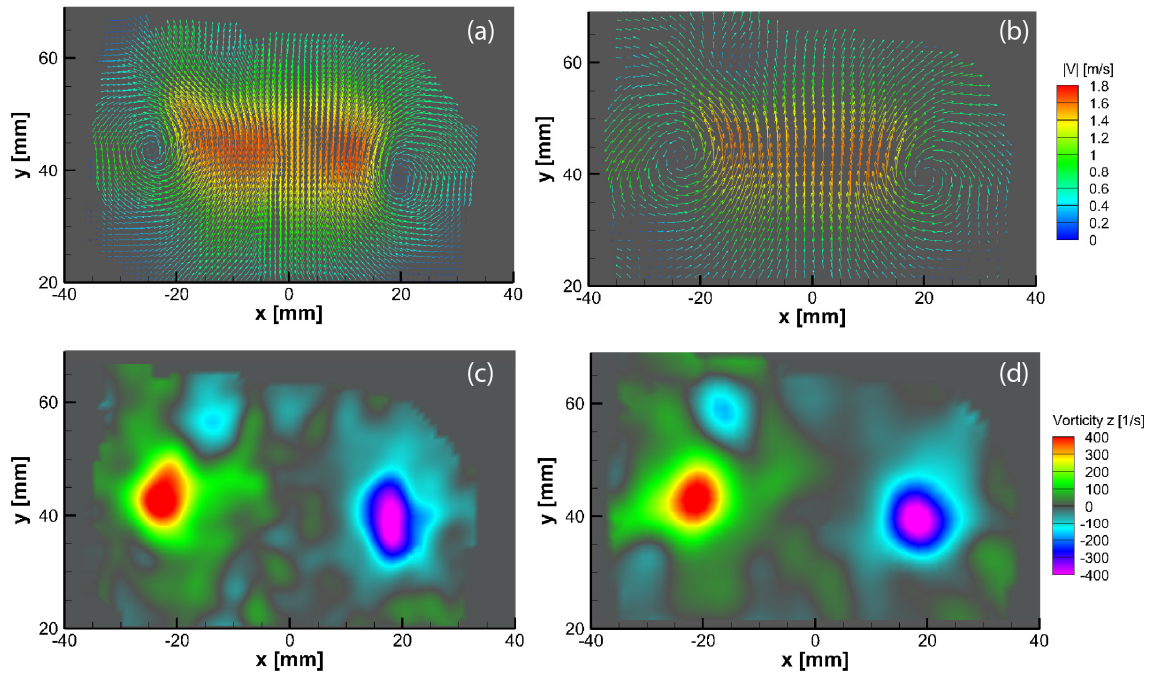


Figure 3.17. Side by side comparison between velocity magnitude on the center plane XY for (a) High-resolution Red camera system and (b) High-speed Smartphone camera system. Contour plots of Vorticity magnitude are presented for (c) High-resolution camera system and (b) high-speed Smartphone camera system. Visually one can notice the difference in spatial resolution of the two systems.

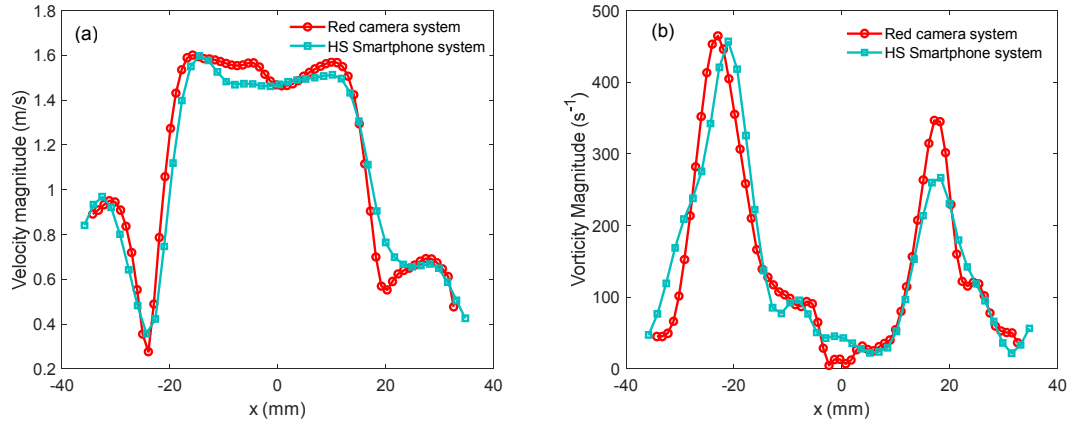


Figure 3.18. Comparison of the results along  $y = 44 \text{ mm}$  for (a) Velocity magnitude and (b) Vorticity magnitude. The red lines represent the results obtained from the Red Cinema camera system. Cyan curves represent the results by the “slow-mo” smartphone system proposed in this chapter.

### 3.3 Conclusions

In this Chapter, we have demonstrated the use of smartphones capable of recording High-Speed video at 960 fps for time-resolved measurements in a Tomographic PIV setup. The proof of concept presented herein will facilitate the study of turbulent flows without the need for expensive specialized equipment. The camera and LED illumination system are similar to the one proposed in the previous chapter [48]. However, synchronization of the cameras is critical for this section due to the high-speed nature of the technique and limited number of frames recorded at 960 fps. Synchronization was accomplished by using high-performance optocouplers that have a typical response time of 500 ns to a TTL pulse from a signal generator. The main challenges are presented and discussed within this chapter, such as out of phase clocks of the sensors, random delay in the camera recording startup, control of shooting parameters and binning of the image when shooting in high-speed mode. Strategies to overcome such challenges are presented in this chapter.



To test the proposed technique, measurements of a vortex ring with approximately 40 mm in diameter were carried out. The Reynolds number of the tested rings is  $Re = \frac{\Gamma}{\nu} = 16,000$ . The maximum velocity magnitude measured in these rings is approximately 1.8 m/s. A total of approximately 5.2 million individual vectors are reconstructed over the whole time sequence (approximately 90,000 vectors per time step) with a pitch of 1.6 mm in every direction. The results obtained are then verified in a similar way to the one proposed in Chapter 2, i.e., circulation around the core in different vertical planes as well as the verification of the closure of the continuity equation. The increase of circulation as a function of the radial distance from the core is compared at different time steps and vertical planes, yielding similar profiles in all cases. Continuity verification produced a mean normalized residual of  $\delta_{cont} = 6.27 \times 10^{-4}$ .

Furthermore, concurrent experiments measuring the vortex ring with the proposed Tomo-PIV Smartphone system and an Ultra high resolution (4K resolution) system using four Red cinema cameras are carried out. The Red cinema system allowed us to benchmark our result to a simultaneous much higher spatial resolution velocity field. However, Red Cinema cameras can record only up to 30 fps at the 4K resolution, for this reason, we use the technique proposed in Chapter 2 using colored shadows to encode time in both cases. The benchmark shows very similar qualitative and quantitative results.

## **Chapter 4 : 3D PIV/PTV using single color cameras**

This chapter is the result of a collaboration with the Visual Computing Center (VCC) group at KAUST. The collaborators include Jinhui Xiong, Ramzi Idoughi, Abdulrahman B. AlJedaani, Xiong Dun, Qiang Fu, Prof. Wolfgang Heidrich and Prof. Sigurdur T. Thoroddsen.

As previously discussed in earlier sections, the typical techniques for reconstructing 3D flows are tomographic PIV and 3D PTV. Both of these techniques take advantage of the use of multiple cameras viewing the ROI from different angles, but as described earlier, this comes with a financial and complexity cost, especially if highly specialized cameras are used.

In this chapter, we propose the use of a single camera and a special illumination system using either collimated lights or chromatic light profiles from commercially available projectors. This reduces the complexity during alignment of cameras, as well as reducing computational costs.

The first approach of this technique involves the use of a high-resolution color camera, such as the RED cinema camera model 6K Epic Dragon or the Red Scarlet-X DSMC with a linear chromatic filter and collimated white light source. This collaboration produced a high-quality paper accepted for the SIGGRAPH 2017 conference [62], one of the most important for the computer graphics and interactive techniques fields. The cameras can record 6K video (6144 x 3160 px ~19 Mpx) at a framerate up to 75 fps for the Epic Dragon model and 4K (3840 x 2160 px) video at 30 fps for the Red-Scarlet model. These features make it perfect for high resolution capturing, color fidelity and the chance

of recording RAW footage. Thus, this characteristics will decrease the difficulty of color separation and depth extraction.

For a second iteration, we use chromatic volume illumination with an LCD projector. The depth position, perpendicular to the camera, is encoded in the color of the gradient. Using a 3-LCD projector the video camera records the 2-D motion of a 3-D particle field within a fluid, which is perpendicularly illuminated with depth gradients of color illumination. Both mentioned iterations involve mainly encoding the depth position perpendicular to the camera, in the color of each particle image.

#### **4.1 Rainbow PIV/PTV using a linear chromatic filter and a single camera (first iteration).**

This technique comprises the use of a high-resolution color camera (Red Cinema cameras described previously). The camera is placed perpendicularly to a color gradient generated by a linear color filter. The camera lens uses a Diffractive Optic Element (DOE) to increase the brightness of the captured particles reducing the number of out-of-focus particles. Therefore, the depth position of the particles is encoded in the color scattered from each particle. The images are then processed with an optimization algorithm that reconstructs the depth position of the particles to compute a 3D-3C velocity field. The technique is then tested with a “static” particle field created with ultra-high viscosity silicone oil and with different three dimensional flows.

#### 4.1.1 Experimental setup

Opposed to 2D PIV, the proposed technique uses a collimated light source(HPLS245, from Thorlabs) that passes through a linear variable Bandpass filter, rather than the thin laser sheet used in traditional 2D PIV. Therefore, depth information is encoded in the different color wavelengths or hue values, allowing us to extract particle positions in the Z axis. See Figure 4.1 (a, b)[62].

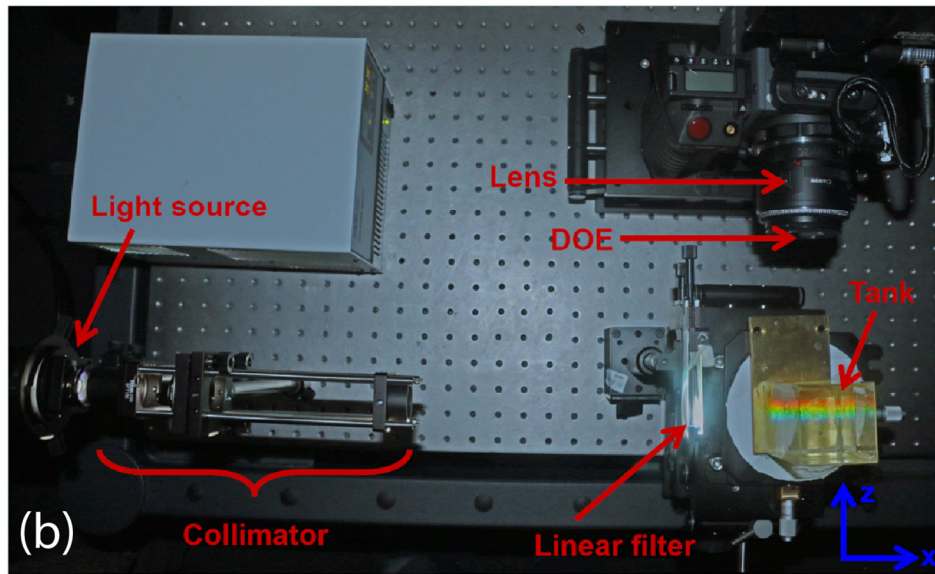
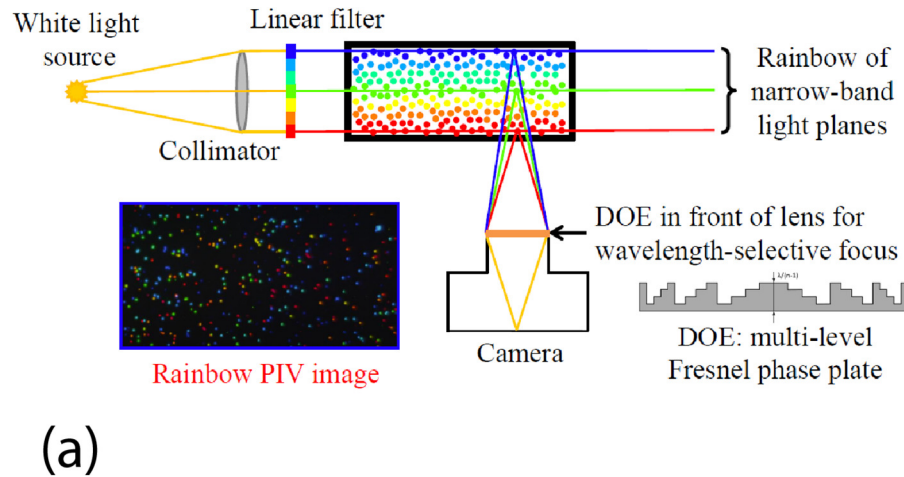


Figure 4.1. (a) Schematic representation of Rainbow PIV system by Xiong, J., et al.[62]. (b) Actual photograph of the experimental setup. (Figure reproduced from Xiong, J. et al. [62]. )

Due to the linear color filter, the light intensity is reduced on the ROI making necessary to open the aperture of the camera lens. As a consequence, the depth of field in the recorded image is reduced dramatically, making most of the particles to be out-of-focus as seen in Figure 4.2 (b-d). To overcome this problem a Diffractive Optic Element (DOE), initially proposed by Peng, Y., et al. [63] from VCC at KAUST ( Figure 4.3), in the form of a Fresnel phase plate, is placed in front of the camera lens. This device will provide a wavelength-selective focus in the camera optics, bringing all the particles to be in focus, as observed in Figure 4.2 (a).

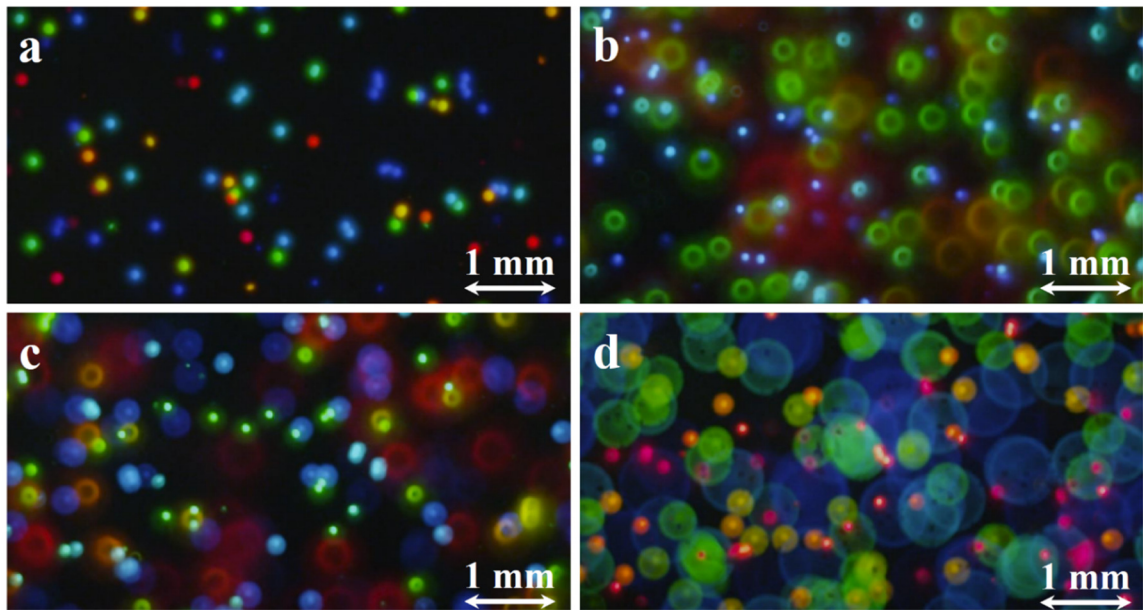


Figure 4.2. Comparison of images captured using (a) DOE + regular lens and (b, c, d) using a regular lens for different focal planes corresponding approximately to the blue green and red levels. It is important to notice the narrow focal depth due to the large aperture used.[62] (Figure is reproduced from Xiong, et al. [62]).

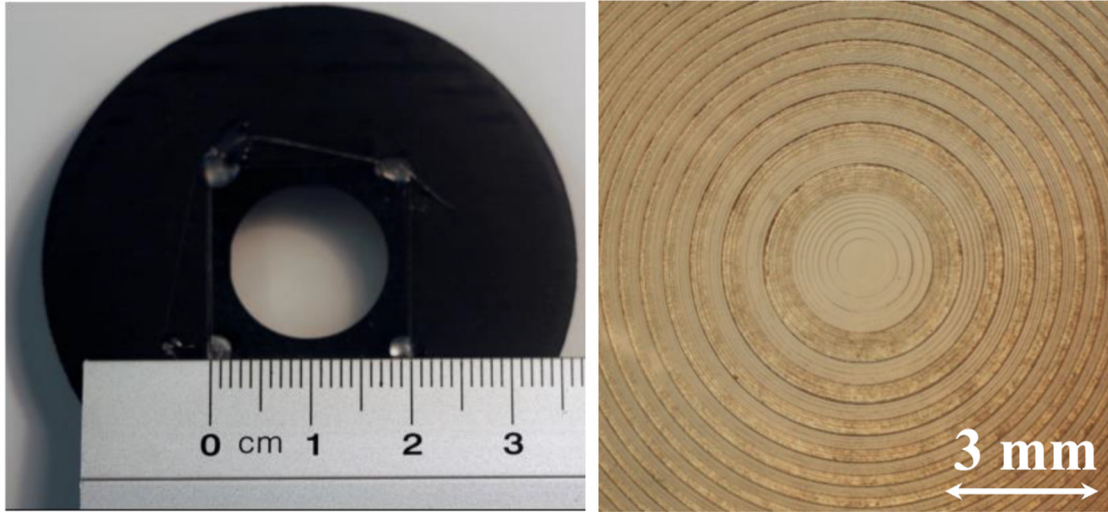


Figure 4.3. (Left) The Diffractive Optical Element (DOE) mounted on a support. (Right) Magnification of the central region of the DOE.[62]

#### 4.1.2 Reconstruction procedure.

The main reconstruction goal is to estimate the depth position from the recorded color in the images; these particles can be then tracked in time obtaining a 3D-3C velocity field. Since the images captured are in RGB color space, an iterative approach is used. The algorithm was developed by the Visual Computing Center at KAUST, managed by Professor Wolfgang Heidrich. It involves an optimization problem that ensures particle motion consistency assuming flow continuity and inviscid flow with a negligible pressure gradient. Thus, an initial position estimate will give a first estimate of the time-dependent velocity field. This velocity field is used to refine the position when applying physical models that link all the frames in time. More details of the algorithms can be found in Xiong, J., et al.[62]

### 4.1.3 Results

In order to test the capabilities of the algorithm and the technique, simulated images and data are generated using random particle locations in a  $100 \times 100 \times 20$  (X x Y x Z) volume. Additionally, experiments using a 1,000,000 cSt pure silicone fluid are carried out to “freeze” the position of white polyethylene particles with a size of 90-106  $\mu\text{m}$  in the fluid. The container is then translated in the X and Z direction with micro-meter stages. Also, rotation of the color gradient is done in order to avoid tilting the tank and distorting the volume. Hence, having a reference for the particle displacements in advance. Before running the reconstruction algorithms and obtaining any velocity field, the images (4K resolution) are passed through a Gaussian Filter and are down-sampled by a factor of 8, to a  $512 \times 270$  pixels, the color depth position is discretized with 20 levels, corresponding to 900  $\mu\text{m}/\text{level}$ . In Figure 4.4 we can see the results after running the reconstruction algorithms.

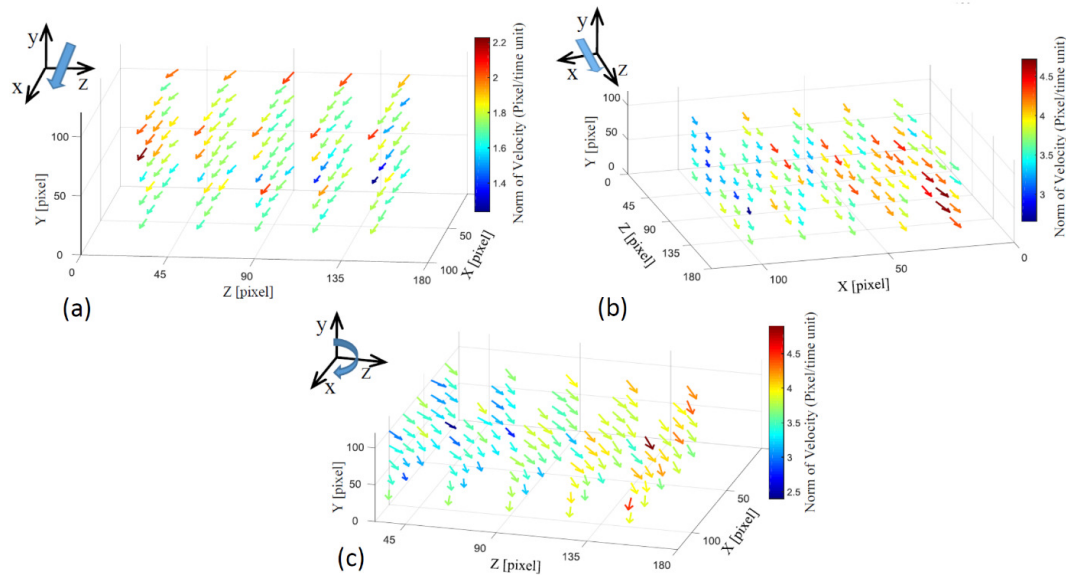


Figure 4.4. Resulting velocity fields after translation in the (a) X axis, (b) Z axis and (c) Rotation around Y axis. [62]

Furthermore, some real flow measurements were carried out in water for a jet inside the water, a drop impact on the pool, a single vortex by stirring the fluid and a dual vortex interaction. The results of these experiments can be consulted in Xiong, J., et al.[62] A US patent application No. 15498317 for this technique has been published on 30<sup>th</sup> August 2018 [64].

#### **4.1.4 Areas of opportunity**

The use of a linear color filter reduces the light intensity dramatically on the tested ROI. Due to this reduction in the intensity, a large aperture in the camera lens has to be used, minimizing the depth of focus on the image. In order to overcome this problem, a DOE has to be used. However, this kind of DOE has to be designed specifically for a fixed setup. Thus, the reuse of the same DOE for a different configuration or ROI size becomes very difficult.

## **4.2 Single camera: Rainbow 3D PIV/PTV using LCD projectors**

In order to further expand the applications of the previous technique, in a second iteration, we propose the use of a 3LCD projector as an illumination source. One of the main advantages of using a projector for the illumination, is the flexibility of the structured light. This versatility adds simplicity to the modifications and adjustments of the illuminated volume size, as well as the control of the projected framerate and intensity patterns. There is, however, a trade-off between the size of the illuminated volume vs the brightness recorded from the particles.



#### 4.2.1 3LCD technology

3LCD technology in projectors was developed and first introduced by Epson in the 1980s. Typically this technology consists of a white light source that is projected into a combination of dichroic mirrors that split the light into RGB colors. Each colored light is then passed through an LCD chip (one for each color channel) that reads electrical signals in order to create an image. The colored lights are then combined with a prism, creating a full color image that is passed through the lenses and projected finally onto the screen. A schematic representation of this process is presented in Figure 4.5 [65].

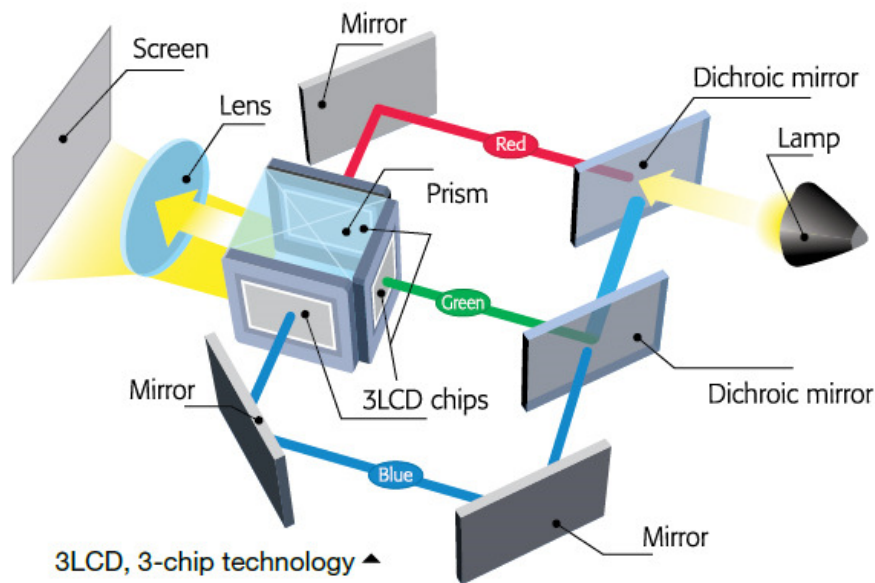


Figure 4.5. Schematic representation of a 3-LCD projection system. Red, Green and blue light is separated with dichroic mirrors, in order to pass through a single LCD for each of this colors to form the desired color channel. The 3 colored images are combined within a prism and then projected onto the screen forming a full color image.(Figure is reproduced from Epson [65])

#### 4.2.2 Projector specifications

The chosen projector for this iteration is a 3LCD Epson EX9200 Pro, this projector has a WUXGA (1920 x 1200 px) native resolution, with a Color and white brightness of 3200 lumens (each), contrast ratio of 15,000:1 and can reproduce up to 1.07 billion

colors, i.e., 10-bit per color channel. In principle, the color gamut produced by this kind of projectors, expand the possibility to increase the depth resolution of 20 levels achieved by using a linear color filter. Of course, this will also be limited by the bit resolution of the camera used. A stock image of the projector is presented in Figure 4.6.



Figure 4.6. Projector Epson EX-9200 Pro proposed to be used due to the high resolution and relatively low cost. (Figure is reproduced from Epson, official website [66])

#### 4.2.3 Experimental setup

The experimental setup for this technique is very similar to the one used in section 4.1.1. The collimated light source and linear color filter are replaced with the 3LCD projector, while keeping the camera looking in a perpendicular position with respect to the projector, see Figure 4.8. The motion of the illuminated particles is recorded by a Red 6K Epic Dragon video camera, equipped with a Nikkor 105 mm lens. see Figure 4.7.



Figure 4.7 Red 6K Epic Dragon™ camera. (Figure is reproduced from Red[67])

Due to the expanding nature of the projector optics, we are required to use an additional set of optics in order to reduce the rapid expansion of the light beam. A convex lens  $\varnothing=75$  mm,  $F=150$ mm is used just in front of the projector; this allows us to reduce the angle of expansion of the beam, concentrating the light into our ROI of approximately  $60 \times 60 \times 50$  mm<sup>3</sup>. This configuration gives us an approximate depth of focus of 20mm for the projected image.

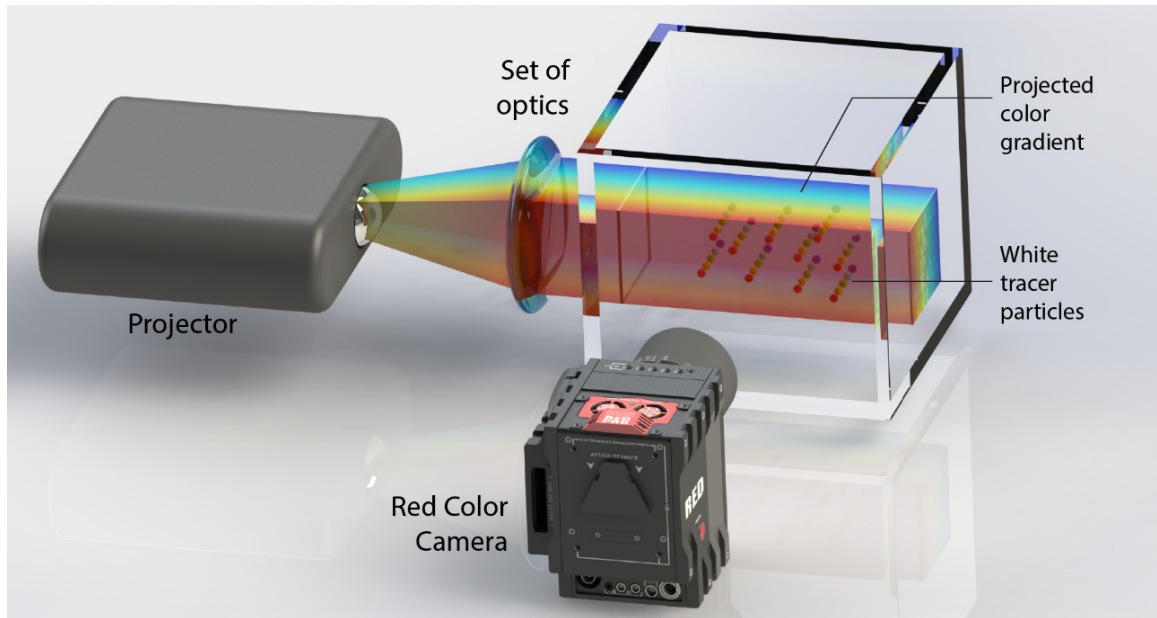


Figure 4.8. Schematic of the rainbow PIV system using the 3LCD projector.

#### 4.2.3.1 Color Space (HSV and RGB)

The first experiments in RGB color photography were done by James Clerk Maxwell in 1860[68]. The additive color model RGB uses mixtures of its three primary colors (Red, Green, and Blue) to reproduce a vast array of color or gamut (see Figure 4.9 a). Nowadays, most of our Televisions, displays, cameras and other digital image processing devices use this model. However, other color spaces have been created to describe and mix digital colors in a more intuitive way, similar to the way artists mix different paints. Smith, A. R. [69] introduced first the HSV (Hue, Saturation, Value) color space. This model is a polar coordinates representation of color where varying H corresponds to an angular change in the color circle. Decreasing S will increase the “whiteness of the color” or mix other hue colors (similar to mixing with white paint). Decreasing V will increase the darkness (similar to mixing with black paint). This process is better understood if we look at the color space in cylindrical coordinates (see Figure 4.9 b). Furthermore, Smith, A.R. [69] provides a conversion algorithm to convert from RGB to HSV color space as presented in the following equations:

$$V = \max(R, G, B)$$

$$X = \min(R, G, B)$$

if  $\max(R, G, B) = R$  :

$$H = \frac{60(G - B)}{V - X}$$

Else if  $\max(R, G, B) = G$  :

$$H = \frac{60(B - R)}{V - X} + 120^\circ$$

Else if  $\max(R, G, B) = B$ :

$$H = \frac{60(R - G)}{V - X} + 240^\circ$$

$$S = \frac{\max(R, G, B) - \min(R, G, B)}{\max(R, G, B)}$$

Where  $V$  is the “value” ( $V \in [0,1]$ ),  $S$  is saturation ( $S \in [0,1]$ ) and  $H$  is the hue value in degrees ( $H \in [0^\circ, 360^\circ]$ ).  $R, G, B$  are the normalized values for each color channel, i.e.,  $R \in [0, 1], G \in [0, 1], B \in [0, 1]$ . When  $R=G=B$ ,  $H$  is undefined.

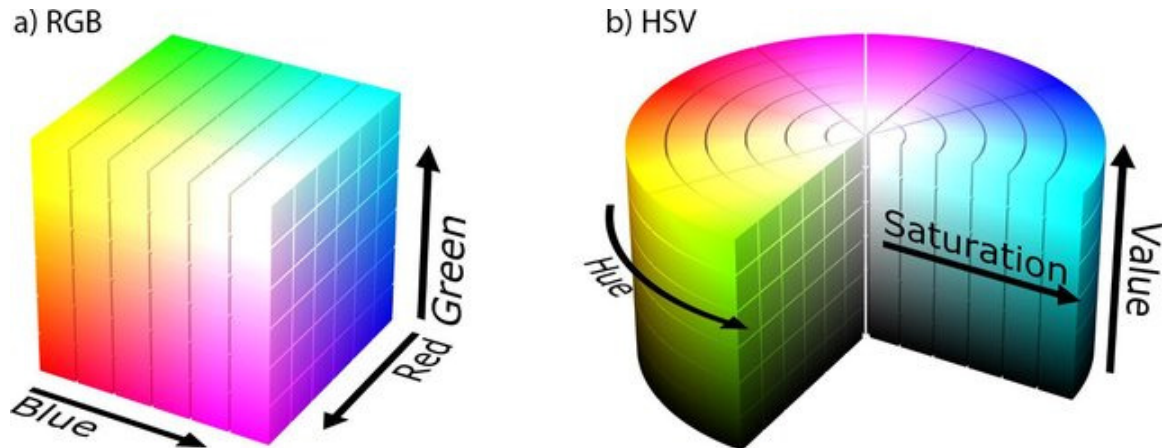


Figure 4.9. (a) Cartesian Coordinates of RGB color space and (b) HSV color space cylindrical coordinates. (Images by Michael Horvath, available under Creative Commons Attribution-Share Alike 3.0 Unported license)

#### 4.2.3.2 Light and camera characterization.

With the intention of understanding the projector light behavior, we project different gradients onto a 45 degrees plane with a dotted calibration target from Edmund

Optics, this plane is submerged in water. The space between the dots will allow us to understand how the pixel size behaves in space. Since part of the projected image onto the target is not very sharp due to the smaller depth of focus of the projector, we decided to create some alternative gradients regrouping several pixels with a single color level. Thus, we capture images that group 2, 4, 8, 10 and 16 pixel width columns, see Figure 4.10. In this figure, we observe the intensity levels plotted for each channel for the 16 pixel groups case.

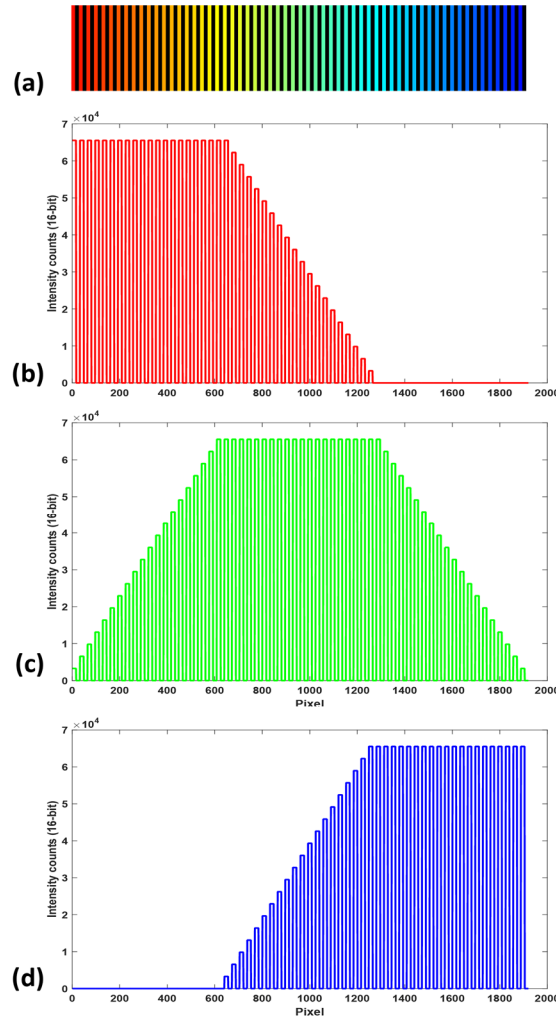


Figure 4.10. (a) Gradient for every 16 pixels group. (b,c,d) Represent the intensity levels for the red, green and blue channels respectively.

The captured images by the camera and their corresponding intensity levels plot can be observed in Figure 4.11. From this figure, we can observe the region where the projection is in better focus. This is important to quantify and understand the effects of the narrow depth of focus in the projector, allowing us to determine the optimum number of color levels to be used.

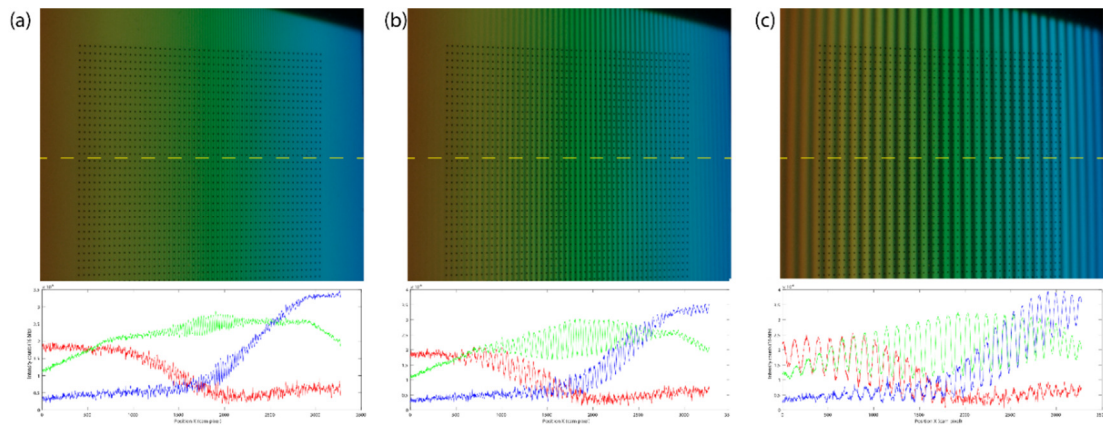


Figure 4.11. Red Cinema camera response and an intensity plot along the yellow dashed line for grouping pixels in (a) 4 px, (b) 8 px, and (c) 16 px in width. Each dot is separated by 1 mm on the calibration plate. The plate is placed at 45° with respect to the camera.

Additionally, a different kind of patterns can be projected onto the same surface to understand pixel size and quantify chromatic aberrations. For this purpose, checkered patterns of groups of 10 pixels are used, see Figure 4.12.



Figure 4.12. Camera response images from projected checkered patterns of 10 px for (a) purely red, (b) purely green, (c) purely blue projected images.

#### 4.2.3.3 *Color gradients design*

The color gradients are designed and manipulated in Matlab, producing 1900x 1200 px images using 10-bit color intensity levels. The flexibility provided by the projector allows us to create different types of color gradients to adapt better to the camera response signal, therefore, minimizing any noise or color cross-talk.

For this section, we have decided to create gradients that always have a saturated color channel with a linear RGB profile as shown in Figure 4.13. Thus, we can perceive three main regions, one for each color saturation, while the other color channels have an increasing or decreasing intensity. In Figure 4.13(a) we can see the color gradient with its corresponding intensity plot Figure 4.13(b). This is done in order to always obtain high-intensity light from the projector, helping us to capture the video. On the other hand, having non-saturated channels reduces the brightness excessively. To minimize the out of focus regions and avoid overlapping of certain color, the color gradient is discretized by having 2 pixels in black for every 4 pixels with the same hue value.

We, therefore, proceed to project a single RGB value at a time in a real white polyethylene particle field with thousands of tracers to characterize the camera response signal (see Figure 4.14). It is important to note that the aperture of the lens is F# 7.1. This is a relatively high aperture and will produce particles to look different sizes. However, this is also used to our advantage to produce a smooth particle color and increase brightness. Statistics such as the mean Hue (H) value for each particle and the standard deviation will allow us to optimize the color profile to be used. In Figure 4.13 (a,b) we see



the projected RGB linear profile and the camera response in HUE color space is plotted in Figure 4.13 (c).

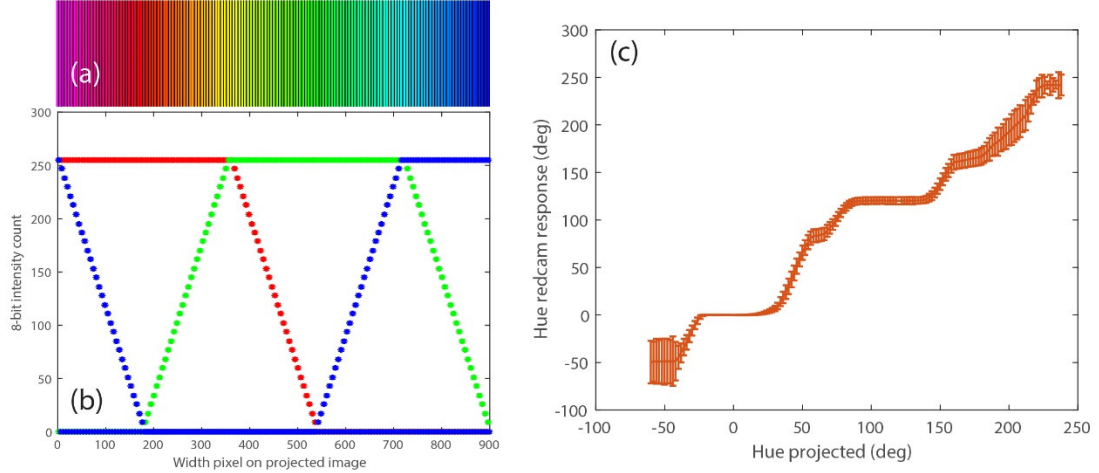


Figure 4.13 (a) Projected color image, (b) the respective RGB linear profile and the (c) camera mean response curve with error bars representing the standard deviation  $\pm\sigma$

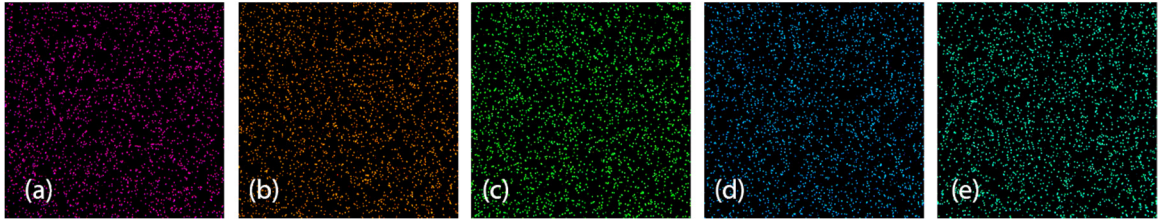


Figure 4.14. Typical color camera response used for projector-camera system characterization with real particles, a single Hue (R,G,B) value is projected in each case: Hue of (a)  $H=-60^\circ$  (255, 0, 255); (b)  $H=0^\circ$  (255, 0, 0); (c)  $H=120^\circ$  (0, 255, 0); (d)  $H=240^\circ$  (0, 0, 255); (e)  $H=180^\circ$  (0, 255, 255)

From Figure 4.13 (c), one can see that the camera response has a very low sensitivity to change in color near the  $0^\circ$ ,  $120^\circ$ , and  $240^\circ$  hue. These regions have large “plateau” regions corresponding to the saturated pure Red, Green and Blue colors in the RGB space. For this reason, it is required that we use a different profile that increases or decreases rapidly close to the saturation points for each color channel. We, therefore, choose to use piecewise atanh functions to assemble different color profiles for each color channel (RGB), the main equation is presented below:

$$P(x_t) = \frac{1}{5} \operatorname{atanh}(a * (x_t - 0.5)) + 0.5$$

Where:

$P(x)$ : represents the normalized piecewise intensity for each color channel

$x_t$ : pixel column for a portion of the image

$a$ : variable coefficient for adjusting the slope in the linear profile. (1.9, 1.95, 2.0)

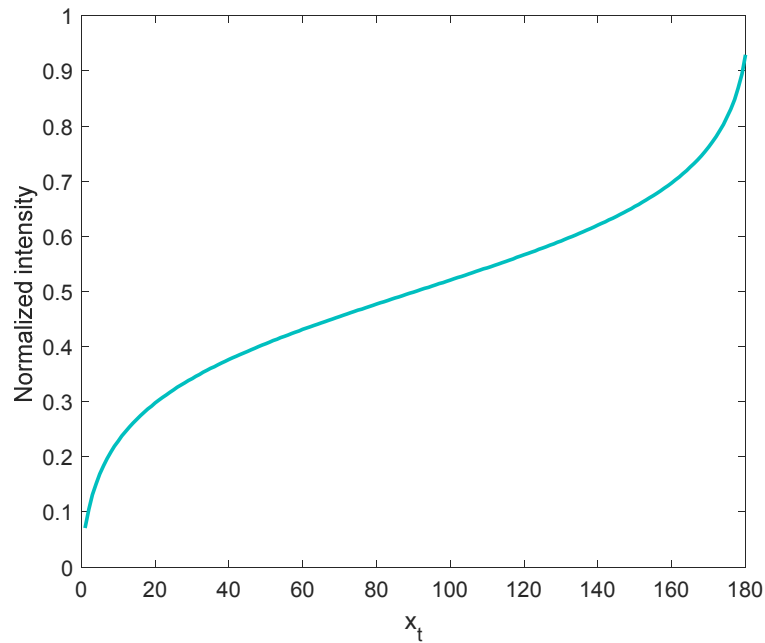


Figure 4.15. Typical atanh piecewise function used for creating color profiles.

We, therefore, tested different profiles based on  $P(x_t)$ , using different values for  $a$  coefficient (1.9, 1.95 and 2.0). The profiles generated in Matlab can be seen in Figure 4.16 (a,c,e) , their respective statistical mean color response is presented in Figure 4.16 (b, d, f)

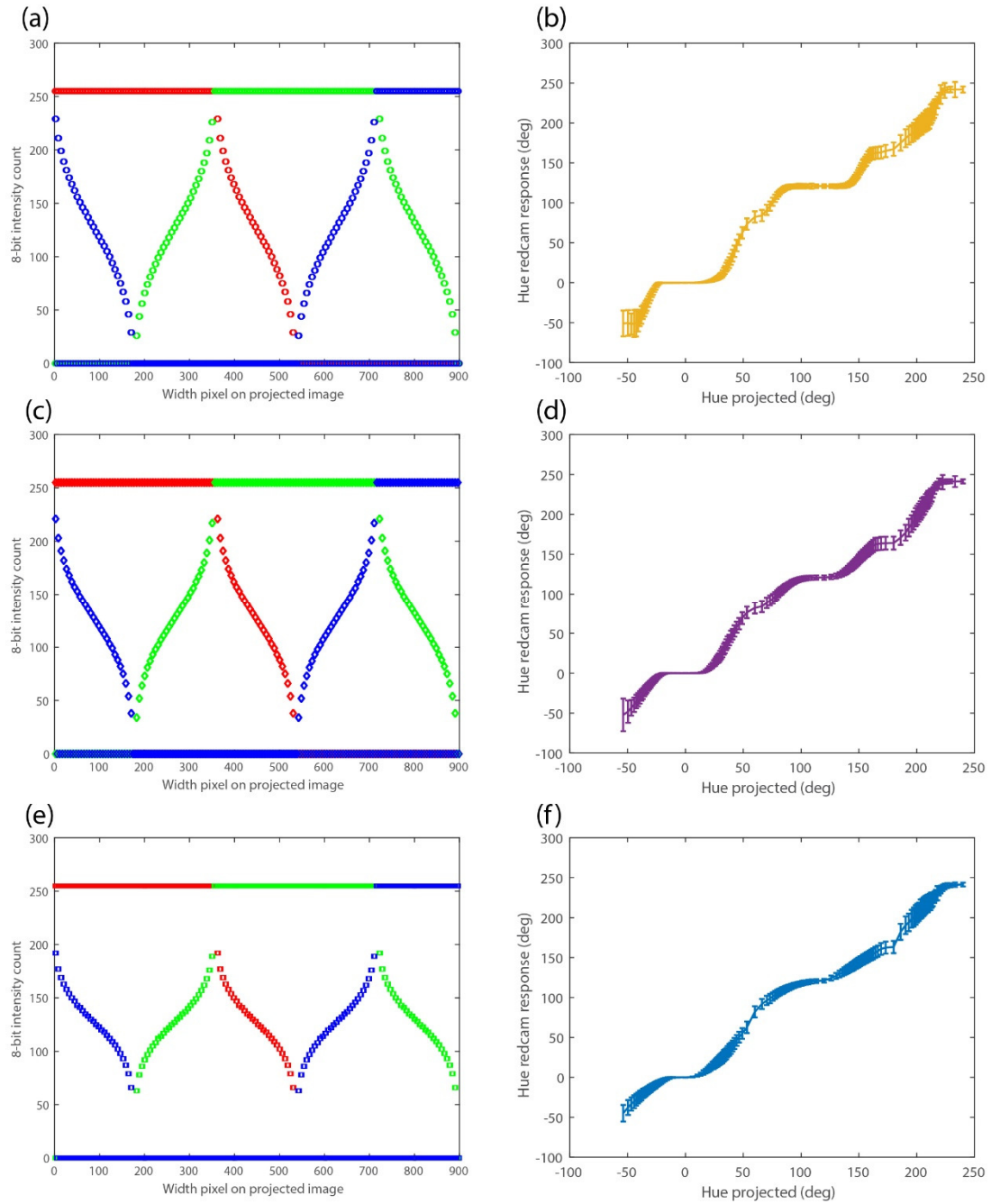


Figure 4.16 Projected RGB profile (Red, Green and Blue channels) for (a)  $a=1.9$ , (c)  $a=1.95$  and (e)  $a=2.0$ . With the respective Hue color space camera-projector mean response curve (b, d, f). Error bars represent  $\pm$  the standard deviation ( $\sigma$ ). Note that the horizontal responses as the projected hue changes are reduced as the coefficient  $a$  increases.

From the previous figure, it is important to note that the “Ideal” response curve would be a straight line with a slope of  $45^\circ$  slope. Compared to the linear color profiles,

those based in *atanh* have a better response. However, one can clearly see that at certain projected hue levels ( $0^\circ$ ,  $120^\circ$ , and  $240^\circ$  corresponding to the saturated pure Red, Green and Blue RGB colors), the slope of the curve is close to 0. This is translated into a lack of sensitivity for the color detected in the camera, since different projected hue values provide very similar (if not the same) response in the camera. The best response is observed in Figure 4.16 (f) where the plateau areas are much smaller. Nevertheless, trying to get high depth resolution for these cases (900 different projected HUE levels) will not produce accurate results due to the large “flat” areas and large error in the response.

We are forced to change our depth detection strategy in order to get higher accuracy with the tradeoff of losing depth resolution. Therefore, we take advantage of the variable projected frames in time to use this temporal information. Based on the previous camera response curves in Figure 4.16 we can then choose arbitrarily 20 different Hue levels, making sure that the standard deviation of such colors doesn't overlap with any of the other chosen Hue values and that the selected values are not in a “plateau”. (see Figure 4.17).

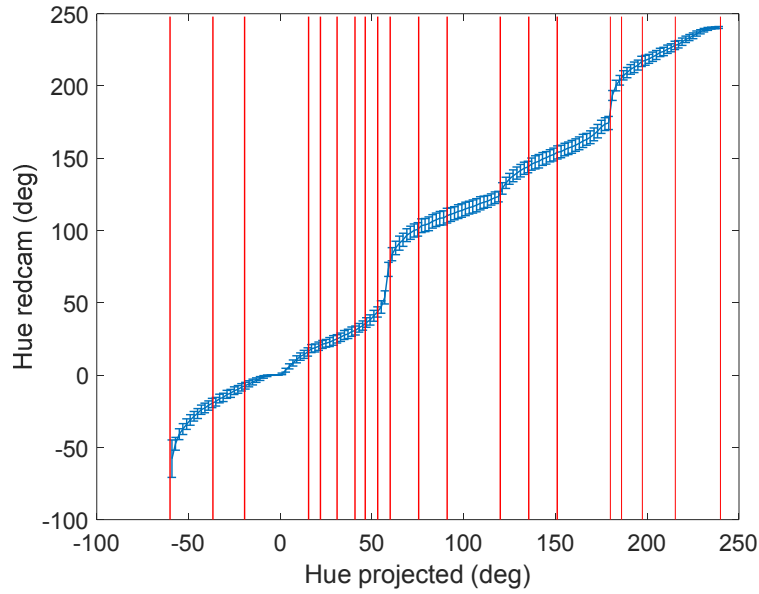


Figure 4.17. Twenty selected Hue projected values represented as red vertical lines. The plot of the camera response (blue line) is presented for reference.

#### 4.2.3.4 Illumination sequence

The Hue values chosen are projected in two different frames. The illumination cycle consists of 10 frames in time. The first frame contains only 10 sectors ( $L_{10}$ ) for a coarse depth estimation (see Figure 4.18 (a)). The subsequent 9 video frames contain 20 different Hue values (see Figure 4.18 (b)). In principle, this will allow us to have 200 depth levels of resolution. It is important to mention that the Saturation and Value in the HSV space is 100%, this will help us obtain more brightness in the projected image.

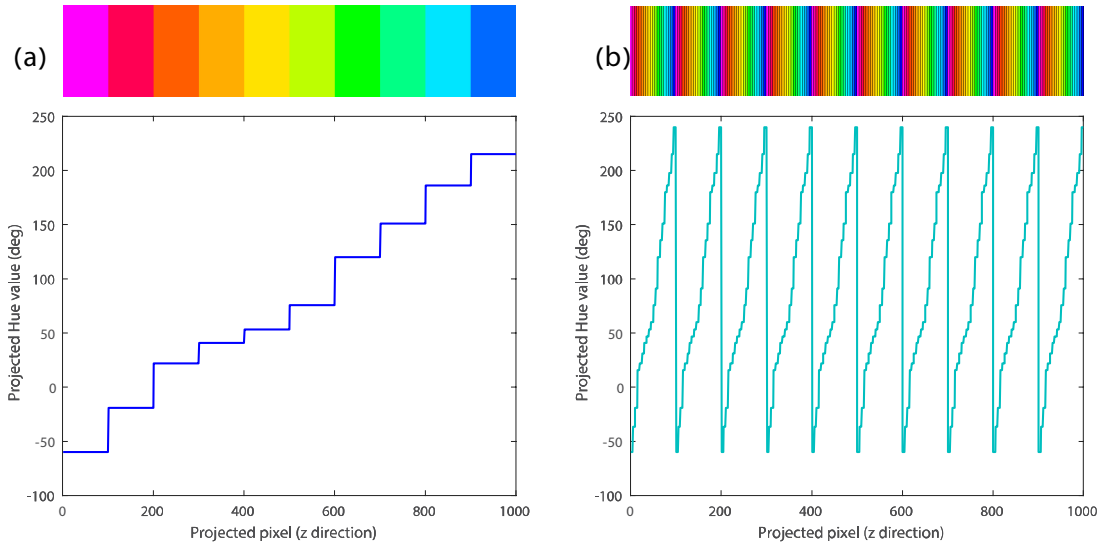


Figure 4.18. Projected images with their corresponding Hue values plot. (a)  $L_{10}$  Hue levels (from left to right  $H = -60^\circ, -19.3^\circ, 21.9^\circ, 40.7^\circ, 53.2^\circ, 75.5^\circ, 120^\circ, 151.1^\circ, 186.1^\circ, 215.3^\circ$ ). (b)  $L_{20}$  Hue levels (from left to right  $H = -60^\circ, -36.7^\circ, -19.3^\circ, 15.5^\circ, 21.9^\circ, 31.1^\circ, 40.7^\circ, 46.4^\circ, 53.2^\circ, 60^\circ, 75.5^\circ, 91.1^\circ, 120^\circ, 135.5^\circ, 151.1^\circ, 180^\circ, 186^\circ, 197.4^\circ, 215.3^\circ, 240^\circ$ .)

#### 4.2.3.5 Vortex ring flow test

One of the tested velocity fields is a vortex ring, similar to the one produced in section 2.1. The vortex ring generator has been designed to fit the volume of interest (see Figure 4.19 of the vortex ring generator design). This device is to be produced by 3D printing, allowing us to have flexibility and adapt the size of the vortex ring to the appropriate size of our illuminated volume.

We place the vortex ring generator on the bottom of a transparent acrylic tank filled with water containing white polyethylene microparticles as tracers (see Figure 4.8). The previous illumination cycle is then played in a loop to allow to track particles in time of a generated vortex ring. Figure 4.22 (a), shows a typical image obtained from the red camera, these images are obtained with a resolution of 6144 x 3160 pixels (6K resolution). However, the studied images are cropped to 4545 x 3160 pixels.

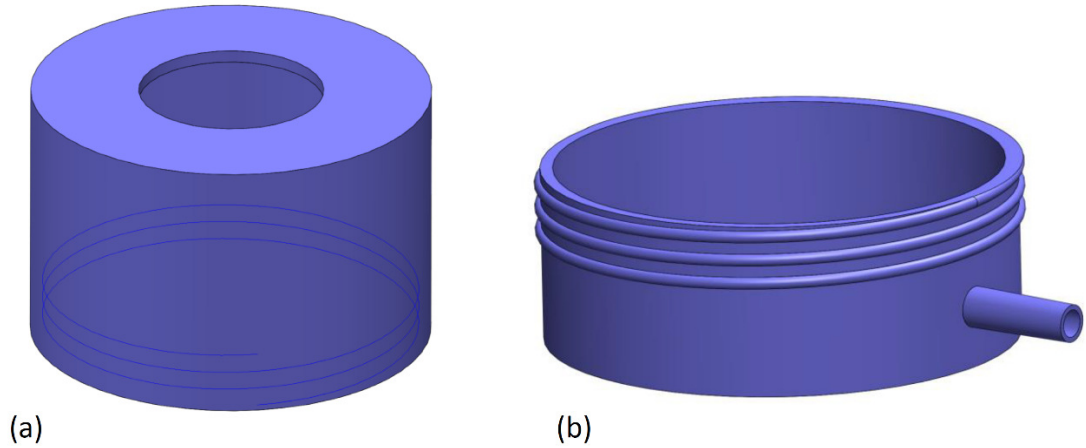


Figure 4.19. 3D model of the vortex ring generator components. (a) top chamber and (b) bottom chamber. Both parts are assembled having a flexible membrane between them.

#### 4.2.4 Particle Tracking and depth ( $z'$ ) estimation.

The digital planar coordinates ( $x', y'$ ) are obtained using the “Trackmate” module available in the opens-source image processing software “FIJI” [70]. More details on this process are specified in section 5.3.1.

In order to ease the detection of the 2-D positions of the particles in “Trackmate”, it is necessary to convert our images to grayscale. This process allows us to do particle-linking with the *Linear Assignment Problem (LAP)* by Jaqaman *et al.* [71]. The LAP algorithm is integrated into Trackmate. Particles are then tracked during the recorded frames obtaining the 2-D digital position ( $x', y'$ ) shown in Figure 4.20



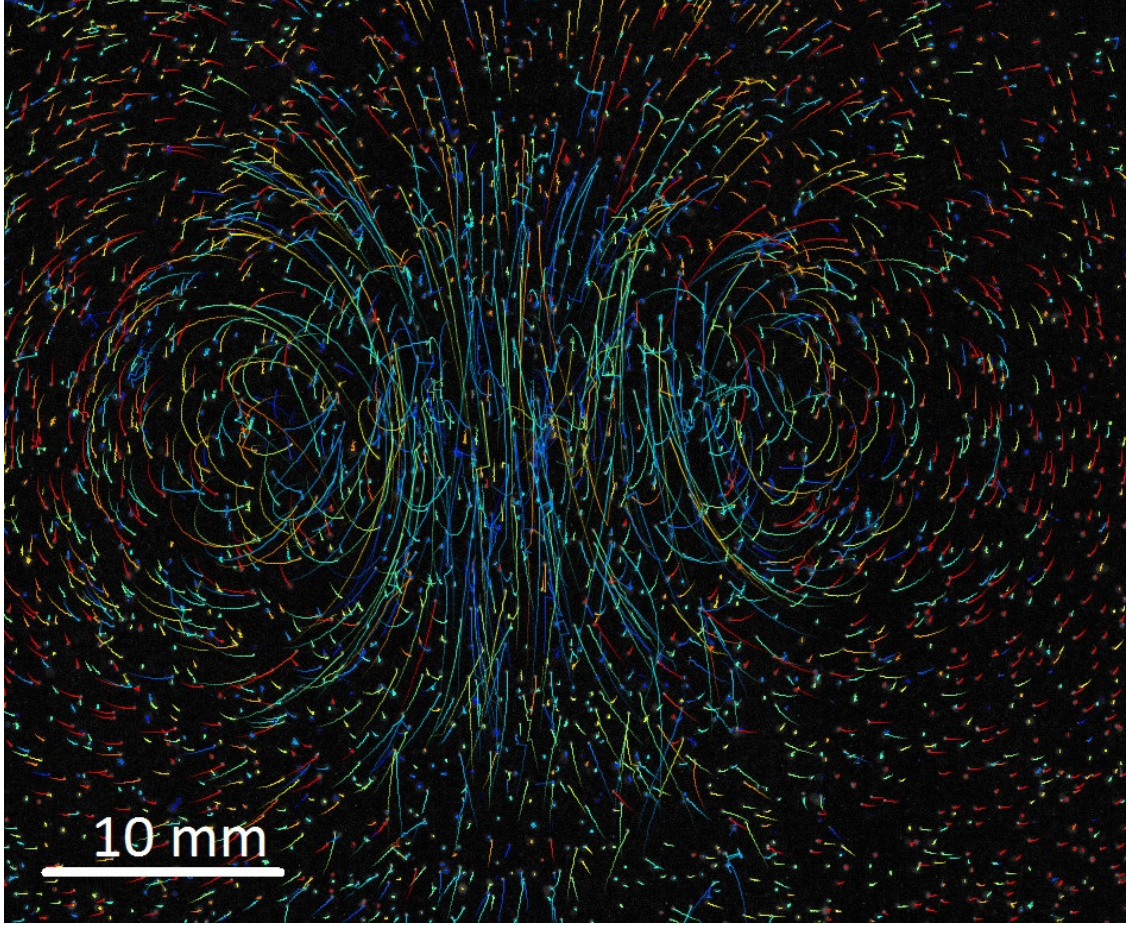


Figure 4.20. 2-D projection of the vortex ring particle field showing the pathlines during 20 time frames.

On the other hand, we process the color images obtained from the Red Cinema camera to estimate a 2-D Gaussian weighted average color for RGB and Hue color space. This estimation is done for each particle detected by the “imfindcircles” function in Matlab, which uses circular Hough transform [72-74]. The output of the function includes the center coordinates and the radius of each particle in pixels. The 2-D Gaussian weight function  $w(x, y)$  is presented in the following equation and plotted in Figure 4.21:

$$w(x, y) = e^{-\left( \frac{\left(x - \frac{x_0}{2}\right)^2}{2 \left(\frac{x_0}{6}\right)^2} + \frac{\left(y - \frac{y_0}{2}\right)^2}{2 \left(\frac{y_0}{6}\right)^2} \right)}$$



From where:

$w(x, y)$ : is the 2-D Gaussian weight assigned to pixel  $(x, y)$  with respect to the center of the particle.

$x_0, y_0$ : Coordinates of the particle center

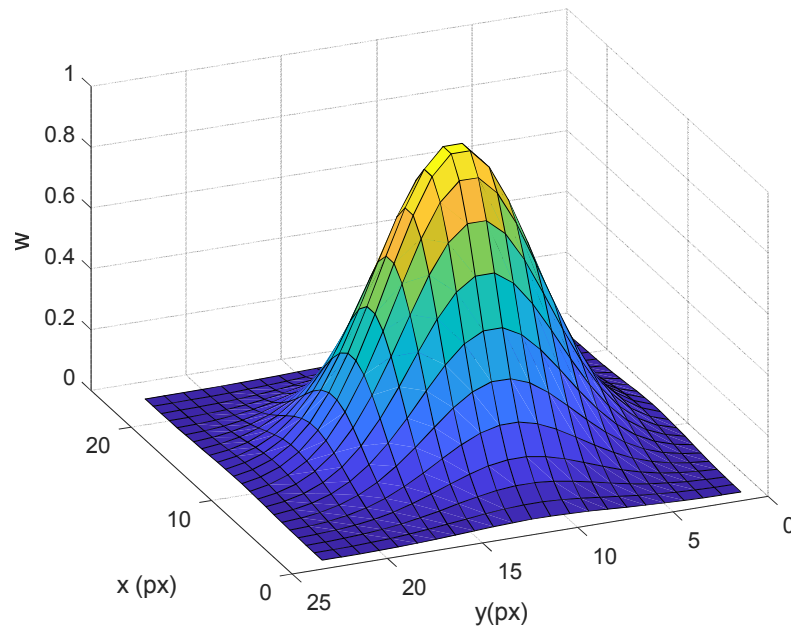


Figure 4.21. Typical weight function ( $w$ ) for a particle that is 23 pixels in diameter.

The Gaussian weighted average is therefore obtained by using the following equation:

$$w_{avg,p} = \frac{\sum_{i=1}^n p_i \cdot w_i}{\sum_{i=1}^n w_i}$$

From where :

$w_{avg,p}$ : is the Gaussian weighted average of parameter “p”.

$p_i$ : is the parameter of pixel “i” to be measured. In this case R,G, B color channels or Hue value (H)

$w_i$ : is the weight of pixel “i” obtained from the 2-D Gaussian weight function

$n$ : is the total number of pixels of a single particle.

With the previous values, we can generate an “artificial” image of each particle. Therefore, we replace all the pixels of a single particle, which have variable Hue values, with a constant weighted average value (as shown in Figure 4.22 b). This process simplifies the color detection by just registering the Hue value of the center of each particle, using the 2-D coordinates provided by “Trackmate”.

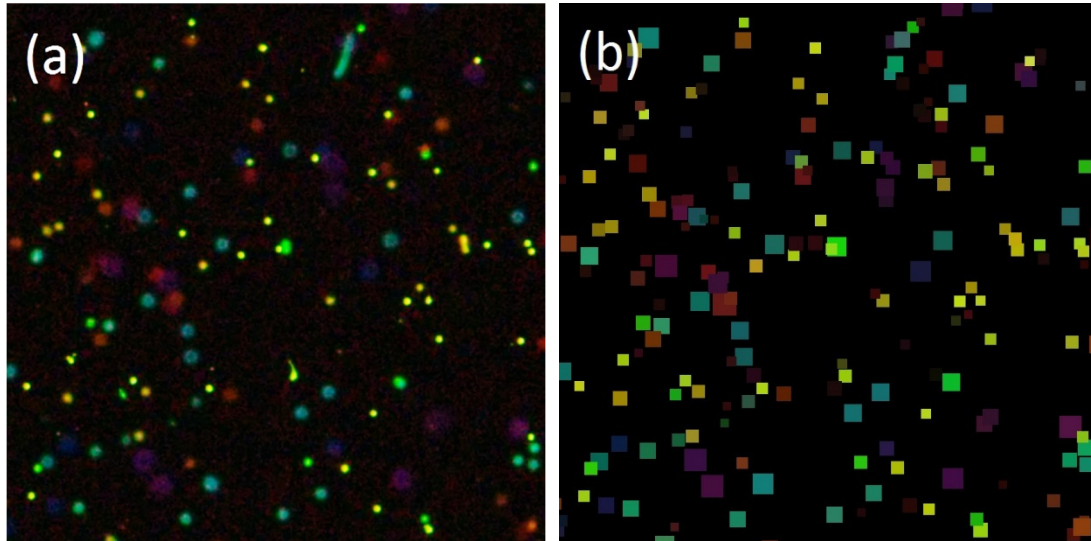


Figure 4.22. (a) Red camera image region of 700 x 700 pixels showing the multiple colors sensed. (b) Same region after obtaining the Gaussian weighted average Hue ( $w_{avg,H}$ ) of each particle. This process aids assigning a single Hue value for every (x, y) coordinate of each particle.

Once we obtain the 2-D location and statistics of each particle ( $w_{avg,H}, w_{avg,R}, w_{avg,G}, w_{avg,B}$ ) in time, we proceed to estimate the corresponding digital depth ( $z'$ ). Initially, RGB color space was used ( $w_{avg,R}, w_{avg,G}, w_{avg,B}$ ) to estimate the depth by normalizing each pixel by the largest color channel, therefore saturating the color of each particle. However, the results with RGB space were very poor, and the depth was strongly biased to certain  $z'$  planes. (See Figure 5.21).

To improve this issue, the HSV color space is used instead of RGB by using the weighted average Hue parameter ( $w_{avg,H}$ ) of each particle, yielding slightly better results (see Figure 4.23). However, even though the results are better than the RGB case, we can clearly observe that depth estimation is biased towards certain planes. This is noticeable where many particles accumulate in multiple  $z'$  planes. The detailed algorithm used to obtain the estimated depth  $z'$  is presented in appendix A1 and A2.

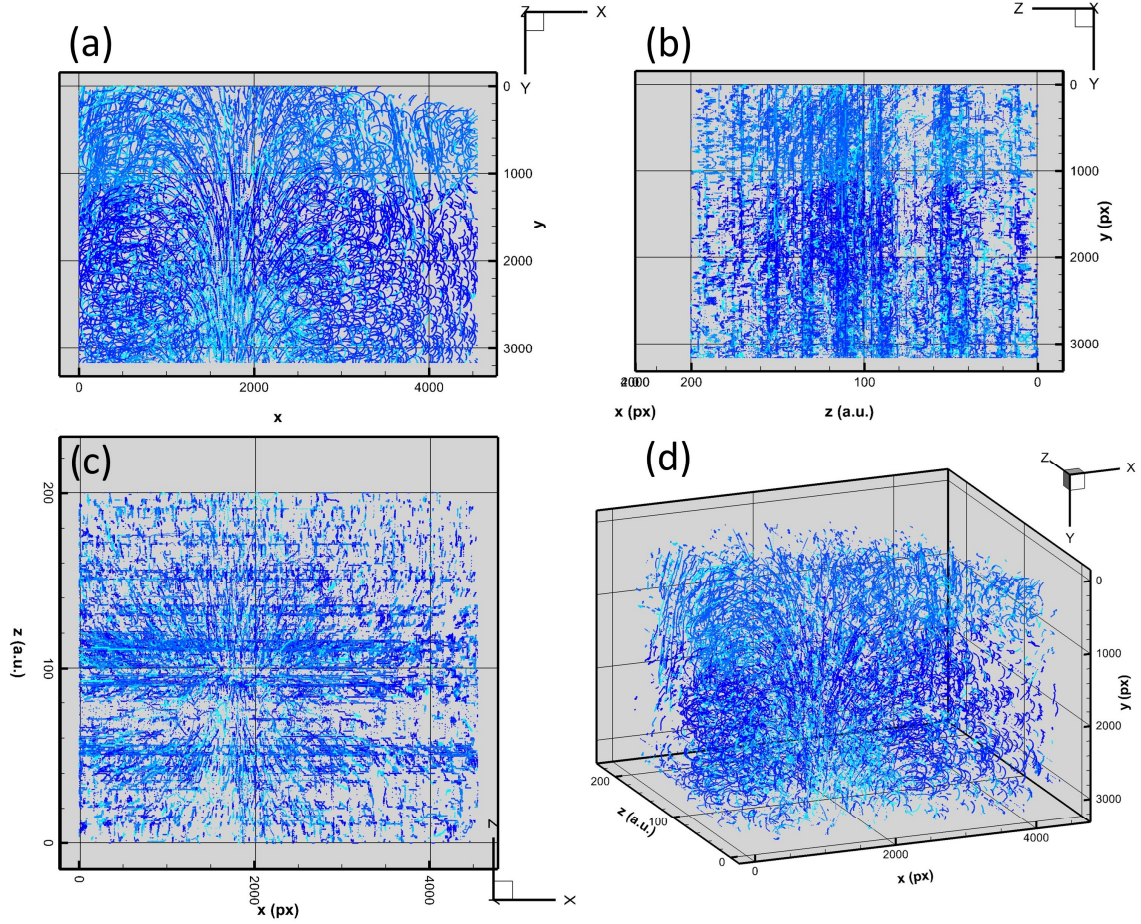


Figure 4.23. Pathlines views of every other 3 particles in the 3D result. (a)  $x'y'$  plane. (b)  $y'z'$  plane. (c)  $x'z'$  plane and (d) 3D view of the reconstructed volume. It is clear from (b) and (c) that many of the depth estimations ( $z'$ ) are biased towards certain planes.

### 4.3 Conclusions

In this chapter, we have presented an alternative technique to Tomographic PIV and 3D-PTV, where instead of recording with multiple cameras from different angles, we use a single color camera that is placed perpendicularly to a chromatic illumination system to encode the depth position ( $z'$ ). The proposed techniques, therefore, reduce the complexity of the hardware setup and eliminate the use of dangerous lasers.

We presented two iterations that use a chromatic illumination. In the first iteration, a white light source is passed through a linear color filter to produce a continuous wavelength spectrum, thus encoding the depth position of each particle in its color. However, the filter reduces the amount of light significantly on the particles, limiting the video frame rate. To circumvent this difficulty, a Diffractive Optic Element (DOE) [63] designed in-house by the Visual Computing Center (VCC) at KAUST is placed in front of the camera lens. This allowed increasing the aperture in the camera lens without reducing the depth of focus of the studied volume. Using an optimization algorithm developed by the same group, velocity fields are successfully reconstructed in three-dimensional space with a depth resolution (perpendicular to the camera plane) of 20 levels.

As a second iteration, to increase the flexibility of the illumination system, a 3-LCD color projector is used to produce color gradients perpendicular to the camera and encode the depth ( $z$ ). A high-resolution color camera record 2D trajectories of particles seeded in water. Particle tracking in 2D is carried out with the open-source program “Trackmate”. The use of the projector increases the flexibility of our illumination system and eliminates the need of a DOE due to the high-intensity light. Therefore, we can manipulate the projected color gradient profiles and even modify them in time. The projector-camera response signal is characterized and modified empirically to achieve a better signal to noise ratio. Two multiple discrete color gradients are projected in a loop, in principle providing 200 different depth levels ( $z'$ ). Experiments in a vortex ring are carried out to test the technique.

Although hypothetically this iteration was promising due to the high number of color combinations, the 3-D reconstruction is biased towards certain color detections. This reduces the intended depth resolution of 200 levels drastically. The biased color detection arises especially from the use of a Bayer filter in the color camera, therefore, losing information during the color interpolation process. Furthermore, the algorithm for the depth estimation can be further improved by implementing advanced computational techniques, such as machine learning tools [75] or neural networks[76].

For this reason, we expand further our experimentation to reduce the false-color detection. In the following Chapter, we will describe a slightly different approach using monochromatic light in a similar setup. Instead of encoding the depth in color, we intend to encode the depth position based on the intrinsic brightness of each particle.

## **Chapter 5 : Single-Camera 3-D PTV using particle intensities and monochromatic structured light (3D-IPTV)**

Similarly to the previous section, we take advantage of the time variable frame projection to structure monochromatic green light with the same 3 LCD projector. As mentioned previously, the use of monochromatic light will reduce the uncertainty of the light intensity in each pixel due to the lack of a Bayer filter. For this purpose, a monochromatic s-CMOS PCO 5.5 camera is used instead of the Red Cinema Dragon camera due to its high sensitivity. The following section has been submitted for publication to the Experiments in Fluids Journal.

In this chapter we use structured mono-chromatic volume illumination with spatially varying intensity profiles, to achieve 3D Intensity Particle Tracking Velocimetry (3D-IPTV) using a single video camera. Similarly to the system proposed in Chapter 4, the video camera records the 2-D motion of a 3-D particle field within a fluid, which is perpendicularly illuminated with depth gradients of the illumination intensity. The light-intensity field is calibrated using a 3D laser-engraved glass cube containing a known spatial distribution of 1100 defects. This is used to correct for the distortions and divergence of the projected light. We use a sequence of changing light patterns, with numerous sub-gradients in the intensity, to achieve a resolution of 200 depth-levels.

## 5.1 Experimental setup

We use the consumer LCD projector (Epson EX9200 Pro) described in 4.2.2 for illuminating particles seeded in a transparent acrylic tank, containing a BK7 glass refractive index-matched liquid. A mixture of silicone based heat transfer fluids number 510 and 710 is used as the working fluid. The motion of the illuminated particles is recorded by the 5.5 Mpx s-CMOS B/W video camera (pco.edge 5.5) with high quantum efficiency (see Figure 5.1), capable of recording images at 16-bits. This camera is placed perpendicularly to the projected illumination, as sketched in Figure 5.2. We use green light of different intensities from the projector, to minimize possible chromatic aberrations due to diffraction from the particle or through the walls of the acrylic container. The illuminated volume for the actual experiments was approximately  $60 \times 60 \times 50 \text{ mm}^3$ . One of the main advantages of using a projector for the illumination, is the flexibility of the structured light, making it simple to modify and adjust the illuminated volume size, as well as controlling the projected framerate and intensity patterns. There is, however, a trade-off between the sizes of the illuminated volume vs the brightness recorded from the particles.



Figure 5.1. PCO edge 5.5 camera used for this iteration. The camera has a high quantum efficiency which translates to high sensitivity. This camera produces 16-bit images.



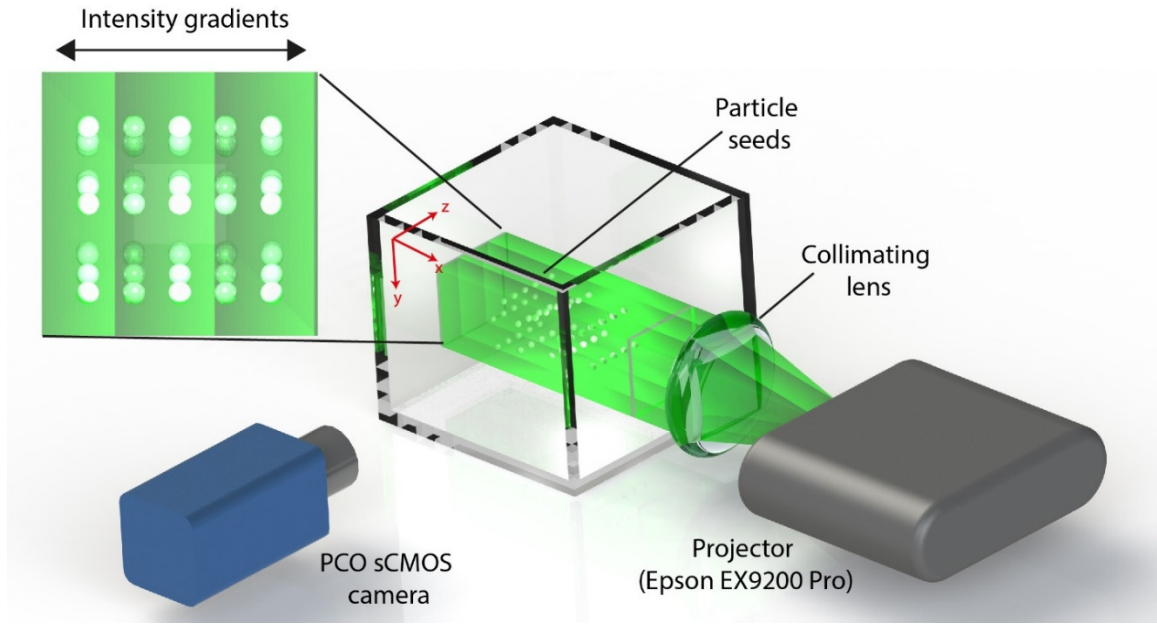


Figure 5.2. Experimental setup of the monochromatic camera and the illuminating projector. The multiple intensity gradients are produced in the depth direction with respect to the camera planes.

## 5.2 Illumination sequence

The illumination sequence used is shown in Figure 5.3. The basic principle is to change the illumination to refine the location of the particles in subsequent video images. Each illumination cycle starts with projecting a single frame of uniform lighting to calibrate the intrinsic brightness of each particle, see Figure 5.3(a). Subsequently, we include a step-like structured lighting, or discrete linear gradient over the entire depth, to get an approximate depth-location ( $L_{10}$ ) (10 sectors in this experiment), see Figure 5.3(b). The following frame is a mirrored image of the previous one to minimize any error, see Figure 5.3(c). To finish, this is followed by a stack of multiple intensity- gradients, to refine these locations ( $L_{20}$ ) (20 levels for each sector), see Figure 5.3(d). This image is projected for five subsequent frames. Thus, the projected image sequence allows us to obtain 200 digital depth levels of resolution in the z-direction, which are not visible by the camera.

The total length of the projected video sequence is 8 frames, allowing for five separate depth estimates. This illumination cycle is repeated in a loop and allows us to track particles in time. We use white polyethylene spherical particles (Cospheric) of size 125-150  $\mu\text{m}$  and a density of 1.25  $\text{g}/\text{cm}^3$ . This material has a matte surface and allows the particle to scatter enough light in order to be detected by the camera sensor, while minimizing the contamination to the signal intensity of neighboring particles. There are obviously a plethora of possibilities in the patterns and sequences projected.

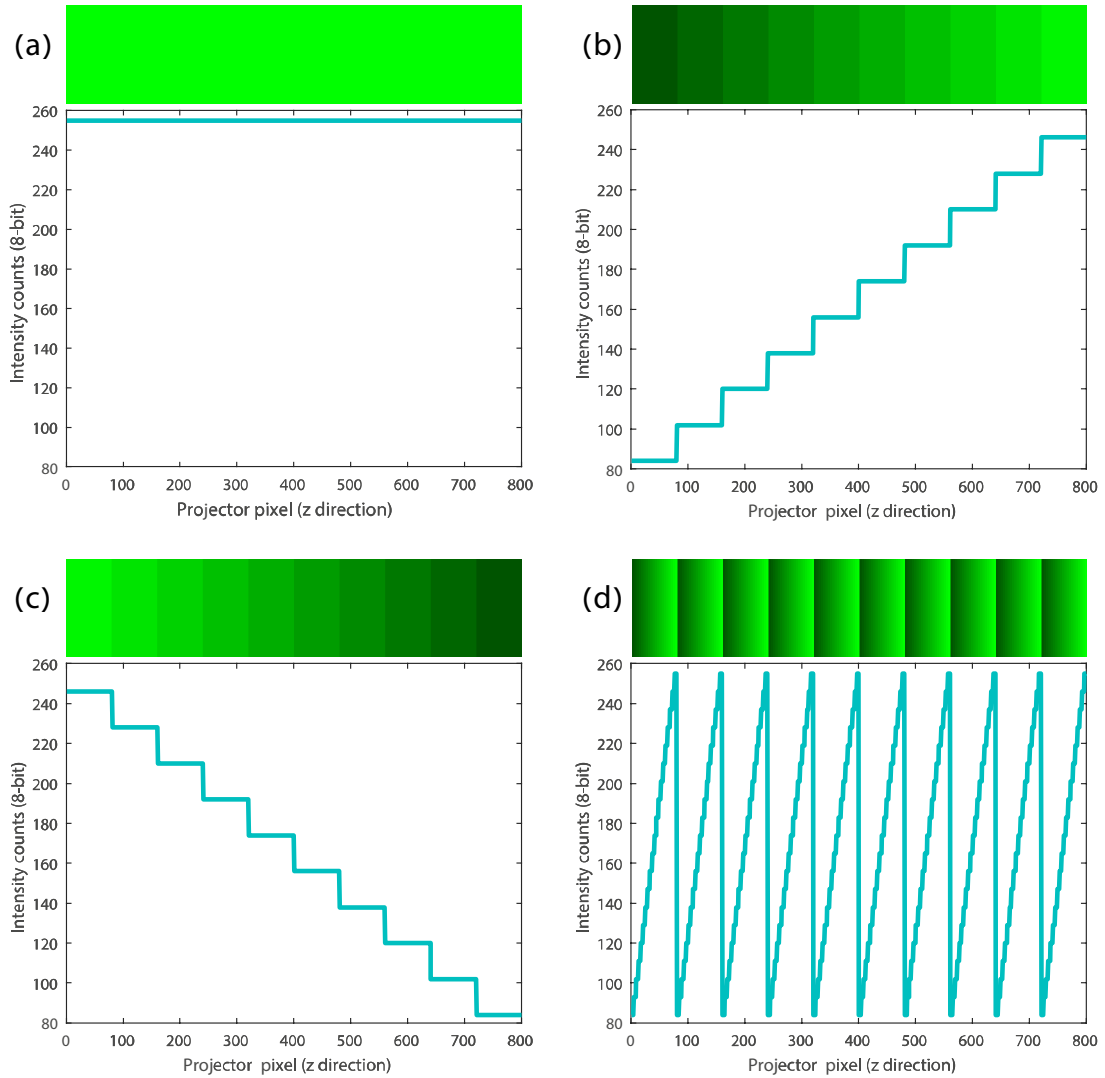


Figure 5.3. Projected images with their corresponding intensity profile. (a) Constant intensity. (b) 10 sectors of different intensities ( $L_{10}$ ). (c) 10 sectors mirrored. (d) 10 subgradients with 20 intensity levels each ( $L_{20}$ ).

## 5.3 Calibration

### 5.3.1 Light Intensity calibration with a 3-D calibration glass cube and particles

This technique relies on the intensity of light scattered by the particles. Thus, it is crucial to minimize any noise or fluctuation in the observed intensity due to size dispersion, surface roughness or imperfections of the particles. Furthermore, particles that are closer to the camera and the projector will show a higher intensity. Therefore, it is necessary to calibrate the intrinsic light intensity of each particle. First, a master light curve is produced from the statistics of thousands of particles in the field of view of the camera, with no motion applied to the fluid. A sequence of uniform intensity 8-bit images are projected, to illuminate all the particles. The response signal is recorded with the PCO camera. This is repeated for the 20 different intensity levels starting from 84 counts to 255 (the maximum counts of an 8-bit monochromatic image), these intensity levels are the same used in the gradients presented in Figure 5.3 (d). The digital 2-D planar pixels-coordinates ( $x'$ ,  $y'$ ) of the particles are obtained using software for Particle Tracking available in Fiji, Trackmate [70]. The original intended use for Trackmate was for cell detection and tracking, among other biomedical and biological applications. However, the flexibility and robustness of this program makes it a very good choice for 2-D particle tracking in a flow field. The main detection algorithm is based on the Laplacian of Gaussian segmentation. The particle-linking algorithm is based on the Linear Assignment Problem created by Jaqaman et al.[71] In this way, many of the features of every single particle can be measured, such as the effective particle intensity ( $I_o$ ) and the maximum intensity pixel ( $I_{max}$ ) within each particle for every illumination intensity level. Such parameters

are described in further detail in section 5.3.2. The response signal for each particle at all levels is then normalized by the value obtained when the image of 255 counts is projected. The mean response signal (see next subsection) and a second degree polynomial fit are presented in Figure 5.4, as well as their standard deviation dispersion. This curve serves primarily to calibrate the projector-camera intensity response, thereby allowing us to determine the depth level ( $z'$ ) in which the particle is contained using the algorithm described in 5.4.1.

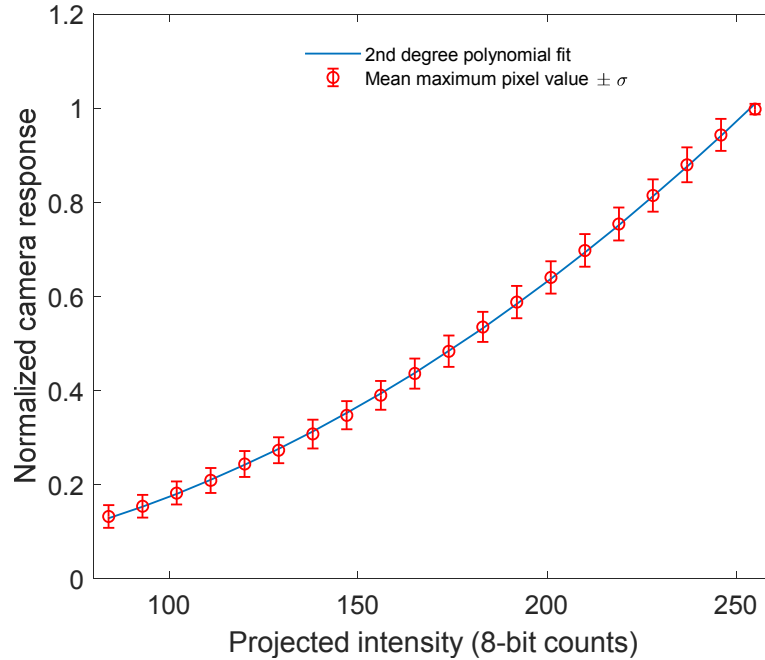


Figure 5.4. Typical projector-camera system response obtained from a real particle field. Error bars represent  $\pm\sigma$  (std. deviation). The solid lines represent a typical master curve used for light intensity calibration.

### 5.3.2 Intensity of Isolated Particles

To test the potential of this technique, we illuminate a slowly moving field of a few particles with a uniform volume illumination. This is used to quantify how constant the scattered light from individual particles remains as their images are shifted over pixel

boundaries on the s-CMOS sensor. Figure 5.5 shows a sequence of real pixel intensities for a typical particle. It shows clearly how the distribution of intensities spreads among the pixels, making them vary strongly from frame to frame. For this randomly selected particle in Figure 5.5, the peak 8-bit pixel intensities take the following values: 176, 188, 170, 183, 187, 175, 187, 186 & 190 varying over a min-max range of  $\simeq 11\%$ . The effective particle intensity must, therefore, be estimated from a weighted integral of over the particle area, thereby incorporating both its intensity  $C$  and  $R$ . We fit the intensity-profile of each particle with a 2-D Gaussian shape:

$$I(x, y) = C e^{-\frac{x^2+y^2}{R}}$$

From where:

$C$ : Is the central Intensity of the particle

$R$ : is the radial width of the particle

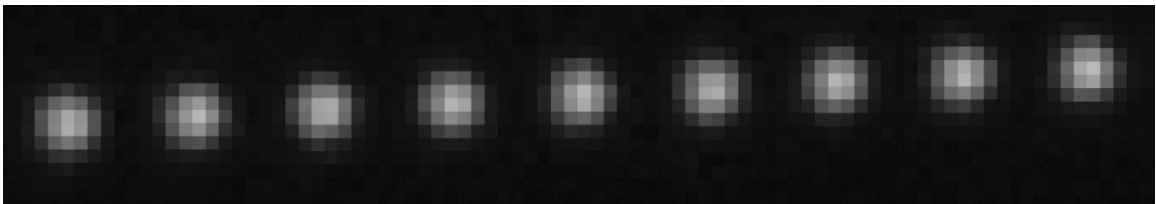


Figure 5.5. Typical Intensity signature of a random particle, this particle is shown over 9 consecutive video frames with a uniform projected illumination. The radial width ( $R$ ) of the particle is approximately  $R \approx 2$ .

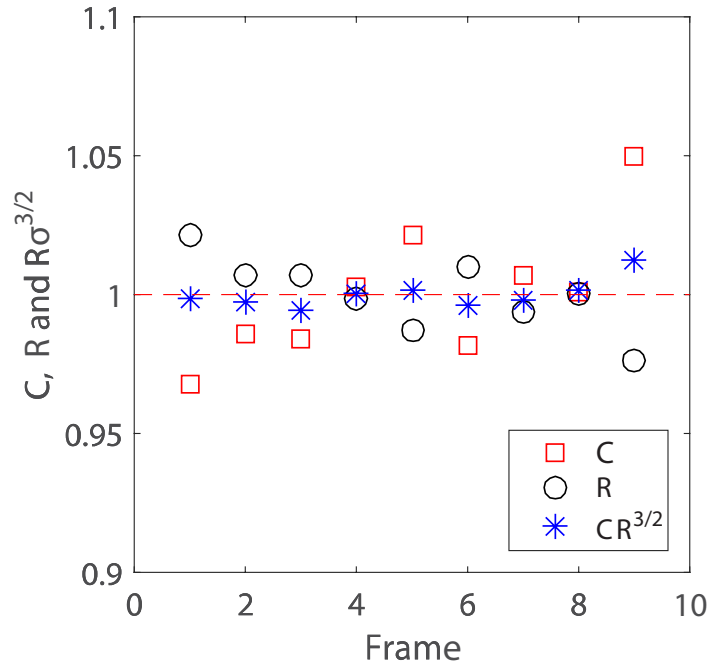


Figure 5.6. The best fit values of  $C$ ,  $R$  and  $C R^{3/2}$  for the particle in Figure 5.5 over 9 consecutive frames with uniform illumination. The values are normalized by their corresponding averages.

This profile is fit by shifting the sub-pixel peak location  $(x_o, y_o)$  and adjusting the magnitude  $C$  and width  $R$ . The least-square best fit only uses pixels around the peak, where the intensity exceeds a certain threshold. Figure 5.6 shows these best fits for  $C$  and  $R$  following this particle over a number of subsequent video frames. As expected the peak intensity and the width are anticorrelated. However, empirically we find the best intensity estimate by combining the central intensity and the image width as

$$I_o = C R^{\frac{3}{2}}$$

From where:

$I_o$ : Is the effective particle intensity

$C$ : Is the central Intensity of the particle

$R$ : is the radial width of the particle

Repeated tests show that the variation of this quantity is within bounds of  $\pm 2\%$ . Theoretically, with 10 subgradients of the illumination intensity, we should be able to distinguish 250 depth levels for the particles.

### 5.3.3 3-D spatial Calibration cube

In this section, we describe the correction for the projector light divergence and perspective distortion. In order to calibrate the real space coordinates  $(x, y, z)$  from the projected frames and correct lens distortions, a 3D calibration cube of  $80 \times 80 \times 80 \text{ mm}^3$  is designed in-house. We take advantage of the flexibility to design and produce a 3D array of micro-cracks in 10 different planes, containing 110 micro-cracks each. Each plane is rotated with respect to the previous one by  $32.7^\circ$  in order to ensure that no other crack will block the illumination from the projector, nor block it from the camera. This allows us to simulate a static particle field of 1100 particles, as shown in Figure 5.7.

The first iteration of this artificial particle field is fabricated using a Laser cutter/engraver on PMMA. Several layers of a 5 mm thickness PMMA are engraved and cut. Subsequently, the PMMA layers are stacked together and placed in an oven at  $150^\circ\text{C}$  (slightly higher than the Glass transition temperature of the PMMA), to fuse the layers together and form the 3D structure[77]. The main disadvantage for this technique is the minimal control over the heating and cooling rates, which can distort the geometry. As well, it is very difficult to remove trapped air bubbles at the layers interface. A test light

projection for this iteration is shown in Figure 5.8; large trapped air bubbles are clearly observed and affect the material refractive index.

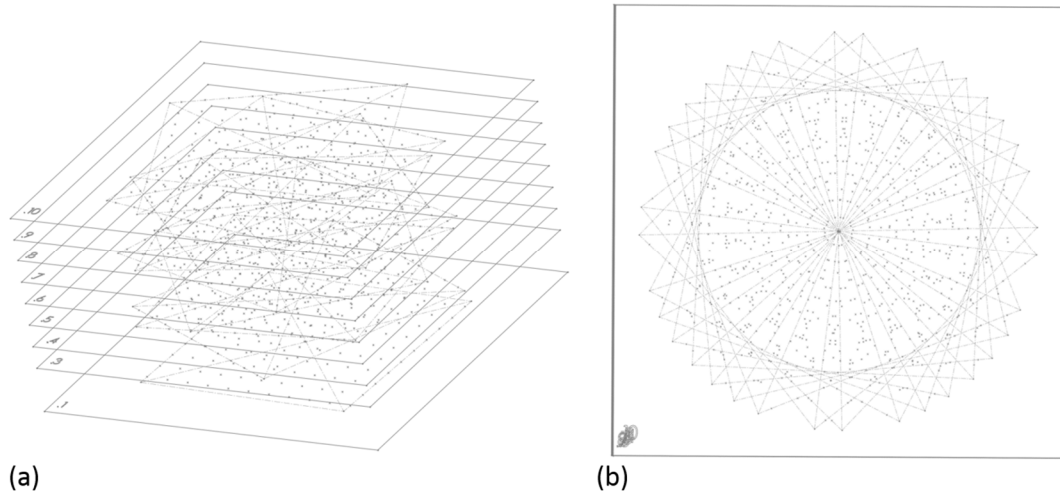


Figure 5.7. Design of a 3D calibration dotted pattern in (a) 3D view and (b) top view. Auxiliary lines are visible.

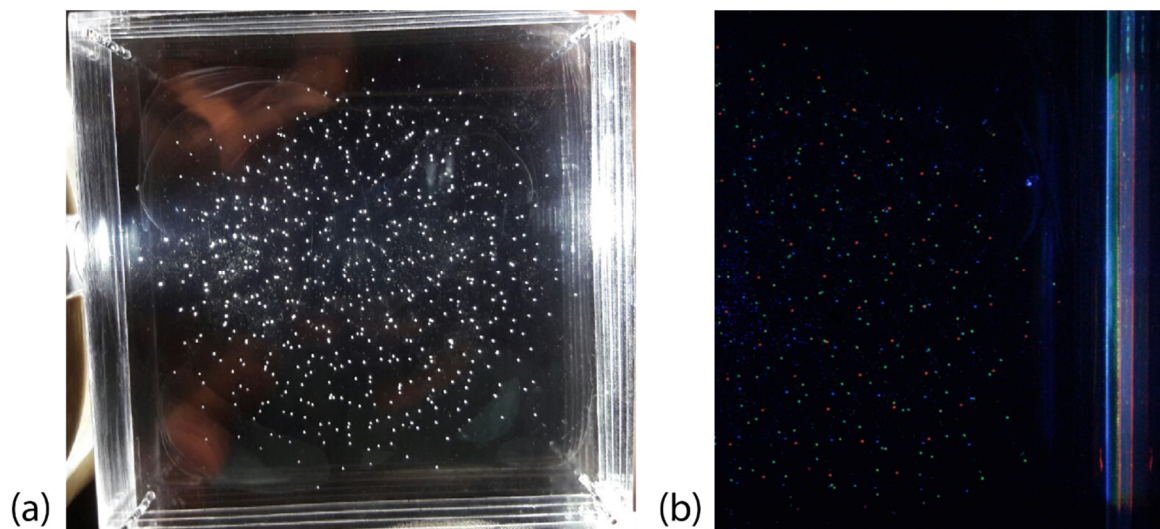


Figure 5.8. (a) 3D pattern in PMMA, illuminated by a white light, notice the air bubbles trapped during the bonding process. (b) Color gradient test with the projector, notice the planes clearly delimited by different colors or RGB values.



As a second iteration, we use a 3D laser engraved crystal. The 3D laser engraving process in glass is a well-known industrial process used for the production of trophies, rewards, and souvenirs. It consists of a high power laser that produces micro cracks in a structured way inside the glass where the focal point of the laser is placed. The material of the cube used herein is BK7 optical glass, which has a refractive index of 1.519 at 20 °C and a wavelength of 527 nm [78]. We, therefore, reproduce the same design as the PMMA case in the glass avoiding the previous bubble problems (see Figure 5.9).

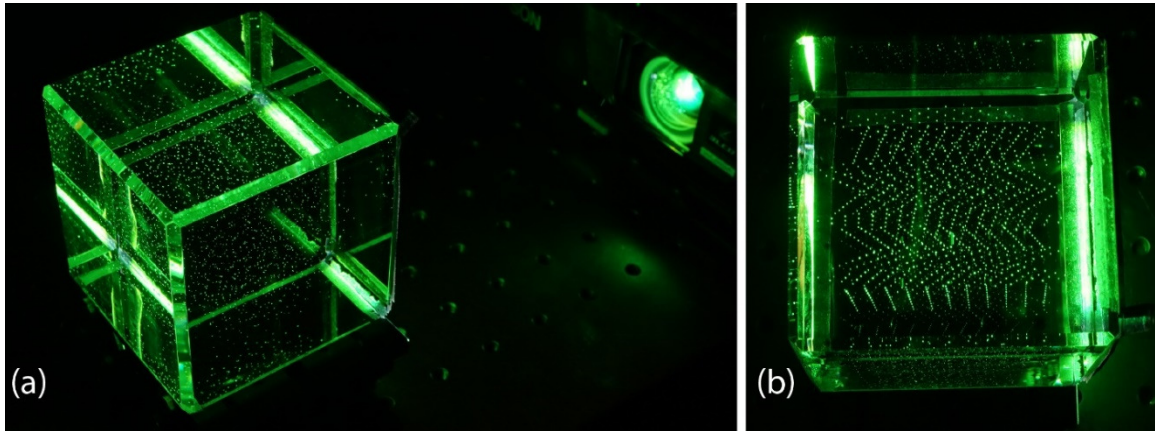


Figure 5.9. (a) Real cube illuminated by the projector. (b) Top view of the cube showing the multiple planes present in the cube

A light intensity calibration (described in the previous section) is applied using the same 20 intensity levels to obtain the digital depth position ( $z'$ ) implementing the algorithm described in section 5.4.1. The digital coordinates ( $x', y'$ ) with subpixel accuracy of the particles in the cube are obtained using Trackmate. Subsequently, the video sequence with multiple frames and gradients (see Figure 5.3) is projected in the static cube the same way as it is done for the real particle field. Both calibrations (light intensity and spatial calibration) allow us to reconstruct the 3D pattern of the cube simulated particles, see Figure 5.10. Subsequently, a 3-D mapping function is obtained to correct

distortions and connect the digital space coordinates  $(x', y', z')$  to real space coordinates  $(x, y, z)$  as described in section 5.4.2.

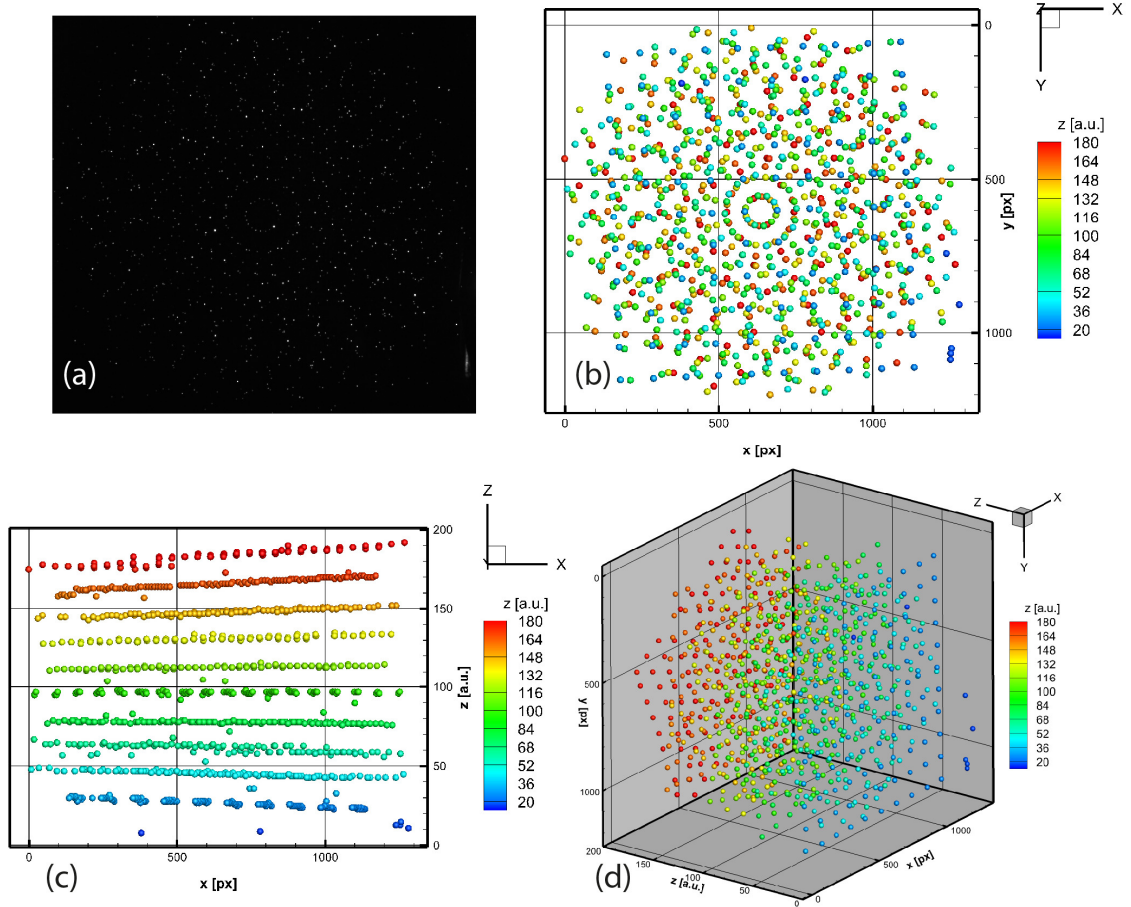


Figure 5.10. (a) Typical frame from the PCO camera of the calibration cube illuminated by a uniform intensity frame. Note the different intensity levels for each particle. (b) XY view of the cube reconstruction. (c) XZ (top view) of the cube reconstruction. Note the volume distortion due to the projection divergence. (d) 3D view of the reconstructed cube, particles are colored by their depth position ( $z'$ ).

## 5.4 Computational algorithm

### 5.4.1 Obtaining the depth position $z'$

In order to obtain the depth position ( $z'$ ) for every particle, it is necessary to analyze its recorded intensity in space and time. For the current setup, the particles are not of uniform size, having a range  $\sim 4 - 8$  pixels in diameter. Therefore, we compare three

different parameters within each particle: maximum pixel intensity ( $I_{max}$ ), Gaussian-weighted average intensity ( $I_w$ ) and the effective particle intensity ( $I_o$ ) defined in section 5.3.2. First, these parameters are normalized with the maximum value of each illumination cycle. This allows us to quantify the intrinsic intensity for every single particle during multiple illumination cycles and thereby deduce the corresponding depth position. A plot comparing the statistical dispersion as Mean Absolute Deviation (MAD) in a light intensity calibration of the above parameters is presented in Fig. 8. The MAD is defined as:

$$MAD = \frac{1}{N} \sum_{i=1}^N |I_i - \bar{I}_i|$$

From where:

$N$ : is the number of sampled particles

$I_i$ : is the parameter being studied ( $I_{max}$ ,  $I_w$  or  $I_o$ )

$\bar{I}_i$ : is the mean of that parameter

The MAD measure of variability is used since it is more robust in identifying the parameter that produces the smallest error deviation, thereby being more resilient to outlier data points and assigning more weight to the data points closer to the fit. From Figure 5.11 we can clearly see that  $I_o$  presents the lowest dispersion values. Therefore,  $I_o$  is the parameter of choice to continue, providing a low error reconstruction. Hence, a master light curve using  $I_o$  is obtained as described in section 5.3.1.

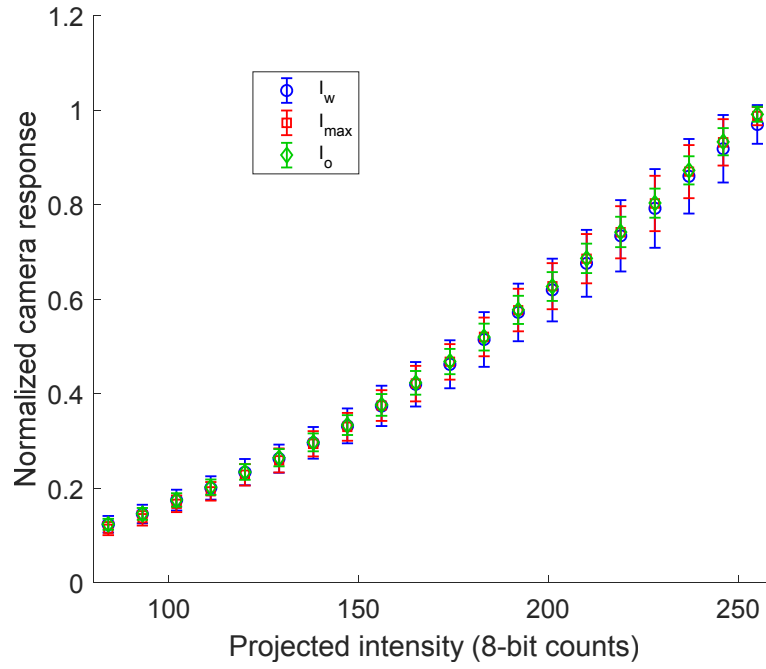


Figure 5.11. Comparison of the mean camera response with three different parameters  $I_w$ ,  $I_{\max}$  and  $I_o$ . The total length of the error bars represents two times the Mean Absolute Deviation (MAD) around the mean response value.

We now describe the general algorithm used to determine the depth  $z'$  of each particle. A Flow-chart summarizing the process is provided in Figure 5.22. Each particle is assigned to a bin depending on its  $I_o$  value at every projected frame. Such bins are created based on the theoretical camera response obtained by the light calibration curve shown in Figure 5.4. In the first video frame (Figure 5.3a) a solid green color is projected to calibrate the intrinsic intensity of the particle, thus, it does not require a bin. For the second video frame (Figure 5.3b), 10 equally distributed bins are created with their midpoints ( $I_{mid}$ ) starting from 84 to 255 intensity counts in steps ( $2\delta_s$ ) of 18 counts, after normalization by the maximum intensity of an 8-bit image (255 counts). The upper and lower limits are defined by  $Lim = I_{mid} \pm \delta_s$ . The third projected frame (Figure 5.3c) is

a mirrored version of frame 2. Frame 4-8 (Figure 5.3d) consist of 20 bins (84-255 counts) with  $2\delta_s = 9$  counts.

Every particle is then allocated to the corresponding depth bin ( $L_{10}$  for projected frames 2 and 3 and  $L_{20}$  for projected frames 4-8) at every recorded video frame by evaluating the master light curve (see section 5.3.1) with the detected  $I_o$ .

It is important to mention that LCD projectors have a transition time between projected frames. Therefore due to the unsynchronized camera-projector system, one can notice a periodical single transition frame recorded with the PCO camera for every projected frame. This frame is neglected for the depth estimation, however 2D information of the particles in those frames is evaluated. In future implementations, this transition frame can be eliminated with appropriate synchronization and exposure timing. One of the main advantages of oversampling the projected video frames (four frames in the recorded video at, 60 fps, represent one projected frame at 15 fps) is that we can use temporal statistics for correcting spurious depth estimations in  $L_{10}$  and  $L_{20}$ . These spurious depth estimations are mainly due to overlapping particles, as seen in Figure 5.12, where clear deviations occur intermittently, when the tracking jumps to erroneous particles. In order to fully define the digital depth position  $z'$  at any time it is necessary to define  $L_{10}$  and  $L_{20}$  for every particle at every time. Therefore, if the statistical mode frequency of  $L_{10}$  from projected frames 2 and 3 is  $Mo(L_{10}) \geq 4$ ,  $L_{10}$  is defined during that illumination cycle. Additionally if  $\max(L_{20}) - \min(L_{20}) < 10$ , i.e., when the particle stays in the same  $L_{10}$  bin,  $L_{20}$  is defined and the digital depth ( $z'$ ) can

be initially estimated for that particle and illumination cycle. This is valid for particles which do not have very high velocities in the depth direction ( $z'$ ).

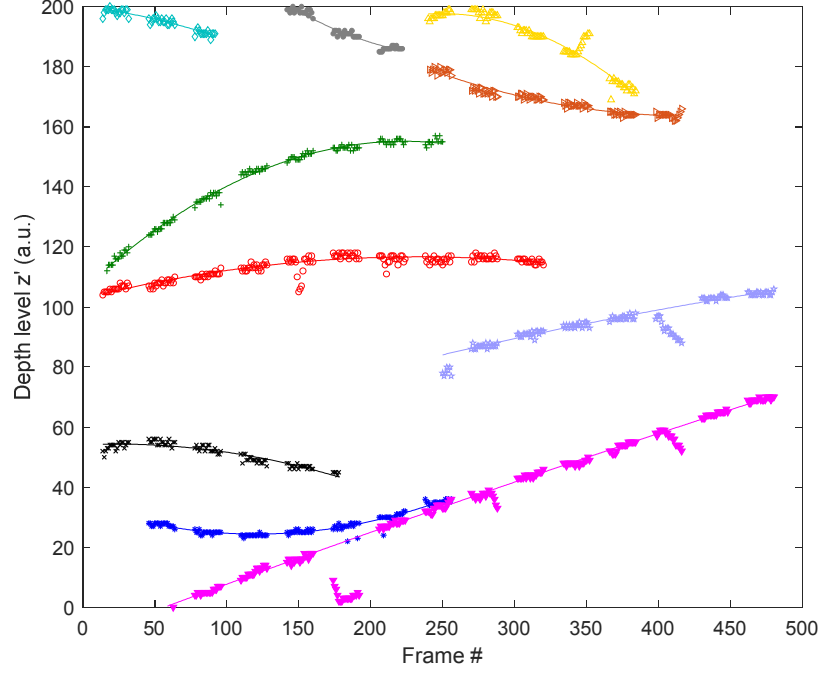


Figure 5.12. Estimated depth ( $z'$ ) vs Frames in time for different particle trajectories. The solid line of each trajectory represents the polynomial fit of the depth while the markers show the initially estimated depth. Note that erroneous depth detection is corrected during this process.

However, if  $\max(L_{20}) - \min(L_{20}) \geq 10$  for a single illumination cycle, it is assumed that the particle has crossed the boundary of a bin in  $L_{10}$ . Therefore, to establish the depth in those cases, it is necessary to look into the last and first few frame levels ( $L_{10}$  and  $L_{20}$ ) from the previous and next illumination cycle respectively. The linkage of temporal information allows us to define most of the remaining depth positions for every particle.

Furthermore, the initial estimation of the  $z'$  component of the particle trajectories is refined by a bisquared weighted least-squared fitting  $z' = f(t)$ . This iterative fitting

method assigns smaller weights to the positions that are far away from the original fit. The quadratic polynomial fit is obtained for every single particle. A comparison of a few particle trajectories vs the quadratic polynomial fit are shown in Figure 5.12. The few outliers do not significantly distort the true trajectory. The particles that are moving into the test volume, during the frames with the finest intensity gradients, can be dealt with by tracking them backwards in time, starting from subsequent uniform lighting.

#### 5.4.2 Mapping functions: from digital $(x', y', z')$ to real world coordinates $(x, y, z)$

Here we describe the mapping from digital space  $(x', y', z')$  to real space coordinates  $(x, y, z)$ . Using the data collected in section 5.3.3, it is observed that the reconstructed cube has distortions due to the divergence of the illumination and lens aberrations (see Figure 5.10 c). Therefore, we can link the digital coordinates with the real space using the known coordinates of the particle field of the cube. It is assumed that the real space coordinate  $z = f(x', z')$ , since the projected light is vertical and the pattern projected does not vary in the vertical axis  $y$ . The mapping function is obtained by a bisquared weighted polynomial 3-D surface fit of degree 2 in  $x'$  and  $z'$ . The polynomial model is presented in the following equation:

$$z(x', z') = a_0 + a_1x' + a_2z' + a_3x'^2 + a_4x'z' + a_5z'^2$$

The polynomial coefficients of this equation are summarized in Table 3. A 4-D nonlinear regression fit is used for mapping  $x = f(x', y', z)$  and  $y = f(x', y', z)$  as specified in the following model equations:

$$x(x', y', z) = a_0 + a_1x' + a_2y' + a_3z + a_4x'^2 + a_5y'^2 + a_6z^2 + a_7x'y' + a_8x'z + a_9y'z$$

$$y(x', y', z) = a_0 + a_1 x' + a_2 y' + a_3 z + a_4 x'^2 + a_5 y'^2 + a_6 z^2 + a_7 x' y' + a_8 x' z + a_9 y' z$$

The coefficients for each approximation are presented in Table 3. A flowchart summarizing the algorithm process for the 3-D reconstruction is presented in Figure 5.22, the Matlab code created is presented in appendix A 3-8. After applying the mapping functions in the cube (see Figure 5.13) we find that the error in the 3-D reconstruction of the cube has an  $|RMS_e| = 0.273 \text{ mm}$ , where the depth component of the error ( $e_z$ ) is the greatest component with  $RMS_{e_z} = 0.271 \text{ mm}$ . This value represents approximately 0.5% of the 50 mm depth from the reconstructed volume or approximately the size of a single depth level.

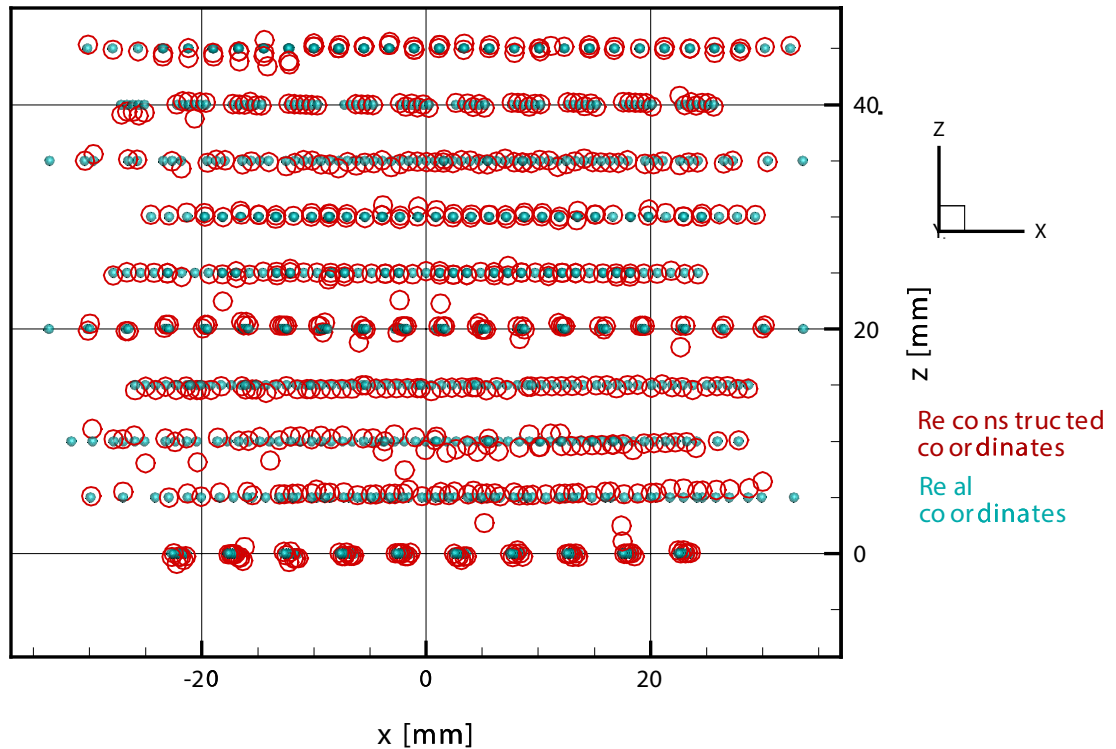


Figure 5.13. Top view (x, z) of the corrected reconstruction (red) of the calibration cube after applying the mapping functions. Real coordinates of the reconstructed cube (cyan).



	$z(x', z')$	$x(x', y', z)$	$y(x', y', z)$
<b>a0</b>	-10.0869	-29.9733	-28.4576
<b>a1</b>	0.0025	0.0470	8.22E-06
<b>a2</b>	0.3191	0.0001	0.0474
<b>a3</b>	5.61E-07	-0.0570	-0.0570
<b>a4</b>	-3.58E-05	1.75E-07	-5.96E-08
<b>a5</b>	-3.40E-05	8.90E-09	-1.32E-07
<b>a6</b>	---	2.10E-05	-3.13E-05
<b>a7</b>	---	3.78E-08	-1.21E-10
<b>a8</b>	---	9.02E-05	4.09E-07
<b>a9</b>	---	2.62E-07	9.09E-05
<b>RMSe (mm)</b>	0.2714	0.0263	0.0181
<b>R2</b>	0.9998	0.9999	0.9999

Table 3. Mapping functions polynomial coefficients and goodness of fit data.

## 5.5 Tracking results

### 5.5.1 Experiments in a rotational flow

We produce a rotational flow in a tank full of a heat transfer fluid mix with a disc attached to a controllable speed motor (Von Karman pump), as depicted in Figure 5.14. The liquid is seeded with white polyethylene particles. The acrylic tank of 120 x 120 x 250 mm<sup>3</sup> is filled with a mixture of heat transfer fluid 510 and 710. The refractive index of the mix is 1.515 measured at 22 °C. This is to match the refractive index of the BK7 calibration cube.

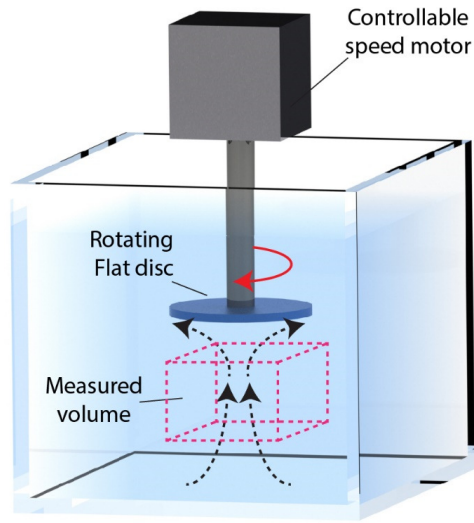


Figure 5.14. Schematic drawing of a von Karman pump. The studied region of the flow is enclosed in the magenta dashed box.

Firstly, the light intensity calibration is carried out as described in section 5.3.1. The motion of the particles is tracked using “Trackmate” software. Providing us with the 2-D digital coordinates  $(x', y')$  with subpixel accuracy, as shown in Figure 5.15. Spatial calibration using the crystal cube is carried out as described in section 5.3.3. The disk is rotated at 60 rpm and the 2D trajectories in time allow us to obtain the intensity profile for every particle in each recorded frame. Thus, using the algorithm described in section 5.4.1, we can obtain the corresponding depth position ( $z'$ ). The 3-D spurious reconstructions are filtered to the ones that have a  $z'(t)$  polynomial fit with  $R^2 > 0.9$ , described at the end of section 5.4.1. Subsequently, the mapping function defined in section 5.4.2 is applied to the digital coordinates  $(x', y', z')$  to transform them to the real world coordinates  $(x, y, z)$ . See Figure 5.16 a-d. An animated video of the 3-D pathlines is presented in Supplementary video S3.

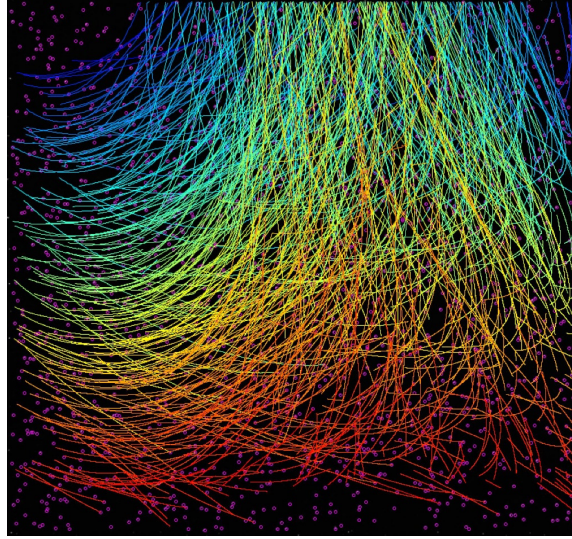


Figure 5.15. 2-D projection of the 3-D particle pathline obtained with Trackmate. The rotating plate is 15 mm above the top of the image. The colors are fixed for each particle. The width of the image spans  $\approx 60$  mm inside the tank.

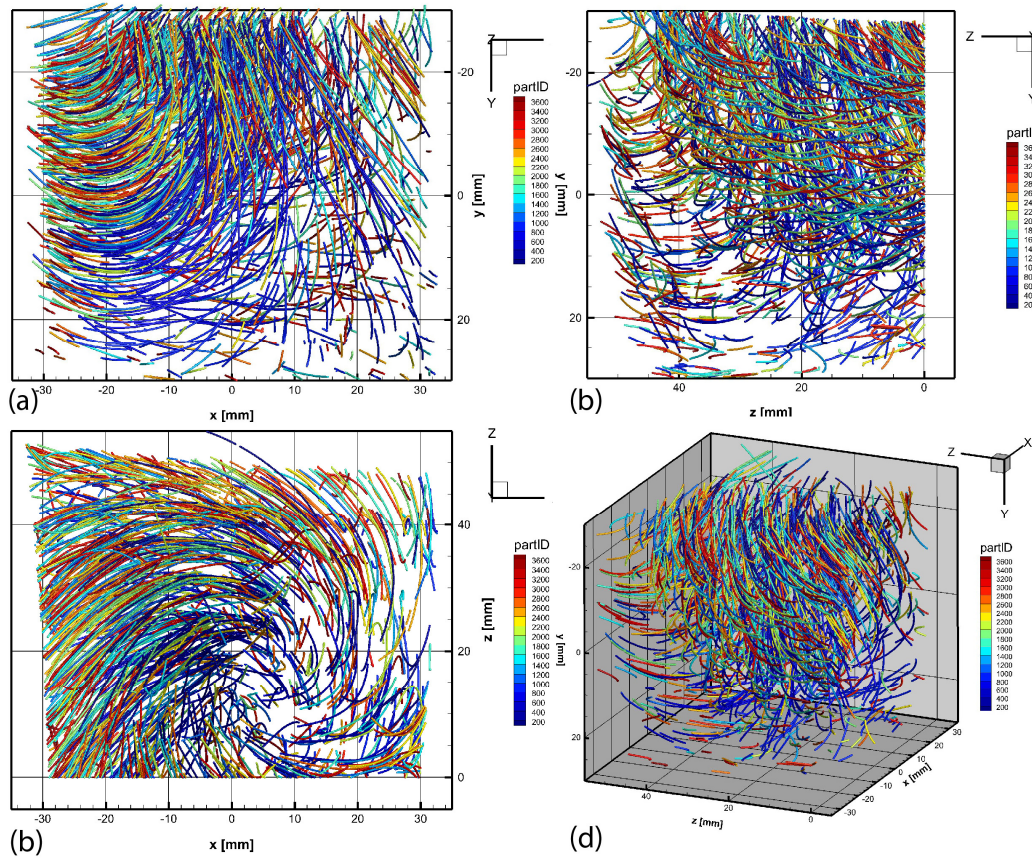


Figure 5.16. Reconstructed rotating flow pathlines of 960 unique particles. (a) xy view. (b) yz view. (c) xz view (top) view. (d) 3D view of the pathlines. Note that (b) and (c) views are not visible by the camera.

## 5.6 Conclusions

Herein, we have demonstrated the implementation of Intensity 3-D PTV with a single monochromatic s-CMOS video camera and a consumer grade LCD projector as a light source. We reconstruct and track particles in 3-D inside a liquid by structuring the projected light, with numerous depth gradients in intensity. This new methodology increases the depth resolution of previous single camera 3-D PTV systems dramatically, up to 200 levels, while increasing the reconstructed volume size and at the same time minimizing the complexity of the hardware setup. This increment in resolution represents up to an order of magnitude higher than previous attempts.

Conceptually, this technique is very simple and in principle, using a fast high-sensitivity low-noise camera, one could achieve finer depth-levels than the in-plane pixel spacing. This will, however, be more dependent on the quality of the structured light, than the sensor sensitivity.

It remains to optimize the illumination sequence since numerous possibilities can be tested. This technique can be further tested by experimenting with higher framerates for turbulent flows. However, the light engine capabilities used in that case will be crucial for obtaining accurate results. The challenge, in this case, is to develop or adapt a high-power light intensity projector or laser system in order to produce fast refreshing rate images. For instance, if a recording of 1000 fps is used, the necessary projection framerate would be at least  $\frac{1}{4}$  of that (250 fps) with the currently proposed illumination sequence.

Digital Light Processing (DLP) projectors are available, where Digital Micromirror Devices (DMD) are used (Arrays of micromirrors, where each micromirror represents a single pixel projected). Such mirrors are flipped by piezoelectric actuators to turn them on and off at very high frequencies. However, this type of grade consumer projectors has limited light intensity compared to LCD ones. Perhaps, modifying their light engine with a high power laser may yield satisfactory results, but one has to keep in mind that high power lasers may require an appropriate cooling system to avoid damage on the DMD.

## SUMMARY AND OVERALL CONCLUSIONS

Tomographic PIV is becoming the preferred technique for 3D quantification of turbulent flow fields. However, the hardware required for tomographic PIV is prohibitively expensive, primarily due to the need for multiple high-resolution CMOS or CCD cameras as well as a powerful pulsed light source, which can illuminate a volume of the flow regime. For a conventional Tomographic PIV system, the hardware represents the greatest cost. For instance, a system comprising four dual frame CCD cameras (only capture two frames at a high frequency), a 200 mJ double pulsed laser which provides enough power to illuminate a similar volume size to the experiments presented in this Thesis, a time unit control and optical components to produce laser volumes could sum up to \$ 200,000 USD. Therefore, Tomographic PIV is accessible only to a minority of research institutions or corporations, limiting experimental research in fluid mechanics worldwide.

Additionally, the illumination system is usually accomplished with lasers, which are expensive and additionally pose safety issues in the lab. The operations, synchronization, and control system are also not trivial. Finally, the software required to reconstruct the 3-D particle distribution and calculate the velocities through cross-correlations demands specialized algorithms which are still being optimized to overcome the tremendous computational cost.

In this work, we have demonstrated the feasibility of using simpler and lower costs systems than the traditional ones used for 3D-PTV or Tomographic PIV. Firstly, we

produced comparable results to a dual frame CCD tomographic camera system (not high-speed), using four Nokia smartphones in a tomographic setup. The laser illumination is replaced with a set of colored high-power LED's. This proposition is expanded to a time-resolved and high-speed Tomographic PIV using four Xperia™ XZ premium. In this iteration, we are capable of measuring the velocity field of a vortex ring for approximately 60 ms at a frequency of 960 Hz. In both cases, the overall cost of the hardware does not exceed \$6,000 USD which represents a reduction of 3,300 % of a conventional system that is not high-speed . Further reduction on the cost of these systems can be achieved by using in-house made LED drivers and using open source hardware to design a pulse generator for synchronization. A comparison with high sensitivity and high resolution camera systems show that the proposed techniques have great potential for industrial, scientific and educational applications. Especially in applications where extreme accuracy in the results can be traded off with cost.

One of the main limitations faced here is the lack of exchangeable lenses and fixed aperture in the smartphones optics. However, magnifying lenses are already beginning to appear on smartphone cameras and will soon allow their application in more general configurations. Another limitation we encountered herein, is the multiple phone camera sensor synchronization. This will become even more critical if one uses the video capabilities of these cameras, which are improving rapidly, both in pixel resolution, as well as higher frame-rates for “slow-mo” recording [79]. Using previously synchronized internal clocks, or even the GPS signal clock might overcome this problem.

Herein, we have used smartphone cameras to acquire the images and subsequently transferred them to dedicated computers running specialized LaVision software to extract the 3-D velocities. One can envision taking advantage of the growing computing power of the smartphones themselves for the data reduction. Therefore, a full portable tomographic-PIV system may become feasible in the near future for industrial, scientific and educational applications.

The viability of a simpler approach was also demonstrated in this work using single camera systems (chromatic and monochromatic) for reconstructing individual particles 3D flow paths. The use of fewer hardware components directly reduces the complexity and time consumption of the hardware setup. Additionally, using conventional consumer electronics projectors for generating the required structured light, lowers the entry bar for industry and research groups not familiar to these flow visualization techniques. By using a consumer grade projector as our light source, and reducing the number of cameras the cost is reduced by at least 75%. However, this cost reduction is just an estimate, and a more detailed costs determination should be done. Moreover, the computing power required to reconstruct a relatively high-density particle is also drastically reduced.

The main purpose of using consumer electronics to replace specialized equipment in this work, is to exploit the economics of scale by piggy-backing on the hundreds of millions of consumers using projectors, smartphones or consumer grade cameras. The nature of electronics mass production reduces the cost of consumer products by a



hundred-fold, compared to specialized scientific instruments. Therefore, our proposed techniques will enable industrial, scientific and educational institutions to access experimental techniques for 3-D flow visualization previously out of reach due to the complexity or extremely high-costs associated with the hardware required. Thus, expanding the use of three-dimensional visualization and measurement techniques for applications in energy, biological, engineering and medical fields.

### **Future work**

In principle combining both techniques proposed in Chapter 2 and 3 could allow us to triple the framerate and number of frames captured with the high-speed camera system (i.e., 540 frames and 2880 fps video). Additionally, using 4k-video and frame-straddling offers tantalizing new opportunities to increase temporal and spatial resolution.

Similarly, a combination of the techniques in Chapters 4 and 5 would increase the spatial resolution in the depth direction with the possibility of creating a single depth level per pixel column of the projector. To increase the temporal resolution of this technique, high frame-rate or Digital Light Processing (DLP) projectors could be used to refresh the projected frames at a higher frequency such as the “Dynaflash” projector used for three dimensional reconstruction of a single moving rigid object by Maruyama, M., et al. [80]. This kind of technology offers new opportunities to further improve the proposed techniques in this work.

Additionally, our group, in collaboration with the “Condensed Matter Physics Laboratory” in UCI managed by Prof. Peter Taborek, started doing experiments on superfluid Helium with a cryostat designed and constructed in the University of California, Irvine. An excellent application for the single camera systems, proposed in Chapters 4 and 5, is the 3D reconstruction of Quantum vortices present in superfluid Helium IV. In this case, the use of lasers and multiple optical access windows is not practical because of the heat load this condition provides to the cryostat used to generate superfluid Helium. We therefore, propose the use of the techniques proposed in this Dissertation to circumvent these problems. A schematic representation of the proposed experiment is presented in Figure 5.23.

The ultimate goal of the experiments with tracer particles seeded in superfluid Helium IV, is to map the 3D behavior of the particles trapped in the quantum vortices cores. The proposed single camera system, in principle, will allow the system to achieve very low base temperatures  $\sim 1.2$  to  $1.3$  K. Imaging experiments in this regime are very scarce or non-existent to the best of our knowledge, even for 2D. If these experiments can be implemented successfully, they may open-up a new wave of scientific advancements in the understanding of superfluid Helium, superconductors and even in the Quantum Computing field.

## REFERENCES

1. Adrian, R.J., Particle-Imaging Techniques for Experimental Fluid Mechanics. Annual Review of Fluid Mechanics, 1991. 23(1): p. 261-304.
2. Westerweel, J., G.E. Elsinga, and R.J. Adrian, Particle image velocimetry for complex and turbulent flows. Annual Review of Fluid Mechanics, 2013. 45: p. 409-436.
3. Willert, C.E. and M. Gharib, Digital particle image velocimetry. Experiments in Fluids, 1991. 10(4): p. 181-193.
4. Prasad, A.K., Stereoscopic particle image velocimetry. Experiments in fluids, 2000. 29(2): p. 103-116.
5. Hori, T. and J. Sakakibara, High-speed scanning stereoscopic PIV for 3D vorticity measurement in liquids. Measurement Science and Technology, 2004. 15(6): p. 1067.
6. Elsinga, G.E., et al., Tomographic particle image velocimetry. Experiments in fluids, 2006. 41(6): p. 933-947.
7. Atkinson, C. and J. Soria, An efficient simultaneous reconstruction technique for tomographic particle image velocimetry. Experiments in Fluids, 2009. 47(4): p. 553.
8. Discetti, S., et al., On a novel low cost high accuracy experimental setup for tomographic particle image velocimetry. Measurement Science and Technology, 2013. 24(7): p. 075302.
9. Geoghegan, P., et al., Time-resolved PIV measurements of the flow field in a stenosed, compliant arterial model. Experiments in fluids, 2013. 54(5): p. 1-19.
10. Hagsäter, S., et al., Investigations on LED illumination for micro-PIV including a novel front-lit configuration. Experiments in fluids, 2008. 44(2): p. 211-219.
11. Jaw, S., et al. Micro-flows measurement from a LED micro-PIV system. in Image and Signal Processing (CISP), 2012 5th International Congress on. 2012. IEEE.
12. Tien, W.-H., et al., A color-coded backlighting defocusing digital particle image velocimetry system. Experiments in Fluids, 2008. 44(6): p. 1015-1026.
13. Willert, C., et al., Pulsed operation of high-power light emitting diodes for imaging flow velocimetry. Measurement Science and Technology, 2010. 21(7): p. 075402.
14. Buchmann, N.A., C.E. Willert, and J. Soria, Pulsed, high-power LED illumination for tomographic particle image velocimetry. Experiments in fluids, 2012. 53(5): p. 1545-1560.

15. Casey, T.A., J. Sakakibara, and S.T. Thoroddsen, Scanning tomographic particle image velocimetry applied to a turbulent jet. *Physics of Fluids*, 2013. 25(2): p. 025102.
16. Klinner, J. and C. Willert, Tomographic shadowgraphy for three-dimensional reconstruction of instantaneous spray distributions. *Experiments in fluids*, 2012. 53(2): p. 531-543.
17. Estevadeordal, J. and L. Goss. PIV with LED: particle shadow velocimetry (PSV). in 43rd AIAA aerospace sciences meeting and exhibit, meeting papers. 2005.
18. McPhail, M., et al., Correcting for color crosstalk and chromatic aberration in multicolor particle shadow velocimetry. *Measurement Science and Technology*, 2015. 26(2): p. 025302.
19. Maas, H.G., A. Gruen, and D. Papantoniou, Particle tracking velocimetry in three-dimensional flows. *Experiments in Fluids*, 1993. 15(2): p. 133-146.
20. Nishino, K., N. Kasagi, and M. Hirata, Three-Dimensional Particle Tracking Velocimetry Based on Automated Digital Image Processing. *Journal of Fluids Engineering*, 1989. 111(4): p. 384-391.
21. Schanz, D., S. Gesemann, and A. Schröder, Shake-The-Box: Lagrangian particle tracking at high particle image densities. *Experiments in Fluids*, 2016. 57(5): p. 70.
22. Willert, C.E. and M. Gharib, Three-dimensional particle imaging with a single camera. *Experiments in Fluids*, 1992. 12(6): p. 353-358.
23. Pereira, F., et al. Aperture coded camera for three dimensional imaging. 1998 ~2.
24. Rohaly, J. and D.P. Hart. Monocular three-dimensional imaging. 2006 ~2.
25. Wu, M., J.W. Roberts, and M. Buckley, Three-dimensional fluorescent particle tracking at micron-scale using a single camera. *Experiments in Fluids*, 2005. 38(4): p. 461-465.
26. Toprak, E., et al., Three-dimensional particle tracking via bifocal imaging. *Nano letters*, 2007. 7(7): p. 2043-2045.
27. Kreizer, M. and A. Liberzon, Three-dimensional particle tracking method using FPGA-based real-time image processing and four-view image splitter. *Experiments in fluids*, 2011. 50(3): p. 613-620.
28. Gao, Q., H.P. Wang, and J.J. Wang, A single camera volumetric particle image velocimetry and its application. *Science China Technological Sciences*, 2012. 55(9): p. 2501-2510.
29. Peterson, K., et al., Single-camera, three-dimensional particle tracking velocimetry. *Optics express*, 2012. 20(8): p. 9031-9037.

30. Lindken, R., J. Westerweel, and B. Wieneke, Stereoscopic micro particle image velocimetry. *Experiments in Fluids*, 2006. 41(2): p. 161-171.
31. Maekawa, A. and J. Sakakibara, Development of multiple-eye PIV using mirror array. *Measurement Science and Technology*, 2018.
32. Hoyer, K., et al., 3D scanning particle tracking velocimetry. *Experiments in Fluids*, 2005. 39(5): p. 923.
33. Cierpka, C., et al., A simple single camera 3C-3D velocity measurement technique without errors due to depth of correlation and spatial averaging for microfluidics. *Measurement Science and Technology*, 2010. 21(4): p. 045401.
34. Hain, R. and C.J. Kähler, 3D3C time-resolved measurements with a single camera using optical aberrations, in 13th Int. Symp. on Applications of Laser Techniques to Fluid Mechanics. 2006.
35. Ng, R., et al., Light field photography with a hand-held plenoptic camera. *Computer Science Technical Report CSTR*, 2005. 2(11): p. 1-11.
36. Cenedese, A., et al., 3D particle reconstruction using light field imaging, in *International Symposium on Applications of Laser Techniques to Fluid Mechanics*. 2012.
37. Skupsch, C. and C. Brückner, Multiple-plane particle image velocimetry using a light-field camera. *Optics express*, 2013. 21(2): p. 1726-1740.
38. Rice, B.E., et al., Comparison of 4-camera Tomographic PIV and Single-camera Plenoptic PIV, in 2018 AIAA Aerospace Sciences Meeting. 2018. p. 2036.
39. Shi, S., et al., A detailed comparison of single-camera light-field PIV and tomographic PIV. *Experiments in Fluids*, 2018. 59(3): p. 46.
40. Ido, T., et al., Single-camera 3-D particle tracking velocimetry using liquid crystal image projector, in ASME/JSME 2003 4th Joint Fluids Summer Engineering Conference. 2003. p. 2257-2263.
41. Zibret, D., et al., 3D Flow Investigations by Rainbow Volumic Velocimetry (RVV): Recent Progress. *Journal of Flow Visualization and Image Processing*, 2004. 11(3).
42. Malfara, R., et al., Evaluation of the Rainbow Volumic Velocimetry (RVV) Process by Synthetic Images. *Journal of Flow Visualization and Image Processing*, 2007. 14(1): p. 1-15.
43. McGregor, T.J., D.J. Spence, and D.W. Coutts, Laser-based volumetric colour-coded three-dimensional particle velocimetry. *Optics and lasers in engineering*, 2007. 45(8): p. 882-889.
44. Ruck, B., Colour-coded tomography in fluid mechanics. *Optics & Laser Technology*, 2011. 43(2): p. 375-380.

45. Watamura, T., Y. Tasaka, and Y. Murai, LCD-projector-based 3D color PTV. *Experimental Thermal and Fluid Science*, 2013. 47: p. 68-80.
46. Murai, Y., et al., Color Particle Image Velocimetry Improved by Decomposition of RGB Distribution Integrated in Depth Direction, in *ASME/JSME/KSME 2015 Joint Fluids Engineering Conference*. 2015. p. V01AT20A003-V01AT20A003.
47. Dennis, K. and K. Siddiqui, A Multicolor Grid Technique for Volumetric Velocity Measurements, in *ASME 2017 Fluids Engineering Division Summer Meeting*. 2017. p. V01BT06A020-V01BT06A020.
48. Aguirre-Pablo, A.A., et al., Tomographic Particle Image Velocimetry using Smartphones and Colored Shadows. *Scientific Reports*, 2017. 7(1): p. 3714.
49. GSMarena. Nokia Lumia 1020 specifications. 2013 [cited 2016 August]; Available from: [http://www.gsmarena.com/nokia\\_lumia\\_1020-5506.php](http://www.gsmarena.com/nokia_lumia_1020-5506.php).
50. Luminus. PT-120. 2017 [cited 2017 15/May]; Available from: <http://www.luminus.com/products/PT-120.html>.
51. Wieneke, B., Volume self-calibration for 3D particle image velocimetry. *Experiments in Fluids*, 2008. 45(4): p. 549-556.
52. Nakamura, S., T. Mukai, and M. Senoh, Candela-class high-brightness InGaN/AlGaIn double-heterostructure blue-light-emitting diodes. *Applied Physics Letters*, 1994. 64(13): p. 1687-1689.
53. Scarano, F., Tomographic PIV: principles and practice. *Measurement Science and Technology*, 2012. 24(1): p. 012001.
54. Malvar, H.S., H. Li-wei, and R. Cutler. High-quality linear interpolation for demosaicing of Bayer-patterned color images. in *2004 IEEE International Conference on Acoustics, Speech, and Signal Processing*. 2004.
55. Gharib, M., E. Rambod, and K. Shariff, A universal time scale for vortex ring formation. *Journal of Fluid Mechanics*, 1998. 360: p. 121-140.
56. Krueger, P.S. and M. Gharib, The significance of vortex ring formation to the impulse and thrust of a starting jet. *Physics of Fluids (1994-present)*, 2003. 15(5): p. 1271-1281.
57. McPhail, M., et al., Multicolor particle shadow accelerometry. *Measurement Science and Technology*, 2015. 26(4): p. 045301.
58. Farrugia, N., S. Kanne, and D.A. Greenhalgh, Three-pulse digital particle image velocimetry. *Optics Letters*, 1995. 20(17): p. 1827-1829.

59. Prasad, A.K. and K. Jensen, Scheimpflug stereocamera for particle image velocimetry in liquid flows. *Applied Optics*, 1995. 34(30): p. 7092-7099.
60. Sonymobile. Sony Xperia XZ premium. 2017 [cited 2017 1-May]; Available from: <https://www.sonymobile.com/global-en/products/phones/xperia-xz-premium/>.
61. Sternberg, S.R., Biomedical image processing. *Computer*, 1983(1): p. 22-34.
62. Xiong, J., et al., Rainbow particle imaging velocimetry for dense 3D fluid velocity imaging. *ACM Transactions on Graphics (TOG)*, 2017. 36(4): p. 36.
63. Peng, Y., et al., Computational imaging using lightweight diffractive-refractive optics. *Optics express*, 2015. 23(24): p. 31393-31407.
64. Heidrich, W., et al., Rainbow Particle Imaging Velocimetry for Dense 3D Fluid Velocity Imaging, U.S. 15/498317, Editor. 2018.
65. Epson. 3LCD overview. 2017 [cited 2017 1-Mar]; Available from: <http://www.3lcd.com/explore/>.
66. Epson. EX9200 Pro Wireless WUXGA 3LCD Projector. 2015 [cited 2017]; Available from: <https://epson.com/For-Work/Projectors/Portable/EX9200-Pro-Wireless-WUXGA-3LCD-Projector/p/V11H722020>.
67. Red. Epic Dragon 6K. 2012; Available from: <http://www.red.com/products/epic-dragon#gallery>.
68. Hirsch, R., *Exploring Color Photography: From Film to Pixels*. 2014: Focal Press.
69. Smith, A.R., Color gamut transform pairs. *SIGGRAPH Comput. Graph.*, 1978. 12(3): p. 12-19.
70. Tinevez, J.-Y., et al., TrackMate: An open and extensible platform for single-particle tracking. *Methods*, 2017. 115: p. 80-90.
71. Jaqaman, K., et al., Robust single-particle tracking in live-cell time-lapse sequences. *Nature methods*, 2008. 5(8): p. 695.
72. Atherton, T.J. and D.J. Kerbyson, Size invariant circle detection. *Image and Vision Computing*, 1999. 17(11): p. 795-803.
73. Yuen, H.K., et al., Comparative study of Hough Transform methods for circle finding. *Image and Vision Computing*, 1990. 8(1): p. 71-77.
74. Davies, E.R., CHAPTER 10 - Circle Detection, in *Machine Vision: Theory, Algorithms, Practicalities*, E.R. Davies, Editor. 2005, Morgan Kaufmann: Burlington. p. 283-313.

75. Hu, C., et al., Vehicle color recognition with spatial pyramid deep learning. IEEE Transactions on Intelligent Transportation Systems, 2015. 16(5): p. 2925-2934.
76. Rachmadi, R.F. and I. Purnama, Vehicle color recognition using convolutional neural network. arXiv preprint arXiv:1510.07391, 2015.
77. Conchouso, D., et al., Three-dimensional parallelization of microfluidic droplet generators for a litre per hour volume production of single emulsions. Lab on a Chip, 2014. 14(16): p. 3011-3020.
78. Inc., S.N.A. Optical Glass Data sheets. 2017 Ma1 5; 13-15].
79. Cierpka, C., R. Hain, and N.A. Buchmann, Flow visualization by mobile phone cameras. Experiments in Fluids, 2016. 57(6): p. 1-10.
80. Maruyama, M., et al. Multi-pattern Embedded Phase Shifting Using a High-Speed Projector for Fast and Accurate Dynamic 3D Measurement. in 2018 IEEE Winter Conference on Applications of Computer Vision (WACV). 2018.



## APPENDIX

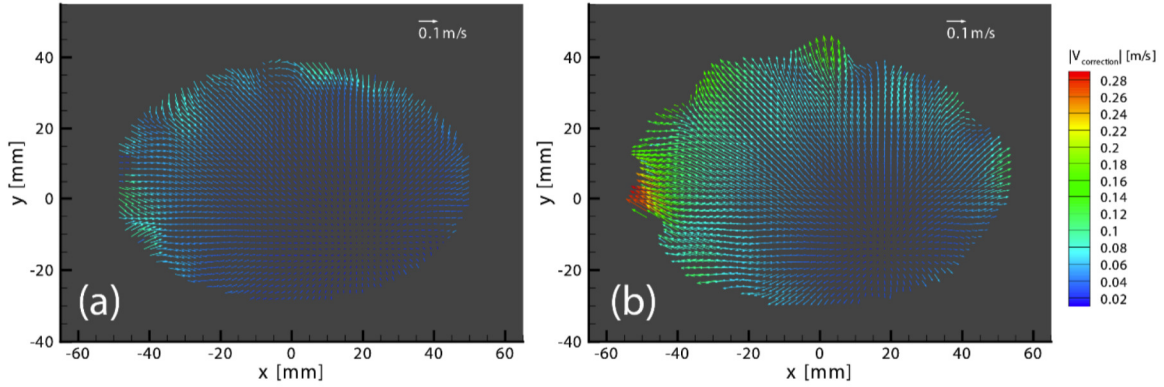


Figure 5.17. Velocity bias errors due to chromatic aberration. They are obtained from the Zero-time-delay images (all colors flashed at the same time) for (a)  $t_1 - t_2$  correlation (Green-red) and (b)  $t_2 - t_3$  correlation (Red-Blue). The arrows in both cases are colored by their vector magnitudes. Both results are presented in plane  $z=0$  mm. Note that most of the fields have aberration magnitudes less than 0.1 m/s. [48]

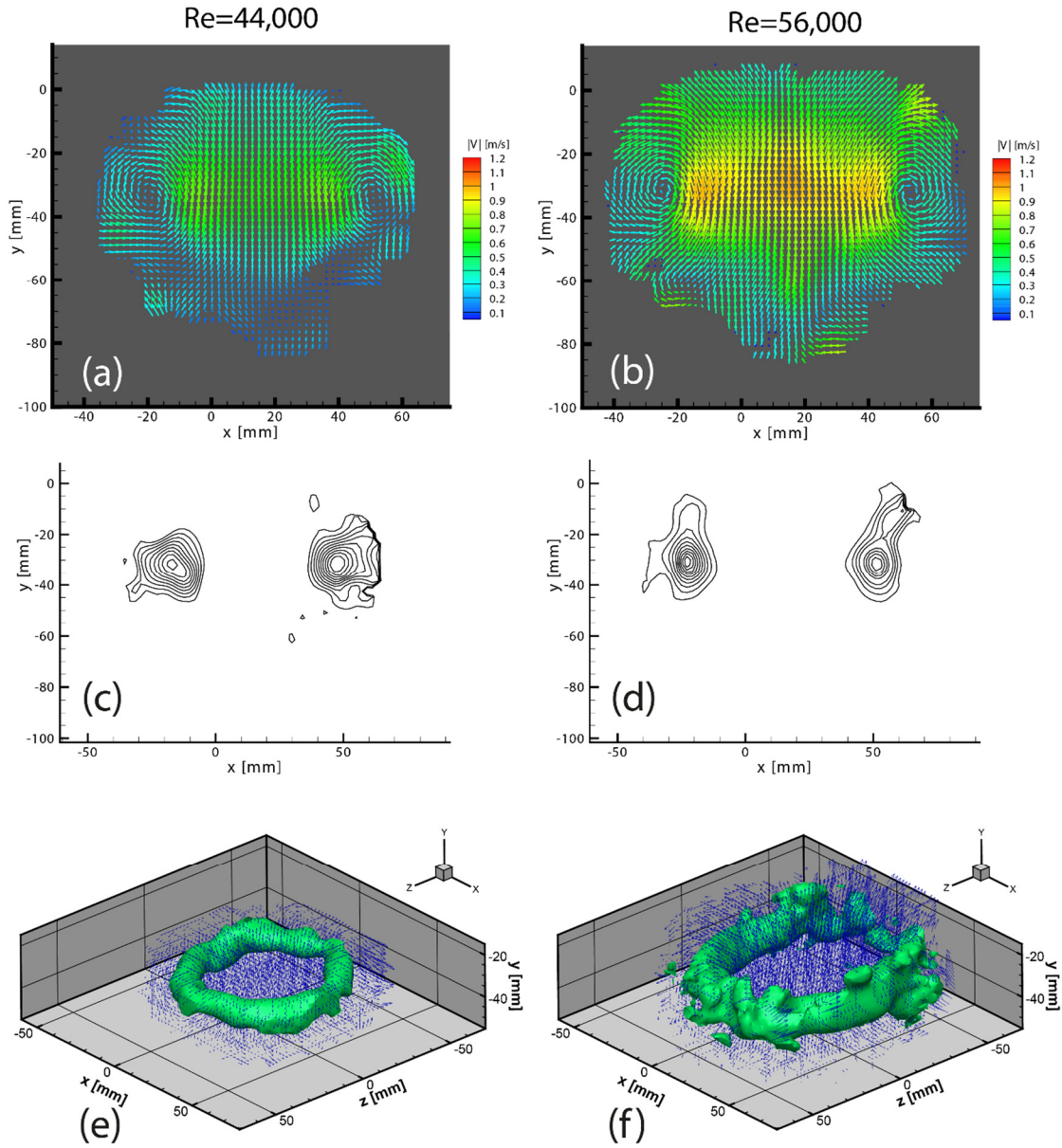


Figure 5.18. Instantaneous velocity fields for a single time step in the plane  $z=0$  mm for (a)  $Re=44,000$ ,  $\Delta t=1000 \mu\text{s}$  and (b)  $Re=56,000$ ,  $\Delta t=500 \mu\text{s}$ . (c,d) The corresponding iso-contours of vorticity magnitude ranging from  $30$  to  $120 \text{ s}^{-1}$  in (c) for the  $Re=44,000$  and (d) from  $40$  to  $220 \text{ s}^{-1}$  for  $Re=56,000$ . (e,f) The vortex ring visualized in 3D by the iso-surface of vorticity magnitude  $90 \text{ s}^{-1}$  as well as every fifth vector of the instantaneous velocity field for  $Re=44,000$  (e) and  $Re=56,000$  (f). [48]

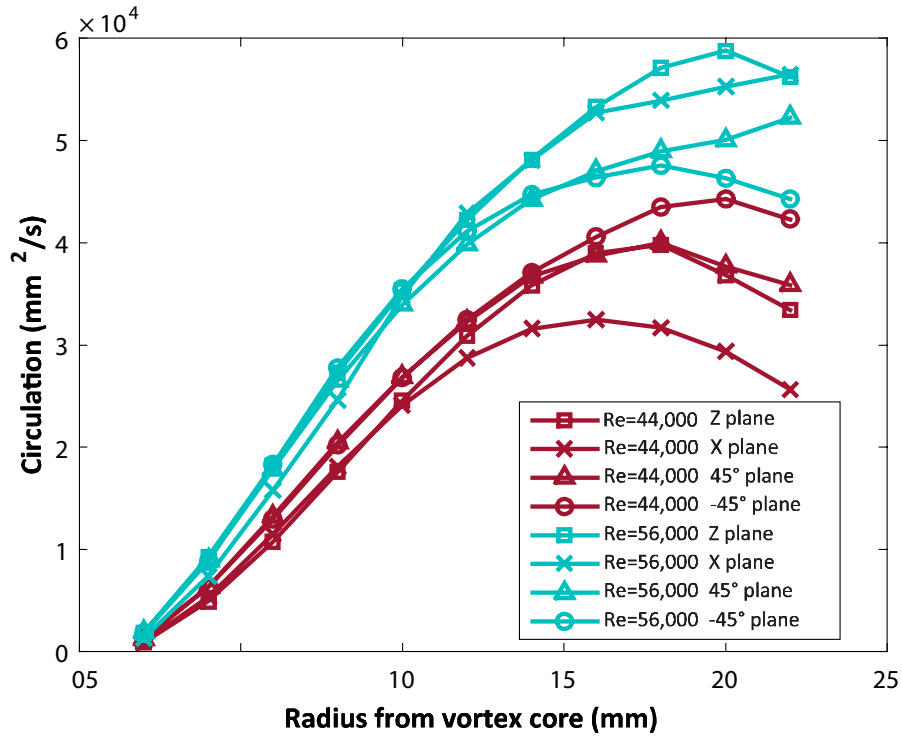


Figure 5.19. Circulation  $\Gamma$  as a function of the radial distance from the vortex core, in four different vertical planes, for  $Re=44,000$ ,  $\Delta t=1000 \mu\text{s}$  (red) and  $Re=56,000$ ,  $\Delta t=500 \mu\text{s}$  (cyan). This shows that the circulation is approximately constant around every cross-section through the vortex core.[48]

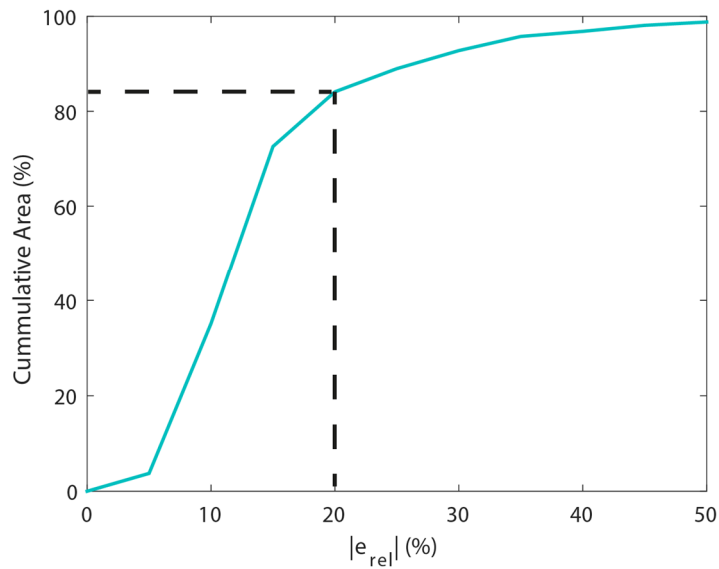


Figure 5.20. Plot representing the cumulative area vs the relative error magnitude ( $|e_{rel}|$ ) in percentage. The dashed lines clearly show that 84% of the vectors have an error of 20% or less. Keep in mind that “error” means here the difference between the simultaneous measurements of the stereo-PIV and tomo-PIV systems. [48]

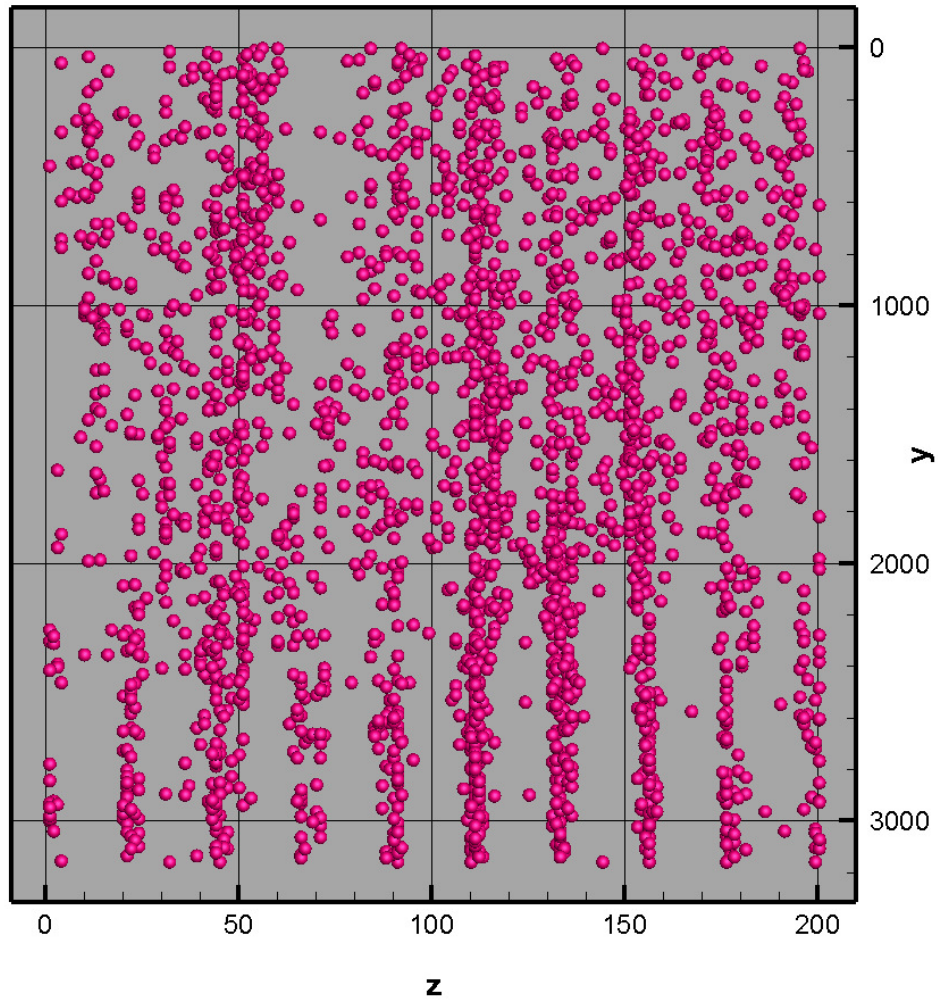


Figure 5.21. Side view (YZ) of the reconstructed particle field based on their RGB values. Note that the reconstruction is biased towards certain planes.

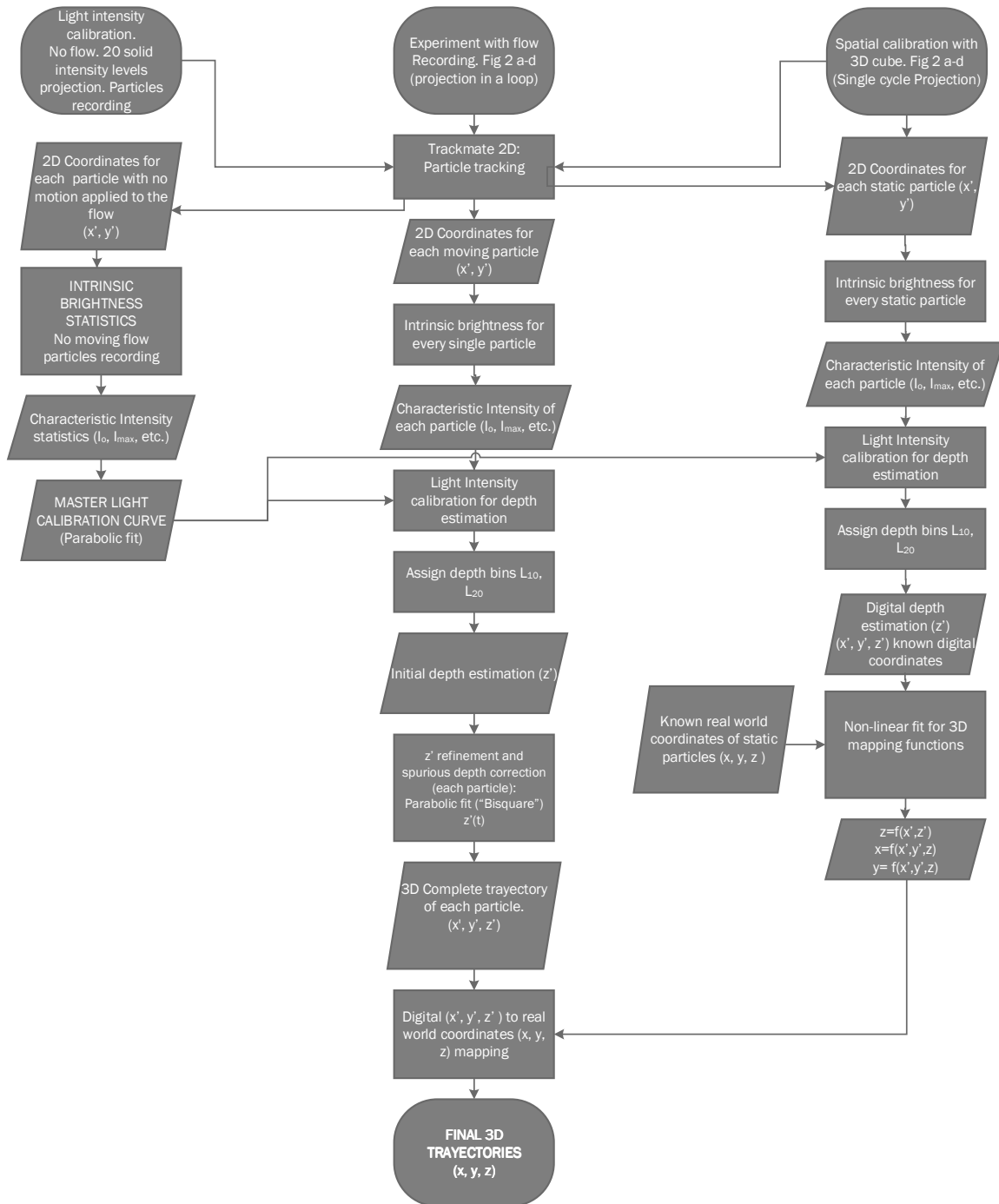


Figure 5.22. Flowchart summarizing the algorithm used to reconstruct the 3D position of multiple particles based on monochromatic structured light and a single camera.

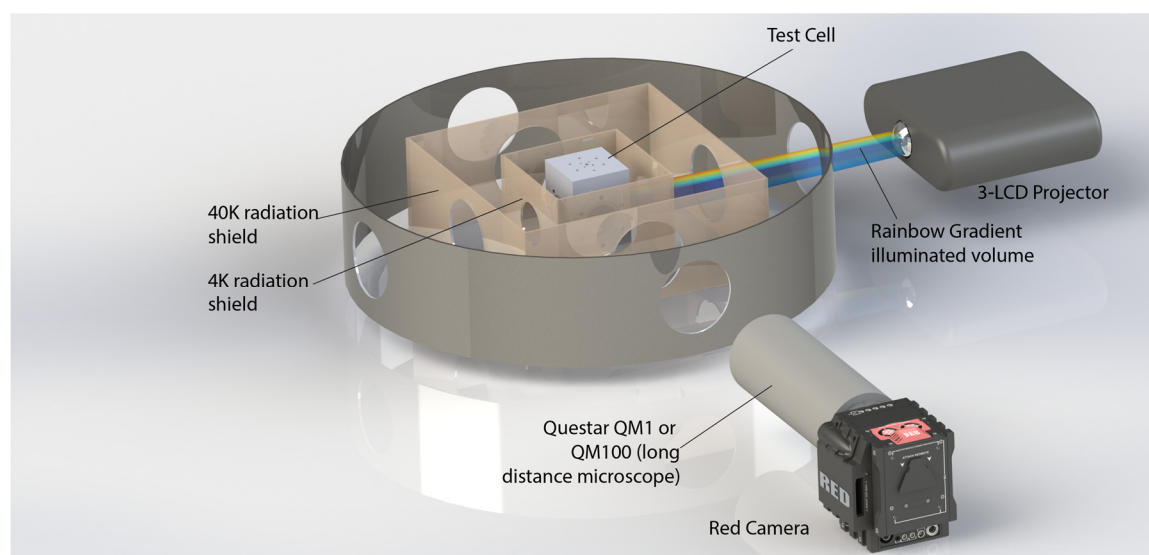


Figure 5.23 Schematic representation of the experimental setup proposed using single camera systems to reconstruct in 3D particle trajectories. This system in principle will reduce the complexity and heat load into the test cell at a temperature of 1.3 K.

A 1 : Matlab code “*Gausswiegthfunction\_colorsquares.m*” for determining the characteristic color in RGB and HUE.

```
%THIS CODE TAKES THE MEAN OF EACH PARTICLE FOUND IN R, G, B AND GETS THE
%MEAN R, G, B VALUE AND Hue

clear all
close all
clc
tic
imFiles= dir('*BW.tif'); %read black and white images
imfilrgb = dir('*crop.tif'); %read color images
nbits=16; %bit depth of images

%% For loop to go through each captured image

for p=1:length(imFiles)

    clearvars -except imFiles p nbits imfilrgb
    close all

    %Parameters for circle finder
    minrad=5; % minimum radius of the particles found in the images
    maxrad=18; % maximum radius of the particles found in the images
    sensitivity=0.96; %0.96 works best for using the nonoise coming from meanbackground

    filename=imFiles(p).name
    filename2=imfilrgb(p).name;
    image=imread(filename); %black and white image
    image2=imread(filename2); %color image

    RGBim=image2;
    HSVim=rgb2hsv(RGBim); %convert RGB color space to HSV

    im=image(:,:,:);
    im=im*50; %enhance brightness
    imshow(im);

    [Y,X,n]=size(im);

    imwr=zeros(size(RGBim));
    imwr2=imwr;
    imwr3=imwr;

    %% Found coordinates of the particles in the BW image using circle finder no normalization

    [centers, radii] = imfindcircles(im,[minrad maxrad],'ObjectPolarity','bright',
'Sensitivity',sensitivity);
    %

    centerround=round(centers);
    radiiround=round(radii);

    [ncircles]=size(radiiround);

    %% For loop to go through each particle found to obtain its characteristic color
    for i=1:ncircles
        clearvars yo xo w x y H S V wavgH R G B
        currx=centerround(i,1);
        curry=centerround(i,2);
        radius=radiiround(i);
        if curry-radius<=0
            lowlimity=1;
        end
    end
end
```

```

else
    lowlimity=curry-radius;
end
if curry+radius>=Y
    highlimity=Y;
else
    highlimity=curry+radius;
end
if currx-radius<=0
    lowlimitx=1;
else
    lowlimitx=currx-radius;
end
if currx+radius>=X
    highlimitx=X;
else
    highlimitx=currx+radius;
end

% OBTAIN RGB MEDIAN IN EACH PARTICLE, THEN OBTAIN HUE

R=RGBim(lowlimity:highlimity,lowlimitx:highlimitx,1);
G=RGBim(lowlimity:highlimity,lowlimitx:highlimitx,2);
B=RGBim(lowlimity:highlimity,lowlimitx:highlimitx,3);

H=HSVim(lowlimity:highlimity,lowlimitx:highlimitx,1);
S=HSVim(lowlimity:highlimity,lowlimitx:highlimitx,2);
V=HSVim(lowlimity:highlimity,lowlimitx:highlimitx,3);

[yo,xo]=size(H);
x=1:xo;
y=1:yo;
%GAUSSIAN WEIGHTED AVERAGE OF H and also RGB

for o=1:yo
    for q=1:xo
        w(o,q)=exp(-(x(q)-(xo/2))^2/(2*(xo/6)^2)+(y(o)-(yo/2))^2/(2*(yo/6)^2));
    end
end

%% OBTAIN CHARACTERISTIC COLOR FROM HSV COLOR SPACE
wavgH=sum(sum(H.*w))/sum(sum(w));
HSVim2(lowlimity:highlimity,lowlimitx:highlimitx,1)=wavgH;
HSVim2(lowlimity:highlimity,lowlimitx:highlimitx,2)=S;
HSVim2(lowlimity:highlimity,lowlimitx:highlimitx,3)=V*1.2;
%}

%% OBTAIN CHARACTERISTIC COLOR FROM RGB COLOR SPACE
wavgR=sum(sum(double(R).*w))/sum(sum(w));
wavgG=sum(sum(double(G).*w))/sum(sum(w));
wavgB=sum(sum(double(B).*w))/sum(sum(w));
imwr3(lowlimity:highlimity,lowlimitx:highlimitx,1)=wavgR*1.4;
imwr3(lowlimity:highlimity,lowlimitx:highlimitx,2)=wavgG*1.4;
imwr3(lowlimity:highlimity,lowlimitx:highlimitx,3)=wavgB*1.4;

end
%{
imwr=uint16(imwr);
fileBW=sprintf('%03d_%s',p,'med_trim3.tif');
imwrite(imwr,fileBW);
%}
imwr3=uint16(imwr3);
fileBW3=sprintf('%03d_%s',p,'RGB_wavg.tif');
imwrite(imwr3,fileBW3);

HSVim3=HSVim2.*(2^(nbits)-1);

imwr2=uint16(HSVim3);

```



```

fileBW2=sprintf('%03d %s',p,'med_weighted_average.tif');
imwrite(imwr2,fileBW2);

end
toc
Gausswiegthfunction_colorsquares.m

```

A 2 : Matlab code “*savebins\_trackmate\_fillmiss.m*” for determining the digital depth of the particle based on the characteristic color detected in the previous algorithm.

```

%THIS ALGORITHM DETERMINES THE DIGITAL DEPTH OF EACH PARTICLE BASED ON THE
%COLOR DETECTED.

clear all
close all
clc
%% organizing the tracks from TRACK MATE
clipZ=true;

addpath('C:\Users\aguirraa\Desktop\Fiji\Fiji.app\scripts')
tic
[tracks, meta] = importTrackMateTracks('Tracks_no_processing_25px_0_15_threshold_linear
LAP.xml',clipZ); %trajectoryID, frame, x, y

ntracks=size(tracks,1);
traject=NaN(1,4);

for i=1:ntracks
    clearvars temp
    temp=cell2mat(tracks(i));
    [row,col]=size(temp);
    temp2=zeros(row,col+1);

    temp2(:,1)=i;
    temp2(:,2:end)=temp;

    traject=vertcat(traject,temp2);
end
clearvars tracks % release memory

traject(1,:)=[]; %REMOVE NAN ROW OF THE TRAJECT
tim=toc;
fprintf('time to load and organizedata: %d \r',tim)

%%
traject=sortrows(traject,2); %trajectoryID, frame, x, y bin10 bin 20 hue
ntraject=max(traject(:,1)); %number of trajectories

xround=round(traject(:,3))+1;
yround=round(traject(:,4))+1;

imFiles= dir('*RGB_wavg.tif'); %USE RGB OR HSV CHARACTERISTIC COLOR.

range20=10; %Threshold that will decide when is the number moving inside the same bin20

%% creating bins for the depth position

```

```

hsvproj_20=[0.8333333333333333,1,1;0.898039215686275,1,1;0.946405228758170,1,1;0.0431372549019608,
1,1;0.0607843137254902,1,1;0.0862745098039216,1,1;0.113071895424837,1,1;0.128758169934641,1,1;0.1
47712418300654,1,1;0.1666666666666667,1,1;0.209803921568627,1,1;0.252941176470588,1,1;0.3333333333
33333,1,1;0.376470588235294,1,1;0.419607843137255,1,1;0.500000000000000,1,1;0.516993464052288,1,1
;0.548366013071895,1,1;0.598039215686275,1,1;0.666666666666667,1,1];
hsvproj_20(:,1)=hsvproj_20(:,1)*360;
for m=1:size(hsvproj_20,1);
if hsvproj_20(m,1)>270;
hsvproj_20(m,1)=hsvproj_20(m,1)-360;
end
end
hsvproj_10=hsvproj_20(1:2:end,:);

binlimit10(1,1)=-90;
for m=2:size(hsvproj_10,1);
binlimit10(m,1)=(hsvproj_10(m,1)+hsvproj_10(m-1))/2;
end
binlimit10(11,1)=269.999;

binlimit20(1,1)=-90;
for m=2:size(hsvproj_20,1);
binlimit20(m,1)=(hsvproj_20(m,1)+hsvproj_20(m-1))/2;
end
binlimit20(21,1)=(hsvproj_20(20,1)+29.999);

%% open each image and find hue of each particle AND ASSIGN TO BIN 10 OR BIN20

tic
p=1
%for p=1:size(imFiles,1);
imname=imFiles(1).name;
image=imread(imname);
imhsv=rgb2hsv(image);
imhsv(:,:,1)=imhsv(:,:,1)*360;

for m=1:size(traject,1);
clearvars sub ind

if p~=traject(m,2)+1
p=p+1

imname=imFiles(p).name;
image=imread(imname);
imhsv=rgb2hsv(image);
imhsv(:,:,1)=imhsv(:,:,1)*360;

end

hue(m,1)=imhsv(yground(m,1),xround(m,1),1);
if hue(m,1)>270;
hue(m,1)=hue(m,1)-360;
end
%assign each particle to each bin
if (p<=5 && p>=1) || (p<=55 && p>=51) || (p<=105 && p>=101) || (p<=155 && p>=151) ||
(p<=205 && p>=201) || (p<=255 && p>=251) %CONDITION FOR 10 COLOR BINS CHECK THIS CONDITION IN THE
CASE OF THE WHOLE FRAME

b=1;
binlimit=binlimit10(b);
while hue(m,1)>=binlimit
b=b+1;
binlimit=binlimit10(b);
end
bfin10(m,1)=b-1;
bfin20(m,1)=NaN;

else

```

```

        b=1;
        binlimit2=binlimit20(b);
        while hue(m,1)>=binlimit2
            b=b+1;
            binlimit2=binlimit20(b);
        end
        bfin10(m,1)=NaN;
        bfin20(m,1)=b-1;

    end

%CORRECT HUE IN TRAJECTORIES IN THE TRANSITIONS

end
traject(:,5)=bfin10;
traject(:,6)=bfin20;
traject(:,8)=hue;

trajectorg=sortrows(traject,1);

trans10=[5;55;105;155;205;255]; %TRANSITION FRAMES BIN10
trans20=[50;100;150;200;250]; %TRANSITION FRAMES BIN20

for i=1:6 % CORRECT TRANSITION OF FRAMES THAT BELONG TO BIN10
    clearvars transition10
    transition10=find(trajectorg(:,2)==trans10(i));
    trajectorg(transition10,5)=trajectorg(transition10-1,5);
end
for i=1:5 % CORRECT TRANSITION OF FRAMES THAT BELONG TO BIN20
    clearvars transition20
    transition20=find(trajectorg(:,2)==trans20(i));
    trajectorg(transition20,6)=trajectorg(transition20-1,6);
end
tim=toc;
fprintf('time to assign bins :%d \r',tim)

%% CHECK RELATION BETWEEN BINS AND ASSIGN FINAL Z POSITION (PIXEL)

medwind=10; %median window size for fill missing
medwindow2=15; %median for big delta in bin20
medwindb10=4;
stdlimit=2; %movind standard dev limit
ntraject=max(trajectorg(:,1)); %number of trajectories

trajectclean=NaN(1,11);
subtrajectclean=NaN(1,11);
filterframes=15;

for o=1:ntraject;
    clearvars tempclean parttraj partbin10 partbin20 partbin10fill partbin20fill in med
    partbin20sub movmed partbin20fill2 rangebin20 rangebin10 part20mean part20std part20med delta
    indelta indelta2 med zsmooth in1
    %extraction of each trajectory

    if sum(trajectorg(:,1)==o)>=filterframes %only consider particles that have more than
the number of frames established.

        ind = trajectorg(:,1) == o;
        parttraj = trajectorg(ind,:); %each particle trajectory
        frames=size(parttraj(:,1));

        if nansum(parttraj(:,5))~=0 && nansum(parttraj(:,6))~=0 %particles that have
both cases

            % DO ALL THE CASES OF THE MOVING PARTICLES
            partbin10=parttraj(:,5);
            partbin20=parttraj(:,6);

            partbin10(partbin10==0)=NaN;
            partbin20(partbin20==0)=NaN;

```

```

rangebin10=range(partbin10);
rangebin20=range(partbin20);

%Fill, then smoothin (2 times)
partbin20fill=fillmissing(partbin20,'movmedian',medwind);
partbin20fill=fillmissing(partbin20fill,'movmedian',medwind);

if rangebin20<=10    %change of bin 20
    % CHECK HOW TO DEAL THIS AREA the else part
    med=nanmedian(partbin10);
    partbin10fill=med;

    partbin20fill=round(medfilt1(partbin20fill));
    partbin20fill2=partbin20fill;
else

    part20std=movstd(partbin20fill,medwindow2);
    part20mean=movmean(partbin20fill,medwindow2);
    part20med=movmedian(partbin20fill,medwindow2);
    [s,t]=size(part20mean);

    for r=1:s

        if part20std(r)<2
            partbin20fill2(r,1)=partbin20fill(r);
        elseif partbin20fill(r)<(part20med(r)+part20std(r))    &&
partbin20fill(r)>(part20med(r)-part20std(r))
            partbin20fill2(r,1)=partbin20fill(r);
        else
            partbin20fill2(r,1)=part20med(r);
        end
    end

    rangebin20=range(partbin20fill2);
    if rangebin20<=10    %reassign after correcting spurious colors
        % CHECK HOW TO DEAL THIS AREA the else part
        med=nanmedian(partbin10);
        partbin10fill=med;

    else
        %if the change is real partbin10
        med=nanmedian(partbin10);
        delta=zeros(s,1);
        delta(2:end,1)=diff(partbin20fill2);
        delta(1,1)=delta(2,1);
        indelta=delta(delta>8);
        indelta2=delta(delta<-8);

        partbin10fill=partbin10;

        for r=2:s
            if isnan(partbin10(r))

                if delta(r)<8 && delta(r)>-8
                    partbin10fill(r)=partbin10fill(r-1);
                elseif delta(r)>0
                    partbin10fill(r)=partbin10fill(r-1)-1;
                else
                    partbin10fill(r)=partbin10fill(r-1)+1;
                end
            end
        end

    end

end

end

```

```

tempclean(:,1:4)=parttraj(:,1:4);
tempclean(:,8)=parttraj(:,8);
tempclean(:,5)=partbin10fill;
tempclean(:,6)=partbin20fill2;
tempclean(1,9)=0;
tempclean(1,10)=0;
tempclean(1,11)=0;
tempclean(2:end,9)=diff(tempclean(:,3)); %velocity x
tempclean(2:end,10)=diff(tempclean(:,4)); %velocity Y

% Here is the modified stuff
tempclean(:,7)=tempclean(:,5)*20-20+tempclean(:,6);
%zsmooth=smooth(tempclean(:,7));
%tempclean(:,7)=zsmooth;

inl=isnan(tempclean(:,7));
tempclean(inl,:)=[];
%tempclean(isnan(tempclean))=[];
%here it finishes
tempclean(2:end,11)=diff(tempclean(:,7)); %velocity Z

trajectclean=[trajectclean;tempclean];

end

end

end

%trajectclean(:,7)=trajectclean(:,5)*20-20+trajectclean(:,6);
trajectclean=sortrows(trajectclean,2);
%inl=isnan(trajectclean(:,7));
%trajectclean(inl,:)=[];
trajectclean(end,:)=[];

for b=1:ntraject

clearvars zsmooth zind
zind=trajectclean(:,1)==b;
zsmooth=trajectclean(zind,7);
zsmooth=smooth(zsmooth,'rlowess');
trajectclean(zind,7)=zsmooth;
end

%% WRITE FILE TO TECPLOT FORMAT
for q=0:max(trajectclean(:,2))
ind2 = trajectclean(:,2) == q;
temp=trajectclean(ind2,:);

filenametraj=sprintf('%03d%s',q,'particle_smooth.dat');
fileID2=fopen(filenametraj,'w');
fprintf(fileID2, 'VARIABLES = "partID" "frame" "x" "y" "bin10" "bin20" "z" "hue" "u"
"v" "w"\r\n');
fprintf(fileID2, 'ZONE T="%d"\r\n',q);
fprintf(fileID2,'%f %f %f %f %f %f %f %f %f %f\r\n',transpose(temp)); %partID
frame# x y bin10 bin20 z
fclose(fileID2);
end

```

A 3 : Matlab code “*Trackmate\_read\_finna\_movingparticles\_v4.m*” used in Chapter 5 to determine the digital depth ( $z'$ ) of each particle based on its intrinsic brightness.

```
%ALGORITHM THAT DETERMINES THE DEPTH POSITION (Z') BY STUDYING DIFFERENT
%INTENSITY PRAMETERS OF EACH PARTICLE IN DIGITAL COORDINATES (IW, IO, IMAX)

clear all
close all
clc

%% parameters section for user: only modify this part
fpscam=60; %frame rate of camera
fpsvid=15; % frame rate of video
nframes=8; %number of different frames projected
nsolid=1; %number of projected frames with solid color

rfps= fpscam/fpsvid;
cicle=nframes*rfps; %length of a full cicle of frames in the camera

radius=3; %threshold of max value for particles
thresmax=1000; %threshold of max value

partpar=6; %CHANGE HERE IF THE VALUE USED IS MEANWAVG=5, MEANMAXV=6, CMIN=10

sublev=20; %how many intensities has the finest subgradients
lmbin=10; %difference to consider the particle is in the next or previous bin
countmax=4; %how many counts for assigning the big bin (in a total of rfps+rfps-transition
frames )

nmovmed=10; %how many continous frames for movmedian interpolation

polthres=36; %minimum sample points for polynomial interpolation
degpoly=2; %degree of polynomial for interpolation

dt=1/fpscam;

imfiles=dir('*processed.tif');
%% organizing the tracks from TRACK MATE
clipZ=true;

addpath('C:\Users\aguirraa\Desktop\Fiji\Fiji.app\scripts') %add necessary scripts to read
output from Trackmate

tic

trackfiles=dir '*.xml'); %read file with 2D PArticle tracking from Trackmate

ID=0;
for j=1:length(trackfiles)
    traject(1,:)=NaN(1,4);
    trackname=trackfiles(j).name;
    [tracks, meta] = importTrackMateTracks(trackname,clipZ); %trajectoryID, frame, x, y

ntracks=size(tracks,1);
% re arrange data by particle

for i=1:ntracks

    clearvars temp
    temp=cell2mat(tracks(i,1));
    %temp=temp(1,:);
    [row,col]=size(temp);
    temp2=zeros(row,col+1);

    temp2(:,1)=i;
    temp2(:,2)=temp(:,1)+1;
```

```

temp2(:,3:end)=temp(:,2:end);

traject=vertcat(traject,temp2);

end

clearvars tracks
    % release memory
end

traject(1, :, :)=[]; %REMOVE NAN ROW OF THE TRAJECT

tim=toc;
fprintf('time to load and organizedata: %d \r',tim)

%% CHECK EACH PLAZE Z INTENSITIES
ID=0;
k=0;

list=zeros(1,12); %/Structure of the matrix by columns: frame Partid X Y normwavg
normmax Plane Xcentroid Ycentroid Cmin Rmin C*Rmin^1.5

for p=1:length(imfiles)
clearvars traject1 centerround trajectext
traject1=traject(traject(:,2)==p,:);
centerround(:,1)=round(traject1(:,3))+1;
centerround(:,2)=round(traject1(:,4))+1;
trajectext(:,1)=traject1(:,1)+max(list(:,2));

filename=imfiles(p).name
currim2=imread(filename);
[Y,X,n]=size(currim2);
imwr3=zeros(size(currim2));

%% find circles no normalization
for i=1:size(traject1,1)
    k=k+1;
clearvars x yo xo w V x y wavgV final
currx=centerround(i,1);
curry=centerround(i,2);
%radius=radiusround(i);
%radius=4;

if curry-radius<=0
    lowlimity=1;
else
    lowlimity=curry-radius;
end
if curry+radius>=Y
    highlimity=Y;
else
    highlimity=curry+radius;
end
if currx-radius<=0
    lowlimitx=1;
else
    lowlimitx=currx-radius;
end
if currx+radius>=X
    highlimitx=X;
else
    highlimitx=currx+radius;
end

V=double(currim2(lowlimity:highlimity,lowlimitx:highlimitx)); %equivalent
to ff
Vmax=max(max(V));
[ymax xmax]=find(V==Vmax,1); %equivalent to jmax and i max respectively
(location of max pixel value in subregion V)

[yo,xo]=size(V);

```

```

x=1:xo; %xo
y=1:yo; %yo
w=zeros(size(xo,yo));

%GAUSSIAN WEIGHTED AVERAGE OF H and also RGB for 6 pixels
%diameter

    for o=1:yo
        for q=1:xo
            w(o,q)=exp(-(x(q)-(xo/2))^2/(2*(xo/6)^2)+(y(o)-(yo/2))^2/(2*(yo/6)^2));
        end
    end

    wavgV=sum(sum(double(V).*w))/sum(sum(w.*(V~=0)));
    Vmax=max(max(V));
    %norm=V./(max(max(V)))*(2^(nbits)-1);

    imwr3(lowlimity:highlimity,lowlimitx:highlimitx,1)=wavgV;
    %imwrnorm(lowlimity:highlimity,lowlimitx:highlimitx,1)=norm;
    list(k,1)=p; % number of frame
    list(k,2)=traject1(i,1); %particle ID
    list(k,3)=currx; %x coord
    list(k,4)=curry; %ycoord
    list(k,5)=wavgV; %Wavg
    list(k,6)=Vmax; % max pixel value
    list(k,7)=j; % Number of Z plane

%% Gauss fit code comes here to determine Io

imax=xmax; jmax=ymax;
[cx,cy,cmin,rmin] = gauss_fit( V, imax, jmax );
itotal(i) =real(cmin * rmin^1.5);
cminall(i) = cmin;
rminall(i) = rmin;
ic = currx + imax - radius; %absolute X position value in the frame of max
pixel
jc = curry + jmax - radius; %absolute Y position value in the frame of max
pixel
xx(i) = double( ic ) + cx-1; %absolute X position value in the frame centroid
(matlab coord starting from 1)
yy(i) = double( jc ) + cy-1; %absolute X position value in the frame centroid
(matlab coord starting from 1)

list(k,8)= xx(i) ; %subpixel Corrected X position
list(k,9)= yy(i) ; %subpixel corrected Y position
list(k,10)= cminall(i) ; %Cmin
list(k,11)= rminall(i) ; %Rmin
list(k,12)= itotal(i); %I total (Cmin*Rmin^1.5)

end

end

list(:,13)=ceil(list(:,1)/cicle); %cycle number
list=real(list);
save('all_workspace.mat');

%% normalize wavg and max values for each particle and obtain mean and std
listnorm=zeros(1,13) %1frame 2Partid 3X 4Y 5normwavg 6normmax 7Plane 8Xcentroid
9Ycentroid 10Cmin 11Rmin 12C*Rmin^1.5 13#cycle

for i=1:max(list(:,2))
    part=list(list(:,2)==i,:);

    if size(part(part(:,6)>thresmax,:),1)>=cicle
        for ncic=1:max(part(:,13))
            clearvars partcycle
            partcycle=part(part(:,13)==ncic,:);

```



```

partcycle(:,5)=partcycle(:,5)./max(partcycle(:,5));
partcycle(:,6)=partcycle(:,6)./max(partcycle(:,6));
partcycle(:,10)=partcycle(:,10)./max(partcycle(:,10));
partcycle(:,11)=partcycle(:,11)./max(partcycle(:,11));
partcycle(:,12)=partcycle(:,12)./max(partcycle(:,12));
listnorm=vertcat(listnorm,partcycle);
end
end
end
listnorm(1,:)=[];

%% Create bins for each frame projected (not counting solid
load('zref_v4.mat','zref'); %Reference of sequence projected normalized (ROw= zlevel,
column=frame in time)
f=load('fit_f11_meanmax.mat'); %fit of calibration curve from the light calibration
f=f.f; %change here .f meanmaxv, .f2 meanwavg, .f3 meanCmin

xfit=transpose((84:9:255)./max((84:9:255)));

listnorm(:,14)=f(listnorm(:,partpar)); %Vfit of light curve ussing 10Cmin 5MeanWAVG
6MeanMaxV

for i=nsolid+2:5 %size(zref,2);
clearvars deltas un
deltas=diff(unique(zref(:,i)));
un=unique(zref(:,i),'stable');
delta(1,i-(nsolid+1))=deltas(1,1);
if i==3
bin2(:,1)=(un(1)-(delta(1,i-(nsolid+1)))/2):delta(1,i-
(nsolid+1)):max(un)+(delta(1,i-(nsolid+1))+0.01)/2;
elseif i==4
bin3(:,1)=flipud(bin2(:,1));
elseif i==5
bin4(:,1)=(un(1)-(delta(1,i-(nsolid+1)))/2):delta(1,i-
(nsolid+1)):max(un)+(delta(1,i-(nsolid+1)))/2; %CHECK THIS BIN IF ITS OK
end
end

%% Assign particles to each bin and Compare original sequence vs value to get z level (current
is 200 levels)

%1frame 2Partid 3X 4Y 5normwavg 6normmax 7Plane 8Xcentroid 9Ycentroid
%10Cmin 11Rmin 12C*Rmin^1.5 13#cycle 14Vfit 15bin2 16bin3 17bin4
%18unbin 19unbincount 20rangecycle 21zlvlaw 22zlvsmooth (spline) 23zlvsmooth
(movmedian)

for o=1:size(listnorm,1);
nfr=listnorm(o,1)-(listnorm(o,13)-1)*cicle;
nfrproy= ceil(nfr/rfps);

if nfrproy==1
listnorm(o,15:17)=0;
elseif nfrproy==2
for q=2:size(bin2,1)
if listnorm(o,14)<=bin2(q)
listnorm(o,15)=q-1;
listnorm(o,16)=0;
listnorm(o,17)=0;
break
end
end
elseif nfrproy==3
for q=2:size(bin3,1)
bin3flip=flipud(bin3);
if listnorm(o,14)<=bin3flip(q,1)
listnorm(o,15)=0;
listnorm(o,16)=size(bin3,1)+1-q;
listnorm(o,17)=0;
break
end
end

```

```

end

elseif nfrproy==4 || nfrproy==5 || nfrproy==6 || nfrproy==7 || nfrproy==8
    for q=2:size(bin4,1)
        if listnorm(o,14)<=bin4(q)
            listnorm(o,15)=0;
            listnorm(o,16)=0;
            listnorm(o,17)=q-1;
            break
        end
    end
end

end
%GETTING RID OF TRANSITION FRAMES
if (mod(listnorm(o,1),rfps)==1 && nfrproy<=4)
    listnorm(o,15:17)=0;
end
end

listnorm(:,18:24)=0;

%go each particle and obtain zlevel
for i=1:max(listnorm(:,2)) %go through each particle    obtain mode of the big bins (this
is the most probable big bin)

    % partnorm: %1frame 2Partid 3X 4Y 5normwavg 6normmax 7Plane 8Xcentroid 9Ycentroid
    %10Cmin 11Rmin 12C*Rmin^1.5 13#cycle 14Vfit 15bin2 16bin3 17bin4
    %18unbin 19unbincount 20rangecycle
    clearvars mainbin difpartnorm partnorm
    partnorm=listnorm(listnorm(:,2)==i,:); %each particle

    for ncic=min(partnorm(:,13)):max(partnorm(:,13)) %go through each cycle of illumination:
        adjust big bin in the case of a change of number

        clearvars partcycle mainbin unbin unbinmax peak peakloc partnonzero difpart
        absdifpart indidif change vma indmax meddif
        partcycle=partnorm(partnorm(:,13)==ncic,:);
        mainbin=vertcat(partcycle(partcycle(:,15)>0,15),partcycle(partcycle(:,16)>0,16));
        unbin=unique(mainbin);

        if isempty(unbin) | partcycle(:,17)==0
            partcycle(:,18)=NaN;

        else

            %find if the bin occurs more than 50% else check with the change of
            %bin during frames
            for w=1:size(unbin);
                unbin(w,2)=sum(mainbin(:,1)==unbin(w)); %how many occurrences of bin
            end
            unbinmax=unbin(unbin(:,2)==max(unbin(:,2)),1);
            unbinmaxc=unbin(unbin(:,2)==max(unbin(:,2)),2);

            if size(unbinmax,1)==1
                partcycle(:,19)=unbinmaxc;
                partcycle(:,20)=range(partcycle(partcycle(:,17)~=0,17)); %range of that
cycle

                if unbinmaxc>=countmax;
                    partcycle(:,18)=unbinmax;
                else
                    partcycle(:,18)=NaN;
                end

                if partcycle(:,20)>1mbin %change of bin in the middle of illumination cycle
case
                    partnonzero=partcycle(partcycle(:,17)~=0,:);
                    difpart=diff(partnonzero(:,17));
                    [absdifpart,inddif]=max(abs(difpart));
                    meddif=mean(difpart);

```

```

change=findchangepts(partnonzero(:,17),'Statistic','linear','MinThreshold',3);
    if isempty(change)
    else
        if meddif<0
            [vma,indmax]=max(partnonzero(:,17));
            partnonzero(indmax+1:end,18)=partnonzero(indmax+1,18)+1;
        else
            [vma,indmax]=min(partnonzero(:,17));
            partnonzero(indmax+1:end,18)=partnonzero(indmax+1,18)-1;
        end
    end
    for m=1:size(partnonzero,1)
        fr=partnonzero(m,1);
        partcycle(partcycle(:,1)==fr,18)=partnonzero(m,18);
    end
end

else %particles that dont have majority clear of bin
    partcycle(:,18)=NaN;
    if unbinmaxc==rfps-1;
        partcycle(:,19)=3;
    end
end
end

%partnorm(partnorm(:,13)==ncic,18:20)=partcycle(:,18:20);

listnorm(listnorm(:,2)==i & listnorm(:,13)==ncic,18:20)=partcycle(:,18:20);

end

% ADJUST THE COLUMN INDEX AFTER ADDING THE COUNTS

listnorm(listnorm(:,2)==i & listnorm(:,17)==0,21)=NaN;;
listnorm(listnorm(:,2)==i & listnorm(:,17)>0,21)=(listnorm(listnorm(:,2)==i &
listnorm(:,17)>0,18)-1)*sublev+listnorm(listnorm(:,2)==i & listnorm(:,17)>0,17);

end

%% code to fillup "useless" frames

listnormfix=listnorm;
for i=1:max(listnormfix(:,2))
    clearvars partnorm
    partnorm=listnormfix(listnormfix(:,2)==i,:);
    t=1;
    while t<=2

        for ncic=min(partnorm(:,13)):max(partnorm(:,13))
            clearvars partcycle_1 partcyclebeg partcycle1 partcycleend
            if ncic>1

                partcycle_1=partnorm(partnorm(:,13)==ncic-1,:);
                partcyclebeg=partnorm(partnorm(:,13)==ncic & partnorm(:,17)>0 ,:);

                %DO THIS BUT BACKWARDS
                if isnan(partcyclebeg(:,18)) & size(partcycle_1,1)>=4 &
size(partcyclebeg,1)>=4

                    mend_1=median(partcycle_1(end-3:end,17));
                    mbeg=median(partcyclebeg(1:4,17));
                    if mend_1>=14 & mbeg<=7 %this means that the bin changed to next
                        partnorm(partnorm(:,13)==ncic,18)=median(partcycle_1(end-
3:end,18))+1;

```

```

elseif mend_1<=7 & mbeg>=14 %this means that the bin changed to the
previous one
    partnorm(partnorm(:,13)==ncic,18)=median(partcycle_1(end-
3:end,18))-1;
else
    partnorm(partnorm(:,13)==ncic,18)=median(partcycle_1(end-
3:end,18));
end
end

end
if ncic<max(partnorm(:,13)) %do the same thing but backwards
    partcycle1=partnorm(partnorm(:,13)==ncic+1 & partnorm(:,17)>0,:);
    partcycleend=partnorm(partnorm(:,13)==ncic,:);
    if isnan(partcycleend(:,18)) & size(partcycle1,1)>=4 &
size(partcycleend,1)>=4
        mende=median(partcycleend(end-3:end,17));
        mbeg1=median(partcycle1(1:4,17));
        if mende>=14 & mbeg1<=7 %this means that the bin changed to next
            partnorm(partnorm(:,13)==ncic,18)=median(partcycle1(1:4,18))-1;

previous one
            partnorm(partnorm(:,13)==ncic,18)=median(partcycle1(1:4,18))+1;
        else
            partnorm(partnorm(:,13)==ncic,18)=median(partcycle1(1:4,18));
        end
    end

end

    partnorm(partnorm(:,17)>0,21)=(partnorm(partnorm(:,17)>0,18)-
1)*sublev+partnorm(partnorm(:,17)>0,17);

end
t=t+1;
end
listnormfix(listnormfix(:,2)==i,:)=partnorm;

end

%% obtain polynomial fit for trajectory in Z for each particle & calculate velocity
of particle
% apply mapping function
% partnorm: %1frame 2Partid 3X 4Y 5normwavg 6normmax 7Plane 8Xcentroid 9Ycentroid
%10Cmin 11Rmin 12C*Rmin^1.5 13#cycle 14Vfit 15bin2 16bin3 17bin4
%18unbin 19unbincount 20range cycle 21 zlevraw 22 zlevinterp
%23 R^2 from fit 24 u 25 v 26w 27 RMSE of fit 28 zreal
%29 xreal 30 yreal

%load mapping functions
load('mapping_x.mat'); %mdlX
load('mapping_y.mat'); %mdlY
load('mapping_z.mat'); %f1
listnormfix2=zeros(1,30);
for i=1:max(listnorm(:,2))
    clearvars partnorm frall zfit xfit xfit2 yfit yfit2 u v w xfitfin
    partnorm=listnormfix(listnormfix(:,2)==i,:);
    yfit=partnorm(:,21);
    yfit2=yfit;
    yfit2(isnan(yfit))=[];
    xfit=partnorm(:,1);
    xfit2=xfit;
    xfit2(isnan(partnorm(:,21)))=[];

    if isempty(xfit2)
    else
        partnorm(partnorm(:,1)<min(xfit2),:)=[]; %SO THAT WE DONT EXTRAPOLATE
        partnorm(partnorm(:,1)>max(xfit2),:)=[];
        xfitfin=partnorm(:,1);
    end
end

```



A 4 : Matlab function “*gauss\_fit.m*” used as a reference to calculate  $I_0$ .

```
function [cx,cy,cmin,rmin] = gauss_fit( ff, imax, jmax )
%GAUSS_FIT Finds the intensity of a particle image by least squares
% ci = center intensity of Gaussian best fit
% ra = radius or width of the best fit
% cx, cy = centroids from Gaussian fits to the peak along x,y
% cxy, cyx = centroids from Gaussian fits to the peak along diagonals y=x

% Find the maximum intensity location

% Find the centroid in x,y and along the diagonals
[ cx,cy,cxy,cyx,i_zero,rrx,rry ] = finnacentroid( ff,imax,jmax );

% Finna least-square fit for the particle image,
% varying radius and Intensity plus/minus Ndx percent
Ndx = 20; Np = ( 2 * Ndx ) + 1;
dmin = 10^6; cmin = 0; rmin = 0;
for ic=1:Np
    c_zero = i_zero(1) * ( double( ic + 79 ) / 100. );
    for ir=1:Np
        r_zero = rrx * ( double( ir + 79 ) / 100. );
        ff_fit = ggfit( ff,imax,jmax,cx,cy,c_zero,r_zero );
        dd_diff = ff_diff( ff,ff_fit );
        if dd_diff < dmin
            dmin = dd_diff;
            cmin = c_zero;
            rmin = r_zero;
        end
    end
end
itotal = cmin * rmin^1.5;
end
```

A 5 : Matlab function “*finnacentroid.m*” used to obtain the centroid of the particle and ventral intensities.

```
function [ cx,cy,cxy,cyx,i_zero,rrx,rry ] = finnacentroid( ff,imax,jmax )
%FINNACENTROID Summary of this function goes here

% Find centroid
if jmax<2
    jmax=2;
end

if imax<2
    imax=2;
end

s=size(ff);
if jmax>=s(1)
    jmax=jmax-1;
end

if imax>=s(2)
    imax=imax-1;
end

cx = 0.5 * ( log(ff(jmax,imax-1)) - log(ff(jmax,imax+1)) ) / ...
    ( log(ff(jmax,imax-1)) + log(ff(jmax,imax+1)) - 2 * log(ff(jmax,imax)) );
```

```

cy = 0.5 * ( log(ff(jmax-1,imax)) - log(ff(jmax+1,imax)) ) / ...
    ( log(ff(jmax-1,imax)) + log(ff(jmax+1,imax)) - 2 * log(ff(jmax,imax)) );
cxy = 0.5 * ( log(ff(jmax-1,imax-1)) - log(ff(jmax+1,imax+1)) ) / ...
    ( log(ff(jmax-1,imax-1)) + log(ff(jmax+1,imax+1)) - 2 * log(ff(jmax,imax)) );
cyx = 0.5 * ( log(ff(jmax-1,imax+1)) - log(ff(jmax+1,imax-1)) ) / ...
    ( log(ff(jmax-1,imax+1)) + log(ff(jmax+1,imax-1)) - 2 * log(ff(jmax,imax)) );
cxy = cxy * 2^0.5;
cyx = cyx * 2^0.5;

% Find the Radial spread of the distribution
rrx = (( (1-cx)^2 - cx^2 ) / ( log( ff(jmax,imax) ) - log( ff(jmax,imax+1) ) ) )^0.5;
rry = (( (1-cy)^2 - cy^2 ) / ( log( ff(jmax,imax) ) - log( ff(jmax+1,imax) ) ) )^0.5;
rrxy = ( rrx + rry ) / 2;
% Find the average central intensities
i_zero(1) = ff(jmax,imax) / exp( -(cx/rrx)^2 );
i_zero(2) = ff(jmax,imax) / exp( -(cy/rry)^2 );
i_zero(3) = ff(jmax,imax) / exp( -(cxy/rrxy)^2 );
i_zero(4) = ff(jmax,imax) / exp( -(cyx/rrxy)^2 );
i_zero(5) = ( i_zero(1) + i_zero(2) + i_zero(3) + i_zero(4) ) / 4;

end

```

#### A 6 : Matlab function “*ggfit.m*” that calculates a Gaussian on a matrix x,y locations around the center of the particle

```

function ff_fit = ggfit( ff,imax,jmax,cx,cy,c_zero,r_zero )
%GGFIT Calculate the Gaussian on a matrix of x,y locations around center
r_zero2 = r_zero^2;
center_x = double( imax ) + cx;
center_y = double( jmax ) + cy;
N = size( ff ); NN=N(1); NN2 = N(2);
for i=1:NN2
    for j=1:NN
        dx = double(i) - center_x;
        dy = double(j) - center_y;
        dr2 = dx^2 + dy^2;
        ff_fit(j,i) = c_zero * exp( - dr2/r_zero2 );
    end
end
end

```

#### A 7 : Matlab function “*ff\_diff.m*” that finds RMS difference between data and fit.

```

function dd_diff = ff_diff( ff,ff_fit )
%FF_DIFF Find rms difference between data and fit

N = size( ff ) ;
NN = N(1) ;
NN2=N(2);
% Find the background intensity, summing around the edges ONLY
suma = sum(ff(:,1))+sum(ff(:,end))+sum(ff(1,2:end-1))+sum(ff(end:end-1));
npx= numel(ff(:,1))+numel(ff(:,end))+numel(ff(1,2:end-1))+numel(ff(end:end-1)); %number of
pixels for average
sumave = suma / ( npx ); %perimeter of region
sumdiff = 0.; isum = 0;
for i=1:NN2
    for j=1:NN
        dd2 = ( ff(j,i) - ff_fit(j,i) )^2;
        if ff(j,i) > (1.75 * sumave)
            sumdiff = sumdiff + dd2;
            isum = isum + 1;
        end
    end
end

```

```
        end
    end
    dd_diff = ( sumdiff / double( isum ) )^0.5;
end
```



## A 8 : Matlab function (“*volume\_calibration.m*”) to obtain mapping functions mdlX, mdlY and f1 using the cube and real particles

```

close all
clear all
clc

load('listnorm.mat'); % data from the calibration cube particle tracking (trackmate) using
real images
load('cubecoordinates.mat'); %known coordinates of the fabricated cube

frame4=listnorm(listnorm(:,1)==4,:);
frame4(frame4(:,10)>=20 & frame4(:,10)<=35,11)=0;
frame4(frame4(:,10)>=36 & frame4(:,10)<=52,11)=5;
frame4(frame4(:,10)>=53 & frame4(:,10)<=70,11)=10;
frame4(frame4(:,10)>=71 & frame4(:,10)<=85,11)=15;
frame4(frame4(:,10)>=86 & frame4(:,10)<=105,11)=20;
frame4(frame4(:,10)>=106 & frame4(:,10)<=120,11)=25;
frame4(frame4(:,10)>=121 & frame4(:,10)<=140,11)=30;
frame4(frame4(:,10)>=141 & frame4(:,10)<=155,11)=35;
frame4(frame4(:,10)>=156 & frame4(:,10)<=172,11)=40;
frame4(frame4(:,10)>=173 & frame4(:,10)<=200,11)=45;

%Remove bad points manually
frame4(frame4(:,8)>1200 & frame4(:,10)<20,:)=[];

%frame4:  Frame  PartID  Xround  Yround  maxv  wavg  info  X'  Y'
%Z'  Z  X
%% create a mapping function between X' Z' and Z

figure;
scatter3(frame4(:,8),frame4(:,10),frame4(:,11))
xlabel('X''')
ylabel('Z''')
zlabel('Z')

[f1 gof1] = fit([frame4(:,8) frame4(:,10)],frame4(:,11),'poly22','Robust','LAR');

xprime=0:10:1400;
zprime=0:2:200;

[Xprime Zprime]=meshgrid(xprime,zprime);
Z=f1(Xprime,Zprime);

corrected(:,1:2)=zeros(size(frame4(:,8:9)));
corrected(:,3)=f1(frame4(:,8),frame4(:,10));

hold on
surf(Xprime,Zprime, Z)
hold off

%% create mapping function between X' Y' Z and X

% X' Y' Z X
modelfunX=@(a,X)
a(1)+a(2).*X(:,1)+a(3).*X(:,2)+a(4).*X(:,3)+a(5).*X(:,1).^2+a(6).*X(:,2).^2+a(7).*X(:,3).^2+a(8).
.*X(:,1).*X(:,2)+a(9).*X(:,1).*X(:,3)+a(10).*X(:,2).*X(:,3);
initial=[1 1 1 1 1 1 1 1 1 1]; %initial values for the coefficients a

tableX=[135.7 94.04 0 -23.57
180.4 1151 0 -21.39

```

1133	1111	0	23.57
1089	53.67	0	21.39
118.3	324.6	5	-24.63
722.9	1181	5	4.196
412 374.8	5	-10.69	
713.6	802.9	5	3.721
609.1	109.1	5	-1.314
1091	794.1	5	21.74
305.7	860.2	10	-15.85
882.9	1096	10	11.95
423 572.2	10	-10.21	
712 688.9	10	3.692	
253.2	166.6	10	-18.46
1214	558 10	27.87	
23.11	547.8	20	-26.56
582 1142	20	0.8755	
731.2	1002	20	4.724
451.2	705 20	-8.992	
171.3	408.1	20	-22.71
321.6	268.7	20	-15.43
600.2	568.8	20	1.715
948.7	936.8	20	15.43
683.9	208.7	20	2.344
893.2	430.7	20	12.63
1099	651.8	20	22.92
69.12	982.1	25	-27.88
365 1057	25	-13.33	
854.9	1179	25	10.93
243.4	713 25	-19.4	
634.7	810.7	25	0.0065
928.5	884.8	25	14.56
217.5	394.8	25	-20.62
708.9	517.8	25	3.636
1101	615.6	25	23.04
414.7	28.44	25	-10.93
807.8	126.3	25	8.474
1199	224.5	25	27.88
1094	870.9	30	22.99
715.5	998.7	30	4.044
335.6	1128	30	-14.9
966.5	491.2	30	16.58
587.8	619.2	30	-2.368
206.8	747.4	30	-21.31
934.4	81.14	30	14.9
459.8	240.5	30	-8.78
78.99	368.9	30	-27.72
712.2	983.2	35	3.924
897.8	751 35	13.28	
1146	441.8	35	25.76
479.2	797.1	35	-7.798
603.4	642.4	35	-1.56
727.8	488.5	35	4.679
247.4	611.7	35	-19.52
371.4	456.6	35	-13.28
557.1	225.5	35	-3.924
978.9	1085	40	17.58
1021	693.7	40	19.64
1072	205.6	40	22.21
706.9	858.6	40	3.689
737.6	565 40	5.23	
758.5	370.2	40	6.258
412.8	828.7	40	-11.23
434.1	632.3	40	-10.2
464.2	339 40	-8.662	
1266	777.4	45	32.46
1092	429.2	45	23.44
916.8	81.94	45	14.42
917.5	734.4	45	14.56
830.4	560.5	45	10.05
699.3	300.2	45	3.29
788.3	908.9	45	7.89
656.5	647.8	45	1.127

```

524.4    387.2    45   -5.636
526.4    1041    45   -5.498
394.9    779.5    45  -12.26
263.3    518.6    45  -19.02
];
tX=array2table(tableX,'VariableNames',{'X_','Y_','Z','X'});

opts=statset('nlinfit');
opts.RobustWgtFun= 'bisquare';
mdlX = fitnlm(tX,modelfunX,initial,'Options',opts);
a=mdlX.Coefficients.Estimate;

corrected(:,1)=feval(mdlX,[frame4(:,8),frame4(:,9), corrected(:,3)]);

%% create mapping function between X'Y' Z and Y

modelfunY=@(a,X)
a(1)+a(2).*X(:,1)+a(3).*X(:,2)+a(4).*X(:,3)+a(5).*X(:,1).^2+a(6).*X(:,2).^2+a(7).*X(:,3).^2+a(8).
*X(:,1).*X(:,2)+a(9).*X(:,1).*X(:,3)+a(10).*X(:,2).*X(:,3);
initial=[1 1 1 1 1 1 1 1 1]; %initial values for the coefficients a

tableY=[135.7    94.04    0   -23.99
180.4    1151    0   25.95
1133    1111    0   23.99
1089    53.67    0  -25.96
118.3    324.6    5  -13.22
722.9    1181    5   27.63
412 374.8    5  -10.82
713.6    802.9    5   9.613
609.1    109.1    5  -23.55
1091    794.1    5   9.137
305.7    860.2   10  12.45
882.9    1096    10  23.74
423 572.2   10  -1.446
712 688.9   10   4.197
253.2    166.6   10 -20.99
1214    558 10  -2.176
23.11    547.8   20  0.9803
582 1142   20  30.09
731.2    1002   20  19.59
451.2    705 20   5.039
171.3    408.1   20 -9.517
321.6    268.7   20 -16.37
600.2    568.8   20  1.819
948.7    936.8   20  16.37
683.9    208.7   20 -19.38
893.2    430.7   20 -8.468
1099    651.8   20  2.449
69.12    982.1   25  18.81
365 1057   25  22.44
854.9    1179   25  28.49
243.4    713 25   5.469
634.7    810.7   25  10.31
928.5    884.8   25  13.94
217.5    394.8   25 -10.29
708.9    517.8   25 -4.247
1101    615.6   25  0.5918
414.7    28.44   25 -28.49
807.8    126.3   25 -23.65
1199    224.5   25 -18.81
1094    870.9   30  13.33
715.5    998.7   30  19.75
335.6    1128   30  26.16
966.5    491.2   30 -5.611
587.8    619.2   30  0.8015
206.8    747.4   30  7.214
934.4    81.14   30 -26.16
459.8    240.5   30 -18.14
78.99    368.9   30 -11.73
712.2    983.2   35  19.13

```

```

897.8    751.35    7.404
1146     441.8    35   -8.226
479.2     797.1    35    9.769
603.4     642.4    35    1.954
727.8     488.5    35   -5.861
247.4     611.7    35    0.4108
371.4     456.6    35   -7.404
557.1     225.5    35  -19.13
978.9     1085     40   24.44
1021      693.7    40    4.543
1072      205.6    40  -20.32
706.9     858.6    40   12.95
737.6     565.40   -1.973
758.5     370.2    40  -11.92
412.8     828.7    40   11.41
434.1     632.3    40    1.459
464.2     339.40  -13.46
1266      777.4    45    8.811
1092      429.2    45   -9.04
916.8      81.94    45  -26.89
917.5      734.4    45    6.649
830.4      560.5    45   -2.277
699.3      300.2    45  -15.67
788.3      908.9    45   15.62
656.5      647.8    45    2.231
524.4      387.2    45  -11.16
526.4      1041     45   22.38
394.9      779.5    45    8.995
263.3      518.6    45  -4.394
];
tY=array2table(tableY,'VariableNames',{'X_','Y_','Z','Y'});

opts2=statset('nlinfit');
opts2.RobustWgtFun= 'bisquare';
mdlY = fitnlm(tY,modelfunY,initial,'Options',opts);
a=mdlY.Coefficients.Estimate;

corrected(:,2)=feval(mdlY,[frame4(:,8),frame4(:,9), corrected(:,3)]);

%% WRITE FILE TO TECPLOT FORMAT

temp=corrected(:,:);
q=1;

filenametrax=sprintf('%03d_%s',q,'reconstr_cube.dat');
fileID2=fopen(filenametrax,'w');
fprintf(fileID2, 'VARIABLES = "x" "y" "z"\r\n');
fprintf(fileID2, 'ZONE T="%d"\r\n',q);
fprintf(fileID2,'%f %f %f\r\n',transpose(temp));      %partID frame# x y bin10 bin20

fclose(fileID2);

```

z